Metal-based molecules for biomedical applications: investigation of their biological activities in cancer cells

PhD Thesis

submitted to Cardiff University in accordance with the conditions
governing candidates for the degree of Doctor of Philosophy
(Chemistry)

by

Brech Aikman

June 2021
Cardiff University

Abstract

Cisplatin, a platinum(II) based drug exhibiting potent cytotoxic effects in highly dividing and proliferating cells, is widely applied as chemotherapeutic agent against several forms of cancer. However, current drawbacks and limitations such as its severe nephrotoxicity and increased drug resistance are still of great concern. This doctoral research aimed to address these issues by exploring the potential of new families of metal-based molecules for biomedical applications as either anticancer agents or anticancer drug delivery vehicles for the aforementioned Pt(II) drug.

Two strategies were then deployed. The first part of the thesis describes the study of small molecule gold(III) complexes with different scaffolds designed as aquaporin (AQP) inhibitors. AQP are membrane proteins enabling permeation of water, but also of small solutes, such as glycerol and hydrogen peroxide, across biomembranes, and their expression has been correlated to several types of cancer, making them attractive as diagnostic and therapeutic targets. Based on preliminary data on AQP modulation (inhibition) by metal-based compounds, two series of gold(III) complexes, either coordination or organometallics, were investigated for their ability to target these membrane proteins using different spectroscopic methods, and the compounds' cytotoxic effect were also studied *in vitro*.

The second part of this thesis focuses on another strategy to improve cisplatin`s selectivity and targeting without altering its structure/properties *via* the use of new generation metal-based drug delivery systems, which are able to protect the drug from metabolism (speciation) and to facilitate its uptake in cancer cells. Therefore, supramolecular coordination complexes (SCCs), specifically three dimensional (3D) metallacages, were chosen. These discrete supramolecular entities, formed via self-assembly of ligands and appropriate metal precursors, can not only be exploited for their host-guest properties to achieve drug encapsulation, but they can also be *exo*-functionalized with targeting moieties to improve their delivery at a tumour site. Our study provides the proof-of-concept that a specific family of metallacages of general formula $[Pd_2L_4]^{4+}$ (L= ligand), bioconjugated to integrin targeting ligands, can encapsulate cisplatin and increase its potency in human cancer cells overexpressing the integrin receptors. Moreover, the metallacages can be functionalized with fluorophores to enable the study of their uptake and intracellular distribution by

fluorescence microscopy. As such, the mechanism of accumulation of $[Pd_2L_4]^{4+}$ cages labelled with fluorescent BODIPY moieties was investigated *in vitro*.

Acknowledgements

I would like to start by thanking my supervisor Prof. Angela Casini. Angela, after meeting you in Groningen, I got inspired by your passion for research and decided to pursue this opportunity in Cardiff. It was a pleasure and privilege to have you as my mentor throughout the PhD, always ready to share knowledge and provide support not only at work but also in life. Your ability to make connections between different scientific fields and people is brilliant, and I am glad to have been part of your group, not in the least because of your excellent restaurant choices. I could not have done this without you!

Many thanks to my fellow group members who have been part of the "Casini Crew" during my stay and to the students and visitors who have made my experience in Cardiff very colorful. Thank you Andreia, for guiding me in the cell lab and introducing me to the world of cells and aquaporins. I am very grateful to have met Margot, whom I got to know as a group member and became my dear friend, always there to listen to me and share my love of hikes and chocolate.

I`d also like to express my thanks to Prof. Graça Soveral and her group, for welcoming me in their lab in Lisbon to teach me and as great collaborators. It was a wonderful experience. Special thanks to Prof. Arwyn Jones and Dr. Edward Sayers (School of Pharmacy) for allowing me to use their confocal microscope and for the excellent discussions and feedback.

To the wonderful people I`ve met during my stay, thank you so much. Tim and Sam, thanks for introducing me to the Welsh language and how to properly celebrate a rugby match. Flore & Mathieu, I wish I met you sooner in Cardiff.

A big thank you to my dear parents, Jaqueline and Siegfried, brothers Bas and Rik and sister Puck, family and friends, supporting me when I decided to move to an island, visiting me frequently to share my adventure in Wales. We have made some great memories. I would have never guessed that upon my return back to the Netherlands, we`d still have to continue meeting mainly online.

My “kei-leider”, boyfriend, fiancé, partner, Jurre. Many names describing one person but always my love. I could not have done this without you and your continuous encouragement and support, joining me not only in Wales, but Portugal and Japan as well. Bjørn my beautiful child, you made me a mother. I cannot wait to further explore this world with you.

Table of Contents

List of Figures

List of Tables

Chapter 1: Introduction

1.1 Metallodrugs as anticancer agents

Although the body relies on several essential metal ions to function (copper, zinc, iron etc)[1], and metal-based compounds have been used to treat various conditions and diseases for over centuries, modern medicine for a long time did not consider metals from the transition metals group as possible therapeutics, due to their potential toxic nature. The FDA approval and introduction to the clinic of cisplatin as a successful chemotherapeutic agent changed this attitude in the second part of the 20th century, boosting the field of medicinal inorganic chemistry. Therefore, using transition metal ions, many non-conventional (compared to more traditional organic small molecules) biologically active metal-based compounds saw light. Nowadays, several metal-containing therapeutic and diagnostic agents are used in the clinic, including radiopharmaceuticals containing ^{99m}Tc for single-photon emission computed tomography (SPECT) imaging [2] (e.g. to detect breast cancers or melanoma), magnetic resonance imaging (MRI) contrast agents based on Gd(III) targeting tumour tissues [3], as well as numerous experimental therapeutic metallodrugs, based on different metal ions within the periodic table.[4]

1.2 Cisplatin and derivatives

Cis-diamminedichloroplatinum(II), otherwise known as **cisplatin**, is a platinum(II) based drug exhibiting potent cytotoxic effects in highly dividing and proliferating cells, two well-known characteristics of tumour cells. The molecule was already synthesized by Peyrone in 1844, but Rosenberg and co-workers were the first to report its cytostatic effect in *E. coli* cells in 1965.[5,6] Recognizing its potential as anticancer drug cisplatin was extensively tested in various human cancer cell lines, until the first human patient was treated in 1971.[7] Approval for use in cancer chemotherapy by the by the Food and Drug Administration (FDA) followed soon in 1978. Today, cisplatin remains one of the most prescribed anticancer chemotherapeutics and is applied as monotherapy and in combination regimes to treat several forms of advanced and metastasised cancers of ovary, head, and neck, while it is especially successful in testicular cancer with an overall cure rate of 90%.[8] Despite the widespread application, severe dose-related adverse effects resulting in (cumulative) neuro-, oto-, and especially nephrotoxicity together with increased acquired tumour resistance, limit the use of cisplatin.[9–11]

In an effort to overcome these major obstacles whilst retaining the favourable characteristics of the Pt(II) metal, the search for improved platinum-based complexes with higher selectivity and possibly broader spectrum of activity resulted in a second generation of metallodrugs with different ligand scaffolds such as **carboplatin** and **oxaliplatin**.[12–14] Together with cisplatin, these two are FDA approved analogues and used in clinics around the world. Three other analogues are currently only approved for clinical use in specific countries: **nedaplatin** in Japan[15], **heptaplatin** in South Korea[16] and **lobaplatin** in China[17] (Figure 1.1) All of them show improved toxicity profiles but distinctive side effects as well.

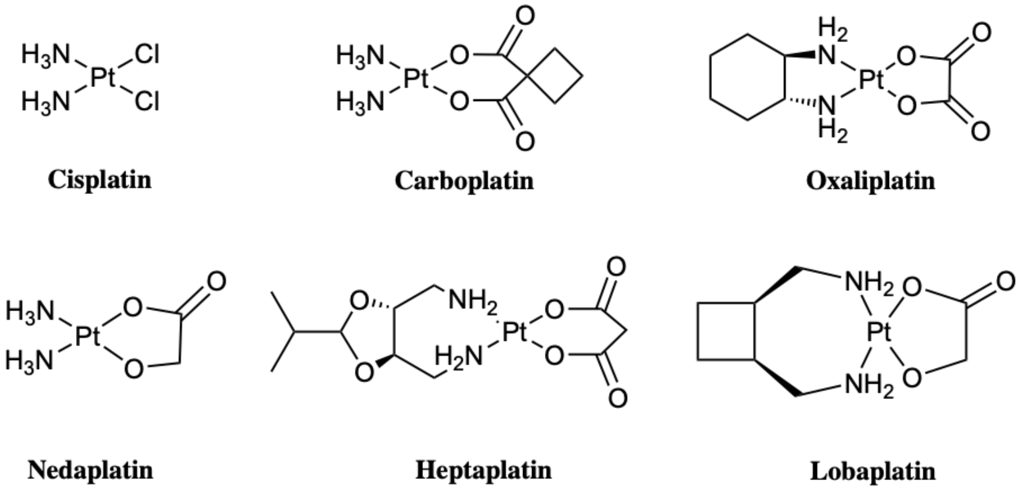

Figure 1.1: Chemical structures of cisplatin and other clinically approved Pt(II) anticancer drugs.

Carboplatin was developed as a more selective and less nephrotoxic cisplatin analogue. [18] It is the second platinum drug approved by the FDA (1989). The complex features a bidentate dicarboxylate ligand instead of the two chlorides. This ligand improves the overall stability of the structure as it is less prone to be reduced compared to cisplatin. The altered reactivity of the metal centre due to the chelating nature of the leaving group might be why there is a higher drug tolerance of the body for carboplatin. Compared to its predecessor, carboplatin shows reduced nephro- and neurotoxicity, but unfortunately new issues arose such as higher myelotoxicity and hypersensitivity.[19] Carboplatin is used to treat ovarian, lung, head and neck cancers.

Oxaliplatin has been developed to overcome the observed carboplatin cross-resistance in cisplatin-resistance in tumours and was found to be particularly effective towards various colon cancer cells lines.[20] FDA approved in 2002, it is a major contributor as chemotherapeutic agent in the treatment of metastatic colorectal cancer when combined with leucovorin and 5-fluorouracil, improving both response rate as the overall survival of patients.[21–23] The drug features a chelating oxalate leaving group ligand and a chelating *R, R*-diaminocyclohexane (DACH) nonleaving group ligand. Oxaliplatin induces less oto- and nephrotoxicity compared to cisplatin and carboplatin, as the compound does not accumulate. It can however induce neurotoxicity leading to peripheral neuropathy and cause hematologic and gastrointestinal tract toxicities.[24]

Several next generation platinum-based drugs have been entered in clinical trials but most were discontinued due to severe side effect; an overview can be found in a review by Wheate et al.[25] Examples of novel entities currently undergoing clinical evaluation are **satraplatin** and **lipoplatin** (Figure 1.2).[26] **Lipoplatin** is the liposome nanoparticle formulation of cisplatin, and tested in combination with other drugs in several phase III trials. **Satraplatin** (*trans,cis,cis*-bis(acetato)amminecyclohexylamine-dichloroplatinum(IV)) is part of the Pt(IV) prodrugs, and especially interesting as it is the first orally active platinum analogue.[26,27]

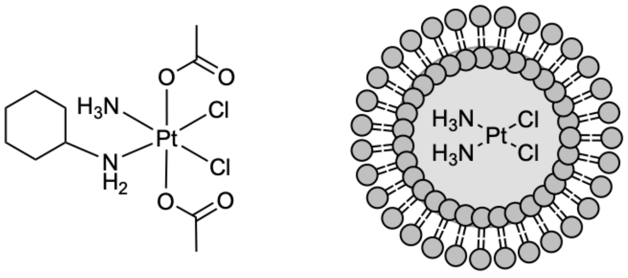

Satraplatin **Lipoplatin**

Figure 1.2*: Next generation platinum complexes* ***satraplatin*** *and lipoplatin. Image represents general scheme of* ***lipolatin****, a liposomal nanoparticle encapsulating cisplatin molecules.*

1.3 Mechanism of action of Pt(II) drugs

Pharmacokinetics & pharmacodynamics

Cisplatin is administrated directly into the bloodstream via intravenous injection. The free drug is quickly distributed through all tissues, with a plasma half-life of 20-30 min after bolus.[28] Less than 10% remains in the plasma after 1h of infusion. The highest accumulation is observed in the liver and kidneys. The platinum clearance peaks in the first 2 h, then decreases as most of the drug is covalently bound to serum proteins such as albumin[29], transferrin[30] and γ-globulin (~90%)[31].[32] Within 24 h, 20-43% of the administrated dose is excreted in urine. From this eliminated cisplatin, roughly 15% is recovered unchanged.[33,34]

The platinum(II) drugs are thought to exhibit a similar mechanism of action, with four important steps that follow intravenous administration: *intracellular uptake*, *aquation or activation*, *DNA binding of the active complex* and finally *apoptosis induced cell death*. Although, it should be mentioned that recent studies point to different targets other than nucleic acids, as in the case of **oxaliplatin** for which ribosome biogenesis stress has recently been observed in cancer cells.[35]

While extensively researched, the uptake mechanism of platinum(II) drugs is still not fully disclosed. Both passive and active modes of uptake could play a role. Passive diffusion over the membrane seems to be the main route, as the small cisplatin complex appears neutral in the bloodstream and experiments demonstrated the uptake to be proportional to the total amount of cisplatin whilst no saturation occurs under increasing concentrations.[36] Nevertheless, numerous studies in the last decades suggest that active transport facilitated by membrane proteins might also be involved, with copper transporter 1 (Ctr1)[37] and organic cation transporters (OCTs)[38] as likely candidates. The exact role of these transporters still needs to be elucidated, but with time more details regarding the mechanism are unravelled. Take the copper transporters for example; although binding of cisplatin to Ctr1 was observed, actual influx through the channel has not been proved. In fact, new data indicates a more mediative role for the Ctr1, where the cisplatin-Ctr1 construct is seemingly internalized via micropinocytosis.[37]

Upon entering the cell, cisplatin undergoes hydrolysis of one or both chloride ligands, subsequently activating the compound into a highly reactive species. It can therefore be considered as a pro-drug. The driving force of this aquation is the low intracellular chloride concentration (4 - 20 mM), which explains why the complex remains intact in the bloodstream where the high chloride concentration (~104 mM) suppresses the ligand exchange.[39] In the cases of carboplatin and oxaliplatin, both their chelating ligands (bidentate dicarboxylate and oxalate respectively) undergo substitution with water molecules, but at a much lower rate than cisplatin. Hence their longer half lives in plasma ($t_{1/2}$ weeks vs hours).[26,33,40,41]

Following hydrolysis, the positively charged diaqua-platinum compound interacts with its primary biological target DNA. It has a high affinity for the nitrogen-rich N-7 nucleobases on guanine (G) and to a lesser extent for adenine (A), displacing its aqua-ligands upon coordination (Figure 1.3-I).[42] Binding to these nucleophilic positions on the same strand or different DNA strand introduces inter- and intrastrand crosslinks, respectively, in the major groove of the DNA helix (Figure 1.3-II).[43]

The covalent adduct formation between the active Pt(II) and DNA results in a dramatic structural distortion. The DNA is unable to unwind, effectively suppressing replication and transcription processes which are essential for cell function and survival. Cell-cycle arrest can occur at the G_2/M checkpoint, and when repair of the damaged DNA fails, cell death through apoptosis follows.[44]

In addition to the 'alkylating' DNA effect, platinum-based drugs can also bind to RNA, phospholipids and amino acids present in enzymes and structural proteins.[45,46] Mitochondrial injury has also been observed, specifically due to inhibition of the respiratory chain, which would increase oxidative stress in cells.[47,48] These effects strengthen the cytotoxicity of cisplatin. Alas, due to the lack of selectivity, healthy cells are targeted in addition to cancer cells. The pharmacokinetics show a distribution of the complex through all tissues in the body, with the highest accumulation observed in the liver and kidneys, organs involved in metabolism and elimination. Concerning toxicity, the prominent renal injury following cisplatin administration might be the result of the compound's increased uptake in the kidneys, due to filtration of the bloodstream and cisplatin`s binding to the highly expressed Na^+,K^+-ATPase, OCT and Ctr1. [36,49]

Where cisplatin and carboplatin feature a similar pharmacodynamic profile, oxaliplatin behaves differently. It presumably inhibits transcription and translation of DNA like the other two, but *via* an alternate route due to the presence of the DACH non-leaving group. The oxaliplatin induced DNA-Pt-DACH adduct is able to activate the p53-dependent DNA damage-independent cascade, rapidly inducing cell death.[50] In combination therapy with 5-fluorouracil, this greatly enhances the cytotoxic effect.[50] Another study suggest the observed p53 activation is caused by oxaliplatin induced defects in ribosome biogenesis, an effect not seen for cisplatin.[35] Ribosomes are involved in biological protein synthesis, translation, guided by mRNA codons to link amino acids in a specific order. Oxaliplatin has been reported to impair this process of protein synthesis, seemingly targeting rRNA and instigating cell death *via* the ribosomal biogenesis stress pathway. [35]

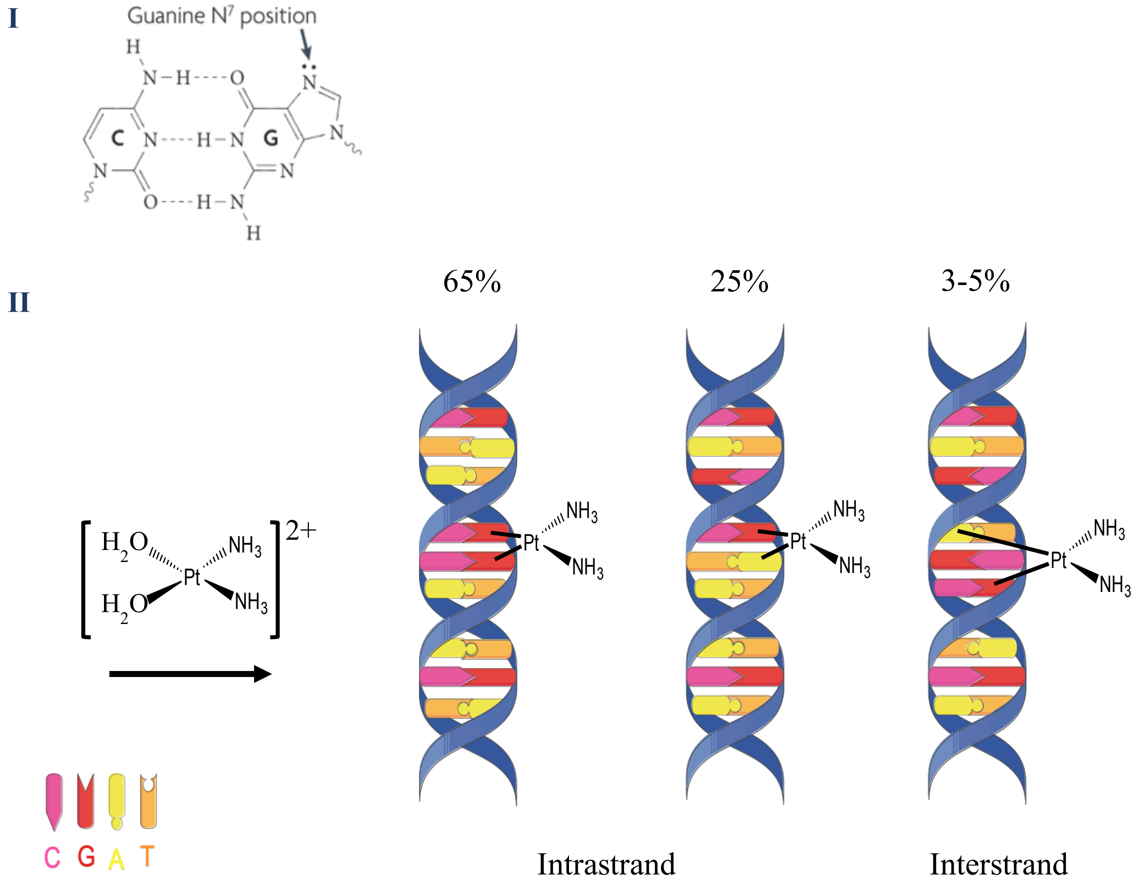

Figure 1.3*: I) Aquated cisplatin covalently binds with nuclear DNA, preferably at the N7 position of the purine base imidazole of guanine (G). II) Most crosslinks occur on the same strand in a GpG 1,2 intrastrand (65%) and ApG 1,2 intrastrand (25%) fashion. Interstrand crosslinks are less frequent, such as the GpXpG 1,3 intrastrand crosslink (3-5%). Figure inspired by reference [51].* [51] *Figure created using images from Servier Medical Art Commons Attribution 3.0 Unported License. (http://smart.servier.com).*

1.3.1 Platinum resistance

Limiting both dose and administration frequency relieves some of the off-target injury of cisplatin, but unfortunately, gives rise to intrinsic or acquired resistance by the tumour.[52] The cancer adapts to the treatment and develops multifactorial resistance mechanisms towards cisplatin, as illustrated in Figure 1.4. Aiming to decrease intracellular drug accumulation and thus inhibiting the drug's effect, tumour cells are able to reduce uptake of cisplatin and at the same time increase its efflux. [39,53] The portion of drug that eventually manages to accumulate in the cell will possibly undergo sequestration by increased levels of glutathione or metallathionein.[52] The glutathione-cisplatin conjugate can also be recognized by the multidrug resistance-associated protein 2 (MRP2), a transporter with increased expression in cisplatin-resistant tumours, reducing the amount of cisplatin available for nuclear interaction.[54,55] Finally, the tumour can show resistance towards platinum species after binding to DNA. An enhanced nuclear tolerance towards platinum-DNA adducts could cause a loss of DNA mismatch repair, bypass of the DNA adducts and, in the end, a decreased apoptosis. The platinum-DNA adducts could also undergo increased repair, by an upregulated nucleotide-excision repair system.[51,53] Interestingly, oxaliplatin is actually administered in cisplatin-resistant tumours. It seems that the bulky DACH ligand prevents biding of proteins responsible for the repair of the DNA lesions caused by Pt(II) crosslinks.[56] Moreover, in the case of oxaliplatin, there is no recognition of the platinum-DNA construct by the important mismatch-repair (MMR).[57] This effect might also be the result of the aforementioned alternative mode of action, whereby oxaliplatin can target mRNA.[35]

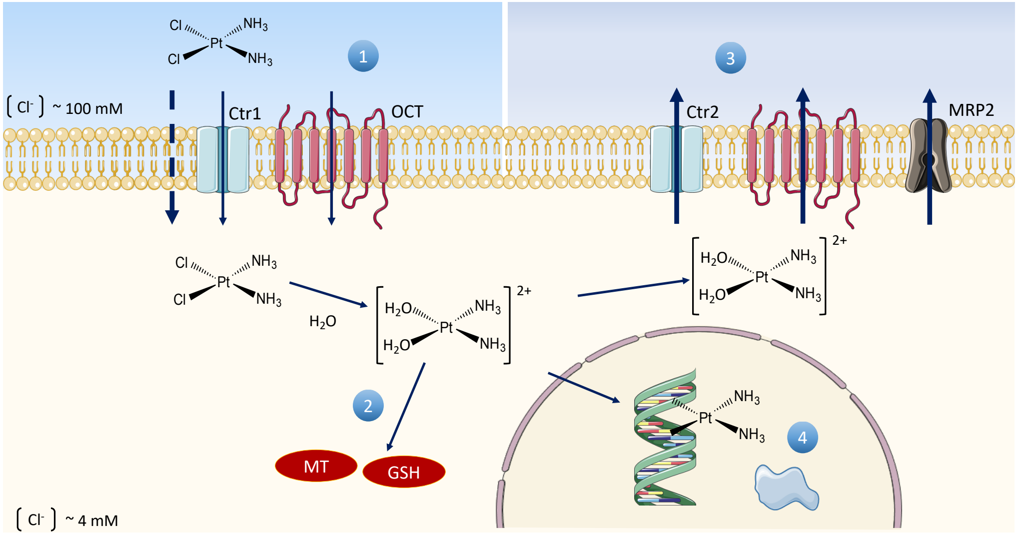

***Figure 1.4**: Potential mechanisms involved in cisplatin resistance. 1) reduced uptake from bloodstream into the cell*[39] *2) increased intracellular reduction via glutathione (GSH)*[58,59] *or metallothionein (MT)*[60]*, 3) enhanced efflux via for example copper transporter 2 (CRT2)*[54] *or the multidrug resistance-associated protein 2 (MRP2) transporter*[55] *4) recovery of altered DNA via DNA repair proteins*[51]*. OCT = organic cation transporter. Figure created using images from Servier Medical Art Commons Attribution 3.0 Unported License. (http://smart.servier.com).*

1.4 Other families of anticancer metallodrugs

In an effort to address the current drawbacks and limitations of cisplatin and its analogues, other metals were explored as an alternative to Pt(II) complexes. Potential candidates are other transition metals of the same d-block from the periodic table, which have unique characteristics to exploit. The transition metals, for example, possess the ability to coordinate ligands in a three-dimensional configuration, allowing structures unique for those individual ligands and metals.[61,62] This enables the formation of structures designed for specific molecular targets, which cannot be realized by conventional organic compounds via, for example, square planar geometry. In addition to differences in coordination geometry, their redox activity, binding preference according the hard and soft acids and bases (HSAB) principle and ligand exchange reactions could provide alternative and/or improved anticancer strategies.[62] As such, complexes containing ruthenium[63], copper[64], iron[65] and gold[66] exhibiting cytotoxicity towards cancer cells have been synthesized and are intensively investigated.

1.4.1 Ruthenium-based anticancer drugs

Inspired by the success of cisplatin, Ru(III) complexes featuring similar am(m)ine- and chloridoligands were considered as potential anticancer agents. In the 80s, Clarke presented several Ru(III) ammine complexes such as $[Ru(NH_3)_5Cl]Cl_2$ that like the platinum-based drugs interact with DNA.[67,68] However, unlike the Pt(II) derivatives, Ru(III) complexes, were reduced to active Ru(II) species by intracellular reducing agents such as glutathione (GSH) and acidic environments.[67] Compared to healthy cells, cancers display higher GSH levels and an overall reducing environment with respect to non-tumorigenic cells.[69,70] Ruthenium complexes would therefore be able to take advantage of these cancer-cell-specific features for their activation and, thus, have increased selectivity.

Research into Ru(III) coordination complexes resulted in the synthesis of two promising anticancer drug candidates that were investigated in clinical trials: imidazolium *trans*-$[RuCl_4(DMSO)(HIm)]$ (**NAMI-A**, HIm - imidazole) and indazolium *trans*-$[RuCl_4(1H\text{-indazole})Ru(III)]$ (**KP1019**). Preclinical *in vitro* studies with **NAMI-A** showed mainly anti-metastatic effects, without signs of cytotoxicity. NAMI-A was the first ruthenium drug candidate subjected to phase I and phase II studies.[68] In phase I studies, completed in 2004, NAMI-A was deemed unsuitable as a monotherapy for various solid tumours but showed promise in combination with gemcitabine to treat non-small cell lung carcinoma.[71] Clinical studies of the combinatory therapy finally stranded in phase I/II after results indicated no improvement over treatment with gemcitabine alone.[71]

KP1019 was the second ruthenium-based drug to enter clinical studies as anticancer agent. Preclinical studies in rat demonstrated a significantly higher activity over the standard anticancer drug in treatment of rat colorectal carcinoma and seemed to be able to overcome drug resistance of human tumour samples.[72] Following these promising results, a phase I clinical study was conducted where disease stabilization was observed with only mild toxicities in various cancers, including colon adenocarcinoma.[73] Phase II trials are currently ongoing.[73,74] Cellular uptake of **KP1019** is suggested to occur mainly via binding with the glycoprotein transferrin, after which receptor-mediated endocytosis can take place. Although the binding of **KP1019** to transferrin is observed in experimental setting, evidence for intracellular accumulation of the adduct is still lacking.[75] Cancer cells have a higher demand for iron, overexpressing transferrin receptors on their surface. Affinity for this transporter could therefore contribute to a more selective drug.

Both complexes are quite similar in terms of overall structure, featuring different N-donor ligands in axial positions (Figure 1.5). Interestingly, these apparently moderate structural differences result in markedly diverse bioactivity. While **NAMI-A** seems to be most reactive with protein targets, **KP1019** can also bind to nucleic acids.[75] This might partially explain their distinct pharmacological profiles, as **NAMI-A** shows only antimetastatic effects, whereas **KP1019** is cytotoxic, promoting apoptosis via the mitochondrial pathway.[63] Some Ru complexes seem to mimic iron and are proposed to take advantage of the existing transport and uptake mechanisms in the body.

In addition, following the hypothesis of an “activation by reduction” for Ru(III) complexes to Ru(II) species in cancer cells, several Ru(II)-based anticancer compounds, such as half-sandwiched Ru(II)-arene complexes, have been developed and screened against cisplatin-resistant cancers.[13] More information regarding the development of these interesting structures can be found in a recent book chapter by Romero-Canelon[76], as well as in a review by Meier-Menches et al.[63].

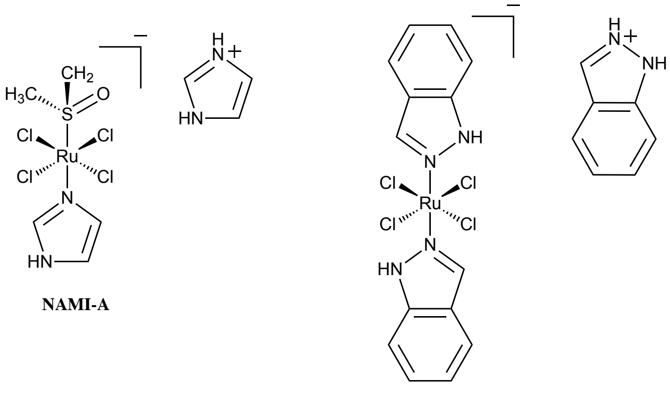

***Figure 1.5**: Chemical structures of Ru(III)-based complexes NAMI-A and KP1019.*

1.5 Gold(III) compounds as anticancer agents

Gold compounds have been widely researched as potential leads due to their unique biological properties. Whilst the oxidation states range from -I to +V, the three states encountered under physiological conditions are Au(0) (colloidal gold), Au(I) and Au(III), with the latter two most commonly investigated for therapeutic purposes. Gold(I) complexes prefer a linear coordination geometry with ‘softer’ alkynyl[77] ligands, phosphanes or selenium and sulphur nucleophiles, whilst the relative ‘harder’ Au(III) centre tends to form square planar complexes with chelating N-donor, but also S-donor ligands.[78] The most well-known gold(I) compound is ([triethylphosphine(2,3,4,6-tetra-O-acetyl-*β*-1-D-(thiopyranosato-S)Au(I)]) **auranofin** (Figure 1.6), an orally administrable Au(I) drug primarily used for treatment of arthritis.[79] Although initially recognized for its anti-inflammatory properties, auranofin was shown to be extremely potent as antiproliferative agent against cancer cells *in vitro.* Interestingly, the cytotoxic effects occurred *via* damage of the mitochondrial pathway, presenting an alternative biological mode of action with respect to DNA-targeting platinum complexes.[80–82] The promising anticancer effects of this coordination complex *in vitro,* therefore, fostered the development of numerous gold-based experimental anticancer agents.

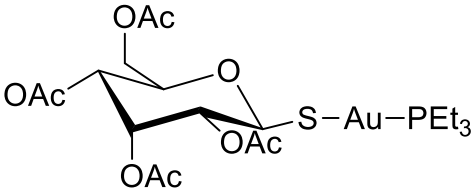

***Figure 1.6**: Chemical structure of the Au(I) complex Auranofin.*

In this context, gold(III) compounds gained attention as this ion is isoelectronic to platinum(II) (both have a d^8 configuration) and features the same square planar configuration in coordination complexes.[83] Interest initially declined due to its tendency to be readily reduced in aqueous environment: gold(III) -> gold(I) -> gold(0).[83–85] Exposure of the reactive Au(III) to physiological conditions would rapidly inactivate the compounds due to formation of colloidal gold by reducing agents, especially intracellular thiols.[52] Therefore, Au(III) complexes are potentially at risk not to be able to reach the tumour site, limiting their application.[69] In the 90s, several novel Au(III) complexes with bidentate ligands were introduced that displayed enhanced stability and favourable anticancer characteristics. In general, the gold(III) complexes can be categorized into two groups: coordination and organometallic complexes, respectively. The latter present at least one direct metal-carbon bond, rendering them more stable to ligand exchange reactions and to reduction in biological environment.[86] Gold(III) coordination complexes currently developed as anticancer compounds contain multi-dentate ligands, with heteroatoms as metal binding sites, such as N^N, N^N^N and tetra-coordinated porhyrins.[87] Examples of gold(III) bidentate complexes featuring a N^N scaffold are $[Au(bipyridyl)(OH)_2][PF_6]$ **Aubipy**, and $[Au(1,10\text{-phenanthroline})Cl_2]Cl$ **Auphen**, whereas $[Au(terpyridine)Cl]Cl_2$ **Auterpy** and $[Au(diethylenetriamine)Cl]Cl_2$ **Audien** are representatives of gold(III) complexes with tridentate N-donor ligands.[78,88,89] Compared to cisplatin, most of these bi- and tridentate complexes screened *in vitro* showed higher cytotoxicity towards cancer cells, including those resistant to cisplatin, with IC_{50} (half maximal inhibitory concentration) values ranging in the micro or even nanomolar range. [78,88,89]

Further research in the field produced more stable complexes with interesting biological properties, using different ligand systems such as the metallacycle **Au(III) porphyrins**[90] or **Au(III) dithiocarbamates**[91] aiming to retain the trivalent oxidation state in reducing environments. Overall, the use of bi- and multidentate ligands in gold(III) complexes provided novel metallodrugs endowed with *in vitro* cytotoxicity values that can rival cisplatin.[66,78,91]

The cyclometalated **$Au(damp)X_2$** compound (damp = 2-[(dimethylamino)methyl]-phenyl, X = Cl) was among the first organometallic complexes to show antiproliferative effects towards bladder and ovarian human cancer cell lines; similarly the Au(III) complexes **$AuCl_3(Hpm)$** (Hpm = 2-pyridylmethanol), **$AuCl_2(pm)$** (pm = 2-pyridylmethanol), **$AuCl_2(mesal)$** (mesal = *N*-

methylsalicylaldiminate) and **$AuCl_2$(esal)** (*N*-ethylsalicylaldiminate) possess antitumor effects toward cisplatin-resistant cell lines, although solubility issues in aqueous conditions limited its applications *in vivo*.[92–95]

The organometallic complexes also feature different bidentate or tridentate ligands, of general formula C^N, C^N^C, C^C^N, N^C^N and C^N^N (Figure 1.7).[96] Such cyclometalated systems may also be classified accordingly to the number of atoms involved in the cycle formation, with 5- and 6-membered ring scaffolds being the most stable and investigated. The great structural versatility of these systems is also provided by the possibility of choosing ancillary ligands (L) endowed with different physical-chemical properties and propensity of ligand exchange reactions in biological environment, leading to either cationic or neutral complexes with different reactivity towards biological nucleophiles.

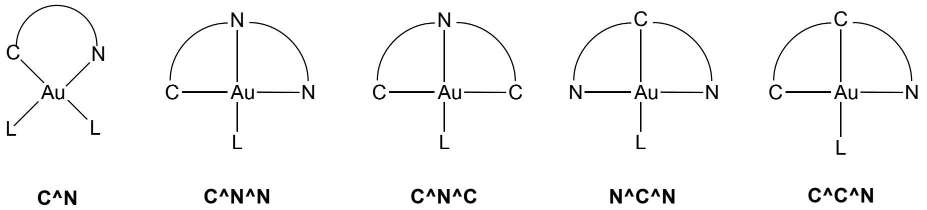

***Figure 1.7**: General scheme of Au(III) cyclometalated complexes.*

An interesting case, among the Au(III) C^N complexes reported so far, is the one of the cyclometalated compound [Au(py^b)PTACl]$^+$ (py^b = 2-benzylpyridine, PTA = 1,3,4-triaza-7-phosphaadamantane).[96] The antiproliferative screening carried out in different human cancerous cell lines showed that the compound was more potent that its dichlorido derivative, most likely due to the presence of the positive charge that, together with the PTA moiety, increases its water solubility. Of note, organogold complexes featuring a similar C^N ligand scaffold have been show to act as 'catalysts' for metal-templated reactions directly in target cells[97]; noteworthy, the [Au(py^b-H)Cl_2] complex was able to promote C-S cross-coupling reactions in physiological environment in the presence of Cys-containing peptides.[98,99] Specifically, following AuC^N-peptide adduct formation, the reaction could proceed to give cysteine arylation (Figure 1.8). This mechanism may be relevant to produce covalent protein inhibitors that can irreversibly modify protein active sites.

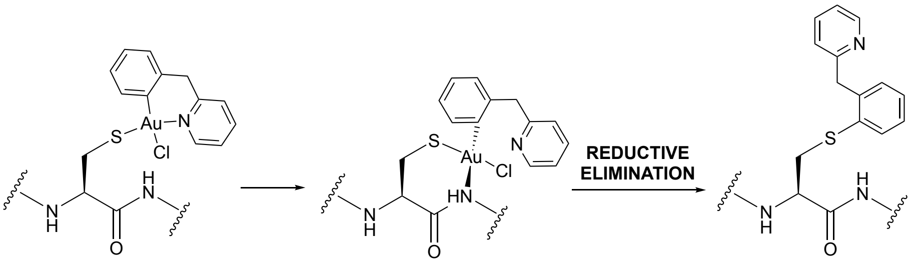

***Figure 1.8**: Proposed mechanism of cysteine arylation by Au(III) C^N complexes via reductive elimination.*

1.5.1.1 Targets of gold compounds

A considerable number of studies investigating the biological effects of gold complexes report cytotoxicity both *in vitro* and *in vivo*.[85,100] At first, gold complexes were expected to display a behaviour akin to Pt(II) complexes due to their similar chemical structure, and were assumed to mainly target DNA. However, the evaluation of auranofin for anticancer purposes suggested the involvement of the mitochondrial damage pathway, showing an alternative mechanism of action.[81] In general, further studies suggested that gold(I) and gold(III) complexes primarily target proteins, and are mostly found bound to sulphur nucleophilic sites, such as the thiol in the side-chain of cysteine residues or thioethers present in methionins.[88,101,102]

Proteins identified as likely targets for metal complexes include the seleno-enzyme thioredoxin reductase (TrxR)[103], zinc-finger domains[104,105] and membrane protein channels,[101] amongst others. These biological targets have also been extensively researched for their relation to cancer. Affinity depends on the type of ligand system used to stabilize the gold ions, as well as on the oxidation state of the gold centre. For example, Au(I) complexes show strong and selective inhibition towards TrxR, whereas Au(III) complexes are efficiently targeting zinc-finger protein domains as well as membrane protein channels, named aquaporins (AQP), responsible for the transport of water and other small solutes across cellular membranes.[82,85,106,107]

As an example, the cytotoxic phenanthroline-based Au(III) coordination complex **Auphen** was shown to be a potent and selective inhibitor of aquaglyceropirin-3 (AQP3), whose level of overexpression has been correlated to several types of cancer (Figure 1.9).[108] Inspired by this success, a similar complex using 1-methyl-2-(pyridin-2-yl)-benzimidazole ligand (**Au1**) has been more recently developed by our group, showing great potential as selective AQP3 inhibitor (Figure 1.9).[109]

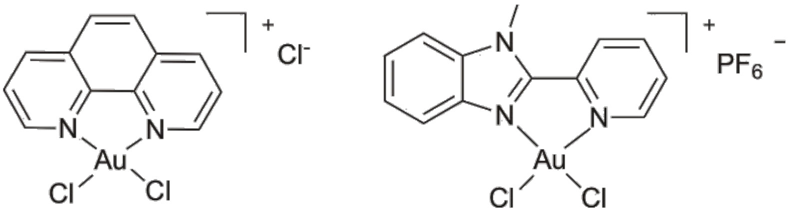

Auphen **Au1**

Figure 1.9: Chemical structures of cytotoxic coordination Au(III) complexes with bidentate N-donor ligands.

Despite recent progress, both compounds require further optimisation in order to guarantee their stability in aqueous environment, and selectivity with respect to AQP inhibition. More studies on their mechanism of action are also necessary to achieve meaningful structure activity relationships. Additionally, understanding of the mechanisms of cancer cellular uptake and sub-cellular distribution *in vitro* will greatly enhance our knowledge of their mode of action. In the future, novel compounds as AQP3 inhibitors can be designed also with the aid of advanced homology models and computational methods, to achieve targeted Au(III)-based compounds as promising alternatives to cisplatin and potent anticancer drugs. Chapter 2 will elaborate on the potential of AQP as Au(III)-drug targets.

1.6 Supramolecular drug delivery systems

The previous sections of this introduction have reported on the state-of-the-art on experimental anticancer metallodrugs of different families and motivated the search for other metal-based complexes as a strategy to address the current drawbacks and limitations of cisplatin. However, there are other approaches to improve selectivity and targeting of cisplatin without altering its structure/properties, such as optimization of new drug delivery systems able to protect the drug from metabolism (speciation) in extracellular media and to facilitate its uptake in cancer cells. In this context, supramolecular structures hold great promise.

In general, supramolecular molecules are based on interactions beyond covalent bonding.[110] They are produced by the association of two or more building blocks held together by weaker and reversible non-covalent interactions such as hydrogen bonding, π-π stacking, van der Waals forces, Coulomb interaction and in the case of supramolecular coordination complexes (SCCs), coordination bonds between metal ions and organic ligands.[110–112] These forces are essential in understanding many biological processes that require more subtle interactions for both structure and function.[113] The double helix structure of DNA for example is the result of reversible hydrogen bonding between two separate complementary strands of nucleotides.[114] This reversibility is indispensable as it allows for unwinding of the helix during replication of genomic information for protein synthesis or cell division purposes.[115] As a result of the low energies of non-covalent bonds, complex formation often occurs without requiring activation energy, if the environment is suitable.[115] Molecular self-assembly occurs as i) *intermolecular self-assembly*, to form a supramolecular assembly such as micelles, vesicles and biological membranes, and ii) *intramolecular self-assembly* or folding, important for protein and nucleic acid to achieve a functional conformation.[113,116]

The concept of supramolecular chemistry has been receiving increasing attention in various areas of drug discovery, particularly due to the potential of some of these molecular entities to display host-guest interactions.[111] In this context, cancer therapy, where conventual chemotherapy is mostly nonselective, causing severe undesirable side effects and even multi drug-resistance, could benefit greatly of supramolecular drug delivery systems with tumour-targeting features.[117]

Therefore, several nanoscale supramolecular materials have been designed and explored as drug delivery vectors, such as liposomes,[118] micelles, [119,120] dendrimers[121] and polymers[122–124] (Figure 1.10).

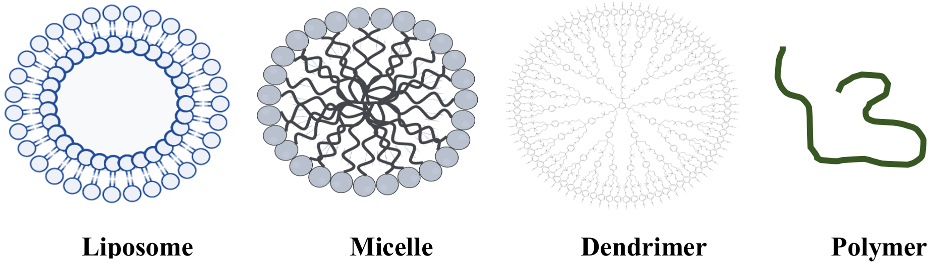

Figure 1.10: *Schematic representation of nanoscale drug delivery vectors. Liposomes: spherical vesicle formed by lipid bilayers. Micelle: spheric amphiphilic polymer with a hydrophobic core and hydrophilic shell. Dendrimer: highly branched macromolecule. Polymer: polymer chain.*

In general, such systems reaches tumour sites via *passive targeting*, taking advantage of the enhanced permeability and retention (EPR) effect in tumour tissues.[125] Tumour vasculature is mostly perturbed and twisted as compared with the vasculature in normal tissues. The vascular endothelium in tumours proliferates rapidly and discontinuously, resulting in a higher number of fenestrations and open junctions than normal vessels. Consequently, drug particles that are sufficiently small (few hundred nm) can passively cross the tumour endothelial barrier through fenestrations. [125] Moreover, the lack of a functional lymphatic network prevents the efficient removal of excess fluid from the solid tumour tissue. It is worth mentioning that the systems, as a result of using larger particle sizes, might increase the half-life of a drug as they can circulate longer through the bloodstream (binding to proteins in the blood or reduction/hydrolyzation of said particles not taken into account). However, there is some controversy regarding the EPR effect. As tumours are heterogenous based on their nature and differences in patients, they cannot all be expected to display leaky vascularity. Furthermore, evidence regarding the effect is based on studies in murine models, but there has been no translation to humans. [126] Rodent tumours grow faster than human tumours, causing poorly developed blood vessels which tend to be much leakier. Size is also of importance, as a ~1 cm diameter tumour grown in 2-4 weeks equals a 1-2 kg tumour in humans. The human equivalent of such a tumour would take years to develop (several years even to grow beyond 1 cm in diameter).[126]

Some of the above mentioned drug delivery systems have been used for Pt(II) drugs. For example, Lipoplatin™ and Aroplatin™ are two successful liposomal formulations of platinum anticancer drugs. Lipoplatin™ is a formulation of cisplatin composed primarily of dipalmitoyl phosphatidyl glycerol (DPPG), soy phosphatidylcholine, and methoxypoly-ethyleneglycol-distearoylphosphatidylethanolamine (cisplatin 8.9%, lipids 91.1%, w/w), with an average diameter of 110 nm. The advantage of this formulation is that the metallodrugs remain encapsulated in the liposome avoiding speciation and binding to extracellular nucleophiles.[127] Lipoplatin™ shows a superior cytotoxicity against non-small cell lung cancer (NSCLC) and renal cell carcinoma cell lines and a much lower toxicity, mainly nephrotoxicity, in normal cells compared with cisplatin.[128,129]

Polymer-platinum conjugates are formed between a polymer with suitable donor groups and a platinum moiety through coordination bonds. Polymers such as poly(amino acids), poly(amidoamine) dendrimers are generally used as carriers because they contain inherent, pendant or terminal ligating groups to which the cytotoxic Pt(II) moiety can be tethered. One of such conjugates, coded AP5346, has entered clinical trials.[130] In AP5346, the 1,2-diaminocyclohexaneplatinum(II) moiety, a fragment of **oxaliplatin**, is bound to a hydrophilic biocompatible polymer with pH-sensitive triglycine side chains and an amino-malonic acid terminal group (Figure 1.11). The conjugate is much more effective than oxaliplatin with exceptional tolerability in a large number of murine tumour models, likely to be due to its higher tumour accumulation.

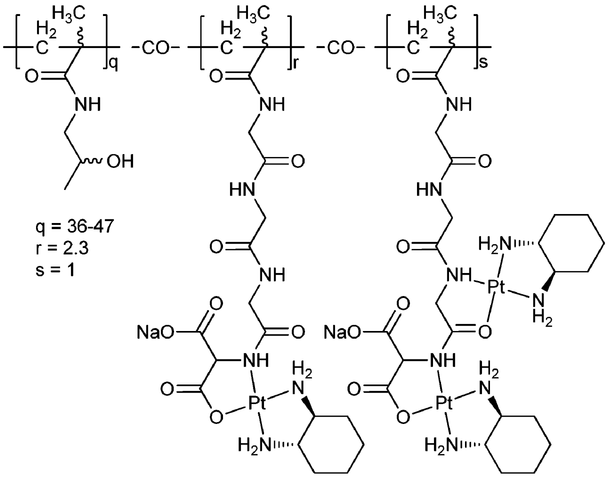

Figure 1.11: *Chemical structure of AP5346.*

1.7 Supramolecular coordination complexes

Supramolecular chemistry complexes based on metals is another group of potential drug-carriers. In metallosupramolecular chemistry, complexes are usually classified into two main branches; metal-organic frameworks (MOFs) and supramolecular coordination complexes (SCCs) (Figure 1.12).[112] Both are formed by self-assembly from organic ligands and metals, and have promising applications in catalysis, fluorescent probe design and drug delivery.[131] MOFs are crystalline structures in which the molecular scaffold creates pores that can be used to trap or store guest molecules. Their pore size is tuneable to contain a variety of sizes, and with possible surface modification MOFs show potential as drug carriers.[132] SCCs, however, have an advantage over MOFs; while the latter are hybrid polymers and porous materials with scarce solubility and biocompatibility, SCCs are well defined and discrete molecular entities with generally increased solubility in biological media.[133] The 3D-structures of SCCs are particularly interesting for drug delivery as the exterior of the scaffold can be functionalized with a targeting or fluorescent moiety. This is for example the case of the so-called **metallacages**, endowed with a cavity within the structure, which can be exploited for its host-guest properties, thus enabling drug encapsulation.

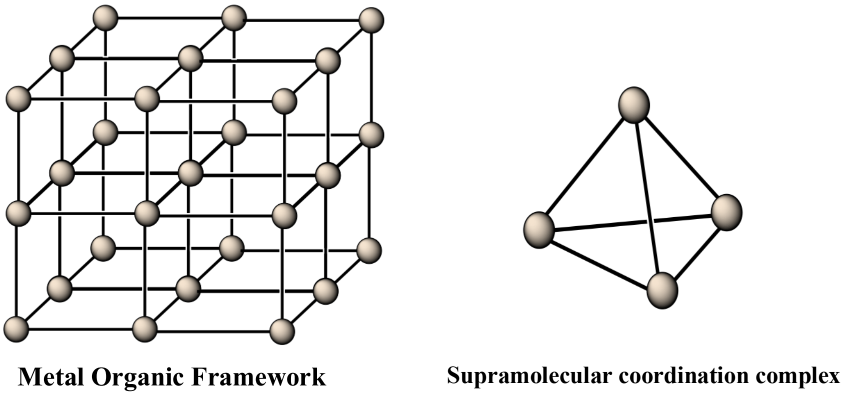

Metal Organic Framework **Supramolecular coordination complex**

Figure 1.12: *Metallosupramolecular chemistry structure examples. Ball: metal, stick: ligand.*

The first coordination cage with anti-cancer effects was reported by Therrien *et al.* in 2008 using a ruthenium-arene metallacage as a “Trojan Horse” type of drug delivery system for hydrophobic Pd and Pt complexes.[134] Further cytotoxicity studies revealed some ruthenium-arene metallacages to have intrinsic toxicity, functioning not only as carrier but drug as well.[135] In 2012, Crowley and co-workers reported the encapsulation of two molecules of cisplatin in a cationic $[Pd_2L_4]^{4+}$ (L = 2,6-bis(pyridin-3-ylethynyl)pyridine) metallacage, featuring N atoms of the central pyridine rings in the endo-position (Figure 1.13-A), studied by NMR spectroscopy and X-ray diffraction analysis.[136] They were the first to present a crystal structure of encapsulated cisplatin, indicating host-guest interaction through hydrogen bonding between the cisplatin molecules and the cavity-facing nitrogen from the pyridine ligands. Interestingly, cisplatin was released from the cavity due to disassembly of the dipalladium(II) cage upon addition of a competing ligand.[137,138] Unfortunately, this particular cage was scarcely water soluble, limiting its use in biological systems, but it did highlight the possibility of applying cages as metallacontainers.

Fascinated by this concept, our group explored the potential of $[Pd_2L_4]^{4+}$ (L=3,5-bis(3-ethynylpyridine)phenyl)) metallacages for biological applications[139] (Figure 1.13-B), as there is limited information on mechanism of uptake and application, since most research focused on synthesis and structural evaluation in non-biological environments.[112] Structural studies by ^{1}H NMR and XRD were performed demonstrating encapsulation of two cisplatin molecules. It is worth mentioning that, at variance with the aforementioned Pd(II) cages by Crowley *et al*, the cavity of the $[Pd_2L_4]^{4+}$ cages is more hydrophobic in this case (featuring a phenyl central ring), and therefore, cisplatin encapsulation was favoured over occupancy of the cavity by water molecules or other polar solvents.[134,135] The cages with and without cisplatin guest molecules were subjected to both *in vitro* and *ex vivo* screening to investigate the antiproliferative effects in cancer cells and possible toxicity in healthy tissues, respectively.[139,140] Depending on the ligand, cages without guest displayed scarce or moderate cytotoxicity. Interestingly, an increased cytotoxicity was observed for the cage-encapsulated cisplatin over cisplatin alone in cancer cells, while the cage-cisplatin complex displayed low toxicity in healthy tissue, illustrating its potential as a drug delivery system. [140]

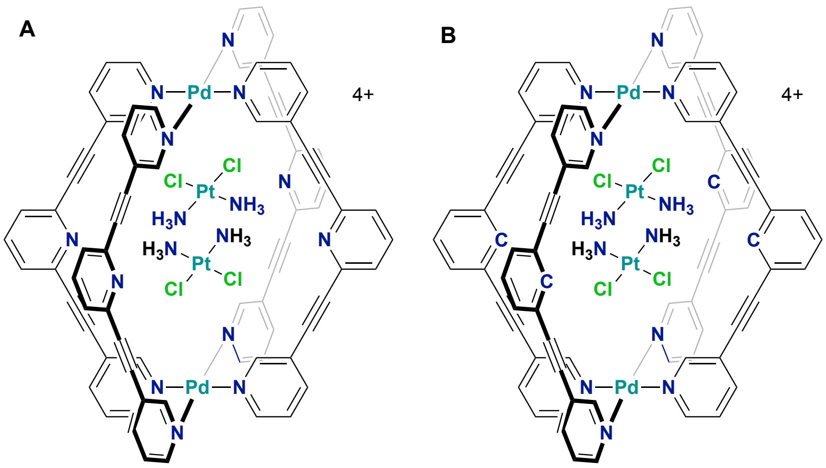

***Figure 1.13**: Examples of $[Pd_2L_4]^{4+}$ cages developed in the Crowley [136] (A) and Casini [139] (B) groups, respectively and schematic representation of cisplatin encapsulation in both systems.*

The exact mechanism of cisplatin delivery in cancer cells by the metallacages is still unknown and needs to be further investigated. Moreover, the molecular weight and dimensions of the selected $[Pd_2L_4]^{4+}$ cages are not sufficient to deliver them to tumour site via the EPR effect. Thus, targeting strategies need to be applied, for example bioconjugating the cage to peptides or antibodies. Furthermore, the mechanism of cellular accumulation (uptake and efflux) of these novel drug delivery systems is still not known. *In vitro* imaging of the cage compounds would greatly enhance our current knowledge and might give more insight into the uptake mechanism. A strategy to visualize the cages intracellularly by fluorescence microscopy exploited the *exo*-functionalisation of the ligands with fluorescent Ru(II) polypyridyl moieties[141] or naphthalene and anthracene groups (Figure 1.14)[140,141]. However, the results obtained so far indicate the need for different luminescent groups to be tethered to the ligand via a longer spacer to avoid the quenching of fluorescence upon cage formation, presumably due to the so-called ‘heavy metal’ effect. [139–142]

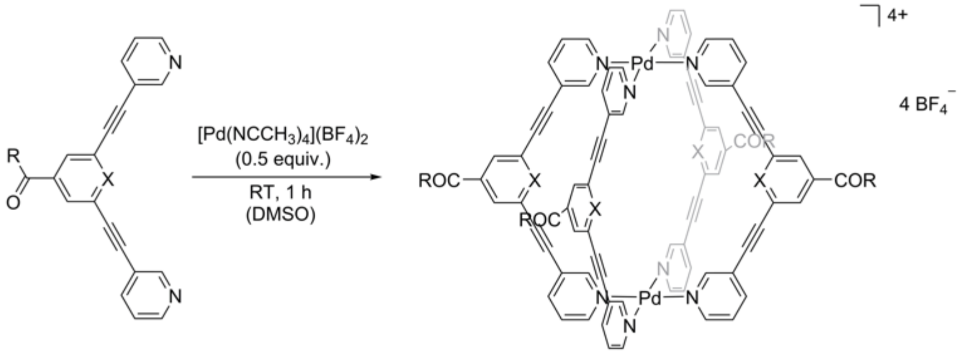

2a - 2d

1a - 1d

Compound	X	R	Yield [%]
a	CH	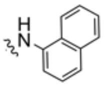	76
b	N	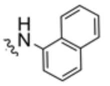	81
c	CH	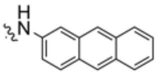	63
d	CH	OH	76

Figure 1.14: *Synthesis of palladium(II) cages via self-assembly using bidentate ligands and* $[Pd(NCCH_3)_4](BF_4)2$ *as Pd(II) precursor. The cages feature different fluorophores attached in exo-position with respect to the central aromatic ring.* [141]

1.8 Aims

This thesis is organized into two parts, whereby the first part (A) covers the study of small molecule cytotoxic gold-complexes as inhibitors of the membrane protein channels aquaglyceroporins (from *Chapter 2* to *Chapter 4*). The second part (B) explores instead supramolecular metal-based entities, namely $[Pd_2L_4]^{4+}$ metallacages, for anticancer drug delivery purposes (from *Chapter 5* to *Chapter 7*).

Part A

The first part of the project aims to investigate several novel Au(III) complexes designed as aquaporin inhibitors, for their potential as anticancer agents and/or as chemical probes to study AQP function in cancer cell proliferation. In details, two series of Au(III) coordination complexes with bidentate N^N donor ligands (*Chapter 3*) and a family of cyclometalated Au(III) C^N compounds (*Chapter 4*) will be evaluated for their effects on different human aquaglyceroporins (AQP3, AQP7, AQP9 and AQP10) in various cellular models.

The inspiration for the synthesis of the new compounds comes from recently published data in our group on the potent and selective inhibition of human AQP3 by the cationic Au(III) complex $[Au(phen)Cl_2]^+$ (**Auphen**, phen = 1,10-phenanthroline). Some of the new compounds are also tested for their anticancer properties in human cancer cells (expressing selected AQP isoforms) *in vitro*, in an attempt to correlate their cytotoxic effects to their AQPs inhibition properties. The experimental results are often supported by computational studies, including DFT (density functional theory) studies and advanced atomistic simulations, performed in collaboration with other groups and post-docs in our laboratory.

Part B

In this section, we study the potential of supramolecular coordination complexes as drug delivery systems for anticancer drugs. Specifically, we are interested in characterizing the anticancer effects of cisplatin encapsulation into self-assembled metallacages *in vitro*. Concerning tumour-targeting properties, although the EPR effect has been suggested as a way for supramolecular coordination complexes to reach their respective tumour site, the typical $[Pd_2L_4]^{4+}$ metallacage would not be able to benefit of this effect. In fact, Pd_2L_4 are roughly 3000 Da and 10 Å wide, which means they are too light and too small to benefit of the EPR effect.[139,140] Therefore, the possibility to *exo*-functionalize the metallacages is exploited here for targeting purposes, by introduction of tumour targeting ligands (*Chapter 5*). It is worth mentioning that in 2017 Casini and coworkers reported on the first example of bioconjugation of self-assembled $[Pd_2L_4]^{4+}$ cages *via* amide bond formation between the -COOH (or $-NH_2$) exo-functionalized ligand/cage and a complementary residue on a model linear peptide [143]. It should be noted that tethering of the peptide to the metallacages also enabled to increase their solubility in aqueous environment, essential to the development of a viable drug delivery system.

Moreover, we aim to improve our understanding of the pathways of uptake and intracellular accumulation of the metallacages. Therefore, we functionalized the Pd_2L_4 cages with fluorescent boron dipyrromethene (BODIPY) moieties (*Chapter 6 and Chapter 7*). BODIPY dyes are widely used in bio-imaging, chemo sensors etc. due to their favourable properties.[139,140] Not only they are highly fluorescent, but BODIPYs are also known for their excellent photostability.[139,140] This photostability enables the study of the cellular uptake of the cage-BODIPY systems *in vitro* using fluorescent microscopy.

.

Part A

Chapter 2: Aquaporins in cancer development

This chapter is based on the following paper:

Aquaporins in cancer development: opportunities for bioinorganic chemistry to contribute novel chemical probes and therapeutic agents

Brech Aikman, Andreia de Almeida, Samuel M. Meier-Menches and Angela Casini

DOI: 10.1039/C8MT00072G

2.1 Introduction

Before the discovery of aquaporins (AQPs), highly conserved membrane protein channels that are permeated by water, the general view on water passage across biomembranes was thought to be solely the result of passive diffusion across the lipid bilayer.[144,145] Along with the identification of AQPs, research from the last decade contributed greatly to the understanding of the diverse roles of AQPs in health and disease. Especially the ability of AQPs to be permeated not only by water but also other small molecules or solutes was the focus of exploration, as this feature enables AQPs to regulate several cell functions, which include osmotic water movement in cell volume regulation, energy metabolism, migration, adhesion and proliferation.[146–149] There have been thirteen mammalian AQP isoforms (AQP0-12) identified so far, ubiquitously distributed throughout the body. The channel proteins are divided into two main groups based on structural and functional characteristics: *orthodox* aquaporins strictly involved in water permeability (APQ0-2, AQP4, AQP5, AQP6 and AQP8) and *aquaglyceroporins*, facilitating transport of small uncharged solutes such as glycerol and urea in addition to water (AQP3, AQP7, AQP9, and AQP10).[150] Peroxiporins, AQP able to permeate hydrogen peroxide, are a further subclass of AQPs that comprise both orthodox aquaporins (AQP1, AQP8) and aquaglyceroporins (AQP3 and AQP9). Lastly, AQP11 and AQP12 are classified as *S-aquaporins* due to their subcellular localization.[151,152] Much is still uncertain regarding the nature of selective permeability for the latter as they show less sequence similarity to the other isoforms, but there are indications of AQP11 facilitating water and glycerol transport.[153,154]

Altered aquaporin function as a result of dys-, up- or down-regulated AQPs expression have been correlated with numerous pathophysiological conditions of human disorders (Figure 2.1).[155] Nephrogenic diabetes insipidus and Sjörgens syndrome are just two examples of disorders that are linked to the impaired water permeability of AQPs.[156] Both the dysfunction of aquaglyceroporins' ability to permeate glycerol, as well as their abnormal expression in certain tissues, have dire consequences for cell proliferation, epidermal water retention and adipocyte metabolism. Consequently, aquaglyceroporins have been linked with metabolic disorders such as obesity, diabetes and skin diseases, *e.g.* atopic dermatitis.[157,158] Intriguingly, studies report isoforms of both orthodox aquaporins and aquaglyceroporin related to different types of cancer, often showing a strong correlation between the level of AQP expression and the tumour grade.[148,159–161] In addition to human isoforms, parasite aquaglyceroporins are quite relevant as well regarding certain human diseases, such as malaria, where parasite transmission takes place through bites of infected mosquitos.[162]

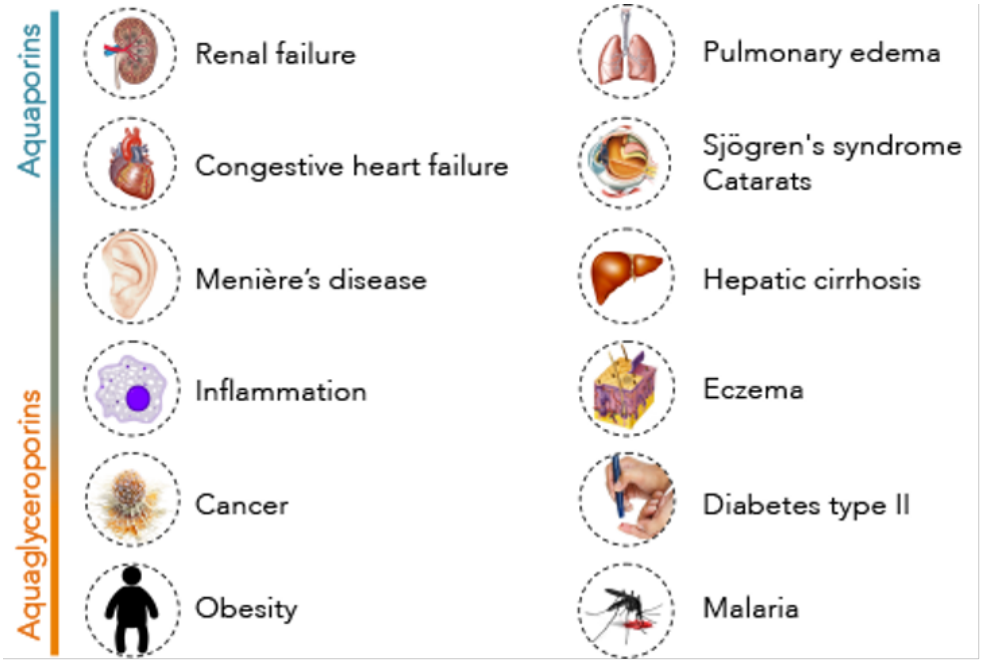

***Figure 2.1**: Examples of human diseases related to an abnormal function or altered expression of different AQPs isoforms. Reproduced with permission of The Royal Society of Chemistry from ref [163].* [163]

Due to their significance in various important physiological and pathophysiological processes, aquaporins have gained increasing attention as promising targets for therapeutic intervention. Despite the challenges in discovering selective AQP modulators (inhibitors), the search continues as such inhibitors would not only be useful as novel therapeutic agents but can also be utilised as chemical probes in order to validate AQPs function in biological systems, to be used in parallel to genetic approaches (*e.g.* knockout animal models). First, a general overview on AQP structure and expression in both healthy and tumour tissue will be presented in this perspective, followed by a focus on the role of AQPs in tumorigenesis and tumour metabolism and finally summarize the state-of-the-art literature on the most promising AQP-targeted metal-based inhibitors highlighting their possible uses in medicine and cancer pathophysiology.

2.2 Aquaporin protein structure

The aquaporins are homo-tetrameric complexes which reside in the cell membrane, with each monomer of ~ 30 kDa containing six transmembrane α-helices connected by five loops, two half helices and both N- and C-termini located on the cytoplasmic side of the membrane.[164,165] Three of the loops are located extracellularly while two of the loops are intracellular domains.[164] Each of the four AQP monomers in the membrane creates a single narrow *hourglass*-shaped pore spanning the lipid bilayer (Figure 2.2),[166] contributing to the remarkable selective nature of AQPs for permeation of water and other small solutes. Additionally, another specific feature of this channel is the presence of two highly conserved constriction sites acting as selectivity filters.[147,164] The first constriction site located adjacent to the extracellular entrance is known as the aromatic/arginine selectivity filter (ar/R SF) (Figure 2.2). The diameter of this filter determines whether small polar solutes may permeate the pore in addition to water. Pore size varies depending on the isoform, for example in orthodox aquaporins the pore's diameter at the ar/R SF is ca. 3 Å, preventing permeation of molecules bigger than water (2.8 Å).[164] In aquaglyceroporins, the size of the pore is larger and can reach up to ~3.4 Å in diameter allowing permeation of for example glycerol.[165,167,168] In this constriction site, the arginine is fully conserved in all mammalian AQPs isoforms, but the composition of the remaining amino acids creating the ar/R SF might vary depending on the permeability for water or glycerol. This explains why orthodox aquaporins have an ar/R SF formed by four residues, while aquaglyceroporins have an ar/R SF formed by only three residues, accounting for the differences in pore sizes and selectivity.[165]

The second constriction site or selectivity filter is composed of two conserved asparagine-proline-alanine (NPA) motifs. Interestingly, they are located in the centre of the channel where the positive N-terminal ends of the two half helices meet, forming a dipole moment that creates an electrostatic barrier, subsequently preventing the passage of positively charged ions through the pore.[169] Especially the amide position of the Asn side chain appears to be structurally critical to this functionality, whilst the amide nitrogens aid in directing water or solute molecules by acting as hydrogen bond donors.[170] As evidenced by molecular dynamics (MD) simulations, electron microscopy and X-ray crystallographic structures of AQPs, water molecules were discovered passing through the channel in a single file, orienting themselves along the local electrical field.[167,171] Contrasting to the previously mentioned structural difference found between AQPs and aquaglyceroporins in the ar/R SF, the NPA region is conserved in most human AQP isoforms, with the exception of AQP7 (NAA-NPS), AQP11 (NPC-NPA) and AQP12 (NPT-NPA). However, all AQPs preserve the two Asn residues creating the dipole moment, thus emphasizing its importance.

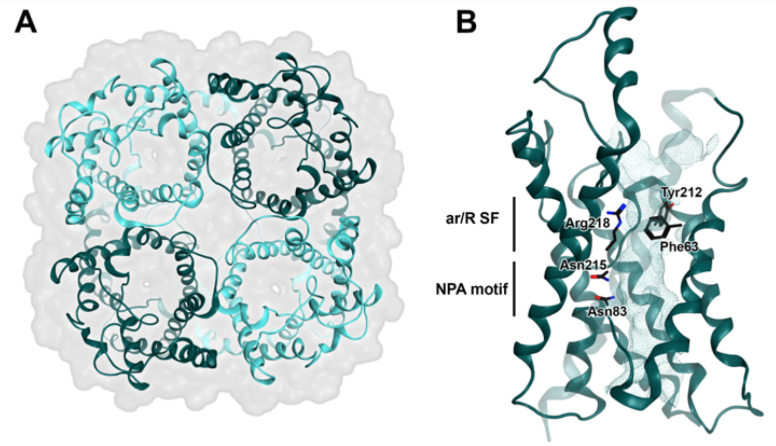

***Figure 2.2**: Homology model of human AQP3. (A) Extracellular top view of the tetrameric form of hAQP3. (B) Side view of a monomer of hAQP3, highlighting the conserved aromatic/Arginine selectivity filter (ar/R SF) and the NPA motifs in black. Reproduced with permission of The Royal Society of Chemistry from* [163].

2.3 Aquaporins in health and tumour physiology

There are numerous studies reporting a correlation between AQP expression levels in cancer cells and cancer malignancy.[148,159,172] In most cases, multiple AQP isoforms were reportedly involved in tumours at different stages.[159,173] In fact, some tumours also presented up-regulated expression of AQPs isoforms which are not native to the tissue of origin. An overview of different AQP isoforms presence in various human cancer types (studied in cancer cells or tumour tissue samples) and possible related functions is presented in Table 2.1. Aquaporin association with tumours can be partially due to the nature of their substrate permeability, as will be explored further in the next sections. Here, we will summarize some of the studies that in our opinion best describe the function of different AQP isoforms in cancer development.

2.3.1 Water permeation

Water permeation across the cell membranes is facilitated by the presence of AQPs in human tissues, allowing fast cellular responses to changes in the osmotic gradient. Hence, AQPs are abundantly present in tissues involved in maintaining water-based homeostasis, with a need for rapid fluid turnover such as the kidneys (AQP1, AQP2, AQP3, AQP4),[174] the airways (AQP1, AQP3, AQP5)[174,175] and the central and peripheral nerve system (AQP1, AQP4, AQP9).[176,177] This ability of AQPs to transport water was also proven to be involved in multiple aspects of tumour malignancy, *e.g.* enhanced cell migration,[178] affecting tumour invasion[179] as well as oedema formation,[176,180] as detailed in the sections below.

Table 2.1*: Expression of AQP isoforms in different human tumours and cancer cell lines and their function.*[163]

AQP isoform	**Tumour and sample type**			**Function in tumour**
	Tissue	**Tissue & Cells**	**Cells**	
AQP0				Unknown
AQP1	Brain[176,181], Breast[182], Colorectal[183], Cervical[184], Laryngeal[185], Lung[186], Ovarian[187], Renal[188], Mesothelium[189]	Bone[190], Breast[191]*, Colorectal[192], Lung[179]		Grade, prognosis, proliferation, angiogenesis, necrosis, migration, invasion and metastasis.
AQP2				Unknown
AQP3	Cervical[184], Bladder[193], Colorectal[183], Liver[194], Lung[161,186], Oesophageal[195], Pancreas[173], Renal[196], Uterus[197]	Colorectal[192], Head and Neck[198], Stomach[199,200], Prostrate[201]	Breast[202], Skin[203]	Grade, prognosis, angiogenesis, invasion, migration and energy metabolism.
AQP4	Brain[176,180], Cervical[184]	Thyroid[204], Lung[179]		Grade, migration, tumour-associated oedema, adhesion, invasion and apoptosis.
AQP5	Breast[205], Cervical[184,206], Colorectal[183], Liver[194], Lung[207], Oesophageal[195], Ovarian[208], Pancreas[173]	Breast[209], Colorectal[192,210], Myeloblast[211], Prostate[212], Stomach[213,214], Tongue[198]	Lung33, Ovarian[216]	Prognosis, proliferation, invasion, migration and drug resistance.
AQP6	Ovarian[217]			Grade
AQP7	Thyroid[218], Uterus[197]			Unknown
AQP8	Brain[219], Cervical[184,220], Ovarian[217]		Myeloblast[221]	Migration, invasion, metastasis and anti-apoptosis, grade, proliferation.
AQP9	Brain[222], Liver[223], Ovarian[224], Uterus[197]	Liver[225]		Grade, drug resistance, and energy metabolism.
AQP10				Unknown
AQP11			Lung[226]	Prognostic
AQP12				Unknown

*Primary cells

2.3.2 Migration of tumour cells

Migration of tumour cells enables tissue invasion and metastasis, both associated with a poor cancer prognosis.[227] The main AQP isoforms involved in general cell migration are AQPs 1, 4 and 5. In healthy tissue, AQP1 expression is polarized on the leading edge of cell protrusions in migrating cells, which is hypothesized to enhance the process of cell movement.[178] Due to the combination of increased water permeability, actin cleavage and ion uptake at the tip of the lamellipodia, a local osmotic gradient is created, driving water influx and ultimately enabling lamellipodia extension and cell migration.[178,228] AQPs are hypothesized to facilitate the rapid changes in cell shape that take place as a migrating cell squeezes through the extracellular matrix. These cell volume changes are likely to require a rapid water flow in and out of the cell, therefore justifying the presence of AQPs water channels.[178] In the case of tumour cells, overexpression of AQPs could, therefore, enhance their ability for tissue invasion and metastasis. As such, cancer cell lines over-expressing AQP1 demonstrate an increased ability to extravasate across blood vessels and to invade local tissue *in vitro* and *in vivo*.[229] Likewise, over-expression of AQP1 in pulmonary adenocarcinoma tissue samples prompted a stronger capacity of cancer cell migration, invasion and metastasis.[186] The decreased ability of cells to migrate when AQP expression is impaired has been confirmed by several *in vitro* and *in vivo* assays.[230,231]

The expression of AQP4 in astrocytes induces a similar effect. Healthy brain tissue expresses AQP4 primarily around tight junctions of astrocytic end-feet at the cerebral microvessels facing the blood-brain barrier, which are formed by endothelial cells. Therefore, AQP4 facilitates the movement of water between blood and the brain and between the brain and cerebrospinal fluid compartments.[232] In brain tumours and especially diffuse astrocytomas, AQP4 expression is greatly upregulated and an intracellular redistribution across the plasma membrane of the cancerous astrocytes can be observed, showing a completely different morphology from healthy cells.[176] Additionally, this change in phenotype facilitates astroglial cell migration. The influence of AQP4 presence and migration has been demonstrated by comparing wild-type and AQP4-null astrocytes, where the latter displayed slow migration.[176,180] Remarkably, detecting the expression levels of AQP4 to distinguish between benign and malign thyroid nodules was the claim of a recent patent, based on the discovery that AQP4 immunostaining of suspected follicular neoplasm can facilitate the distinction of benign from malign oncocytic lesions.[233] This would contribute greatly to deciding which thyroid nodules should be dissected or removed in thyroid surgery.[233]

For the case of AQP5, upregulation was linked in several tumours to enhanced migration and invasive phenotypes compared to expression in healthy tissue.[209,234] In fact, overexpression of this isoform has been correlated with lymph node metastases in several cancers of the ovarian[208], prostate[212], colon[183], cervical[184], lung[207] and oesophageal[195] type. For example, AQP5 expression in lung cancer cells *in vitro* was associated with increased cell migration, while AQP5 knockdown led to a decrease in cell migration and invasion properties.[215] A similar effect was seen in the migration of gastric carcinoma[214] cells and invasion of breast cancer cells[209]. Another *in vitro* study, using human glioma cells showed that increased AQP5 mRNA expression was positively correlated with proliferation rates and silencing inhibited cell proliferation, reduced migration and promoted cell apoptosis.[235] The role of AQP5 in hepatocellular carcinoma metastasis was also recently evaluated,[93] reporting that AQP5 was highly expressed in hepatocellular carcinoma cell lines and its downregulation inhibited the cells' capacity of invasion and metastasis, both *in vitro* and *in vivo*. [236]

2.3.3 Tumour oedema

In addition to their influence on migration, upregulation of AQPs as water channels may also contribute to oedema formation as patients with tumour oedema in the brain display an increased morbidity and mortality rate.[176] AQP1 for example, was found upregulated in glioblastomas, enhancing the water permeability in perivascular areas such as the blood-brain barrier.[181,237] Based on these studies, AQP1 has the potential to be applied in glioblastoma as a survival prognosticator.[238] Also, over-expression of AQP4 was associated with tumour oedema in the brain.[180] However, due to the upregulation of AQP4 in the peritumoral area rather than the tumour core, its involvement in migration might be even more relevant.[239] Follow-up experiments demonstrated that AQP4 deletion in mice increased oedema formation around implanted melanoma in the brain, suggesting that increased AQP4 expression by reactive astrocytes in and around the tumour could facilitate elimination of brain oedema fluid.[240]

2.3.4 Glycerol transport

Aquaglyceroporins (AQPs 3, 7, 9, 10 and 11) have, in line with their roles in physiology, a high expression particularly in tissues involved in glycerol metabolism such as adipocytes and liver, and thus influences several metabolic pathways.[241,242] Glycerol in the systemic circulation derives from fat lipolysis, glycerol absorbance from the gastrointestinal tract or re-absorbance in the proximal tubules in the kidney, [100] and is an important intermediate in gluconeogenesis, lipid metabolism and in an electron shuttle system into mitochondria. [243] The latter carries reducing equivalents from cytosol to mitochondria for a process named oxidative phosphorylation.[244] Depending on the cellular energy status, glycerol metabolism can take place in the outer mitochondrial membrane.

Under normal physiological conditions, glycerol is stored in adipose tissue in the form of triacylglycerol (TAG), as a result of glycolysis. The TAG precursors are CoA-activated fatty acids and glycerol-3-phosphate (G-3-P), produced either from the reduction of dihydroxyacetone phosphate (DHAP) or by the phosphorylation of glycerol.[245] Since adipose tissue or muscles do not express glycerol kinase (GK), the enzyme required for glycerol phosphorylation, they acquire G-3-P from glycolysis. In adipose tissue, AQP7 is the primary glycerol transporter and abundantly expressed in the plasma membrane of adipocytes (Figure 2.3).[246] Interestingly, a recent study has identified AQP11 as aquaglyceroporin in human adipocytes, in the vicinity of lipid droplets.[153]

During fasting, glycerol released by adipose tissue upon lipolysis is taken up by the liver, most likely via AQP9,[223] and used as a non-carbohydrate precursor to induce gluconeogenesis in hepatocytes.[245] Thus, AQP7 seems to facilitate glycerol efflux from adipose tissue, whereas AQP9 mediates glycerol influx into hepatocytes.[246,247]

Like the orthodox aquaporins, aquaglyceroporins play a role in osmoregulation. In fact, glycerol is one of the main osmoprotective solutes found in mammalian cells.[244] As such, in response to external gradients, cells can react by altering intracellular levels of glycerol whilst reducing or increasing membrane permeability. Similar to water, glycerol permeation across the lipid bilayer can occur *via* passive diffusion. However, this process is relatively slow and since the presence of aquaglyceroporins highly increases glycerol permeability, the latter is preferred as it provides a faster and more energy efficient process. AQP3 is the most abundantly expressed isoform in the skin, in particular in keratinocytes residing in the basolateral layer of the epidermis.[248]

Under physiological conditions, water and glycerol are essential in preserving optimal skin moisturisation. Glycerol acts as a humectant to prevent water evaporation, upholding the barrier function of the skin.[249] For example, deletion of AQP3 in mice is demonstrated to impair this barrier function by reducing elasticity and hydration, as well as showing delayed wound healing and reduced cell proliferation in the stratum corneum.[250]

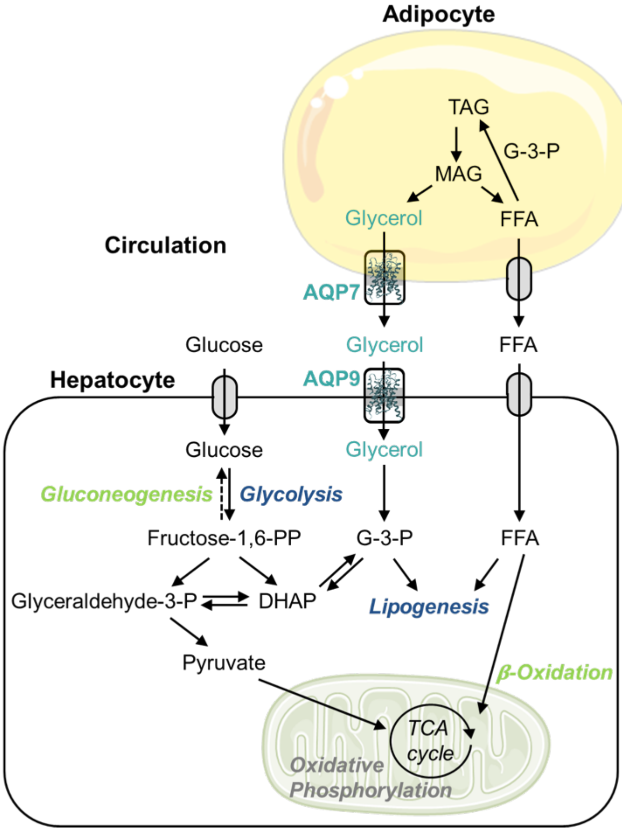

Figure 2.3*: Aquaglyceroporins and their relation to glycerol metabolism in liver and adipose tissue. Abbreviations: G-3-P = glycerol 3-phosphate, DHAP = dihydroxyacetone phosphate, TCA = tricarboxylic acid, FFA = free fatty acid, TAG = triacylglycerol, MAG = monoacylglycerol. Reproduced with permission of The Royal Society of Chemistry from* [163].

2.3.5 Role of glycerol in cancer cell proliferation

Based on the experimental evidence describing increased aquaglyceroporin expression in tumours (Table 2.1), glycerol was hypothesised to contribute to tumour growth and cancer cell proliferation in two possible ways: i) as a building block in phospholipid synthesis, and/or ii) as intermediate or regulator of ATP production.[241] Both pathways are essential to fast proliferating cells such as cancerous ones, therefore AQP inhibition is predicted to reduce both tumour cell proliferation and migration. The next part will summarise studies that substantiate our hypotheses regarding the interplay between glycerol and cancer.

Among the four human aquaglyceroporin isoforms, AQP3 is the most studied also in relation to cancer, since it is widely distributed throughout the body in epithelial cells.[249,251] A recent *in vitro* study by our group demonstrated AQP3 inhibition reduced cell proliferation in various cell lines, including cancer cells. [252] Furthermore, *in vitro studies* found that AQP3 silencing induced downregulation of several lipid synthases in gastric cancer cells.[253] It was therefore postulated that lipid synthesis impairment by AQP3 knockdown is not only the consequence of reduced glycerol uptake, but also related to lipid synthesis system inhibition. The phosphatidylinositol-4,5-bisphosphate 3-kinase (PI3K)/ protein kinase B (Akt) signalling pathway, involved in the impaired lipid and ATP production, was inhibited after AQP3 knockdown as well.[253]

Cancer cells divide at higher rates, therefore requiring more lipids for membrane synthesis and more energy to sustain the vigorous proliferation related to malignant behaviour. Moreover, phospholipids are used to form the various plasma membranes, but can also be catabolized to generate ATP by β-oxidation.[254,255] As mentioned above, glycerol can be metabolized to be the backbone of triglyceride (TAG), essential for maintaining cell proliferation and survival. In detail, tumour cells can convert TAG into free fatty acid (FFA) by lipolytic processes (Figure 2.3), generating ATP via fatty acid oxidation (FAO) to support the cancer development.[256] Blockage of this lipid synthesis *via* aquaglyceroporins inhibition or down-regulation, may result in a depletion of material and energy supply.

The second main hypothesis regarding the role of AQP3 in tumour cell migration and proliferation relates to the fact that over-expression of this isoform provides cells with a higher glycerol permeability, thus leading to higher ATP content,[257] required for a greater demand for biosynthesis. Hara-Chikuma and Verkman postulated the correlation between glycerol and ATP production in 2008 after observing a remarkable resistance to skin tumorigenesis in AQP3-deficient mice.[203] Based on this study, it was suggested that glycerol permeability via AQP3 is required for epidermal cell proliferation and tumorigenesis, since the cellular glycerol levels were positively correlated with cellular ATP content.[203] Specifically, the AQP3-deficient mice displayed a reduction of glycerol in epidermal cells, of the metabolite G-3-P and ATP, without impairing mitochondrial function.[203] Interestingly, the supplementation of glycerol corrected this reduced proliferation and ATP content under AQP3 deficiency.

It was therefore suggested that glycerol could be a key regulator of cellular ATP, subsequentially justifying the overexpression of AQP3 in some cancers.

It must be noted that this hypothesis needs some careful reflection regarding the biochemical pathways possibly linking glycerol to ATP synthesis, particularly in relation to cancer cell metabolism. Tumours generally display a deregulated metabolism to meet the high demand for nutrients used to support both cell proliferation and survival, while maintaining a balanced redox status.[258] Therefore, glucose and glutamine are often the main energy sources in cancer.[259,260] In the 1920s, Warburg theorized that impaired mitochondrial respiration would drive tumorigenesis, creating an increased consumption of glucose reflected by a high lactate production, *i.e.* aerobic fermentation, named the *Warburg effect*.[261] Though current research challenges this interpretation, postulating that tumours retain their capacity to perform oxidative phosphorylation despite the hypoxic environment, and metabolic changes are rather an effect of various malignant cellular transformations than a direct cause of tumorigenesis.[258,262]

There is an increased need for precursors and intermediates for biosynthesis and reducing equivalents in proliferating cancer cells, which the catabolism of glucose and glutamine can meet.[262] Oxidation of carbon skeletons produced from glucose for example, allows the cells to capture electrons in the form of reduced nicotinamide adenine dinucleotide (NADH), which are then introduced into the mitochondrial electron transport chain *via* the malate-aspartate shuttle. This process contributes to cellular respiration and ATP generation.[262] Its seems that proliferating tumour cells prefer converting excess pyruvate into lactate, which contributes to maintaining the cytoplasmic level of the NAD^+/NADH ratio to promote a continued glucose metabolism.[262,263]

Within this framework, tumours overexpressing aquaglyceroporins are thought to use glycerol as an intermediate for pyruvate through the glycerol 3-phosphate shuttle (G-3-P shuttle) leading to ATP production (Figure 2.4). This G-3-P shuttle is a complex process used to transfer electrons from cytosolic NADH to the mitochondrial electron transport chain (Figure 2.4).[264] The enzyme called cytoplasmic glycerol-3-phosphate dehydrogenase 1 (cGPDH) is essential for this shuttle, as it converts dihydroxyacetone phosphate to G-3-P by oxidizing one molecule of NADH to NAD^+, whilst the mitochondrial glycerol-3-phosphate dehydrogenase (mGPDH) converts G-3-P to DHAP by reducing flavine adenine dinucleotide (FAD^+)[264] This system supports oxidative phosphorylation in mitochondria by regenerating cytosolic oxidized nicotinamide adenine dinucleotide (NAD$^+$), thus production of adenosine triphosphate (ATP). In humans, the G-3-P shuttle functions mainly in the skeletal muscle and the brain.[245]

For proliferating cells, glycerol phosphorylation is catalysed by Glycerol Kinase (GK), converting glycerol to G-3-P.[244] The glycerol 3-phosphate can be utilised in two ways: i) in the biosynthesis of phospholipids as an important structural component of cellular membranes or ii) enter the glycolytic pathway, when converted to DHAP by mGPDH.[244,245,265] However, the latter is less likely to occur, since proliferating cells interconvert DHAP to G-3-P in order to re-oxidize cytosolic NADH generated from glycolysis, transferring reducing equivalents into the electron transport chain. In fact, the enzyme mGPDH shows an increased activity in prostate cancer cells, melanoma and breast cancer, thought to uphold glycolysis and facilitating the oxidation of NADH.[266]

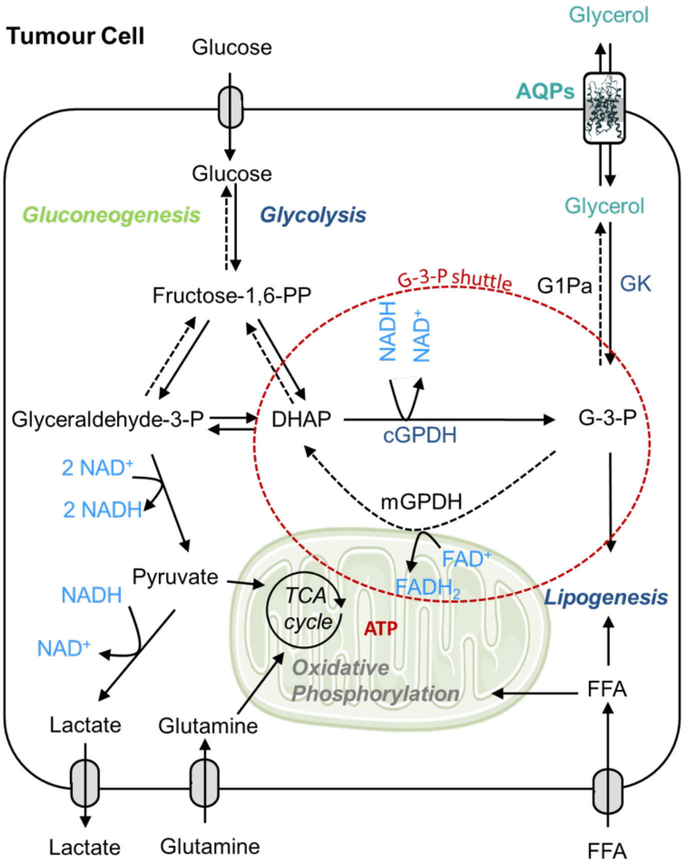

Figure 2.4: *Proposed model of aquaglyceroporin involvement in glycerol metabolism of proliferating tumour cells. Abbreviations: ATP = adenine triphosphate, DHAP = dehydroxyacetone phosphate, FAD$^+$ = flavine adenine dinucleotide, FADH$_2$ = hydroquinone form of flavine adenine dinucleotide, FFA = free fatty acids, cGPDH and mGDPH = cytosolic*

and mitochondrial, respectively, glycerol-3-phosphate dehydrogenase, G1Pa = glucose 1-phosphate-adenyltransferase, G-3-P = glycerol 3-phosphate, GK = glycerol kinase, TCA = tricarboxylic acid, NAD^+ *= oxidized nicotinamide adenine nucleotide, NADH = reduced nicotinamide adenine nucleotide. Reproduced with permission of The Royal Society of Chemistry from* [163].

It is important to recognize that the metabolisms in cancer cell is continuously adapting and reprogramming to optimize their use of available nutrients. Although glycerol is more likely to contribute to tumour cell growth as a precursor for phospholipids, its interplay in the generation of ATP cannot be ruled out, and this aspect would warrant further investigation.

While AQP3 being the most studied isoform in relation to cancer, the other aquaglyceroporins have also been shown to be expressed in cancer tissue, with an established correlation to several types of cancers (Table 2.1).

AQP7 for example, showed marked expression in immunostained plasma membranes of benign epithelial ovarian cancer, while being located in the nuclear membrane of borderline and malignant cells.[224] Interestingly, despite the selective nuclear staining in malignant tumour tissue, western blot analysis of protein levels showed that AQP7 expression is actually significantly higher in malignant and borderline tumour compared to benign tumour and normal ovarian tissue. This highlights that translocation and expression of this isoform may be crucial for ovarian carcinogenesis.

AQP9 presence has been demonstrated for human glioblastoma, where most glioma cells showed high AQP9 protein expression on the cell surface.[267] Other authors indicated AQP9 mRNA presence in specific subpopulations of glioma cells and leukocytes infiltrating the tumour tissue.[268] Moreover, work by Fossdal et al. revealed that AQP9 mRNA and protein expression is amplified in glioblastoma stem cells.[269] AQP9 expression in glioblastoma may indicate a role in glioma-associated lactic acidosis, by facilitating glycerol and lactate excretion, and/or involvement in the energy metabolism of glioma cells. This example emphasises the crucial role of AQPs not only in glycerol uptake but also in the regulating of the substrate efflux (Figure 2.4). In epithelial ovarian cancer, AQP9 was shown to be localized in the basolateral membranes of both benign and borderline tumour cells, while it was widely distributed throughout membranes of malignant cells.[224] Furthermore, protein expression analysis using western blot revealed that there is a significant difference between tumour types as follows: ovarian malignant > borderline > benign/normal tissue. In fact, AQP9 was shown to be higher expressed in mucous than serous ovarian tumours, and again correlated with tumour grade: higher expression in undifferentiated (grade 3) than well differentiated (grade 1/2) tumours.[222,224] Therefore, increased AQP9 expression may be related to poor prognosis, highlighting once more the importance of understanding the role of aquaglyceroporins and glycerol in carcinogenesis.

The type of organ or tissue is also relevant as, interestingly, AQP9 was shown to be down-regulated in hepatocellular carcinoma.[225] Moreover, its overexpression actually suppressed cell invasion, both *in vitro* and xenograft tumour growth, as well as hepatoma cell invasion by inhibiting epithelial-to-mesenchymal transition. This example clearly shows that the role of aquaglyceroporins in cancer development may differ according to specific tissue types and the tissue's original requirement of either glycerol uptake or efflux.

To date, there is little known about the role and expression of AQP10 and 11 in cancer. One study, that used microarray data to investigate prognostic values of AQP mRNA expression in human ovarian cancer, demonstrated that AQP3, 10 and 11 are correlated with improved overall survival in ovarian cancer patients.[270] However, nothing is known about the actual protein expression of AQP10 and 11 in either cancer cells or tissues.

After establishing the correlation of aquaglyceroporins with several types of cancers (Table 2.1), as anticipated in the previous examples, the need of tumours for glycerol could be dependent of their type and stage of differentiation. It could therefore occur that metastatic and non-metastatic cancers have different aquaglyceroporin expression, even within the same tissue origin. In melanoma for example, it was shown, using high-throughput technology with microarray datasets, that the transition to an increased malignant phenotype was correlated to a reduced expression of AQP3 compared to normal skin and benign nevi. [271] Thus, the need for glycerol might decrease, as the focus shifts from tumour proliferation to migration.

The role of AQP3 downregulation as a potential indicator for the invasive character was also observed in prostate tumours.[271] The study of Jain *et al.* where the consumption and release of 219 metabolites in the medium of the 60 cell lines of the NCI-60 screen was examined supports these findings.[259] Their results indicate increased consumption of glycerol in some non-metastatic over metastatic cancer cell lines.

Finally, it is important to note that glycerol requirements may vary depending on the specific tissue of origin, malignancy, differentiation and metastatic properties, making aquaporins quite challenging to study. Furthermore, due to the bi-directional nature of AQPs mediated permeation, tumours' need to control glycerol uptake or efflux may lead to decreased expression of particular isoforms.

2.3.6 Hydrogen peroxide transport

H_2O_2 was originally thought to freely cross the cell membrane by means of passive diffusion, in a similar fashion to water. However, experimental studies suggested rapid diffusion through the lipid bilayer was probably facilitated by membrane protein such as AQPs.[272–274] Presently, there is evidence for H_2O_2 permeation by AQP3,[275] AQP8[276] and AQP9[277], while hydrogen peroxide permeation of AQP1 is still controversial.[274,275] Isoforms from both orthodox AQPs and aquaglyceroporins have hydrogen peroxide as a substrate. Thus, to enable distinction, they are referred to as peroxiporins. AQP3 and AQP9 can both be found in the plasma membrane, whereas AQP8, in addition to its plasma membrane localisation, resides in the inner membrane of mitochondria as well, which are a major source of reactive oxygen species (ROS) for animals and plants.[278] Marchissio et al. for example examined whether knockdown of mitochondrial AQP8 (mtAQP8) in human hepatoma cells using siRNA had an effect on mitochondrial H_2O_2 efflux.[279] Indeed, the authors found that, compared to wild-type mitochondria, isolated mtAQP8 knockdown mitochondria had a lower H_2O_2 efflux ability, while the cells suffered from reduced viability. Hydrogen peroxide belongs to the ROS that comprise superoxide, superoxide radicals and hydroxyl radicals. Under physiological conditions, ROS play a significant role in maintaining cell homeostasis, where intra- and extracellular concentrations of ROS are controlled using scavenging systems to balance ROS generation and elimination.[280] Generally, ROS are generated as a by-product of aerobic metabolism, with nicotinamide adenine dinucleotide phosphate oxidases (NOX) and the mitochondrial electron transport chain (mETC) as the main sources.[281] To limit ROS accumulation, cell utilise scavenging enzymes and antioxidant agents such as superoxide dismutase (SODs), catalase, glutathione peroxidases, the thioredoxin system, heme-oxygenase and nicotinamide adenine dinucleotide phosphate (NADPH)/ nicotinamide adenine dinucleotide ($NADP^+$).[281,282]

ROS are involved in physiological or pathological changes depending on their concentration, and can activate signalling pathways to stimulate cell proliferation, differentiation, migration, apoptosis, adaption to hypoxia, immune function, and other processes.[283] Therefore, any alterations in cells' ability to transport ROS can have a profound effect on their viability.

Overall, increased ROS levels, particularly hydrogen peroxide, are found in pathological conditions such as cancer.[281,284,285] Hydrogen peroxide plays a role in (mitochondrial) NOX and ERK (extracellular-regulated kinase)-PI3/Akt. Both are activated by receptor tyrosine kinase (RTK) mediated cell signalling, and involved in several processed such as cell survival, protein synthesis, proliferation and mTORC2 induced cell migration (Figure 2.5).[286]

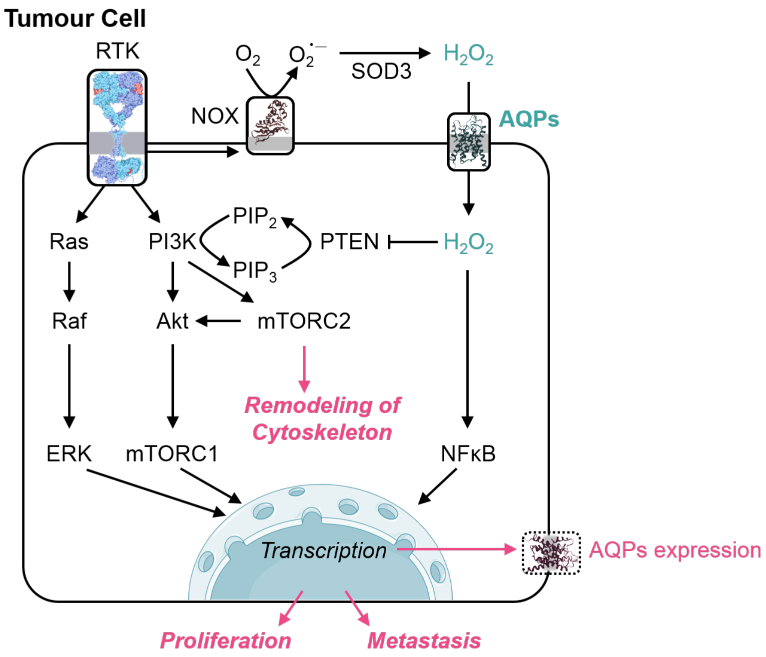

Figure 2.5: *Proposed pathways of AQP-permeated hydrogen peroxide interaction in cancer cells. Abbreviations: Akt = Protein kinase B, AQPs= Peroxiporins, ERK = Extracellular-regulated kinase, mTORC1 = Mammalian target of rapamycin complex 1, mTORC2 = Mammalian target of rapamycin complex 2, NF-κB = Nuclear factor kappa-light-chain-enhancer of activated B cells, NOX = Nicotinamide adenine dinucleotide phosphate oxidases, PI3K = Phosphatidylinositol-4,5-bisphosphate 3-kinase,* PIP_2 *= Phosphatidylinositol (4,5)-bisphosphate,* PIP_3 *= Phosphatidylinositol (3,4,5)-trisphosphate, PTEN = Phosphatase and tensin homolog, RTK = Receptor tyrosine kinase, SOD3 = Superoxide dismutase 3.*[163] *Reproduced with permission of The Royal Society of Chemistry from ref [163].* [163]

Intriguingly, several authors have reported an association between peroxiporins and ERK, NOX, mTOR or PI3K/Akt, both in healthy[287] and cancerous cells[288,289]. In human epidermal keratinocytes for example, the involvement of AQP3 in the ERK pathways was demonstrated *in vitro*, where inhibition of ERK phosphorylation via ARNT (aryl hydrocarbon receptor nuclear translocator) activation led to both a downregulated expression of AQP3 and inhibited cell proliferation.[287] However, the correlation between the peroxiporins and these pathways, linked to their ability to facilitate H_2O_2 transport, was not uncovered until recently. Hara-Chikuma *et al.* unexpectedly found that AQP3 was expressed not only by keratinocytes but also by skin-infiltrating T-cells, regulating their trafficking in cutaneous immune reactions.[290] Specifically, they demonstrated the necessity of AQP3 mediated H_2O_2 permeation in chemokine-dependent T-lymphocyte migration in mice, where knocked-down expression of AQP3 proved to impair movement of the cells during immune response.[290] As such, hydrogen peroxide is suspected to be involved in a signalling cascade that results in the actin polymerization needed for cell movement, indicating that cell migration may be at least partially dependent on H_2O_2. A recent study showed AQP3 to mediate hydrogen peroxide-dependent responses to environmental stress in colonic epithelia.[291] Here, the increased membrane permeability to H_2O_2 in AQP3-expressing colonic endothelial cell allowed them to respond to external H_2O_2 at concentrations relevant for cellular signalling processes (1–100 µM), such as migration and pathogen recognition.[291]

Based on these results, it appears that modulated expression of AQPs in cancer cells can, therefore, be related not only to their ability to transport water or glycerol, but also H_2O_2. Hara-Chikuma et al. also demonstrated that AQP3 permeated H_2O_2 is necessary for keratinocyte migration and proliferation, suggesting this to be the same processes which have been implicated in cutaneous wound healing and tumorigenesis.[292] It is most likely that the elevated concentrations of intracellular peroxiporin permeated H_2O_2 in cancer cells may result in downstream signalling events. Currently, the exact nature of this association is widely investigated for its role in cancer cell regulation of proliferation, survival, differentiation, invasion and metastasis.[202,221,225,230,276,293]

AQP3 expression in tumour cells for example, was correlated with NOX2 and epidermal growth factor receptor (EGFR) dependent cancer progression *via* hydrogen peroxide permeation. Knockdown of AQP3 reduced intracellular H_2O_2 concentrations, subsequently impairing EGF-induced ERK and Akt activation and ultimately causing decreased tumour growth and migration.[230] Another study focusing on breast cancer cells indicated a role for AQP3-mediated H_2O_2 uptake, produced by NOX2, in cell migration. This AQP3-transported H_2O_2 activated the PI3K/Akt pathway by oxidizing PTEN (phosphatase and tensin homolog), illustrating that overexpression of AQP3 promoted migration of breast cancer cells in association with elevated H_2O_2 both *in vitro* and *in vivo*.[202] AQP8-transported H_2O_2 produced by NOX upon vascular endothelial growth factor (VEGF) stimulation seems to act in a similar way, by upholding the activation of Akt through oxidation of PTEN in leukaemia cell lines.[221] Remarkably, a different effect was seen for AQP9, where a downregulated expression was correlated with hepatocellular carcinoma cell migration. As such, the over-expression of AQP9 resulted in decreased levels of PI3k/Akt and suppressed cell invasion *in vitro* and xenograft tumour growth *in vivo*.[225]

These relatively recent studies on the potential role of AQPs in H_2O_2 permeation in relation to cancer highlight their possible importance as new therapeutic targets or biomarkers requires further investigation, as is illustrated by pharmacological ascorbate, a promising treatment in cancer therapy, that unfortunately shows a large variation in susceptibility.[294,295] Following intravenous administration, the ascorbate readily generates extracellular H_2O_2, which permeates the cancer cell membrane and accumulates intracellularly, ultimately inducing cell death due to excessive ROS presence.[296] The latest findings by Erudaitius *et al.* suggested that the success of pharmacological ascorbate treatment of pancreatic cancer may depend on peroxiporin (AQP3) expression.[297] In addition to AQP3, AQP8 and AQP9, other isoforms are still explored as potential peroxiporins. For example, AQP5 is an interesting candidate due to its association with ERG and PTEN in prostate cancer,[298] with EGFR/ERK in human glioma cell lines,[235] and in hepatocellular carcinoma metastasis with NF-κB[236]. Interestingly, a recent study on rat AQP5 in yeast showed its ability to facilitate H_2O_2 membrane diffusion.[299] Therefore, more research should be conducted to elucidate AQP5's possible role as peroxiporin in human cancers.

2.4 Aquaporin Inhibitors

There is strong evidence for AQPs as drug targets in different diseases, including cancer. Moreover, analysis of AQP involvement in the life cycle of disease-causing organisms (e.g. malaria parasites) suggests additional opportunities for pharmacological intervention in relation to the treatment of human diseases. Nonetheless, the identification of AQPs modulators (inhibitors) for both therapeutic and diagnostic applications has turned out to be extremely challenging. So far, to the best of our knowledge, four classes of AQP-targeting small molecules have been described: (i) metal-based inhibitors; (ii) small-molecules reported to inhibit water conductance (*e.g.*, sulfonamides); (iii) small-molecules targeting the interaction between AQP4 and the neuromyelitis optica (NMO) autoantibody; and finally, (iv) agents that act as chemical chaperones to facilitate the cellular processing of nephrogenic diabetes insipidus (NDI)-causing AQP2 mutants.[300] Despite numerous efforts, studies for several of the small organic compounds to date have no validation of their selectivity reported. We will therefore, in the following chapters, focus on the most promising metal-based AQPs inhibitors and their possible mechanisms of action described at a molecular level.

2.4.1 AQPs inhibition by metal ions

Under normal physiologic conditions, AQPs can be regulated by various factors such as protein phosphorylation, pH and metal ions. The latter are mainly divalent cations, such as first-row transition metals, some of them being physiologically relevant. Zelenina *et al.* for example, have investigated the effects of Ni^{2+} ($NiCl_2$) on the water permeability of AQP3 in human lung epithelial cells. They showed that Ni^{2+} can decrease water permeability to only 30%, at a concentration of 1 mM after 1 min of incubation.[301] This inhibition was shown to be reversible and Ni^{2+} did not have any effect on AQP4 or AQP5. The same authors conducted follow-up studies into the effects of Ni^{2+} (as $NiCl_2$) and Cu^{2+} (as $CuSO_4$) on glycerol permeability and found that both ions reduce AQP3 permeability at a concentration of 1 mM in HEPES buffer. [302] Interestingly, the Pb^{2+} and Zn^{2+} ions had no effect on AQP3 permeability. Furthermore, AQP7, another aquaglyceroporin, was insensitive to copper.

In an effort to elucidate which amino acid residues are involved in the inhibitory mechanism of both Ni^{2+} and Cu^{2+} ions, Zelenina *et al.* performed site-directed mutagenesis studies, and suggested serine, histidine and tryptophan residues as possible binding sites. [301,302] Interestingly, Ser152 was identified as a common determinant of both Ni^{2+}/Cu^{2+} and pH sensitivity. In fact, all these residues are in the extracellular loops of the AQP3 monomers, and loop movement was observed in the "gating" mechanism of several AQPs and appears to be a crucial feature in channel closure.[303–305] Histidine residues in such loops for example, can ''tune'' the pH sensitivity of AQP3 towards certain pH values, as suggested by molecular modelling.[306]

Despite their scarce selectivity and extreme toxicity, the benchmark mercurial compounds pCMBS (p-chloromercurybenzene sulphonate) and $HgCl_2$ have been widely applied in *in vitro* biochemical assays to study AQPs function. Their mechanism of inhibition involves direct binding of Hg^{2+} ions to AQPs *via* modification of cysteine residues, based on the classical hard soft acids and bases (HSAB) theory. To confirm such mechanism, several studies were performed on Cys-mutated isoforms of human AQP1. For example, the effects of mercury inhibition were evaluated in *Xenopus oocytes* transfected with Cys-mutated AQP1 isoforms.[307] From all cysteine residues in AQP1, only one was shown to confer sensitivity to the mercurial salt $HgCl_2$, namely Cys189. Mutation of this cysteine to either serine or glycine slightly decreased water permeability of the oocytes, indicating that this residue may be of importance for water transport. Furthermore, cells expressing the Cys189Ser mutant lost sensitivity to $HgCl_2$.

Two mechanisms of inhibition of AQPs by mercury have been described in current literature: i) is simple occlusion of the water pore by the mercury ions found in the vicinity of the cysteine residues lining the pore; ii) is conformational change (collapse of the water pore) at the selectivity filter (namely, the (ar/R) SF) region, induced by mercury bound to a cysteine residue nearby.

The first hypothesis was formulated after the atomic-resolution structure of human AQP1 (hAQP1) was solved, showing Cys189 to be positioned inside the channel, just above the ar/R SF.[171] Therefore, it was hypothesized that Hg^{2+} binding to this site was likely to prevent passage of water molecules *via* steric effects, acting like a cork.

The second mechanism of AQP inhibition by mercurial compounds was first proposed in an *in silico* study on the basis of molecular dynamics (MD) simulations of bovine aquaporin AQP1 (bAQP1).[308] This bAQP1 contains a cysteine residue (Cys191) in the ar/R SF region, which may bind Hg^{2+} similarly to hAQP1. According to the MD simulations comparing both free AQP1 and Hg-bound AQP1 using the calculated free energy profiles for water transport through the AQP obtained with the umbrella sampling technique, the energy barrier for Hg-AQP1 is much higher than that of free AQP1 at the ar/R SF. Additionally, further calculations show that mercury binding induces a collapse of the orientation of amino acid residues at the ar/R SF and the constriction of the space between Arg197 and His182.

Later on, our group investigated the molecular mechanism of inhibition of human AQP3 by Hg^{2+} using MD approaches.[309] Interesting, our findings support of the second mechanistic hypothesis, as we observed important protein conformational changes upon binding of metal ions to Cys40 leading to a collapse of the ar/R SF, and subsequent blockage of water permeation.

2.4.2 Gold complexes as inhibitors of aquaglyceroporins

Recently, coordination gold(III) compounds have been identified as selective aquaglyceroporin inhibitors. Specifically, we have reported for the first time on the potent and selective inhibition of human AQP3 by the water-soluble gold(III) compound $[Au(phen)Cl_2]Cl$ (phen = 1,10-phenanthroline, **Auphen**, Figure 2.6).[107] Interestingly, Auphen had a selective effect, inhibiting only glycerol transport in human red blood cells (hRBC), with an $IC_{50} = 0.8 \pm 0.08$ µM, whilst having no inhibitory effect on water permeability mediated by the orthodox water channel AQP1.

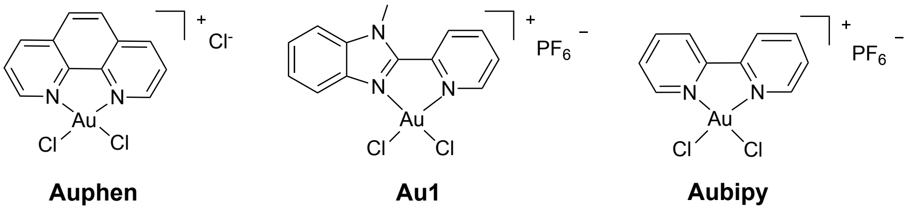

***Figure 2.6**: Structure of the gold(III) complexes $[Au(phen)Cl_2]Cl$ (phen = 1,10-phenanthroline, **Auphen**) and $[Au(1\text{-methyl-}2\text{-(pyridin-}2\text{-yl)-benzimidazole})Cl_2]PF_6$ (**Au1**), and $[Au(bipy)Cl_2]PF_6$ (bipy = 2,2'-bipyridine, **Aubipy**), inhibitors of human AQP3.*

A follow-up study examined **Auphen**'s capacity of inhibiting cell proliferation in various cell lines with different levels of AQP3 expression, demonstrating a direct correlation between AQP3 expression levels and cell growth inhibition by the gold(III) compound. [252] Additional functional studies also showed AQP3 inhibition in the cell lines where proliferation was affected by treatment with the gold compound.

With molecular modelling, the non-covalent binding of **Auphen** to AQPs was investigated at a molecular level. The observed isoform selectivity was due to the accessibility of Cys40, of which the thiol group is a likely candidate for direct binding to Au(III) complexes.[107] Involvement of this particular residue in the inhibition mechanism was further confirmed in a subsequent study by site-directed mutagenesis.[252] Additional results on other Au(III) compounds with different N^N ligand scaffolds allowed us to establish preliminary structure-activity relationships. In detail, the most effective compounds were those featuring at least one positive charge, one ligand that could be exchanged to allow metal coordination to protein residues, and aromatic ligands.[108] Surprisingly, Au(I) complexes did not show any AQP inhibition properties, implying that the hard-soft acid-base (HSAB) theory is not sufficient to predict the affinity for a metal compound for a certain protein binding site. Quantum mechanics/molecular mechanics (QM/MM) calculations suggested that the ligand moiety may play a major role in orienting the selectivity towards a certain isoform,[108] stabilizing the position of the inhibitor in the extracellular binding pocket.

Thus, the reversibility of AQP3 inhibition was studied in hRBC, by pre-treating cells with the gold compounds for 30 min at r.t. and, subsequently, washing with either excess of the thiol-containing reducing agent *β*-mercaptoethanol, the sulphur donor L-Cys, or the N-donor His.[108,109] For all compounds, treatment with the competitor molecules led to an almost complete recovery of glycerol permeability, ruling out possible oxidative modification of amino acid residues by the Au(III) complexes.

After including the 1,10-phenantroline derivatives of Pt(II) and Cu(II) in the investigation to compare the effects of metal substitution on the AQP3 inhibition potency, remarkably, the inhibition potency decreased drastically in the order: **Auphen** > Cuphen (IC_{50} = 81.9 ± 4.1 μM) >> Ptphen (IC_{50} > 200 μM).[108]

A recent MD study was conducted for the first time on another potent and selective inhibitor - the compound [Au(1-methyl-2-(pyridin-2-yl)-benzimidazole)Cl_2]PF_6 (**Au1**, Figure 2.6) - bound to Cys40 of AQP3 (Figure 2.7). A protein conformational change was shown upon metal binding to Cys40, indicating that rather than direct steric blockage of the channel by the metal compound, this was mostly responsible for the observed inhibition of water and glycerol permeation (Figure 2.8).[109]

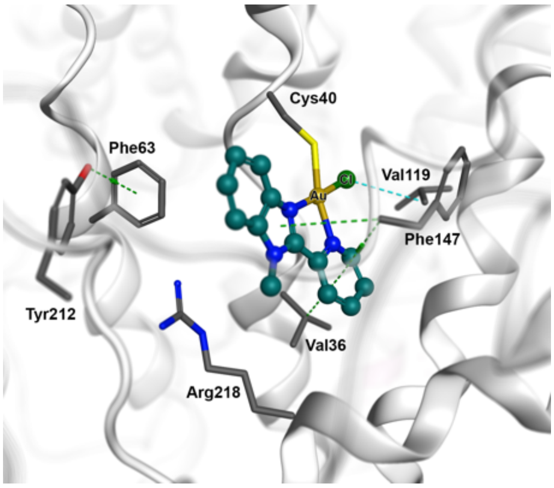

Figure 2.7: *Representation of the mechanism of inhibition of AQP3 (white ribbon) by the gold(III) complex* ***Au1*** *(dark teal ball and stick representation). Relevant amino acids are shown in grey stick representation, with the backbone and hydrogens hidden for clarity. Interactions are shown in dashed lines: cyan for H-bonds and green for arene-H. Reproduced with permission of The Royal Society of Chemistry from ref [163].* [163]

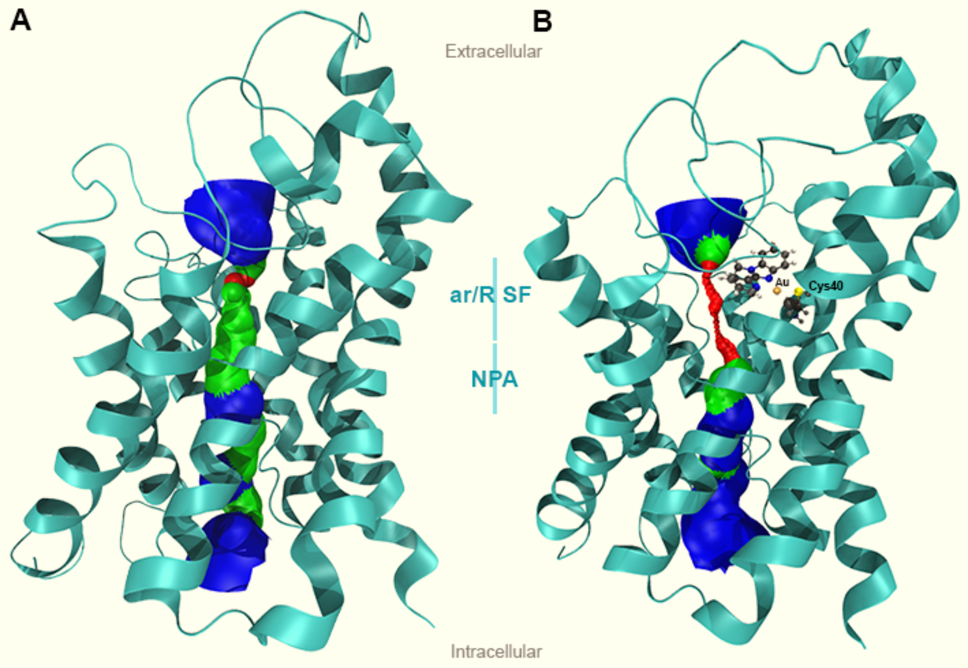

Figure 2.8: *(A) Human AQP3 monomer and* ***(B)*** *hAQP3 with Cys40 bound to the Au(III) complex* ***Au1****, showing the effect on pore size (based on VDW radii): red = smaller than single* H_2O*, green = single* H_2O*, blue = larger than single* H_2O*. Complex* ***Au1*** *and Cys40 are shown in ball and stick representation.*

Interestingly, these findings are in line with the aforementioned studies on AQP inhibition by mercury. What's more, it appears that binding of **Au1** in one monomer also affects substrate permeability in an adjacent one, altering the overall extracellular distribution of hydrophobic/hydrophilic surfaces of the tetramer which, in turn, orients the approach of substrates to the pore. In this study, a correlation between the affinity of the Au(III) complex towards Cys binding and AQP3 inhibition was highlighted, while no influence of the different oxidative character of the metal complexes was observed.[109]

Another selective AQP3 inhibitor has been part of further studies. The gold(III) cationic complex $[Au(bipy)Cl_2]PF_6$ (bipy = 2,2’-bipyridine, **Aubipy**, Figure 2.6), bound to the protein channel, was evaluated by means of a multi-level theoretical workflow that includes QM, MD and QM/MM approaches.[310] Specifically, three key aspects for AQP3 inhibition by gold compounds have emerged in this study: i) speciation of the gold(III) complex prior protein binding (formation of aquo-complexes), ii) the stability of non-covalent adducts between the aromatic ligand of the compound and the extracellular pore side, and iii) coordinative binding of Au(III) ions induced conformational changes within the pore leading to pore closure, in line with the above-mentioned study on **Auphen**.

The latter study suggested that presence of thiol binding sites in AQP3 is necessary, but not sufficient to determine the selectivity of **Aubipy**.[310] Instead, the formation of stable non-covalent Aubipy-AQP3 adducts is required to compensate the thermodynamic and kinetic barriers associated with the formation of the final covalent Au-Cys adduct. Specifically, the overall **Aubipy**-AQP3 binding process may be described as proposed in Figure 2.9.

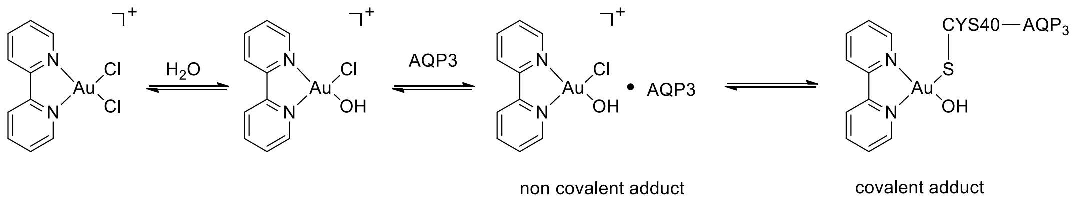

Figure 2.9*: Scheme showing proposed mechanism of interaction of the Au(III) complex* ***Aubipy*** *with AQP3.*

Overall, the results of these studies are substantial for future inhibitors’ design, showing that amino acid residues other than those lining the pore could be targeted, provided that their modification induces the necessary conformational changes to achieve channel closure. Furthermore, the careful fine-tuning of the interactions between the metal complex and specific residues at the pore extracellular entrance, leading to the formation of the first non-covalent adduct, may be achieved by different substituents on the ligand bound to Au(III), as well as by the use of different aromatic scaffolds (e.g., C^N-cyclometallated and benzimidazole ligands). As such, the selectivity of the compound for inhibition of AQP3 might be increased compared with other aquaglyceroporin isoforms.

To deliver a targeted therapy dependent on the isoform of interest, selectivity of aquaglyceroporin inhibition is essential. In fact, **Auphen** was also observed to inhibit AQP7, but to a lesser degree compared to AQP3, with a different mechanism of inhibition, as indicated by permeability studies and molecular modelling approaches, respectively.[311] In detail, whilst Cys residues corresponding to Cys40 in AQP3 are not available, several thioether containing Methionine side chains are accessible, on either the extracellular or the intracellular side of human AQP7, for binding to Au(III) complexes.

The fact that the inhibition mechanism of the same compound with two different aquaglyceroporins may be different, indicates that it is possible to take advantage of even the slightest structural differences between isoforms to optimize the inhibitor's chemical scaffold and, thus, to achieve selectivity.

2.5 Conclusions and Perspectives

Clinical and preclinical studies correlate AQP expression to several forms of cancer. This gave rise to an intensive investigation in recent years into the biological functions and signalling pathways of AQPs in cancer, using genetic approaches to generate a condition of AQP depletion. Additionally, AQPs are involved in the carcinogenesis and pathogenesis of tumour-associated oedema, tumour cell proliferation and migration. However, the exact nature of this correlation is still the subject of discussion, emphasizing the need to develop targeted modulators to study the mechanism of these potential therapeutic targets. Indeed, numerous *in vivo* and *in vitro* studies have shown several attractive opportunities for AQP-targeted therapy. Furthermore, it has been postulated that some of the aquaglyceroporins are responsible for the uptake of inorganic chemotherapeutics, such as the anti-leukemic arsenic trioxide.[7]

The possible contribution of bio-inorganic chemistry is therefore crucial to, taking advantage of the promising studies on gold(III) compounds as selective aquaglyceroporins inhibitors, and in combining highly integrated investigational approaches, optimize new metal-based complexes to target specific AQPs isoforms. Copper complexes have been considered as alternative promising candidates to gold compounds, and ongoing studies in our lab aim at designing new ligand systems able to favour the binding of Cu(II) and Cu(I) ions to AQPs. Therefore, the design and use of either coordination or organometallic metal compounds may unravel unexpected roles of AQPs in the molecular mechanisms of diseases and provide new tools in chemotherapy and imaging.

Finally, inorganic chemistry offers important advantages with respect to organic chemistry. In fact, metal complexes constitute an ideal drug design platform, where not only the geometric properties of the molecule can be easily varied, but also offering the possibility of "fine-tuning" the reactivity of the compounds via appropriate ligand choice, maintaining AQP inhibition activity whilst reducing the side-effects.

Chapter 3: Gold(III) coordination complexes designed as aquaglyceroporin inhibitors & anticancer drugs

This chapter is based on the following papers:

Gold(III) Pyridine-Benzimidazole Complexes as Aquaglyceroporin Inhibitors and Antiproliferative Agents

Brech Aikman, Margot N. Wenzel, Andreia F. Mósca, Andreia de Almeida,Wim T. Klooster, Simon J. Coles, Graça Soveral and Angela Casini

DOI: 10.3390/inorganics6040123

&

Insights into the Mechanisms of Aquaporin-3 Inhibition by Gold(III) Complexes: the Importance of Non-Coordinative Adduct Formation

Margot N. Wenzel, Andreia F. Mósca, Valentina Graziani, **Brech Aikman**, Sophie R. Thomas, Andreia de Almeida, James A. Platts, Nazzareno Re, Cecilia Coletti, Alessandro Marrone, Graça Soveral, and Angela Casini

DOI: 10.1021/acs.inorgchem.8b03233

Gold(III) complexes synthesized by Dr. Margot Wenzel
DFT, MD and quantum mechanics/molecular mechanics QM/MM studies performed by the group of Prof. Nazzareno Re (University of Chieti, Italy)

3.1 Introduction

As the second leading cause of death globally, cancer is a group of diseases in need for new treatments (WHO 2020).[312] In fact, the existing chemotherapies are still associated with severe side effects and limited by the development of cancer cells' resistance, which renders essential the discovery of improved anticancer therapies. Specifically, the discovery of new compounds with the ability to tackle the hallmarks of cancer is nowadays the focus of intense research. In this context, metal-based complexes hold promise since they act *via* the interaction with different proteins and secondary DNA structures, as well as by altering of the intracellular redox balance. Within the metal-based niche, gold complexes have attracted attention in the last years and numerous families of Au(I) and Au(III) compounds have been synthesized and studied for their anticancer properties *in vitro* and *in vivo*.[66,94] Interestingly, for some of these gold compounds, mechanistic studies enabled the identification of their preferential protein targets, ruling out DNA as the unique or major pharmacological target.[313]

As described in Chapter 2, AQPs are membrane proteins that serve as channels facilitating transfer of water and in some cases, small solutes across the membrane. Depending on their permeability features regarding solute selectivity, a divide can be made between the 13 mammalian AQPs that have been identified so far: i) *orthodox aquaporins* (AQP0, AQP1, AQP2, AQP4, AQP5, AQP6 and AQP8), which are primarily water selective and facilitate water movement across cell membranes in response to osmotic gradients,[314] ii) *aquaglyceroporins* (AQP3, AQP7, AQP9 and AQP10), facilitating the permeation of small uncharged solutes such as glycerol,[315] and iii) *unorthodox* aquaporins (AQP11, AQP12), found in intracellular membranes, reported to facilitate both water and glycerol permeation.[150,151,153] Specifically, aquaglyceroporins are known to regulate glycerol content in various tissues, such as epidermis or fat, and have been proposed to be involved in skin hydration and wound healing, cell proliferation, lipid metabolism and carcinogenesis.[316]

Several studies demonstrated that AQPs are closely associated with cancer proliferation and invasion and are expressed in at least 20 human cancers.[163] Furthermore, AQPs expression is related to tumour types, grades, proliferation, migration and angiogenesis, highlighting the potential use of these transport proteins as both diagnostic and therapeutic targets in cancer.[163]

Therefore, in general, the use of selective AQPs inhibitors would complement genetic approaches in studying the roles of AQPs in health and disease states and hold great promise also to develop AQP-targeted therapies. However, so far, no reported organic small-molecule AQPs inhibitor possesses sufficient isoform selectivity to be a suitable candidate for further clinical development.[155,241,317]

In recent years, the potent and selective inhibition of glycerol permeation via human AQP3 by a series of Au(III) complexes with bidentate N^N ligands was reported,[107,108] using human red blood cells (hRBC) as models. The most potent inhibitor of the series, **Auphen** ($[Au(phen)Cl_2]Cl$, phen = 1,10-phenanthroline, Figure 3.1) had an IC_{50} value (concentration at which 50% of the maximum inhibition effect is induced) in the low micromolar range (0.8 ± 0.08 μM) and was thus far more effective than the benchmark AQP inhibitor, the mercurial compound $HgCl_2$.[107] In a subsequent study, **Auphen**'s capacity of inhibiting cell proliferation was examined in various cancerous and non-cancerous cell lines, with different levels of AQP3 expression, and showed a direct correlation between AQP3 expression levels and the inhibition of cell growth by the Au(III) compound.[252] AQP3 inhibition was also demonstrated in the cell lines where proliferation was mostly affected by treatment with **Auphen**.[252] To optimize the design of an AQP3 inhibitor and its selectivity, structure-activity relationships were established investigating other Au(III) compounds with different N^N ligand scaffolds.[108]

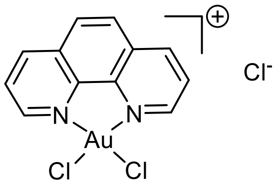

Auphen

$IC_{50} = 0.80 \pm 0.08$ μM

*Figure 3.1: Structure of the Au(III) compound **Auphen**.*

In the pursuit of designing more potent and selective AQP3 inhibitors, we have recently observed that charge might play a pivotal role. The newly synthesized cationic complex $[Au(pbzMe)Cl_2]PF_6$ (**C1**, pbzMe = 1-methyl-2-(pyridin-2-yl)-benzimidazole, Figure 3.2) was even more effective than **Auphen** regarding inhibition of glycerol permeation *via* AQP3,[66] and ca. 3-fold more effective than the neutral related complex $[Au(pbzH)Cl_2]$ (**C10**, pbzH = 2-(pyridin-2-yl)-benzimidazole).[109] Combined with molecular dynamics (MD) and density functional theory (DFT) studies, our group showed that the gold centre of **C1**, upon binding to Cys40 in AQP3, is able to induce protein conformational changes leading to the shrinkage of the channel, consequently preventing glycerol and water permeation and does not function as a "cork" which directly sterically hinders substrate permeation.[109]

Following these promising results, a new series of Au(III) complexes was synthesized based on the 2-(2-pyridyl)benzimidazole (pbzH) N^N donor ligand, which is known to inhibit hepatic enzymes,[318] and exhibits anticancer activities *per se*.[319] In fact, metal complexes based on 2-(2′-pyridyl)benzimidazole scaffolds have attracted attention in various established and potential application areas, including medicinal inorganic chemistry.[320–322] Thus, we report here on the synthesis and structural characterization of eight novel cationic Au(III) derivatives with functionalization at the non-coordinated benzimidazole nitrogen, as well as two neutral complexes featuring extended aromatic scaffolds (pyrene and anthracene) endowed with luminescence properties. The compounds have been tested for their AQP inhibition properties in human Red Blood Cells (hRBC) using a stopped-flow method and were compared to the established **C1** [Au(pbzMe)Cl_2]PF_6 and **C10** [Au(pbzH)Cl_2]. Afterwards, the compounds` antiproliferative effects were evaluated in a small panel of human cancer cells with different levels of AQP3 expression.

In a second phase of our investigation, we also evaluated a number of derivatives of **Auphen** for both their AQP3 inhibition properties and anticancer activities.

3.2 Results and Discussion

3.2.1 Au(III) complexes with bi-dentate 2-(2′-pyridyl)benzimidazole ligands

The library of functionalised pyridylbenzimidazole ligands **L1-L9** (Figure 3.2, top) has been obtained by Dr. Margot Wenzel through nucleophilic substitution on the non-coordinated nitrogen atom of the commercially available pyridylbenzimidazole by reaction with a halogenated substituent (R-X) in the presence of a base.[323] To study the influence of both steric hindrance and the electronic effect on the biological properties of the final gold complexes, several types of functional groups have been explored. In parallel, two additional ligands (**L11-L12**) featuring luminescent properties[324] have also been synthesized with the idea to allow monitoring of their fate in cancer cells with fluorescence microscopy. Through the use of ligands **L1-L9**, which possess a functionalised amine, corresponding Au(III) cationic complexes (**C1-**

C9) were obtained via reaction between an equimolar amount of **L1-L9** and $NaAuCl_4$, in the presence of an excess of KPF_6 (Figure 3.2, top). The pure cationic gold complex products can then easily be isolated following precipitation, washing and filtration. On the other hand, reaction between ligands **L10-L12** and $NaAuCl_4$ in presence of a base leads to the formation of the neutral complexes **C10-C12** (Scheme 1, bottom).[109] Both the identity and the purity of the complexes **C1-C12** was confirmed by NMR, IR and UV-Visible spectroscopies, as well as by mass spectrometry and elemental analysis.

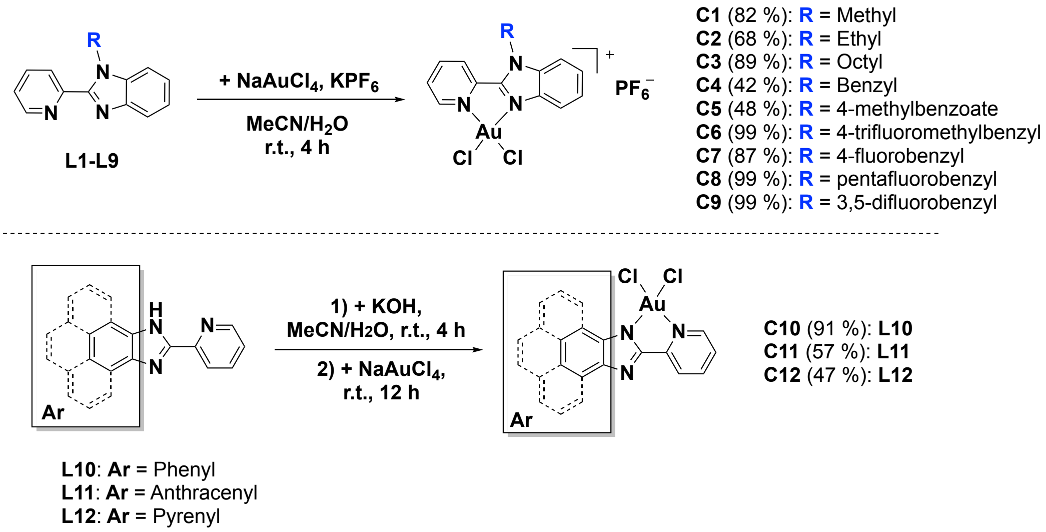

***Figure 3.2**: Synthetic pathways to the series of cationic (top) and neutral (bottom) Au(III) complexes **C1-C9** and **C10-C12**, respectively.*[325]

Crystals were obtained for complexes **C6** and **C7**, allowing the use of X-ray crystallography to determine the molecular structures.[326] The X-ray structure of the compound confirmed a bidentate coordination mode of the ligand **L6** onto the gold centre *via* the nitrogen of the pyridine and the benzimidazole rings, thus giving rise to square planar complexes (Figure 3.3-A). In line with already described similar ligands and copper complexes, the 4-trifluoromethylbenzyl functional group added on the benzimidazole moiety always points out of the plane.[321] Interestingly, the C6 structure also revealed the presence of $AuCl_4^-$ counter ions in the lattice, hinting at decomposition. However, the relatively slow process of crystallisation (10-15 days) needs to be taken into consideration, as this may actually favour the partial decomposition of these complexes, specifically the de-coordination of the gold centre and exchange of counter anions. Furthermore, when attempting to crystallize compound **C7** using the same conditions, the resulting X-ray structure confirmed the de-coordination of the gold centre from one of the nitrogen of the pyridine ligand, thus, leading to a neutral gold complex with three coordinated chlorido ligands (Figure 3.3-B).

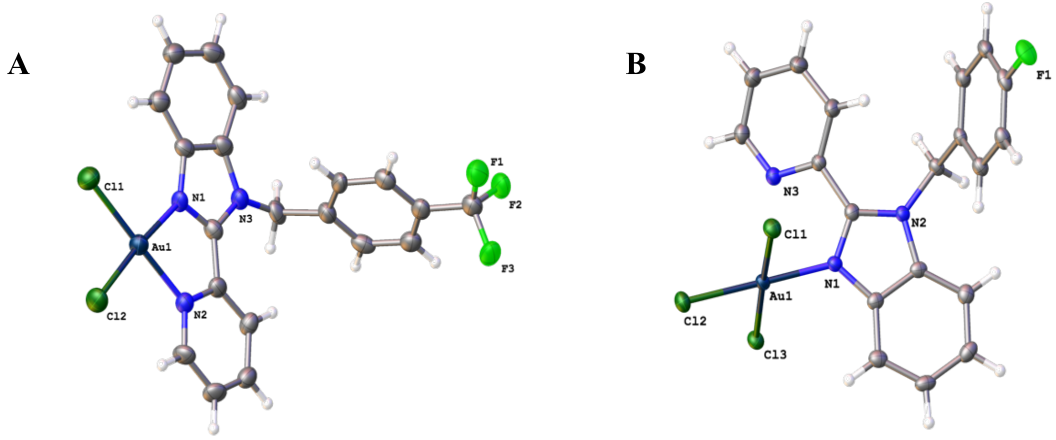

Figure 3.3: *Thermal ellipsoids drawn at the 50% probability level, derived from crystal structures of A)* ***C6*** *and B)* ***C7****. Carbon is shown in grey, hydrogen in white, chloride in dark green, fluor in light green, nitrogen in light blue and gold in dark blue.*[325]

3.2.2 Absorption and Luminescence properties

The gold(III) complexes **C1-C12** and their corresponding ligands **L1-L12** have been investigated for their photophysical properties (Table 3.1 and 3.2). Corresponding graphs can be found in the supplementary information (Figures S1-S24, Appendix A1). Both the ligands **L1-L10** and complexes **C1-C9** exhibit a strong absorption band centred nearby 310-315 nm, which can be attributed to π->π* transitions and/or in the case of the Au(III) complexes ligand-to-metal charge transfers (LMCT). Due to the minimal peak shifts observed in this region upon gold introduction, a LMTC might be less likely to occur in the other Au(III) complexes. Examples of graph overlap can be found in the supplementary information (Figure S25, Appendix A1). The absorption spectra of ligands **L11-L12** and corresponding complexes **C11-C12**, with the extended conjugated systems, show several bands attributed to similar transitions between 330 and 390 nm. Ligands **L1-L10** and complexes **C1-C9** all have single fluorescence emission bands centred around 375-380 nm, representing a Stokes shift of roughly 65 nm.

***Table 3.1**: Photophysical data obtained by UV-Visible spectrophotometry and fluorescence spectroscopy for the ligands in DMSO.*[325]

Compound	**$\lambda_{max\ (Abs)}$ [nm]**	**ε_{max} [M^{-1} cm^{-1}]**	**$\lambda_{max\ (Em)}$ [nm]**	**ϕ_F [%]**[a]
L1	311	20 260	369	60
L2	312	21 645	367	54
L3	313	27 357	370	50
L4	312	24 729	370	27
L5	313	14 123	370	30
L6	313	23 130	363	38
L7	312	21 244	369	32
L8	312	29 031	369	42
L9	312	22 425	369	36
L10	313	24 475	367	69
L11	333, 362	20 088, 15 966	415	74
L12	338, 353, 366, 387	25 928, 24 139, 15 420, 15 708	439	61

[a] Reference standard for QY assessment was quinine sulphate (at 0.5 M, $\varphi = 55\%$ in H_2SO_4 at room temperature).[327,328]

***Table 3.2**: Photophysical data obtained by UV-Visible spectrophotometry and fluorescence spectroscopy for the gold(III) complexes in DMSO.*[325]

Compound	**$\lambda_{max\ (Abs)}$ [nm]**	**ε_{max} [M^{-1} cm^{-1}]**	**$\lambda_{max\ (Em)}$ [nm]**	**ϕ_F [%]**[a]
C1	314	23 949	370	48
C2	316	21 654	369	39
C3	315	16 006	378	27
C4	315	21 527	368	23
C5	312	23 448	367	29
C6	312	24 699	389	32
C7	312	25 542	371	26
C8	311	23 441	370	36
C9	313	14 367	370	30
C10	328	12 883	390	4
C11	335, 362	20 891, 16 528	415	58
C12	338, 353, 366, 388	28 904, 28 264, 19 892, 20 031	441	71

[a] Reference standard for QY assessment was quinine sulphate (at 0.5 M, $\varphi = 55\%$ in H_2SO_4 at room temperature).[327,328]

Complexes **C11-C12** and their corresponding ligands possess extended aromatic and conjugated systems, and indeed a shift in the emission bands is observed: ligand **L11** and complex **C11** emit at 415 nm whereas **L12** and **C12** exhibit an emission band around 450 nm. The quantum yield of fluorescence (Φ_F) has been assessed for all the reported compounds. While the ligands with alkane substituents (**L1-L3**) have relatively high quantum yields (50-60%), the ligands with the functionalised benzyl groups (**L4-L9**) have decreased quantum yields between 27 and 42%. The ligands with the extended aromatic systems **L11** and **L12** have quantum yields of 74 and 61%, respectively. In general, upon coordination of the ligands to the gold(III) ion, almost all quantum yields of luminescence are decreased due to the "heavy metal effect",[329] with the exception of complex **C12** ($\Phi_F = 71\%$).

3.2.3 Assessment of stability in biologically relevant environment

As the aromaticity of the gold complexes allowed for UV-Vis spectroscopy, the same technique was used to investigate their stability before further biological testing. Thus, the absorbance of the compounds' solutions in biologically relevent conditions mimicked with 1x PBS buffer (pH 7.4) was measured between 300 and 800 nm at regular time intervals during 24 h at room temperature, allowing the monitoring of the possible compound's transformations such as hydrolysis, reduction and/or precipitation. The presence of the physiologically relevant extracellular chloride concentration provided by the PBS buffer is essential in order to properly study the gold complexes, as Au(III) complexes are either intact or in hydroxy forms at neutral pH and could act as prodrugs.[107] Additionaly, as the Au(III) complexes tend to be reduced in physiological conditions to Au(I) and even Au(0), the reactivity of the compounds with the intracellular reducing agent glutathione (GSH) was monitored in the same conditions.

All the Au(III) compounds exhibit intense transitions in the 300-450 nm range, characteristic of the Au(III) chromophore, that may be straightforwardly assigned as LMCT bands. Interestingly, the maximum absorption wavelength of the aforementioned LMCT bands can be subjected to shifts in dependence of the solvent used (e.g. DMSO or aqueous buffer). Complexes **C1**, **C2**, **C5**, **C6** and **C9** were found to be mostly stable over the first 6 h in PBS buffer (pH 7.4) with no significant change in the UV-Visible spectra (Figures 3.2/S26, S27, S30, S31 and S34 in Appendix A2). To better compare the absorption of the free ligand with the one of the related Au(III) complex, we include the representative absorption spectra of 2-(2'-pyridyl)benzimidazole (pbiH) and its complex **C10** in buffered solution recorded between 200 and 800 nm (Figure S35). Of note, additional bands at ca. 290 nm are attributed to a metal-perturbed intraligand (IL) π−π* transition within the pbiH ligand. Generally, the free N^N donor ligands absorbs between 200-310 nm, with the exception of ligands **L11** and **L12** featuring strong absorption bands *per se* between 300-400 nm (Figure S36), likely due to π–π* transitions located in the heteroaromatic rings. The observed small spectral changes developing with time might be related to the occurrence of partial hydrolysis processes. Instead, the spectra of complexes **C3**, **C4**, **C7**, **C8** and **C10** were found to undergo major changes over the first few hours (Figures 3.2/S28, S29, S32-S33 and S37 in Appendix A2), causing disappearance of the classical LMCT bands, suggesting disruption of the Au(III) complex. Examples of a stable (**C1**) and unstable (**C3**) compound are shown in Figure 3.4. In Figure 3.4-A, **C1** displays marked stability in PBS. However, exposure to glutathione (Figure 3.4-B) induces an immediate reaction, resulting in the complete disappearance of the diagnostic Au(III) complex's bands, possibly due to formation of a stable adduct with GSH likely to result into reduction of the gold centre to Au(I). In contrast, **C3** (Figure 3.4-C) is shown to degrade immediately upon exposure to PBS, with significant batochromic and hypocromic peak shifts, resulting in precipitation as demonstrated by the upwards shift of the baseline. Complexes **C11-C12** were moderately stable in solution (Figures S38-S39 in Appendix A2) featuring hypocromic shifts in their spectra over the first 6 h incubation. In the presence of glutathione (GSH), a rapid dissapeareance of LMCT bands was seen in all the compounds, as they presumably reacted immediately to form adducts leading to the loss of the N-donor ligands from the gold centre in the first hour (Figures S26-S34 and S37 in Appendix A2). Only compounds **C11** and **C12** were less reactive and maintained their spectral features over time after addition of GSH (Figures S38-S39 in Appendix A2).

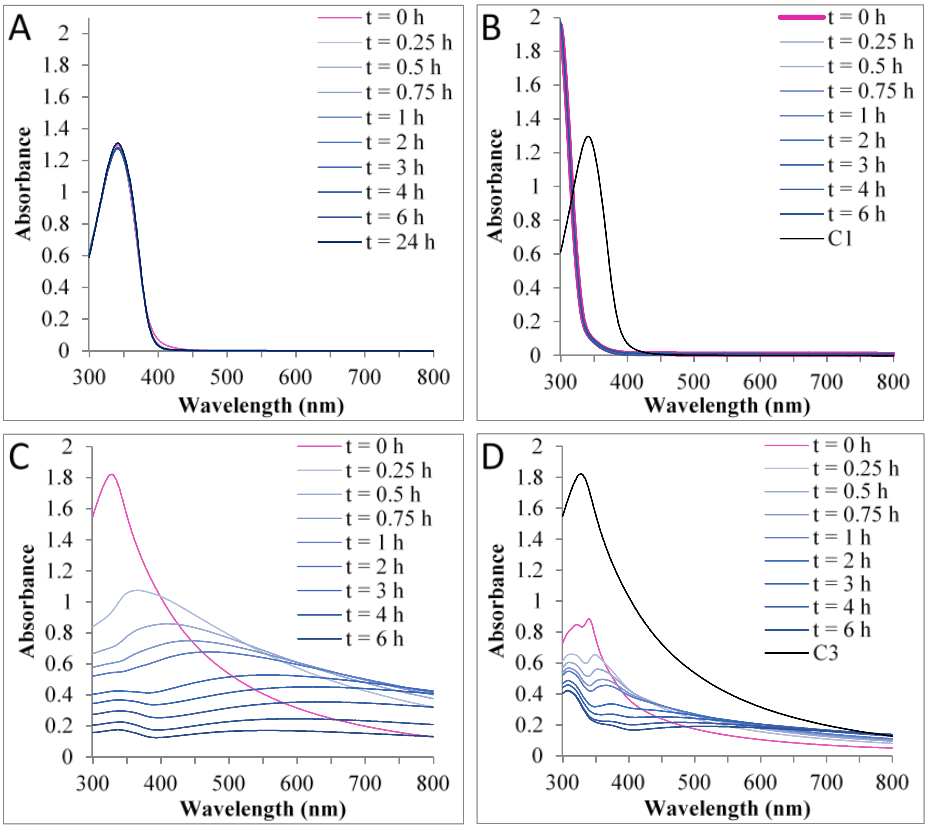

***Figure 3.4**: UV-Visible spectra examples of a stable and unstable Au(III) complex. Stock prepared in DMSO, followed by dilution (10^{-4} M) in PBS. **A**) **C1** (10^{-4} M) and **C**) **C3** (10^{-4} M) in PBS (pH 7.4) recorded over time at r.t.;**B**) **C1** and **D**) **C3** before and after addition of GSH (2 eq.) recorded over time at r.t. The curves labelled **C1** and **C3** in **B**) and **D**) show the spectra of the corresponding Au(III) complexes in PBS before GSH addition.*[325]

3.2.4 Aquaporin inhibition in human Red Blood Cells

Guided by the previously discussed stability studies, the most stable gold complexes were selected for further testing for their AQP1 and AQP3 inhibition properties in hRBC by stopped-flow spectroscopy, according to previously reported methods.[107] Representative IC_{50} curves for the inhibition of glycerol permeation *via* AQP3 after 30 min of incubation by two gold compounds are reported in Figure 3.5. The obtained results are summarized in Table 3.3 and show that interestingly, all the new cationic complexes **C2**, **C4**, **C5**, **C6**, and **C9** are able to selectively inhibit glycerol permeation *via* AQP3, with IC_{50} values in the sub-micromolar level, comparable to **C1** and Auphen. The most effective complex was **C6**, and in line with previous results, the neutral compound **C10** was ca. 1 order of magnitude less effective as AQP3 inhibitor.[109] Surprisingly, the neutral **C11** featuring an aromatic phenanthrene was quite an effective AQP3 inhibitor as well, with an IC_{50} of 0.82 ± 0.13. Interestingly, all the new compounds were inactive as inhibitors of the orthodox water channel AQP1 in the same cellular model (data not shown). The error bars (standard error of the mean from 3-4 biological replicates) seen in Figure 3.5 are charasteristic of the established and well tried stopped-flow method: through accurate measurement of the initial hRBC volume and the osmolarity of the solutions used for osmotic shock, permeablity varies very little between replicates, as the stopped flow traces do not vary much for each cell population.[107]

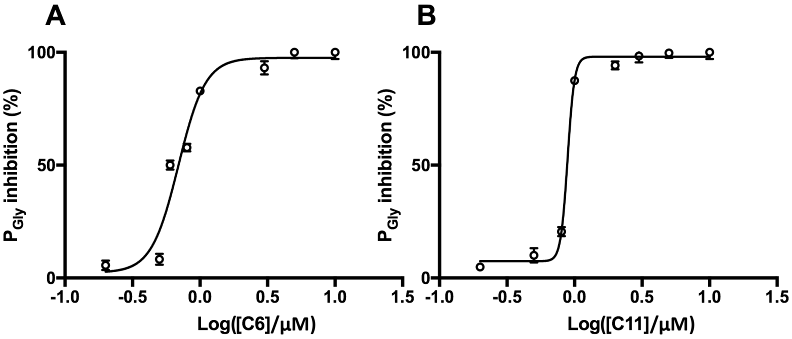

***Figure 3.5**: Representative IC_{50} curves for the inhibition of glycerol permeation via AQP3 by the Au(III) complexes **C6** (A) and **C11** (B) in hRBC after 30 min incubation. Each point represents the mean and SEM of 3-4 biological replicates (Figure S47-D, Appendix A4 shows an example of the individual biological experiments of **C6**).* [325]

***Table 3.3**:* AQP3 inhibitory effects (IC_{50} values) measured in hRBC after 30 min incubation.

Compound	**AQP3 inhibition**
	IC_{50} [µM] [1]
Auphen	0.80 ± 0.08
C1	1.018 ± 0.137
C2	0.881 ± 0.015
C3	1.825 ± 0.017 (n=2)
C4	0.85 ± 0.21
C5	0.80 ± 0.10
C6	0.69 ± 0.06
C7	n.d.
C8	n.d.
C9	0.72 ± 0.05
C10	>50
C11	0.82 ± 0.13 (n=2)
C12	n.d.

[1] Values represented as mean (± SEM) of at least three independent experiments (n), unless otherwise stated. n.d. = non determined.

3.2.5 Expression of AQP3 in Cancer Cells

Following the stability studies reported above, the compounds - with the exception of the highly unstable **C7** and **C8** - were evaluated for their antiproliferative activities against a panel of human cancer cells *in vitro*, namely A549, A375, MCF-7 and SKOV-3. Prior the cytotoxicity screening, the cells were studied for their level of expression of human AQP3. Information on the expression of AQP3 in cancer lines is still limited and most of the data currently available refer to mRNA expression levels.[330] Presence of mRNA is no guarantee for actual protein expression. Therefore, the expression levels of human AQP3 were studied in the cells using flow cytometry (Figure 3.6) using a green labelled secondary Alexa Fluor®488-labeled AQP3 antibody. This would give a quantitative indication of AQP3 cellular presence per cell line, but not the actual membrane- or intracellular location. Therefore, an immunocytofluorescene microscopy assay was performed using again an AQP3 antibody endowed with green-fluorescent probe Alexa Fluor®-488. The results are presented in Figure 3.7.

Both experiments confirm the presence of AQP3 in all cell lines. In line with both literature and mRNA levels [330], the breast cancer cell line MCF-7 highly expresses AQP3. A marked AQP3 expression was also observed in the ovarian cancer cells SKOV-3, followed by the lung cancer cells A549 and the skin malignant melanoma cells A375. The melanoma cells A375 displayed an addition cellular localization of AQP3 in the nuclear membrane (Figure 3.6) as evidenced by fluorescence microscopy.

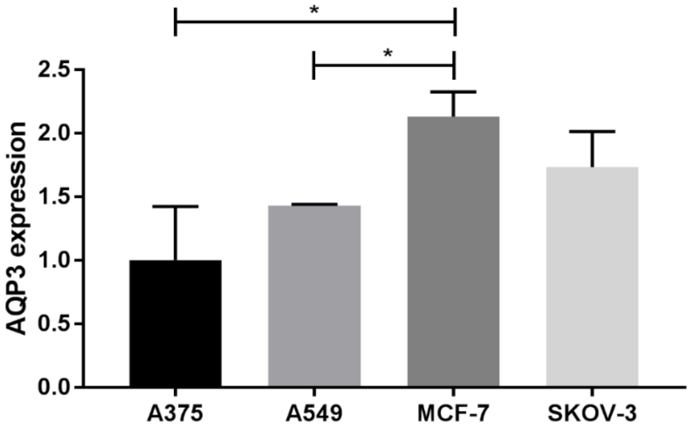

***Figure 3.6**: Normalized mean fluorescence intensity (MFI) of AQP3, detected using a secondary Alexa Fluor®488-labelled antibody. Results were normalized for the sample with the lowest expression (A375) and results are expressed as mean ± SEM of three independent experiments. *$p<0.03$.*[325]

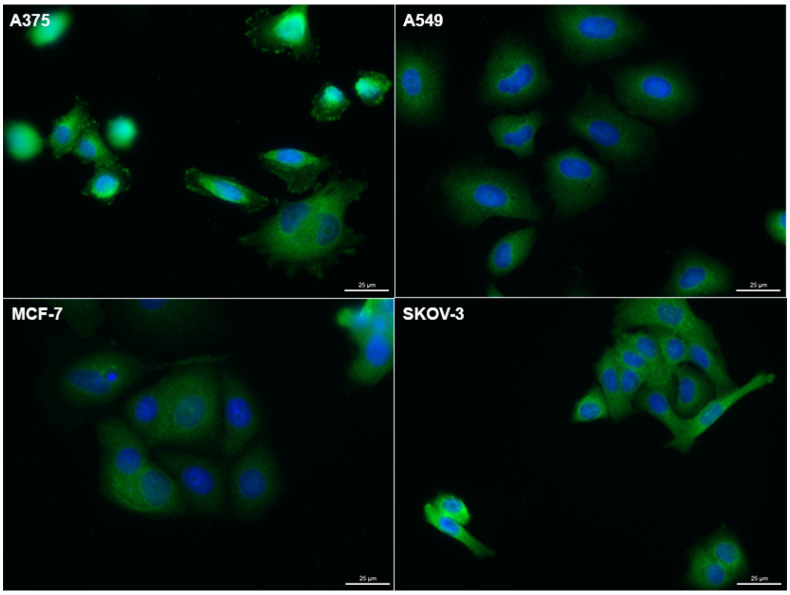

***Figure 3.7**: Confocal laser scanning microscopy images of human AQP3 expression and localization in fixed human cancer cells by immunocytofluorescence. Human AQP3 expression (green) in A549, A375, SKOV-3 and MCF-7 cancer cells, with nuclei stained with DAPI (blue). Scale bars represent 25 µm.*[325]

3.2.6 Antiproliferative effects in cancer cells

The antiproliferative activities of the complexes and their respective ligands were analysed using a classic MTT (3-(4,5-dimethylthiazol-2-yl)-2,5-diphenyltetrazolium bromide) assay,[331] suitable for the required high-throughput screening of a library of compounds. This assay is based on colorimetry and assesses metabolic activity, since mitochondrial reductase enzymes are required to transform the MTT, a yellow tetrazolium, into purple formazan crystals, thus reflecting the number of viable cells. Cell were treated for 72 h hours with the complexes. The findings are summarized in Tables 3.4 and 3.5. Once more, compounds **C7** and **C8** were excluded based on their performance in the stability assay. Overall, the compounds show very moderate anticancer effects in all cancerous cell lines, with compounds **C1** and **C2** being the least toxic ($EC_{50} > 80$ µM) and compounds **C3** and **C4** moderately cytotoxic (EC_{50}`s ranging between 23 ± 1 µM and 81 ± 9 µM), but the scarce stability in aqueous environment of these last two may affect their antiproliferative effects. The most effective compounds in the series were **C10-C12**, particularly against the melanoma A375 cells, where **C10** showed an EC_{50} of 5 ± 2 µM. Remarkably, these three are the only neutral compounds and may therefore display different uptake and accumulation in cancer cells with respect to the cationic derivatives. The corresponding ligands **L1**—

L12 generally showed reduced antiproliferative effects compared to the gold complexes (Table 3.5).

The overall difference of effects between the AQP3 inhibition assays and the antiproliferative studies is quite striking. Based on the strong AQP3 inhibitory activity of the complexes with IC_{50} values in the low-micromolar level, one would expect a similar impact on the antiproliferative activity of the cancer cells overexpressing AQP3. However, it should be noted that both experiments are not directly compatible, as different experimental conditions are applied. For example, the erythrocyte suspension consists of isotonic PBS, whereas the cancer cell culture medium contains serum components which might interact with the Au(III) complexes. Thus, a possible explanation of the moderate cytotoxic effect of the complexes migth concern their extensive *speciation* in biological environment.[332] In general, a number of studies demonstrated that Au(III) complexes with bidentate N^N ligands, can easily hydrolyse the chlorido ancillary ligands and even undergo the rapid loss of the chelating ligand upon reaction with different protein binding sites.[332] Moreover, experimental studies and calculations highlighted mixed chloro-hydroxo species to be the dominant ones for the reaction with endogenous targets.[310]

Another crucial difference amonst the two selected assays is the different incubation periods, seeing that the AQP3 permeability is assessed only after 30 min incubation with the gold complexes, wheras the cancer cells have a 72 h co-incubation time. It is therefore likely that in the latter conditions, intracellular uptake of gold compounds might occur, allowing for interaction with targets other than the intended membrane protein channels. A previous study performed by our group showed efficient cell uptake of Auphen already after 30 min, implying that the Au(III) complex is in fact cell permeable.[107] Whether this permeation is the result of active or passive transport, due to the lipophilicty of the complex, still needs to be elucidated. Overall, it is worth mentioning that, like most metal-based drugs, Au(III) complexes could be multitargeted.[333] Possible likely candidates for binding Au(III) based complexes in addition to AQP3 include for example reductases, mitochondria and zinc finger proteins.[334] Therefore, the possiblity of alternative mechanisms of action as well as of cellular detoxification mechanisms should be also considered and futher investigated.

***Table 3.4**: Antiproliferative activities (EC_{50} values) of Au(III) compounds in human SKOV-3, A375, MCF-7, and A549 cells after 72 h incubation, measured by the MTT assay.*[325]

Compound	**AQP3 inhibition**	**EC_{50} [µM]** [1]			
	IC_{50} [µM] [1]	**SKOV-3**	**A375**	**MCF7**	**A549**
Auphen	0.80 ± 0.08	7.00 ± 2.00	1.74 ± 0.28	3.00 ± 0.05	1.07 ± 0.09
C1	1.018 ± 0.137	>80	>80	>80	>80
C2	0.881 ± 0.015	>80	>80	>80	>80
C3	1.825 ± 0.017 (n=2)	41 ± 13	23 ± 1	40 ± 4	57 ± 2
C4	0.85 ± 0.21	56 ± 12	69 ± 3	63 ± 1	81 ± 9
C5	0.80 ± 0.10	>50	>50	25 (n=1)	>50)
C6	0.69 ± 0.06	>50	34 (n=1)	38 (n=1)	47 (n=2)
C7	n.d.	n.d.	n.d.	n.d.	n.d.
C8	n.d.	n.d.	n.d.	n.d.	n.d.
C9	0.72 ± 0.05	>50	>50	>50	>50
C10	>50	17 ± 7	5 ± 2	12 ± 1	>50
C11	0.82 ± 0.13 (n=2)	33 ± 5	12 ± 2	29 ± 8	>50
C12	n.d.	41 ±13	13 ± 2	17 ± 3	45 ± 3

[1] Values represented as mean (± SEM) of at least three independent experiments (n), unless otherwise stated. n.d. = non determined.

Table 3.5: *Antiproliferative activities (EC_{50} values) of ligands in human SKOV-3, A375, MCF-7, and A549 cells after 72 h incubation, measured by the MTT assay.*[325]

Compound	**EC_{50} [μM]** [1]			
	SKOV-3 **(++)**	**A375** **(+)**	**MCF7** **(++)**	**A549** **(+)**
L1	>80	>80	>80	>80
L2	>80	n.d.	>80	>80
L3	38 ± 12	18 ± 2	44 ± 1	44 ± 3
L4	45 ± 3	53 ± 4	55 ± 3	61 ± 5
L5	>80 (n=1)	>80 (n=1)	31 (n=1)	>80 (n=1)
L6	36 (n=1)	26 ± 3	38 (n=1)	36 (n=2)
L7	>80 (n=1)	59 (n=1)	73 (n=1)	>80 (n=1)
L8	>80 (n=1)	>80 (n=1)	>80 (n=1)	>80 (n=1)
L9	60 (n=1)	45 (n=1)	55 (n=1)	54 (n=1)
L10	>80	>80	>80	>80
L11	>80	20 ± 2	4 ± 1	>80
L12	52 ± 21	17 (n=1)	23 ± 2	73 ± 8

[1] Values represented as mean (± SEM) of at least three independent experiments (n), unless otherwise stated. n.d.= non determined.

Exploring the potential of gold(III) complexes integrating therapeutic and imaging modalities was the rational behind the development of coordination Au(III) complexes endowed with fluorescent properties. Complexes **C11** and **C12** were both candidates with interesting fluorescent quantum yields, (58% and 71%, respectively) but the poor stability of **C12** limited further biologic assays. Therefore, **C11** and corresponding ligand **L11** (QY = 74%) were studied in an attempt to visualise the intracellular site of accumulation. Since the emission peaks are within the UV region (**C11** λ_{max} = 374 nm in 1x PBS) a counterstaining different from the standard DAPI must be used to avoid spectral overlap. For this purpose, the thymidine analogue 5-Bromo-2`-deoxyuridine (BrdU) was applied, immunolabeled with a green-fluorescent Alexa 488® dye. MCF-7 cells were incubated with compound for 30 min and 1 h at 37°C. Figure 3.8 represents images obtained after 1 h of incubation.

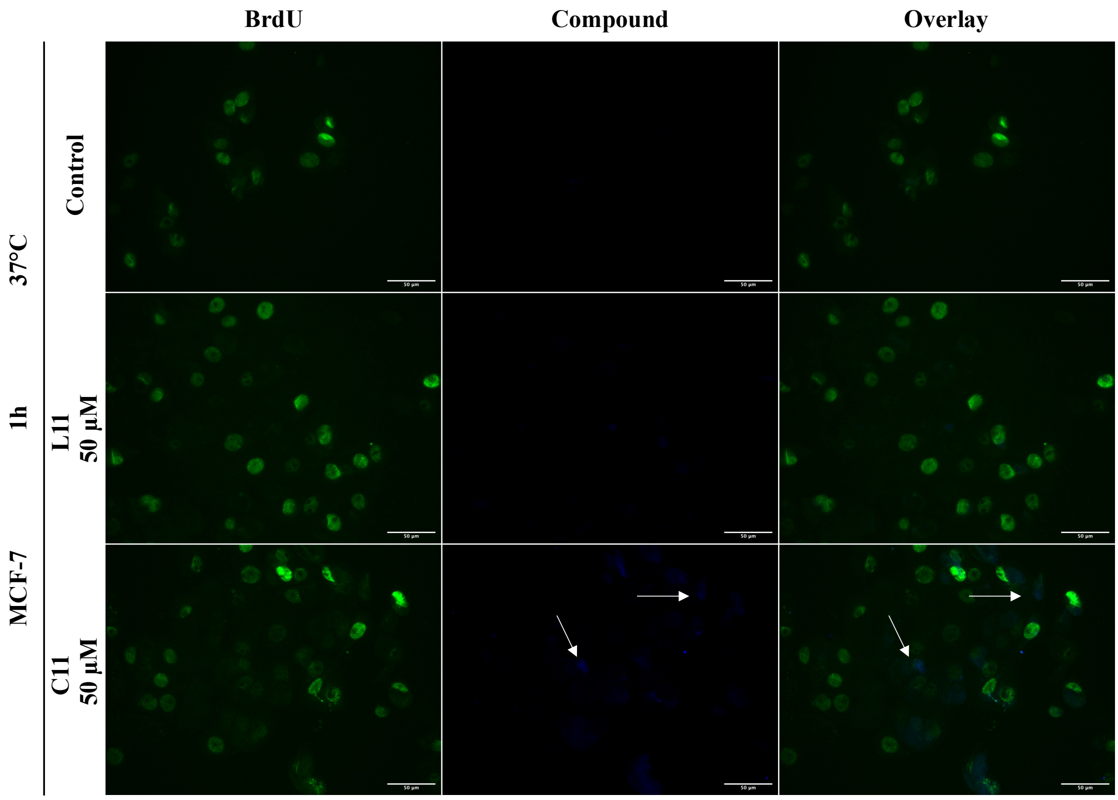

Figure 3.8: Single slice images of fixed MCF-7 cells treated 1 h with 50 µM of either ***L11*** *or* ***C11****. Complexes imaged with DAPI filter. Nuclear counterstaining by immunolabeling of DNA with Alexa488©-BrdU. Arrows indicate complex presence. Scale bar represents 50 µm.*

Unfortunately, the complex was barely visible. **C11** was only detectable in a few spots as indicated by arrows in Figure 3.8, since the fluorescent intensity did not pass the threshold to discriminate a signal from the background. However, this could be due to the incubation conditions, as cellular penetration of the complex might be time depended.

3.2.7 Au(III) complexes with 1,10-phenanthroline ligands

In addition to the previously presented complexes, another series of six cationic Au(III) complexes, of the **Auphen** family, featuring a substituted 1,10-phenanthroline scaffold have been synthesized and characterised by Dr. Margot Wenzel, post doc in our lab (Figure 3.9).

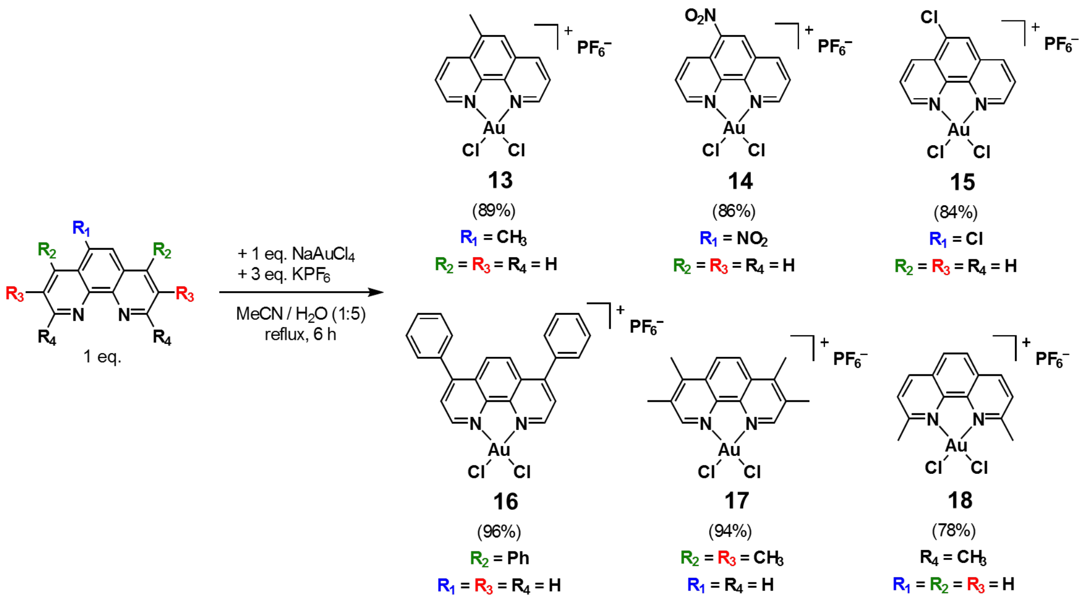

***Figure 3.9**: General scheme for the synthesis of phenanthroline complexes **C13-18** and related yields.*[335]

The speciation of the compounds studied in buffered solution by UV-visible spectrophotometry showed that most of the complexes are stable for several hours. In addition, the gold complexes were monitored in a similar experiment with the addition of 2 eq. of a physiologically relevant reducing agent glutathione (GSH) per equivalent of Au(III) complexes, as they tend to be reduced to Au(I) and even Au(0) in physiological conditions.[336] To monitor possible hydrolysis of the ligands, reductions and/or precipitation, the absorbance was measured between 275 and 700 nm at regular time intervals during 24 h at room temperature. The obtained results are shown in Figures S40-S45 of Appendix A3.[335] Characteristic of the Au(III) chromophore, all the compounds exhibit intense transitions in the 300-400 nm range in the aqueous environment, which might be assigned as ligand to metal charge transfer (LMCT) bands. Representative UV-visible absorption spectra for ligands **L13** and **L17** and those of the related Au(III) complexes **C13** and **C17**, are reported in Figure S46 of Appendix A3. The observed spectral changes might in that case be due to partial hydrolysis. The spectra of complex **16** and **18** however show a marked decrease in intensity of their bands (Figures S43 and S45 of Appendix A3), whilst forming a precipitate. None of the spectra indicate the formation of colloidal gold, as no broad absorption band occurred around 550 nm.

3.2.8 Aquaporin inhibition in human Red Blood Cells

To evaluate the phenanthroline-based Au(III) complexes ability to inhibit AQP1 and AQP3, the previously described stopped flow spectroscopy method was used to test the complexes against benchmark **Auphen** in hRBC. The results are shown in Table 3.6. The IC_{50} values were similar or even lower than **Auphen**. With an IC_{50} of 0.43 ± 0.08 compound **16** was the most active, followed by **14** (0.57 ± 0.04) and **15** (0.57 ± 0.07). Interestingly, all complexes were able specifically inhibit AQP3 glycerol permeability PGly, whilst showing no effect on AQP1 water permeability.

***Table 3.6**: Glycerol permeation inhibiting effects (IC_{50} values) of Au(III)-phenanthroline complexes (**Auphen**, **C13-18**) in hRBC after 30 min incubation. N = number of independent experiments.* [34]

Complex	**IC_{50} (μM)[a]**
Auphen	0.80 ± 0.08
13	0.73 ± 0.09
14	0.57 ± 0.04 (N = 2)
15	0.57 ± 0.07 (N=2)
16	0.43 ± 0.08
17	0.83 ± 0.01 (N=1)
18	0.89 ± 0.14

[a] Values represented as mean ± SEM of at least three independent experiments, unless otherwise stated.

3.2.9 Antiproliferative effects in cancer cells

Since the complexes displayed strong AQP3 glycerol permeation inhibition properties, all of them were included in the cytotoxicity screening against human A549 lung cancer cells. Preliminary data on the antiproliferative activity indicate that the compounds are able to inhibit cell proliferation *in vitro* (Table 3.7), showing marked antiproliferative properties, with EC_{50} values in the low micromolar range < 5 μM. Especially complexes **16** and **17** rival **Auphen**'s potency with EC_{50} values of ca. 1 μM. However, since some of the complexes are potentially subjected to degradation as evidenced by the spectral analyses, the corresponding ligands were evaluated as well.

Table 3.7*: Antiproliferative effects (EC$_{50}$ values) of various Au(III) phenanthroline complexes (****Auphen****, C****13-18****) in human A549 cells after 72 h incubation.* [335]

Complex	**EC$_{50}$ (μM)^{a}**
Auphen	1.07 ± 0.09
13	2.4 ± 0.6
14	2.4 ± 0.6
15	4.4 ± 0.5
16	1.1 ± 0.2
17	1.01 ± 0.04
18	1.8 ± 0.5

[a] Values represented as mean (± SEM) of at least three independent experiments.

Of note, in general the ligands induced similar antiproliferative effects (Table 3.8), in line with previously reported results, where targeting of nucleid acids via DNA intercalation can occur.[337,338] Only in the case of **L16**, solubility issues lead to precipitation preventing the determination of its EC$_{50}$ value. Therefore, at this stage it is difficult to discriminate the differences between the anticancer activity of the Au(III) complexes from their free N^N ligands. The observed effect of the complexes therefore could be due to release of ligand over time. This would suggest that the complexes in their current state are not ideal for further development as anticancer agents unless a reduction of their speciation could be achieved (*via* drug delivery systems for example). Nevertheless, the isoform selectivity of these new entities could still be exploited in the form of chemical probes to study AQP3 function in cancer cells.

***Table 3.8**: Antiproliferative effects (EC_{50} values) of ligands (1,10-phenanthroline, **L13-L18**) in human A549 cells after 72 h incubation.* [335]

Ligand	EC_{50} (μM)[a]
1,10-phenanthroline	6.4 ± 1.3
L13	1.93 ± 0.09
L14	3.5 ± 0.4
L15	5.6 ± 0.5
L17	1.0 ± 0.2
L18	3 ± 1

[a] Values represented as mean (± SEM) of at least three independent experiments.

In collaboration with the group of Prof. Nazzareno Re (University of Chieti, Italy) a multi-level theoretical workflow was applied including DFT, MD and quantum mechanics/molecular mechanics (QM/MM) approaches to evaluate the complexes reactivity with Cys40 and speciation in aqueous environment. Specifically, QM studies of the hydrolysis processes of the compounds suggested that they are thermodynamically less prone to exchange the chlorido ligands with H_2O or OH^-, compared to previously described Au(III) bipyridyl complexes, [310] and therefore, are likely to be in the intact form prior AQP3 binding.

The non-covalent and coordinative binding of the phenanthroline complex **15** to Cys40 in AQP3 was investigated with quantum mechanics (QM), molecular dynamics (MD) and quantum mechanics/molecular mechanics (QM/MM). The results were compared with those obtained in the case of the benchmark **Auphen**. As illustrated in Figure 3.10, there are some differences between **Auphen** and complex **15** binding of AQP3. **Auphen** for example is slightly more buried inside the pore, allowing for interaction of its phenanthroline moiety with Phe63 via π-π stacking, that is not present for complex **15**. These results may account for the lower AQP3 inhibitory potency of **15** in comparison to Auphen. Atoms in molecules (AIM) and natural bond orbital (NBO) analyses combined with the MD predictions provided quantification of the non-coordinative interactions between the compounds and AQP3. Therefore, while AQP3 inhibition is the result of protein conformational changes, upon coordinative gold binding to exposed Cys residues in the channel, which in turn induces pore closure, our study has also unravelled the importance of non-coordinative adducts in modulating the AQP3 inhibition properties of the investigated Au(III) compounds.

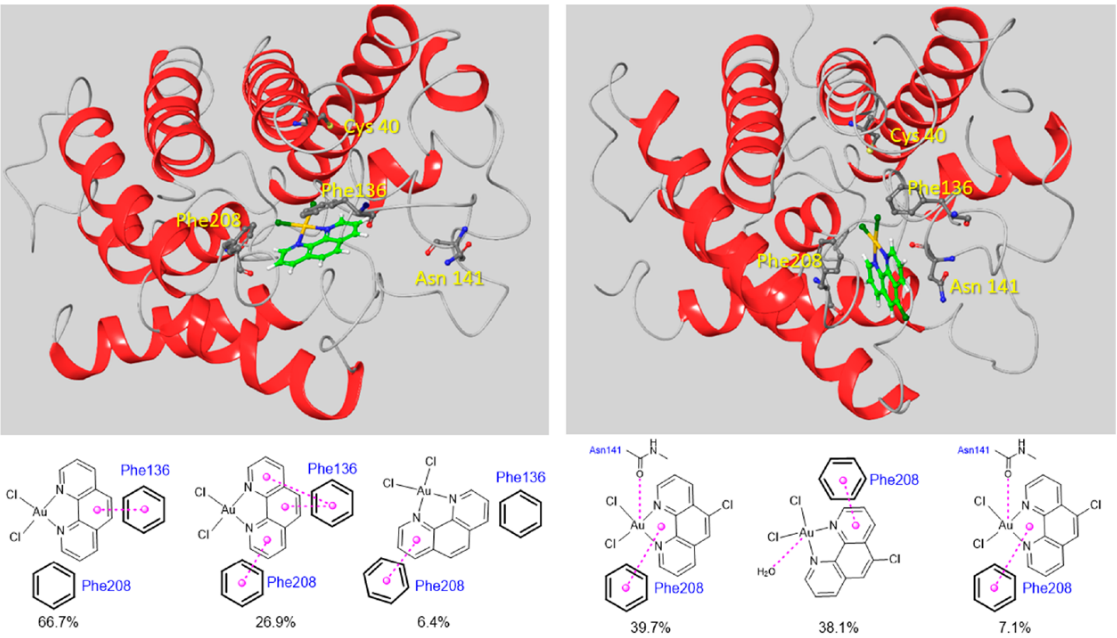

***Figure 3.10**: (top) Representation of noncoordinative adducts (the most representative pose) of **Auphen** (left) and **15** (right) with AQP3. (bottom) 2D sketches of the main noncoordinative interactions detected and weights (percentages) of representative poses. The phenyl ring of either Phe136 or Phe208 is sketched in boldface to highlight that it is placed over the phen scaffold. Reprinted with permission from (Wenzel et al. Insights into the Mechanisms of Aquaporin-3 Inhibition by Gold(III) Complexes: the Importance of Non-Coordinative Adduct Formation, Inorg. Chem.* 2019, 58, 3, 2140–2148*). Copyright (2019) American Chemical Society.*[335]

3.3 Conclusions

In conclusion, a new series of cationic and neutral Au(III) compounds with bidentate N^N ligands has been synthesized and characterized by different methods. The first series featured a pyridine-benzimidazole scaffold, and the second series 1,10-phenanthroline ligands. As demonstrated by UV-visible spectroscopy, changing the ligands' substitution patterns influences the stability of the resulting Au(III) complexes in aqueous environment. In general, all the compounds readily react with the reducing agent GSH, except for **C11-C12**. Most of the gold complexes are also potent inhibitors of the human water and glycerol channel AQP3, while they are inactive as inhibitors of the water channel AQP1, as evidenced by stopped-flow spectroscopy in hRBC.

Amongst the tested derivatives only **C10** is a poor inhibitor of AQP3 ($IC_{50} > 50$ μM), while the other neutral complex **C11** is a very potent inhibitor ($IC_{50} = 0.82 \pm 0.13$). Possibly, the observed difference is due to the lower stability of **C10** in physiological conditions, as observed by UV-visible spectroscopy.

While most of the pyridine-benzimidazole compounds are scarcely active as antiproliferative agents against human cancer cells, the neutral complexes **C10-C12** showed promising anticancer activities, particularly in the melanoma A375 cancer cell line. Interestingly, while all the selected cell lines express AQP3, the melanoma cells display additional protein expression at the level of the nuclear membrane, as evidenced by immunocytofluorescence. Thus, we cannot exclude that **C11** may target AQP3 in the nuclear membrane after being taken up by the cancer cells.

The phenanthroline-based series was designed based on a combination of biophysical techniques with advanced computation methods, resulting in six Au(III) complexes. A few members of this series showed AQP3 inhibition properties which outperformed the benchmark compound **Auphen.** However, further investigation may be necessary to assess the mode of action of this family of Au(III) compounds, which are known to be multitarget agents[334] and whose antiproliferative activity may be due to the combined effects of the Au(III) center and the phenanthroline ligands.

Interestingly, the computational approach elucidated that AQP3 inhibition is the result of protein conformational changes, upon coordinative gold binding to a critical Cys residue, which in turn induces pore closure. However, the computational study also highlighted the importance of non-covalent interactions between the organic phenanthroline ligand and the protein extracellular pocket which may also account for the differences in inhibitory effects. Overall, our results hold promise for the design of novel selective AQPs inhibitors to be used an anticancer agents or as chemical probes to study the function of these interesting membrane channels in cancer spread and development.

3.4 Materials and Methods

3.4.1 Synthesis and Characterisation

To expand our existing library, a new series of Au(III) complexes with different bidentate N-donor ligand scaffolds based on pyridine-benzimidazole was synthesised in our lab by Dr. M. Wenzel. Experimental procedures for the synthesis, characterisation via NMR and mass spectrometry, IR and X-ray crystal data are provided in the supporting information.[325]

3.4.2 Spectroscopic Characterisation

3.4.2.1 UV-Vis stability in physiological medium

The stability of the new gold series was evaluated in aqueous media (1x Phosphate Buffered Saline, PBS, Corning) by UV-vis spectroscopy using a Cary 500 UV-Visible NIR spectrophotometer. Since Au(III) complexes are known to be reduced in physiological conditions to Au(I) and even Au(0), the reactivity of the new complexes was studied in the presence of 2 equivalents of the physiologically relevant reducing agent glutathione (GSH) per equivalent of Au(III) complex in a similar experiment using the same conditions. The absorbance spectra of both series were monitored between 275 and 800 nm at regular time intervals over 24 h at room temperature, at a concentration of 10^{-4} M (stock 10^{-2} M in dimethyl sulfoxide, DMSO, Sigma-Aldrich) in 1x PBS. Additionally, for selected complexes in the gold(III) series the stability in deionised water was studied.

3.4.2.2 Quantum Yield determination

To determine the fluorescent properties of the complexes, a quantum yield was calculated from spectra recorded using a Cary 500 UV-Visible NIR spectrophotometer and a Cary Eclipse Fluorescence Spectrophotometer. The intersection of the absorbance spectra from the compounds (in DMSO) and the quantum yield standard, quinine sulphate (0.5M in H_2SO_4 with emission range of 220 - 340 nm) for the gold(III) complexes, provided a specific wavelength at which both complexes were excited to obtain the fluorescent emission spectra. *Equation 1* was used to determine the quantum yield:

$$\phi_x = \phi_{ST} . \frac{A_X}{A_{ST}} . \left(\frac{\eta_x}{\eta_{ST}}\right)^2 . \left(\frac{Abs_{ST}}{Abs_x}\right) \qquad \textbf{\textit{Equation 1}}$$

ϕ_{ST} = 0.546 (quantum yield of reference QS)

A_X = Integrated fluorescence intensity of the sample

A_{ST} = Integrated fluorescence intensity of standard at same wavelength of the sample

η_X = 1.4793 (refractive index of solvent DMSO)

η_{ST} = 1.332988 (refractive index of water, 5mM H_2SO_4)

Abs_{ST} = Absorbance standard

Abs_X = Absorbance sample

3.4.3 Aquaporin inhibition assay

Performed in collaboration with the group of Prof. Graça Soveral (Research Institute for Medicines-iMed.ULisboa, Faculty of Pharmacy, Universidade de Lisboa, Lisboa, Portugal).

The ability of the complexes to inhibit hAQP1 and/or hAQP3 was tested with stopped-flow spectroscopy experiments. Stopped-flow spectroscopy follows the time-course of cell volume changes induced by osmotic shocks in and without the presence of compounds. This technique allows the determination of the osmotic permeability coefficient of water (P_f) or glycerol (P_{gly}), parameters used to characterize solute permeation rates. Changes in the cell volume were measured using scattered light intensity.[339] The experiments were performed on a HI-TECH Scientific PQ/SF-53 apparatus with temperature control, 2 ms dead time and were interfaced with a microcomputer. To study the inhibitory effects of the new gold(III) series on hAQP3, the compounds were incubated with human red blood cells (hRBC). These cells are known to specifically express large amounts of both hAQP1 as hAQP3, accountable for membrane permeability to water and glycerol. Venous blood samples were obtained from healthy human volunteers in accordance with a protocol approved by the Ethics Committee of the Faculty of Pharmacy of the University of Lisbon (Instituto Português de Sangue Protocol SN-22/05/2007). All participants provided written consent. The blood samples collected in citrate anticoagulant (2.7% citric acid, 4.5% trisodium citrate and 2% glucose) were centrifuged at 750x *g* for 5 minutes at 4 °C. After discarding the plasma and buffy coat, the pelleted erythrocytes were washed three times in PBS (KCl 2.7 mM, KH_2PO_4 1.76 mM, Na_2HPO_4 10.1 mM, NaCl 137 mM, pH 7.4), diluted to 0.5 % haematocrit and immediately used. The mean volume of the hRBC in isotonic solution was determined using CASY-1 Cell Counter (Schärfe System GmbH, Reutlingen, Germany) and calculated as 82 fL. After incubation of the hRBC in isotonic PBS, cells were challenged with either a hypertonic sucrose solution or a hypertonic glycerol solution. The impermeable sucrose would induce cell shrinkage, whereas with the permeable solute glycerol, the cells would shrink initially due to the hyper-osmotic gradient, then re-swell when glycerol uptake restores the equilibrium.[107] The resulting stopped flow traces were fitted using a single exponentional equation: glycerol permeability (P_{gly}) was calculated as $P_{gly} = k\ (V_0/A)$, with V_0/A as the initial human red blood cell volume to area ratio and k as the single exponential time constant that is fitted to the light scattering signal of glycerol influx (see Figure S47, Appendix A4 for illustration).[107] The stopped flow device has this equation built in, as described previously by Martins et al in ref [107]. For each experimental condition, 5-6 technical replicates and a minimum of at least 3 biological replicates were analyzed. Based on the measured cell volume changes and permeability induced by imposed shocks, IC_{50} values were calculated corresponding to the concentration necessary to achieve 50% inhibition of permeability using nonlinear regression of dose-response curves (Graph Pad Prism, Inc). The following equation was used: $y = y_{\mathrm{min}} + (y_{\mathrm{max}} - y_{\mathrm{min}})/1+10^{((\mathrm{LogIC50}-[\mathrm{Inh}])\mathrm{H}))}$, in which y is the inhibitor percentage obtain for each concentration [Inh] and H the Hill slope.[107,339] IC_{50} data were presented as mean ± standard error of the mean (SEM) of at least three/four independent experiments.

3.4.4 Cell lines and cell culture conditions

Human malignant melanoma cell line A375, human lung adenocarcinoma cell line A549, human breast carcinoma cell line MCF-7 and human ovarian adenocarcinoma cell line SKOV-3 were obtained from American Type Culture Collection (ATCC) and maintained in culture as described by the provider. The cells were cultured in Dulbecco`s Modified Eagle Medium (DMEM, 4,5 g/L glucose, Corning), supplemented with 10% fetal bovine serum (One-Shot FBS, Eu-approved South American Origin, Thermo Fisher Scientific) and 1% penicillin/ streptomycin (Gibco), except for MCF-7 where Roswell Park Memorial Institute (RPMI, L-glutamine, Corning) supplemented with 10% FBS and 1% Penicillin + Streptomycin was used. All cell lines were cultured at 37 °C, in a humidified atmosphere with 5% CO_2 and passaged once confluent.

3.4.5 Aquaporin expression assay

3.4.5.1 Flow Cytometry

For flow cytometry evaluation of AQP3 expression, samples of each cell line studied were prepared with 200 000 cells/sample. Cells were initially washed twice with 1x PBS (Gibco) and subsequently fixed with 4% formaldehyde (Alfa Aesar), for 30 min at room temperature (r.t.). Afterwards, cells were incubated with 1:500 dilution of anti-AQP3 antibody (rabbit anti-human, PA1488 Boster), in 1x PBS with 5% normal human serum (NHS, Invitrogen) and 0.1% Triton X-100 (Alfa Aesar) at r.t., for 1 h. Staining with primary antibody was followed by incubation with 1:500 secondary goat anti-rabbit Alexa Fluor®488 (ab150077, Abcam), in 1x PBS with 5% NHS and 0.1% Triton X-100, also for 1 h and at r.t., in the dark. Cells were kept on ice and away from direct light until analysed using a BD FACS Verse Flow Cytometer. Results were analysed using FlowJo 10.5.0. First, samples were gated for live cells. Afterwards, stained and unstained samples were compared, in order to gate the positive population and the mean fluorescence intensity (geometric mean) was taken from each positive sample peak. Data were normalized for the sample with the lowest AQP3 expression and results are shown as mean ± SEM of three independent experiments.

3.4.5.2 Immunocytochemistry of AQP3

Round glass coverslips (Ø 13mm, VWR) sterilized by UV-light were inserted in 24-well tissue culture-treated plates (Corning). Cells were seeded at a concentration of 120.000 cells/mL and incubated at 37°C under humidified atmosphere with 5% CO_2 for 24 h. Afterwards, the glass coverslips were removed from the wells and cells were washed three times with 1x Phosphate Buffered Saline (PBS, Corning) before fixation with 4% formaldehyde (Alfa Aesar), for 20 min at room temperature (r.t.). Coverslips were permeabilized with 0.2% Triton X-100 for 5 min. at r.t., and subsequently incubated with 40 µL 1:300 rabbit anti-human AQP3 antibody (PA1488, BosterBio) in 5% normal human serum (NHS Invitrogen) at r.t. for 1 h. Next, the cells were incubated with 40µL 1:300 AlexaFluor® 488 goat anti-rabbit antibody (AB150077, Abcam) for 30 min at r.t. protected from light. Finally, the cells were incubated for 5 min with 40µL of 1 µg/ml of 4',6-Diamidino-2-phenylindole dihydrochloride (DAPI, Sigma-Aldrich/ MERCK) or 10 µM Hoechst (Sigma-Aldrich) at r.t., in the dark after which the coverslips were mounted on glass microscopy slides (VWR) using

Mowiol® 4-88 (Sigma-Aldrich) and stored at r.t. until dried, protected from direct light. Before and after each step, cells were washed three times with 1x PBS. Fluorescent images were obtained using a Zeiss Axio Vert.A1 microscope and processed using Fiji (ImageJ).

3.4.6 Antiproliferative assay

For evaluation of cell growth inhibition, cells were seeded in 96-well plates (Corning) at a concentration of 15000 cells/well and grown for 24 h in 200 μL complete medium. Solutions of the samples with the required concentration (1 to 100 μM) were prepared by diluting a freshly prepared stock solution (10^{-2} M in DMSO) of the corresponding compound in aqueous DMEM or RPMI medium, accordingly. Auphen (stock 10 mM in DMSO) was used as reference compound for the gold(III) series. The negative control (medium only) was run for all the assays. After 24 h incubation, 200 μL of the compounds' dilutions were added to each well and the cells were incubated for additional 24 h. Afterwards, medium was removed and 3-(4,5-dimethylthiazol-2-yl)-2,5-diphenyltetrazolium bromide (MTT, Fluorochem) in 10x PBS (Corning) was added to the cells, at a final concentration of 0.3 mg/mL and incubated for 3-4 h. Then, the MTT solution was discarded and replaced with DMSO to allow the formed violet formazan crystals to dissolve. The optical density was quantified in quadruplicates for each experiment, measuring absorbance at 550 nm using a multi-well plate reader (VICTOR X, Perking Elmer) (Figure 3.11). The percentage of surviving cells was calculated from the ratio of absorbance of treated to untreated cells. The EC_{50} value was calculated as the concentration showing 50% decrease in cell growth, when compared to controls, using a nonlinear fitting of log[concentration] vs response with GraphPad Prism 7 software. Data is presented as mean ± SEM of at least three independent experiments.

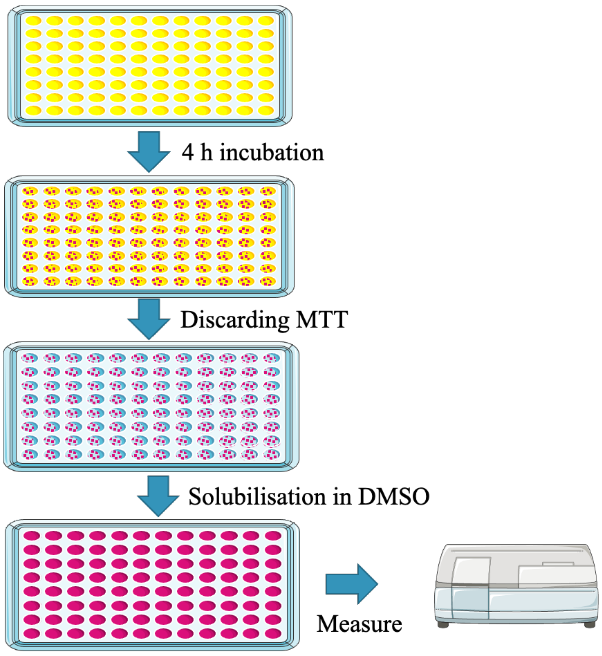

Figure 3.11*: Scheme representing colometric MTT assay steps.*

3.4.7 *In vitro* fluorescence microscopy uptake studies

Round cover glass (Ø 13mm, VWR) sterilized by UV-light exposure were inserted in 24-well tissue culture treated plates (Corning) and pre-treated 1h at 37 °C with 0.1% poly-D-lysine hydrobromide (Corning, Bedford) dissolved in sterile water. After washing the cover glass with 10x PBS, MCF-7 cells were seeded at a concentration of 120.000 cells/mL and incubated at 37 °C under humidified atmosphere with 5% CO_2. After 8 h, cells were incubated with 10 µM 5-Bromo-2'-deoxyuridine (BrdU, Abcam) for 24 h. Afterwards, medium was discarded and fresh medium containing compounds was added to the cells. Following an incubation of 1 h at 37 °C, cells were fixed during 20 min with 4% formaldehyde (Alfa Aesar) and incubated for 5 minutes with 0.2% Triton (ACROS) at room temperature (r.t.). Before each step, cells were washed three times with 1x PBS (Gibco). Next, the cells were incubated for 30 min at r.t. with 2 M HCL (Fisher Scientific) in 1x PBS, then neutralized with sodium-borate (Fisher Scientific) twice for 10 minutes and finally blocked with 3% BSA (Sigma-Aldrich) in 1x PBS. Incubation with 1:300 mouse anti-BrdU antibody (AB8039, Abcam) was performed overnight at 4 °C. Cells were then washed three times with 1x PBS and incubated with 1:300 Alexa Fluor® 488 rabbit anti-mouse antibody (AB15011, Abcam) for 1 h at r.t. and protected from direct light. After three washes with 1x PBS, cover slides were mounted on glass slides using Mowiol and stored at r.t., protected from direct light. Fluorescent images were obtained using a Leica SP2 confocal microscope with DAPI and FITC filters, by courtesy of Bioscience Cardiff University.

Chapter 4: Organometallic gold(III) complexes designed as aquaglyceroporin inhibitors

This chapter is based on the following manuscript:

Mechanisms of irreversible aquaporin-10 inhibition by organogold compounds studied by combined biophysical methods and atomistic simulations

Catarina Pimpão, Darren Wragg, Riccardo Bonsignore, **Brech Aikman**, Per Amstrup Pedersen, Stefano Leoni, Graça Soveral and Angela Casini

Submitted to *BBA – Biomembranes* on April 15th, 2021

The EU Erasmus Program supported a short-term scientific mission at the Universidade de Lisboa

4.1 Introduction

Aquaglyceroporins are a subfamily of aquaporins (AQPs), highly conserved membrane proteins that in addition to facilitating transmembrane diffusion of water, enable permeation of small uncharged solutes like glycerol. To date, four aquaglyceroporin isoforms have been identified: AQP3[340], AQP7[341], AQP9[342] and AQP10[343]. The latter are known to regulate glycerol content in various tissues, such as epidermis or fat, and in their role as a glycerol channel have been proposed to be involved in skin hydration and wound healing, cell proliferation, lipid metabolism and carcinogenesis.[316] Moreover, due to their postulated contribution to body energy homeostasis, aquaglyceroporins are involved in several metabolic and inflammatory pathophysiological human conditions[344–346], therefore, fostering drug development opportunities for AQPs-based therapies.[241]

The remarkable selective nature of the AQP channels is due to the presence of two constriction sites; i) the aromatic/arginine selectivity filter (ar/R SF), located closer to the extracellular entrance determines whether small polar solutes may permeate the pore in addition to water based on size, and ii) the second selectivity filter which is composed of two conserved asparagine-proline-alanine (NPA) motifs, creating an electrostatic barrier, which prevents passage of positively charged ions through the pore. There are slight variations for this 2nd selectivity filter throughout the aquaglyceroporins, though the asparagine responsible for the positive dipole moment are highly conserved.[170] For example, human AQP7 has Asn94, Ala95 and Ala96 (NAA) and Asn226, Pro227 and Ser288 (NPS) motifs instead of the common NPA.[347] In the case of human AQP10, the conserved residues are Arg217 and Ile211 for the ar/R region and Asn82 and Asn214 for the NPA motif, respectively.[348] Of note, AQP10 features a third constriction region, mechanistically unique to this isoform, located in the cytoplasmic pocket (CP) of the pore, which makes the pore fully functional at slightly acidic pH. Specifically, in this region, the configuration and interactions of Phe85 with His80 and Arg94 at pH 7.4 restrict pore size to 0.9 Å, preventing the passage of glycerol, while still allowing for water flux. [348] This region has previously been shown to be responsible for the hAQP10 pH gating mechanism involving the double protonation of the highly conserved histidine (His80). [348]

AQP10 is mostly expressed in human small intestine [349,350] and functions at pH 5.0, whereas the other aquaglyceroporins are open at pH 7.4. AQP10 is also reported to be downregulated in inflammatory intestinal disorders such as celiac disease.[351]

Moreover, AQP10 is expressed in human adipocytes where it has been suggested as an alternative pathway for glycerol efflux from the adipose tissue during lipolysis, preventing from fat accumulation and obesity; while AQP7 is the main glycerol channel in adipocytes involved in its uptake.[311,348,352] Finally, AQP3 is located in many epithelial cells throughout the body such as in digestive, urinary, respiratory tracts and in the epidermis and overexpressed in several cancers,[202,203,293,340,353] while AQP9 has a high expression in hepatocytes and hepatocellular carcinoma but can also be found in tumours of the brain.[223,267]

Previously, our efforts in the design of selective aquaglyceroporin inhibitors was focused specifically on cationic gold(III) complexes with bidentate N-donor ligands, with **Auphen -** $[Au(phen)Cl_2]Cl$ (phen = 1,10-phenanthroline) as benchmark selective and potent inhibitor of glycerol permeation by human AQP3, with moderate inhibitory properties towards human AQP7.[107,311] A combination of *in silico* approaches and site-directed mutagenesis studies revealed that the mechanism of inhibition involves binding of **Auphen** and related compounds to the thiol moiety of a selected Cys residue in AQP3 (Cys40) via ligand exchange reaction of one of the chlorido ligands.[107,108,252] Remarkably, molecular dynamics (MD) studies conducted on Au(III) complexes-AQP3 adducts showed that protein conformational changes, resulting from metal binding to Cys40, are mostly responsible for the observed inhibition of water and glycerol permeation.[109]

As discussed in Chapter 3 we therefore, tested two new series of gold(III) coordination complexes as human AQP3 inhibitors. With the series featuring a pyridine-benzimidazole scaffold scarcely active as antiproliferation agents in human cancer cells, a few complexes of the second series of Au(III) with 1,10-phenanthroline ligands did rival **Auphen** potency, although the overall gold complex stability requires improvement. Additionally, the importance of non-coordinative interactions of aromatic ligands with AQP3 was highlighted.[335]

In an effort to broaden the scope beyond coordination Au(III) complexes, and to evaluate the influence of the compound's charge on AQPs inhibition, a small library of cyclometalated Au(III) complexes featuring C^N ligands - $[Au(C^{CH2}N)Cl_2]$ (**1**, $C^{CH2}N$ = 2-benzylpyridine) [354], $[Au(C^{CO}N)Cl_2]$ (**2**, $C^{CO}N$ = 2-benzoylpyridine) [355], $[Au(C^{NH}N)Cl_2]$ (**3**, $C^{NH}N$ = *N*-phenylpyridin-2-amine) [356], $[Au(C^{NOx}N)Cl_2]$ (**4**, $C^{NOx}N$ = 2-(phenyl-(2-pyridinylmethylene)aminoxy acetic acid) [357] and the cationic $[Au(C^{CO}N)met]PF_6$ (**5**, met = metformin) [358] (Figure 4.1) – was investigated for the effects on glycerol and water permeation on hAQP3, hAQP7, hAQP9 and hAQP10. To the best of our knowledge, no inhibitors of human AQP10 [359,360] have been reported so far, and only a few organic molecules have been shown to inhibit hAQP9.[361,362]

Compound **1** was previously shown to be a moderate inhibitor of human AQP3 in human red blood cells (hRBC).[109] For the purpose of identifying inhibitors of human aquaglyceroporins, the various AQP isoforms were expressed in an optimized yeast expression model [363–365], consisting of a *Saccharomyces cerevisiae* strain depleted from endogenous aquaporins and transformed with a plasmid encoding the respective genes (hAQP3, hAQP7, hAQP9 or hAQP10).[348] Additionally, hRBC known to express only the hAQP3 isoform as aquaglyceroporin were included for comparison with previous results.[366] Permeability assays using stopped-flow fluorescence spectroscopy confirmed the glycerol channelling feature of the aquaglyceroporins and were used to evaluate the inhibitory effect of the selected gold-based compounds on glycerol permeability, as well as to investigate the mechanism of binding.

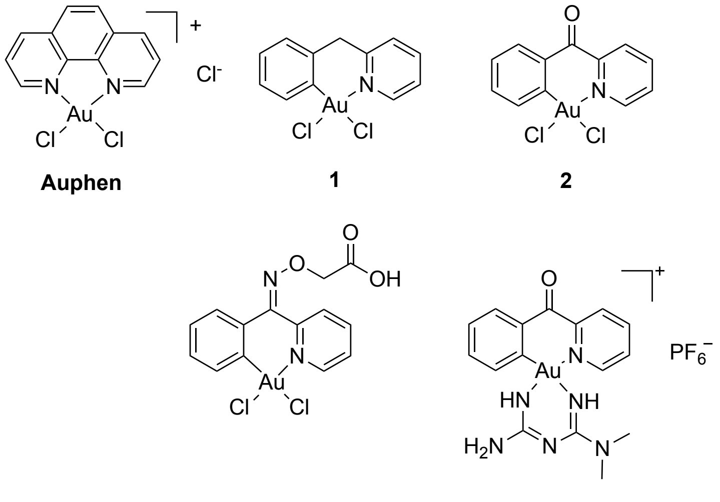

Auphen **1** **2** **3** **4** **5**

Figure 4.1: *Structures of the Au(III) compound Auphen and of cyclometalated Au(III) $C^{\wedge}N$ complexes **1-5**.*

The five gold(III)compounds were selected amongst a family of organometallic derivatives, featuring a direct Au-carbon bond, taking advantage of increased stability in aqueous environment relative to the benchmark inhibitor **Auphen**, as well as featuring a peculiar reactivity with cysteine residues. Specifically, it has been demonstrated that, following $AuC^{\wedge}N$-Cys adduct formation, the reaction of complexes **1-3** with peptides proceeds towards cysteine arylation (Figure 4.2).[98] Formation of the

C^N-peptide adduct is templated by the Au(III) centre facilitating the C–S cross-coupling reaction *via* reductive elimination as demonstrated by combined mass spectrometry and density functional theory (DFT) calculations.[98,99] Therefore, a general reaction mechanism for cysteine arylation was proposed whereby a cysteinate residue binds *trans* to the N of the C^N ligand, while a second peptidic residue X coordinates to Au(III), favouring bond breakage between the nitrogen and the metal to achieve the [Au(C^N)(Cys)XCl] species (Figure 4.2). [97] Formation of the latter intermediate is crucial for promoting the observed C–S cross-coupling.

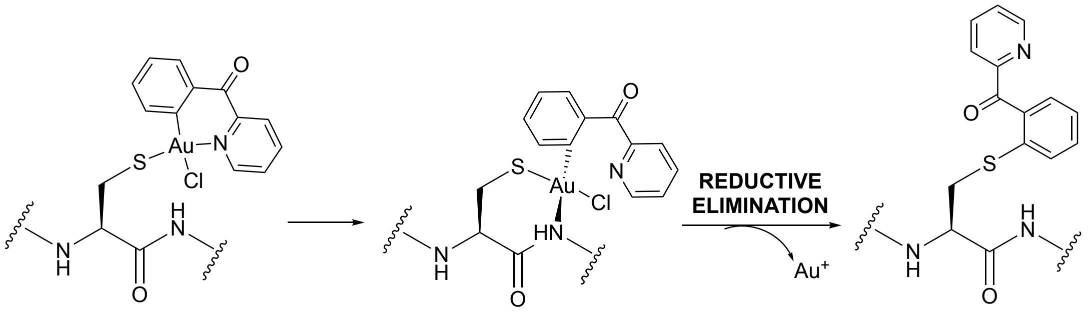

Figure 4.2: *Proposed mechanism of cysteine arylation by Au(III) $C^{CO}N$ complex* ***2*** *via reductive elimination* [98]

4.2 The Method - Stopped-flow spectroscopy

The ability of the complexes to inhibit human aquaglyceroporin 3, 7, 9 and 10 was tested with stopped-flow spectroscopy experiments performed in collaboration with the group of Prof. Graça Soveral (Research Institute for Medicines-iMed.ULisboa, Faculty of Pharmacy, Universidade de Lisboa, Portugal). Stopped-flow spectroscopy follows the time-course of rapid cell volume changes induced by osmotic shocks with and without the presence of compounds in a millisecond to second scale. Exposure to osmotic shocks of a hypotonic or hypertonic nature promptly alters cell shape and size as depicted in Figure 4.3, which can be measured using scattered light intensity for human red blood cells (hRBC) or using a volume sensitive fluorescent dye in the case of yeast (Figure 4.4).[339] This technique allows for the determination of the osmotic permeability coefficient of both water (P_f) and glycerol (P_{gly}), parameters used to characterize solute permeation rates.

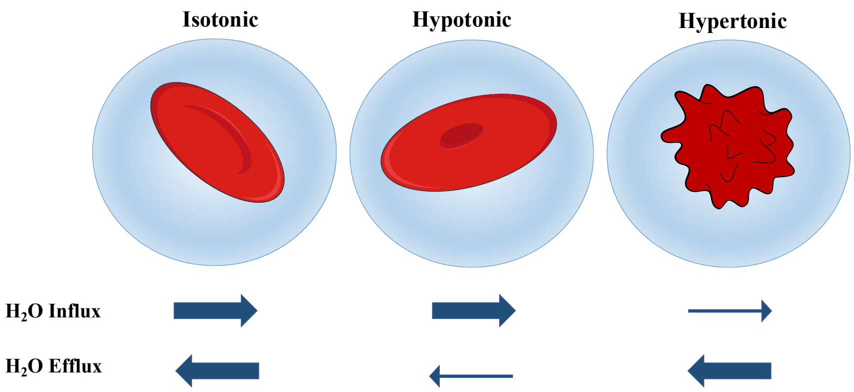

Figure 4.3: *The morphology of human red blood cells (hRBC), specifically their volume, can alter depending on the tonicity of the solution in which they reside. In an isotonic environment, the osmotic pressure is alike, and the hRBC retains its normal size and shape. Exposure to a hypotonic solution of a selected solute will increase water influx in an effort of the hRBC to equalize the osmotic pressure, leading to swelling. An osmotic shock with hypertonic non-permeable solute leads to increased water efflux, thus inducing cell shrinkage. A hypertonic solute like glycerol leads first to increased water efflux, thus inducing cell shrinkage, followed by solute uptake into the cells (swelling).*

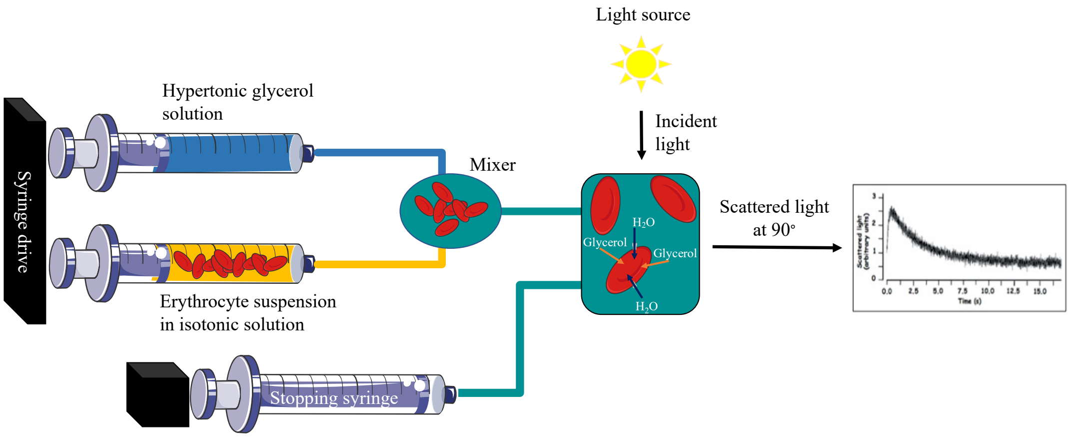

Figure 4.4*: Stopped-flow set-up aimed at monitoring changes in cell volume induced by hypertonic glycerol shock monitored by alterations in the scattered light intensity for hRBC. There are two solutions, one containing the erythrocyte suspension in an isotonic buffer (incubated 30 minutes with inhibitor prior measurement) and the second solution with, in this example, a hypertonic solution. Both will be injected into the mixing chamber together by the syringe drive. Changes in cell volume induced by the osmolarity of the second solution is monitored by alterations in the scattered light intensity (or fluorescence intensity). Data acquisition starts when flow suddenly stops using the third stopping syringe, immediately after the two solutions mix. The interval between the start of mixing and time needed to reach the observation chamber from the mixer is considered as a dead time of 2 ms. Adapted from refs* [367,368].

To study the inhibitory effect of the new organogold series on different AQPs, two types of hypertonic solutions were used, namely a hypertonic sucrose or hypertonic glycerol solution. The impermeable sucrose induces cell shrinkage, whereas with the permeable solute glycerol, cells would shrink initially due to water efflux driven by the hyper-osmotic gradient, then reswell when glycerol uptake restores the equilibrium as depicted in Figure 4.4.[107] Inhibition of AQPs by the gold complexes would prevent glycerol entrance and thus, reswelling of the cells.[339] Figure 4.5 show this effect in the case of hRBC. An example of stopped-flow traces obtained using scattered light intensity for glycerol permeability is shown in Figure 4.6. Based on the measured cell volume changes and permeability induced by imposed shocks, IC_{50} corresponding to the concentration necessary to achieve 50% inhibition of permeability can be determined.[107,339]

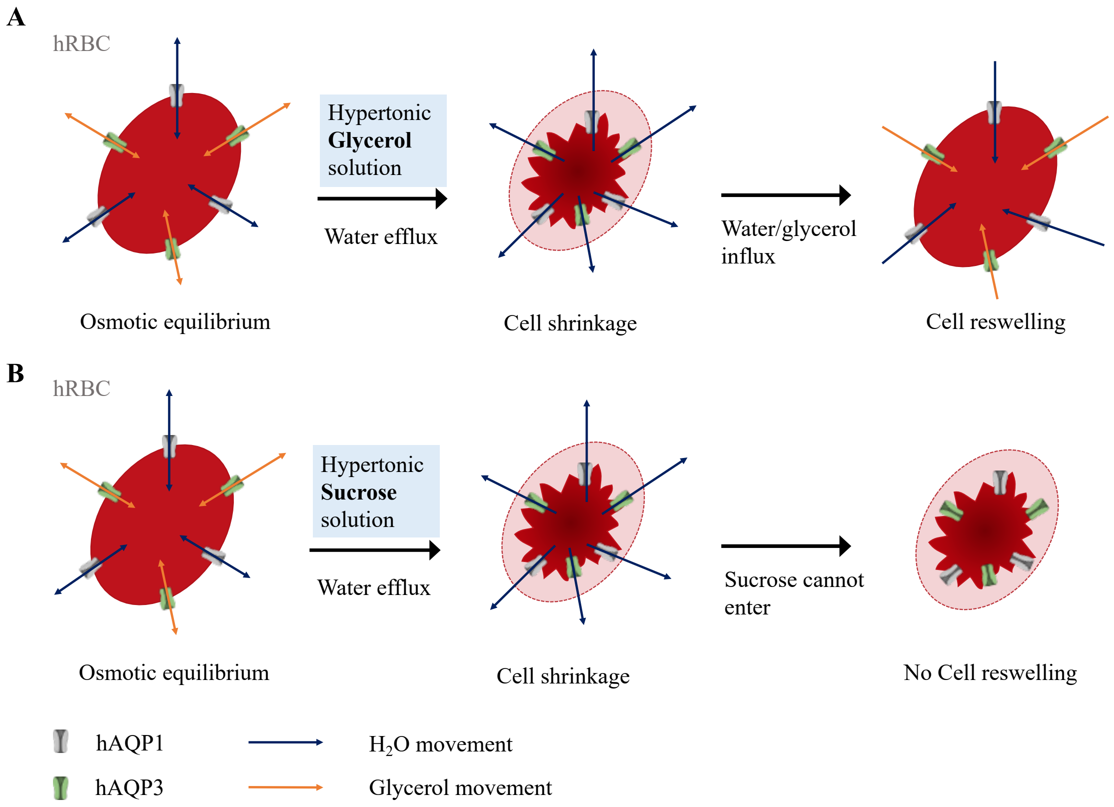

***Figure 4.5**: hRBC volume changes after exposure to **A)** a hypertonic glycerol solution or **B)** a hypertonic sucrose solution. The initial rapid water efflux induces shrinkage, whereas the slower glycerol uptake followed by water restores the osmotic equilibrium (**A**). The large polar sucrose cannot pass the cell membrane, maintaining the imbalance (**B**).*

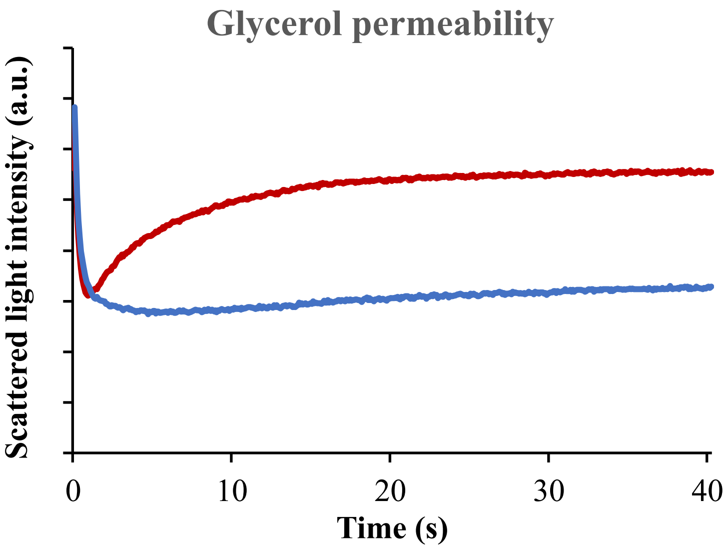

Figure 4.6: Stopped-flow signal illustrating glycerol transport in hRBC over time plotted against scattered light intensity for control (red) and in the presence of an inhibitor (blue).

4.3 Results and Discussion

4.3.1 Inhibition of hAQ3 in hRBC

Benchmark AQP3 inhibitor **Auphen** and the five cyclometalated Au(III) complexes **1 - 5** (Figure 4.1) were synthesized following previously reported procedures by Dr. R. Bonsignore, and evaluated for their water and glycerol inhibition properties on hAQP3 in human red blood cells using stopped flow spectroscopy.[354–358,369] Human red blood cells are known to exclusively express large amounts of hAQP1 (orthodox aquaporin) and hAQP3 (aquaglyceroporin), making them suitable to study membrane permeability to water and glycerol in the presence of possible selective inhibitors.[366] The hRBC were incubated for 30 min with 10 µM of complexes **1 - 5** or **Auphen** prior measurement at pH 7.4, and compared to control cells without an inhibitor present. Results of water and glycerol permeation values compared to control are presented in Figure 4.7. Interestingly, none of the gold complexes interfere with the water transport (P_f) compared to the control cells (Appendix B Table S1). As shown in Figure 4.7-A, **Auphen** gives a near complete specific inhibition of glycerol permeation (almost 100 % inhibition, $p < 0.001$), confirming our expectations. Compounds **4** and **3** were also able to strongly suppress glycerol permeation (99 % and 98 % inhibition, respectively), while moderate effects were observed for **2** and **1** (68 % and 48 %, respectively) and finally virtually no effect was detected for complex **5** (1 %, respectively). The complete lack of effect despite the overall cationic charge of complex **5** might be due to the ancillary metformin bidentate ligand, sufficiently stable (chelate effect) to prevent ligand exchange reactions at the gold(III) centre, and thus, hindering binding of Au(III) to the target thiol groups.

More detailed IC$_{50}$ calculations (Figure 4.7-B, Table 4.1) were performed in the case of the most effective compounds out of this preliminary screening. Of note, complex **4** was designed to evaluate the effect of a potentially anionic complex as aquaglyceroporin inhibitor. The negative charge is accounted for by the deprotonation of the carboxylic acid in aqueous environment. Interestingly, compound **4** shows strong inhibiting properties towards AQP3 glycerol permeation with an IC$_{50}$ value of 2.67 ± 0.04 µM (Figure 4.7-B). Further studies are necessary to evaluate the fraction of deprotonated form of compound **4**, to fully understand the role of the negative charge.

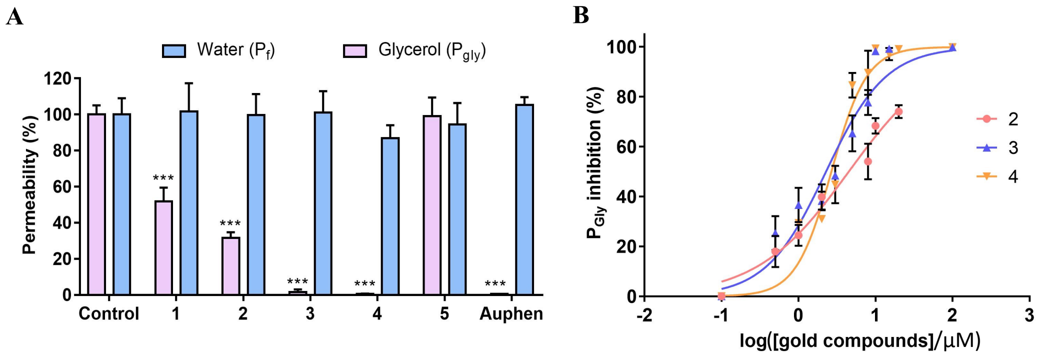

***Figure 4.7**: Effect of gold(III)-based compounds on human red blood cell (hRBCs) water and glycerol permeability. (**A**) Water and glycerol permeability of hRBCs incubated with gold-based compounds **1 - 5** and **Auphen** (10 µM for 30 min). (**B**) Dose–response curves of AQP3 glycerol permeability inhibition by compounds **2 - 4**. Data are shown as means ± SD of three independent experiments. *** $p < 0.001$ treated vs. non-treated cells by student t-test.*

As previously mentioned, the neutral complexes **1-3** can form AuC$^\wedge$N-Cys adducts and are able to react with peptides enabling cysteine arylation. Complex **2** was described as the most reactive species prone to reductive elimination and Cys arylation, followed by **1** with complex **3** being the least reactive.[98] However, this trend is not in line with the IC$_{50}$ values of AQP3 inhibition (Figure 4.7-A), where complex **3** displays strong inhibiting properties (IC$_{50}$ = 2.27 ± 0.07 µM), followed closely by complex **2** (IC$_{50}$ = 4.49 ± 0.06 µM), and finally complex **1** with poor AQP3 inhibition (IC$_{50}$ > 50 µM). This discrepancy may be due to the reactivity of the compounds with other membrane targets containing available Cys residues, which limits their selectivity towards AQP3 inhibition. Additionally, it must be noted that for cysteine arylation to occur after AuC^N-Cys adduct formation, the peptide is seemingly essential to provide additional binding sites for the gold complex to template this reaction, and different proteins (e.g. zinc fingers vs AQP3) with different protein folds would consequently influence the compounds' overall reactivity.[98,370]

The obtained promising data on AQP3 inhibition, prompted us to evaluate the gold(III) complexes for their inhibitory effect on other aquaglyceroporin isoforms, as it will be discussed in the next section.

Table 4.1: *IC_{50} values for AQP3 glycerol permeability inhibition in hRBCs of all complexes*

Complex	**IC_{50} (μM)^a**
Auphen	0.80 ± 0.08^b
1	> 50
2	4.49 ± 0.06
3	2.27 ± 0.07
4	2.67 ± 0.04
5	n.d.

^{a} Data shown as means ± SD of at least three independent experiments. ^{b} Value reproduced from reference [107]. n.d. = non determined.

4.3.2 Inhibition of human aquaglyceroporins in yeast

In the evaluation of inhibitory properties and selectivity of gold(III)complexes for AQP3, hRBC are an excellent testing vehicle. However, a different approach is necessary to study and compare results obtained for other aquaglyceroporin isoforms. For this purpose, *Saccharomyces cerevisiae*-YSH 1770 or yeast was transformed with pUG35 plasmids to express a single human aquaporin isoform (hAPQ3, hAQP7, hAQP9 or hAQP10). To ensure single species expression, endogenous yeast aquaporins are silenced prior transformation. hAQP3 was expressed in yeast as well for comparison, since interspecies assessment of complex effectivity needs to be carefully evaluated if applied beyond indicative purposes to avoid endowing properties resulting from species distinctions to complexes.[109] The cell volume changes in yeast are monitored by fluorescence using 5-and 6-Carboxyfluorescein Diacetate (CFDA). This concentration-dependent self-quenching fluorophore is loaded into the cell as a nonfluorescent substrate and relies on hydrolysis by nonspecific esterases required for intracellular retainment and activation to its fluorescent form (Carboxyfluorescein). Upon cell shrinkage, the fluorophore concentration increases, altering the signal.[371] Therefore, cell volume changes over time of yeast induced by osmotic shock in the stopped-flow set up are monitored by fluorescence.[372]

To confirm successful introduction of aquaglyceroporins in yeast, hAQP3, hAQP7 and hAQP9 were GFP-tagged and expression was subsequently monitored by fluorescence microscopy.[347] Cells transformed with plasmid encoding hAQP10 were compared to cells transformed with an empty expression plasmid for their glycerol and water permeability due to lack of GFP-labelling. As demonstrated in Figure 4.8-A, the functionality of hAQP10 was confirmed, since the measured P_{gly} for hAQP10-expressing yeast cells with a value of $(27.30 \pm 9.62) \times 10^{-8}$ cm s^{-1} was 270-fold higher than for the empty vector $((0.10 \pm 0.001) \times 10^{-8}$ cm $s^{-1})$ at pH 5.0. The water permeability (P_f) was evaluated as well (Figure 4.8-B) and although the hAQP10-expressing yeast value was slightly higher $((4.25 \pm 0.17) \times 10^{-4}$ cm $s^{-1})$ compared to the empty vector $((3.74 \pm 0.15) \times 10^{-4}$ cm $s^{-1})$, the difference was not statistically significant. Additionally, pre-treatment with 10 µM **Auphen** for 30 min initiated only a minor P_f decrease of ~ 10%.

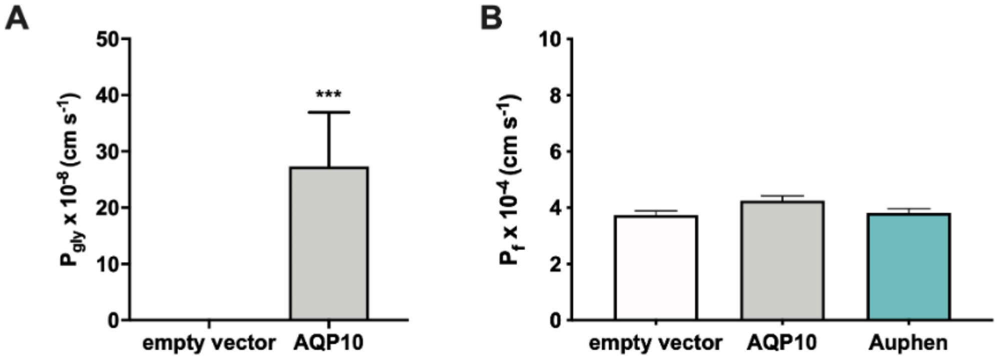

*Figure 4.8: **A)** Glycerol permeability (P_{gly}) and **B)** water permeability (P_f) of yeast cells transformed with the empty vector (control) or expressing hAQP10 measured at pH 5.0. Water permeability inhibition by Auphen (10 µM, 30 min) is also shown. Data shown as means ± SD of three independent experiments. *** $p < 0.001$.*

Auphen and the five cyclometalated Au(III) complexes **1 - 5** (Figure 4.1) were evaluated for their inhibitory properties against hAQP3, hAQP7, hAQP9 and hAQP10. Yeast cells expressing hAQP3, hAQP7 and hAQP9 were incubated prior to the permeability assay for 30 min with 50 µM cyclometalated Au(III) complex or **Auphen**

at their physiological pH of 7.4. The hAQP10 transformed yeast cells were challenged with 10 μM of complexes **1-5** and **Auphen**, since they showed a higher sensitivity to the solvent (DMSO). The hAQP10 assays were performed at its physiological pH of 5.0.[348]

There is a clear diversity in effect seen for the organometallic complexes **1-5** and benchmark **Auphen** per isoform (Table 4.2, Figure 4.9). The strong inhibition of glycerol permeability via hAQP3 is confirmed for **Auphen**, as well as the more moderate effect in hAQP7, as previously reported in adipocytes.[17,20] Interestingly, glycerol permeability of hAQP10 is drastically reduced upon treatment with **Auphen**, up to 98 % ($p < 0.001$). On the other hand, hAQP9 glycerol permeation is hindered the least (58%, $p < 0.001$). Overall, **Auphen**`s inhibitory activity of aquaglyceroporins is as follows: hAQP3 > hAQP10 > hAQP7 > hAQP9.

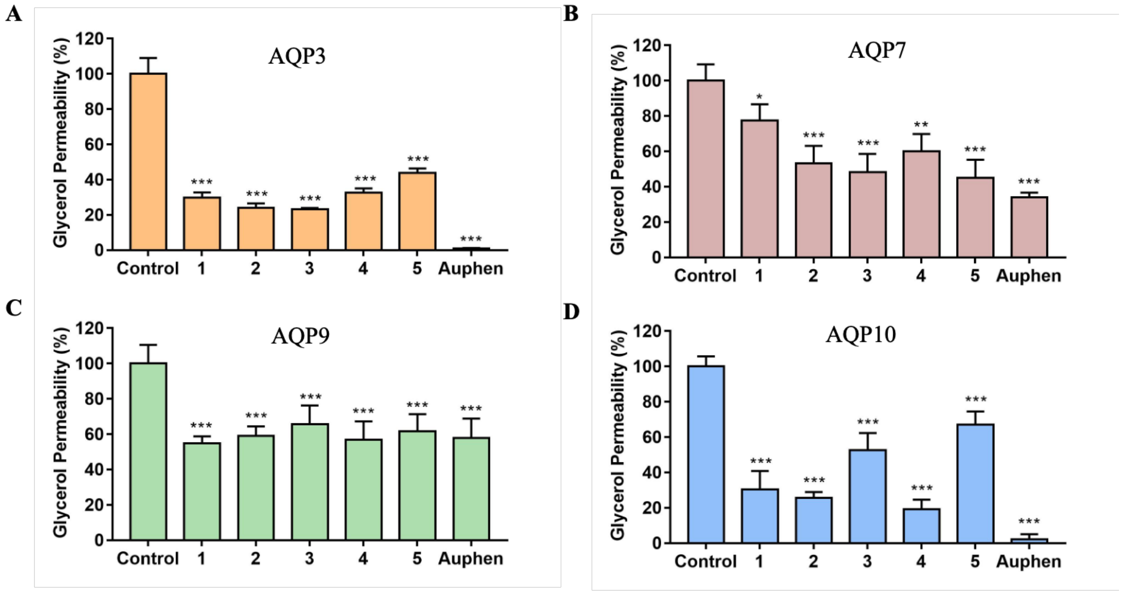

__Figure 4.9__: Effect of gold-based compounds on human aquaglyceroporins expressed in yeast. Glycerol permeability (Pgly) of yeast cells transformed with plasmid encoding hAQP3 (__A__), hAQP7(__B__) and hAQP9 (__C__) non-treated and treated with gold-based compounds (50 μM for 30 min). (__D__) Glycerol permeability (P_{gly}) of yeast cells transformed with plasmid encoding hAQP10, non-treated and treated with gold-based compounds (10 μM for 30 min). Data are shown as means ± SD of three independent experiments. $* p < 0.05$; $** p < 0.01$; $*** p < 0.001$. ** treated vs. non-treated cells.*

***Table 4.2**: Osmotic permeability coefficient of glycerol (P_{gly}) for compound **1-5** and **Auphen** in yeast cells. Yeast cells expressing hAQP3, hAQP7 and hAQP9 were pre-treated with 50 µM of each compound for 30 min, hAQP10 transformed yeast cells with 10 µM of each compound for 30 min.*

Complex	**P_{gly} (% residual permeability vs control)**			
	AQP3	**AQP7**	**AQP9**	**AQP10**
Auphen	1.00 ± 0.25	33.91 ± 2.79	57.81 ± 11.06	2.26 ± 2.83
1	29.78 ± 2.98	77.52 ± 9.11	54.70 ± 4.00	30.37 ± 10.50
2	23.92 ± 2.63	53.22 ± 9.98	58.96 ± 5.51	25.69 ± 3.30
3	23.14 ± 0.80	48.10 ± 10.43	65.63 ± 10.63	52.65 ± 9.69
4	32.57 ± 2.44	59.94 ± 9.95	56.85 ± 10.36	19.26 ± 5.43
5	43.73 ± 2.58	44.96 ± 10.25	61.78 ± 9.57	67.08 ± 7.51

Data are shown as means ± SD of three independent experiments.

As shown in Figure 4.9-A, complex **3** has the strongest suppression of glycerol permeation via AQP3, closely followed by complex **2**. Complexes **1** and **4** are slightly less effective in their inhibition (ca. 30% respectively), and finally complex **5** has the least impact on hAQP3 glycerol permeation (ca. 43%). In general, the organometallic complexes, with the exception of complex **5** that reacts poorly against all isoforms, appear to follow **Auphen** in their potency to inhibit glycerol permeability for hAQP7 and hAQP9 (Figure 4.9-B & C, Table 4.2). In both isoforms, the residual P_{gly} following compounds' treatment compared to control was > 55%, notwithstanding the different compounds' structures and charges (**1-3** neutral, **4** anionic and **5** cationic) (Table 4.2). In yeast cells expressing hAQP10 (Figure 4.9-D), the strongest inhibitory effect on glycerol permeability was observed for the cyclometalated Au(III) complexes **4**, **2** and **1** (ca. 20%, and 30% max), followed by the less potent complexes **3** (ca. 50 %) and **5** (ca. 30 %), respectively.

To further investigate the binding mechanism to hAQP10, an assay was performed to evaluate the reversibility of inhibition by complex **2,** compared to benchmark **Auphen**, following established protocols.[107,109] Briefly, yeast cells were pre-treated with 10 µM compound for 30 minutes, followed by a wash with either isotonic sorbitol buffer or with 100 µM β-mercaptoethanol (βME). The latter is known to react with cysteine sulfhydryl groups and thus, competes with the gold(III) complex for binding to hAQP10. After the wash, glycerol permeability was assessed and compared to control, as presented in Figure 4.10.

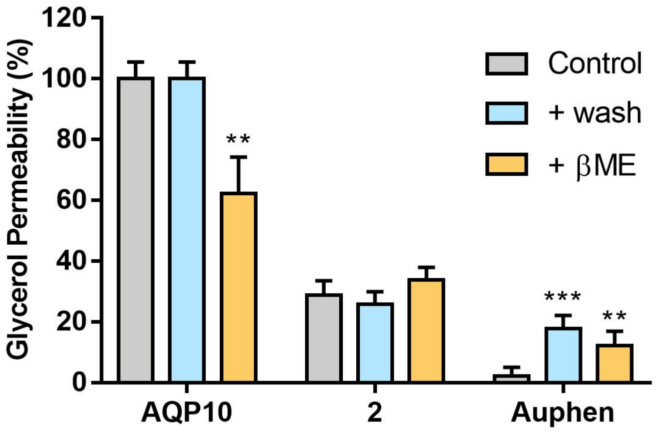

***Figure 4.10**: Glycerol permeability (P_{gly}) inhibition of yeast cells transformed with plasmid encoding hAQP10 after 30 min treatment with 10 µM compound **2** or **Auphen**, and reversibility by washing with 1.4 M sorbitol buffer (pH 5.0) or incubation with 1mM β-mercaptoethanol (30 min). Data are shown as means ± SD of three independent experiments. ** $p < 0.01$; *** $p < 0.001$.*

Interestingly, washing the cells with either isotonic buffer or βME did not affect the recovery of hAQP10 glycerol permeability after treatment with compound **2**, whereas a partial recovery can be observed for pre-treatment with **Auphen**. Considering that βME failed to compete with compound **2**, it is possible that the complex establishes an irreversible covalent bond with cysteine residues present in hAQP10, *via* cysteine arylation. For **Auphen**, the nature of binding might be of a more reversible nature due to the direct Au-Cys coordinative bond.[107,109]

4.3.3 Molecular modelling of aquaglyceroporins

Based on the previous results, it is clear that several factors play a role in the binding of complex to aquaglyceroporin. The selectivity of the gold(III) compounds for certain isoforms might be partially explained by the nature of the pore. Although the general structure of the aquaglyceroporins is highly conserved, small variations in their amino-acid sequence can have a significant impact on substrate and inhibitor binding. In AQP3 for example, the presence of Cys40 in the extracellular side of the pore lining was essential for **Auphen**'s inhibition, as previously illustrated with molecular docking studies and site-directed mutagenesis.[107,108,252] Therefore, it is hypothesized that sulfur donor groups in the form of cysteine and methionine need to be both present and available for binding to induce inhibition by gold complexes.

In an attempt to rationalize the observed AQP inhibition trends, homology model systems of Wild Type (WT) hAQP3, WT hAQP7[373], WT hAQP9 and WT hAQP10[348] were build using Molecular Operating Environment (MOE) software by Dr. D. Wragg. The model of WT hAQP3 was built based on the crystal structure of GlpF as previously reporterd[109,306,309], and WT hAQP9 was built based on the crystal structure of hAQP10 (PDB ID 6F7H).[348] Figures 4.11 and 4.12 present monomers for each aquaglyceroporin with relevant gold-binding residues in the pore linings highlighted.

Figure 4.11-A of the WT hAQP3 monomer shows the Cys40 presence near the extracellular pocket, available for interactions with gold(III) complexes, as reflected in the aforementioned glycerol permeability assays. In WT hAQP7 (Figure 4.11-B), three thioether-containing methionine residues can be observed throughout the pore lining. Of these, Met47 and Met93, were identified as possible binding sides for gold(III) coordination complexes with residues facing the pore lining. [311] Particularly, the glycerol transport inhibition of **Auphen** has been attributed to its binding to Met47 inside the NPA pocket facing the cytoplasm. [311] Despite possible binding to methionine, the inhibitory effect of **Auphen** in this isoform is less potent compared to WT hAQP3.

Overall, availability of cysteine residues appears the key to gold compounds' inhibition. Analysis of the homology model of WT hAQP9 showed that two cysteine residues are close to the pore extracellular entrance: Cys213 and Cys41 (Figure 4.12-A). However, careful evaluation of the orientation of the two residues reveals that one (Cys213) is buried into the pore and not available for metal binding, whilst the other (Cys41) is located close to the most constricting part of the Ar/R SF in the pore lining, therefore likely to be sterically hindered, restricting gold complex approach opportunities. These results may explain why the gold compounds, including **Auphen**, are only moderate inhibitors of hAQP9.

In WT hAQP10, permeability assays demonstrated a potent inhibition in the transport of glycerol, especially for complex **2** and **4**. The model of WT hAQP10 (Figure 4.12-B) reveals the presence of both a methionine and cysteine residue, located near the extracellular side. Specifically, Cys209 was found to be accessible in the pore lining for interaction with the gold(III) complexes. The effects of arylation of Cys209 by **2** was further investigated using metadynamics calculations, comparing pore size with and without complex present. Interestingly, pore shrinkage indeed occurs upon arylation of Cys209, inducing an overall protein conformational change that involves both the intracellular and extracellular pockets, as show in Figure 4.13. Simulating glycerol permeation in both models demonstrated that the covalent binding of the C^N ligand of complex **2** to hAQP10 hinders glycerol permeation, reducing substrate uptake to 65% compared to the non-bonded WT model (82%, respectively).

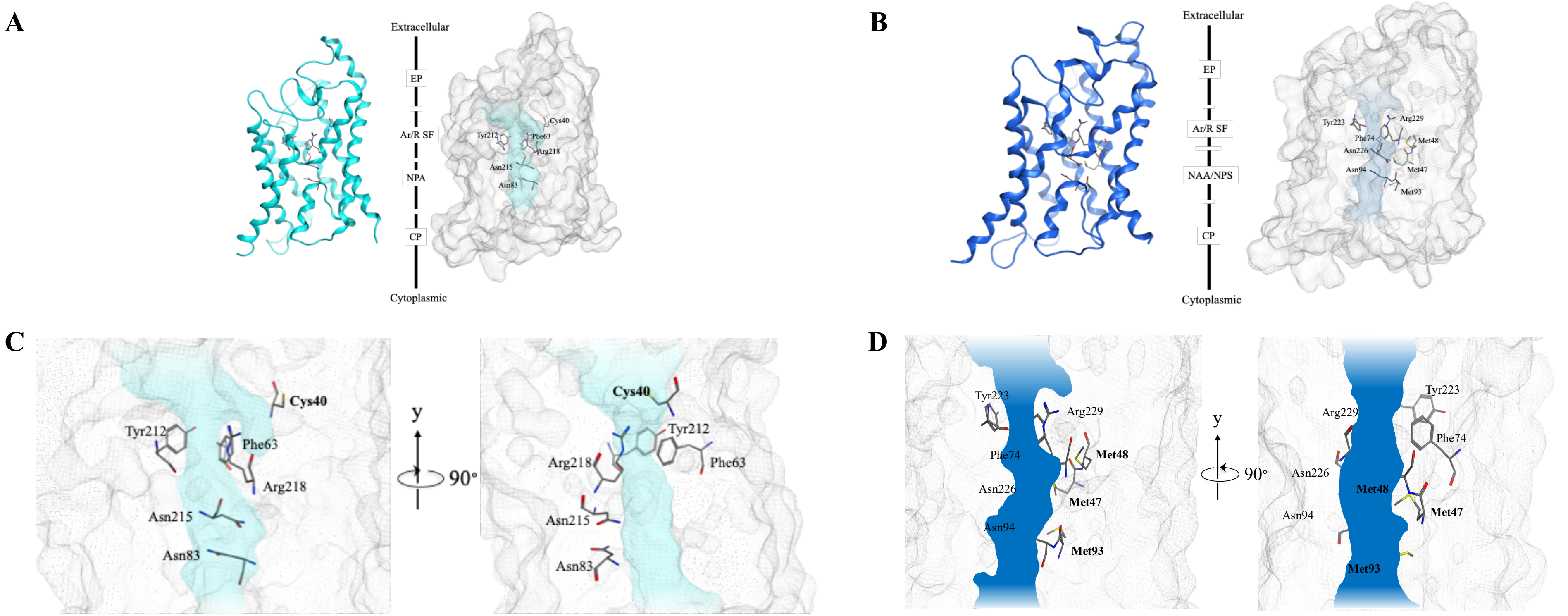

***Figure 4.11**: Homology models for WT hAQP3 (**A,C**) and WT hAQP7 (**B,D**) monomers. **A/B**) Left represents ribbon cartoon of tertiary protein structure and right a surface representation of the channel with key residues lining the pore selectivity filters highlighted. **C/D**) Represents a zoom of two side view sections of key amino acids in pore lining. Sulfur containing amino acids are in bold. EP = extracellular pocket, AR/R SF = aromatic arginine selectivity filter, NPA motifs and CP = cytoplasmic pocket. Figures were generated with MOE by Dr. D. Wragg.*

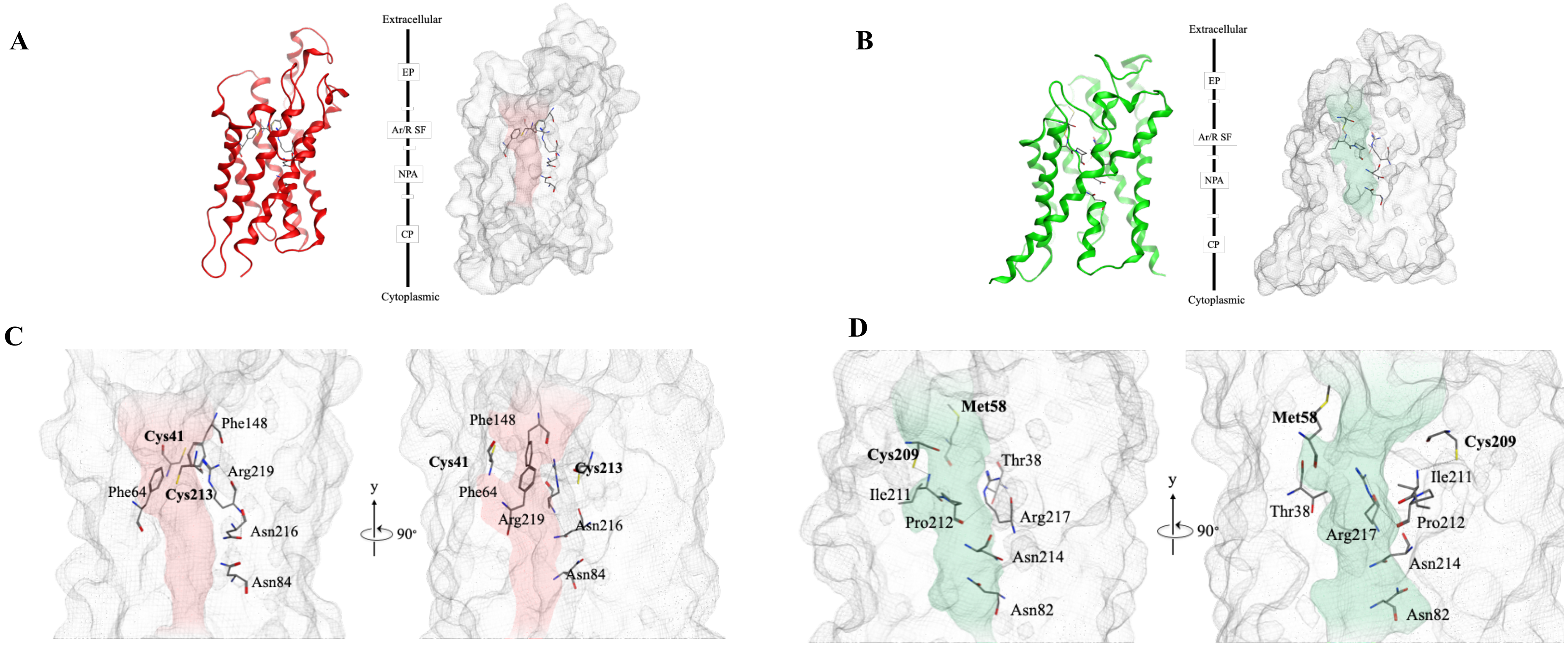

Figure 4.12: *Homology models for WT hAQP9 (**A,C**) and WT hAQP10 (**B,D**) monomers. **A/B**) Left represents ribbon cartoon of tertiary protein structure and right a surface representation of the channel with key residues lining the pore selectivity filters highlighted. **C/D**) Represents a zoom of two side view sections of key amino acids in pore lining. Sulfur containing amino acids are in bold. EP = extracellular pocket, AR/R SF = aromatic arginine selectivity filter, NPA motifs and CP = cytoplasmic pocket. Figures were generated with MOE by Dr. D. Wragg*

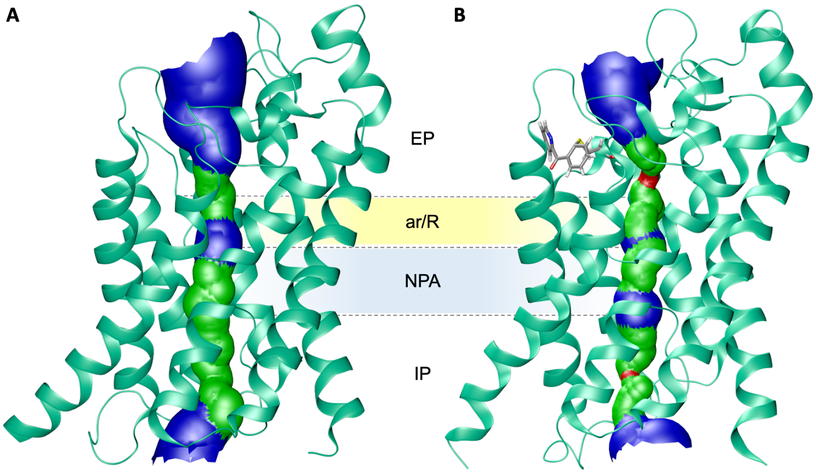

***Figure 4.13**: Homology models of **A**) WT hAQP10 monomer and **B**) hAQP10 monomer with highlighted Cys209-complex **2** adduct. The effect on pore size is presented in 3D, based on Van der Waals radius (red = smaller than single H_2O, green = single H_2O, blue = larger than single H_2O. Figure by Dr. D. Wragg, generated using HOLE[374] and VMD[375] software.*

Finally, another factor likely to affect the gold compounds` inhibitory properties of different AQP isoforms, may be the establishment of favourable non-covalent interactions at the level of the extracellular pocket. For example, possible electrostatic interactions may play a role in the early phases of compound/protein binding before coordination or covalent bonds are established. Thus, we have analysed the extracellular and intracellular electrostatic surfaces of the various aquaglyceroporin isoforms (Figure 4.14). It is striking that, particularly on the extracellular side, markedly positively charged surfaces are evidenced for hAQP7 (pH 7.4) and hAQP10 (pH 5.0), while less pronounced for hAQP9 (pH 7.4). Instead, the hAQP3 (pH 7.4) extracellular surface leans toward a more negative potential, as previously reported by de Almeida et al., possibly favouring approach of gold complexes of a cationic nature.[109]

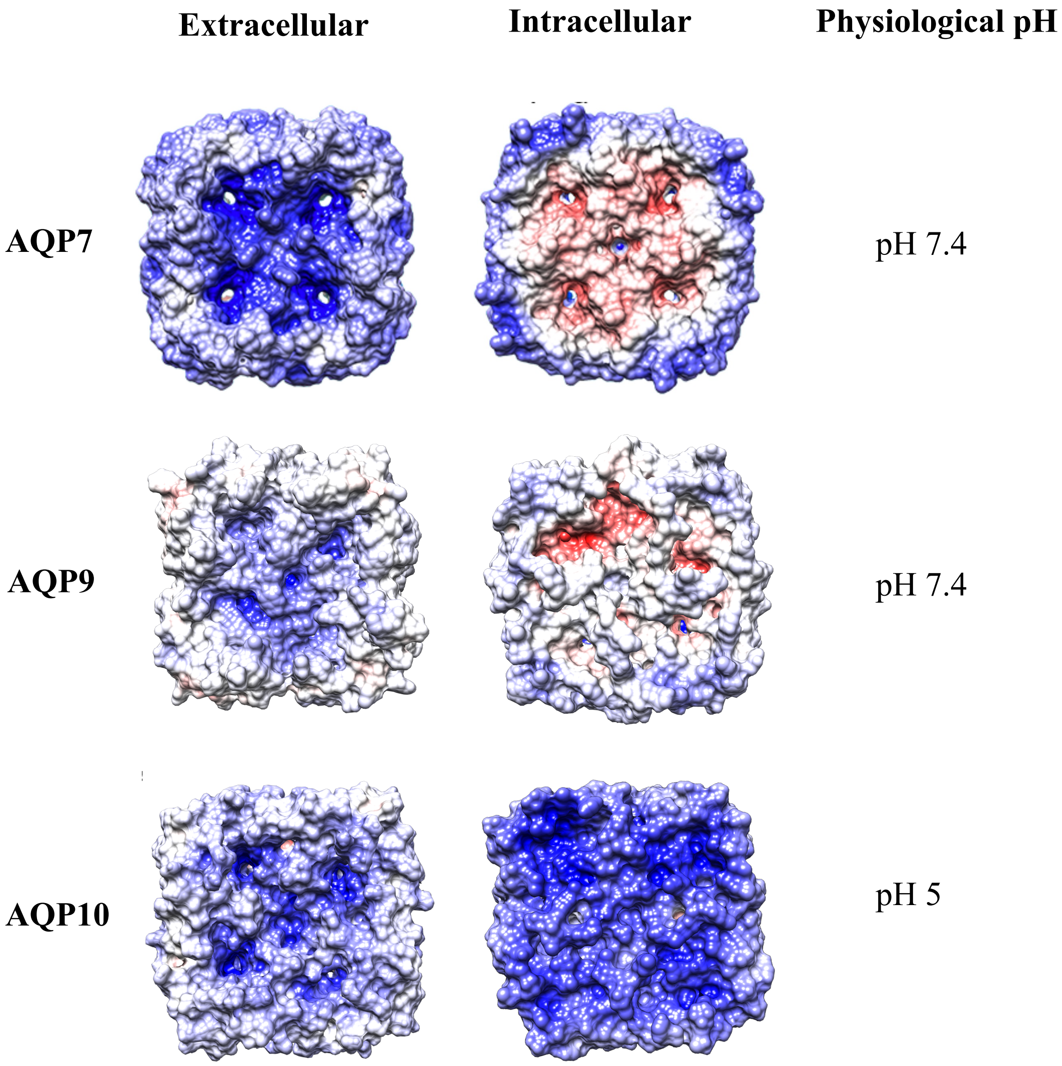

Figure 4.14: *Extracellular electrostatic surfaces of WT AQP7*[347]*, WT hAQP9, WT hAQP10 with the following colour code: positively charged = blue, negatively charged = red, neutral = white. Surfaces were generated using the Adaptive Poisson-Boltzmann Solver (APBS)*[376] *and rendered using Chimera software*[377]*. Images produced by Dr. Darren Wragg.*

4.4 Conclusions

Development of selective AQP inhibitors is essential due to the roles these membrane channels in physiology and disease mechanisms. Inhibitors can be utilised as chemical probes to detect AQP functions in biological systems as well as novel therapeutic agents in a variety of disease. A family of five organogold compounds (**1-5**) was studied for the inhibition of glycerol permeation *via* four aquaglyceroporins in hRBCs and in an optimized *Saccharomyces cerevisiae* model by scattered light intensity and fluorescence stopped-flow spectroscopy, respectively. Potent and irreversible inhibition of glycerol permeation was observed especially against hAQP3 (hRBCs) and in yeast cells expressing either hAQP3 or hAQP10, whilst the effect on hAQP7 and hAQP9 were generally moderate. The organogold complexes are known to react readily with cysteine residues in proteins. In some cases, gold coordination adduct formation at Cys residues can be followed by metal-templated transfer of the C^N ligand to the thiol group (C-S bond formation *via* reductive elimination) leading to irreversible binding to peptides. Compound **2** in the series was one of the most potent inhibitors towards glycerol permeation in hAQP10 overexpressing yeast cells via covalent binding, forming an irreversible adduct as demonstrated in the competition assays with β-mercaptoethanol.

In an attempt to rationalize the observed AQP inhibitor isoform selectivity, homology model systems for all aquaglyceroporins were studied, suggesting compound effect to be partially dependent on availability of Cys residues in pore lining. Further investigation into mechanisms of hAQP10 inhibition by **2** was performed using metadynamics. In details, the advanced atomistic simulation revealed that upon covalent binding of the C^N ligand of complex **2** to Cys209, an overall protein conformational change is induced, leading to shrinkage of the pore and significantly reducing glycerol conductance.

Overall, new insights into the mechanism of action for cyclometalated Au(III) C^N compounds toward aquaglyceroporins, especially hAQP10, were gained by combining inhibition studies *in vitro* with molecular modelling and metadynamics atomistic simulations. Further studies are necessary to obtain more accurate IC_{50} values for the inhibition of the various isoforms by the gold compounds. Moreover, to correlate AQP inhibition to the antiproliferative effects of the gold compounds, a systematic evaluation of their anticancer effects against human cancer cells with different levels of aquaglyceroporins expression may be worth pursuing.

4.5 Materials and Methods

4.5.1 General

Solvents and reagents (reagent grade) were all commercially available and used without further purification. Compounds **1-5** and Auphen were synthesized Dr. R. Bonsignore, adapting procedures already reported in literature [354–358,369], and their purity confirmed by elemental analysis (>98%).

4.5.2 Erythrocyte sampling and preparation

Venous blood samples were obtained from healthy human volunteers in accordance with a protocol approved by the Ethics Committee of the Faculty of Pharmacy of the University of Lisbon (Instituto Português de Sangue Protocol SN-22/05/2007). All participants provided written consent. The blood samples collected in citrate anticoagulant (2.7% citric acid, 4.5% trisodium citrate and 2% glucose) were centrifuged at 750x *g* for 5 minutes at 4 °C. After discarding the plasma and the buffy coat, pelleted erythrocytes were washed three times in PBS (KCl 2.7 mM, KH_2PO_4 1.76 mM, Na_2HPO_4 10.1 mM, NaCl 137 mM, pH 7.4), diluted to 0.5 % haematocrit and immediately used. The mean volume of the hRBC in isotonic solution was determined using CASY-1 Cell Counter (Schärfe System GmbH, Reutlingen, Germany) and calculated as 82 fL. After incubation of the hRBC in isotonic PBS, cells were challenged with either a hypertonic sucrose solution or a hypertonic glycerol solution and immediately used for stopped-flow experiments.

4.5.3 Cloning and Heterologous Expression of hAQP3, hAQP7, hAQP9 and hAQP10 in *S. cerevisiae.*

The aquaglyceroporin expression for hAQP3, hAQP7, hAQP9 and hAQP10 was achieved by transforming *Saccharomyces cerevisiae* strain YSH 1170 with recombinant centromeric plasmids, pUG35. This particular plasmid allows for fusion of green-fluorescent protein (GFP) at the C-terminal, allowing visual inspection of hAQPs to confirm successful expression in yeast. Thus, hAQP3, hAQP7 (pWPi-DEST-AQP7 plasmid)[347] and hAQP9 cDNA was amplified by PCR, and each fused to GFP at the C-terminal of the centromeric plasmid pUG35, using YSH1770 as host strain for heterogenous expression. The hAQP10 expression plasmid was based on a yeast codon optimized cDNA sequence (Genscript, USA) and constructed by homologous recombination in yeast strain YSH1770 by co-transformation of a hAQP10 derived PCR fragment and *Bam*HI, *Sal*I, *Hin*dIII digested pUG35 as described before. [348] The transformed YSH1770 yeast strain produces the native hAQP10 primary structure without any tags.

4.5.4 Yeast Strains and Growth Conditions.

Yeast cultures were grown at 28 °C with orbital shaking in YNB (yeast nitrogen base) without amino acids (DIFCO), with 2 % (w/v) glucose and supplemented with the adequate requirements for prototrophic growth [378]. Yeast transformants were grown to $OD_{600nm} \approx 1$ (corresponding to 1×10^7 cells mL^{-1}), harvested by centrifugation (5,000 × g, 10 min, 4 °C), then washed three times and resuspended in ice-cold sorbitol (1.4 M in 50 mM K^+ -citrate buffer pH 5.0) up to a concentration of 0.33 g (wet weight) mL^{-1}, and kept on ice for at least 90 min. Prior to osmotic challenges, cells were preloaded with the nonfluorescent precursor 5-and-6-carboxyfluorescein diacetate (CFDA, Sigma, USA; 1 mM for 20 min at 30 °C) that is cleaved intracellularly by nonspecific esterases to generate the membrane impermeable fluorescent form carboxyfluorescein (CF) known to remain in the cytoplasm [372]. Cells were then diluted 1:10 in 1.4 M sorbitol buffer and immediately used for stopped-flow experiments.

4.5.5 Permeability assays.

Stopped-flow fluorescence spectroscopy was used to monitor cell volume changes of yeast transformants loaded with the concentration-dependent self-quenching fluorophore CFDA as described above [372]. Experiments were performed on a HI-TECH Scientific PQ/SF-53 stopped-flow apparatus, with 2 ms dead time and controlled temperature, interfaced with an IBM PC/AT compatible 80386 microcomputer. The cells were challenged with an equal volume of shock solution at 23°C and the time course of volume change was measured by following the fluorescence intensity (excitation 470 nm and emission 530 nm). For each experimental condition, 5-7 replicates were analysed. Baselines were acquired using the incubation buffers as isotonic shock solutions. For glycerol permeability (P_{gly}) measurements, a hyperosmotic solution containing glycerol (glycerol 2.1 M in 50 mM K^+ -citrate pH 5.0) was used to create an inwardly directed glycerol gradient. After the first fast cell shrinkage due to water outflow, glycerol influx in response to its chemical gradient is followed by water influx and cell reswelling. Fluorescent traces were corrected by subtracting the baseline slope that reflects the bleaching of the fluorophore. The calibration of the resulting traces followed our previous strategy [379]. Evaluation of P_{gly} was achieved by numerical integrations using a mathematical model implemented in the Berkeley Madonna software (http://www.berkeleymadonna.com/) as described in ref [347]. Specifically, a non-linear regression equation with multiple variables is used, as the internal osmolarity of the yeast cells may vary due to the non-osmotic volume, and as such several variables are fitted at the same time (equations described in ref [347]). This provides a robust and more accurate and sensitive fit than the exponential fit used for hRBC. To assess the effect of the gold compounds, Auphen and the five cyclometalated Au(III) complexes, cells were incubated with compounds for 30 min at RT before stopped-flow experiments.

The reversibility of P_{gly} inhibition was evaluated by pre-treating hAQP10-expressing yeast cells with 10 μM of compound **2** or Auphen and subsequently washing with isotonic buffer or with the reducing agent βME prior to permeability assays. Briefly, cells were centrifuged (5,000 × g, 10 min), washed twice with isotonic buffer or with βME (100 μM) and then resuspended in isotonic buffer prior to permeability assays. Non-pre-treated cells were also washed with βME and used as control.

4.5.6 Statistical analysis.

Results were expressed as mean ± standard deviation SD of at least three individual experiments. Statistical analysis between groups was performed by the unpaired Student's t-test using the Prism software (GraphPad Software Inc., San Diego, CA), with p values < 0.05 considered statistically significant.

Part B

Chapter 5: Integrin bioconjugated metallacages for targeted drug delivery of anticancer drug cisplatin

This chapter is based on the paper:

Bioconjugation of Supramolecular Metallacages to Integrin Ligands for Targeted Delivery of Cisplatin

Jiaying Han, Andreas F. B. Räder, Florian Reichart, **Brech Aikman**, Margot N. Wenzel, Ben Woods, Michael Weinmüller, Beatrice S. Ludwig, Stefan Stürup, Geny M. M. Groothuis, Hjalmar P. Permentier, Rainer Bischoff, Horst Kessler, Peter Horvatovich and Angela Casini

DOI: 10.1021/acs.bioconjchem.8b00682

Integrin-targeting peptides and RGD-functionalised ligands were synthesised and characterised by the group of Prof. Horst Kessler from the Centre of Integrated Protein Science, Technical University of Munich, Germany

5.1 Introduction

Supramolecular coordination complexes (SCCs) have recently attracted attention in the fields of drug delivery, biomolecular recognition and imaging.[112,380] As a result, the number of reports on the bioactivity of three-dimensional SCCs with different shapes, such as helicates,[381] metallacages,[382] cubes,[383] prisms[384] and capsules,[385] and different compositions - (M_nL_m) where M is generally Fe(II), Pd(II), Pt(II), or half-sandwich organometallic clips based on Ru(II), Os(II), or Ir(III) and Rh(III), and L is the ligand of the coordination complex - has substantially increased. In this context, especially supramolecular metallacages offer several properties making them attractive candidates for future drug delivery systems.[386] Similar to metal organic frameworks (MOFs), metallacages form via self-assembly. However, the latter discrete chemical entities have the advantage of featuring a secure cavity to host small drug molecules. In addition, the ability to modify the ligand structure both pre- and post-self-assembly allows for fine tuning of the overall properties like solubility in aqueous environment.[132] Despite these promising properties, the full potential of metallacages as drug delivery vehicles has not been explored so far.[112]

The properties of encapsulating the anticancer drug cisplatin within Pd_2L_4 cages (L = 2,6-bis(pyridine-3-ylethynyl)pyridine as the bidentate ligand), studied by NMR and X-ray diffraction, was reported in 2012 by Crowley and co-workers.[135] Although platinum-based anticancer drugs are still essential for chemotherapy regimens in clinic, the efficacy of cisplatin is badly affected by serious systemic toxicities and drug resistance, and its pharmacokinetics is still under consideration.[54]

Therefore, drug delivery of cisplatin via encapsulation in metallacages could enable a better approach, minimizing the systemic toxicity of the drug whilst reducing its speciation. More recently, similar cationic $[Pd_2L_4]^{4+}$ systems were explored and the *exo*-functionalization of the ligand scaffold to add several different functionalities (e.g. fluorescent tags) were developed.[140,141] Structural studies by ^1H NMR ad X-ray diffraction were performed to demonstrate the encapsulation of cisplatin.[139,387] In addition, the cytotoxicity of these $[Pd_2L_4]^{4+}$ cages have been screened *in vitro* against a small panel of human cancer cells, showing a range of antiproliferative activities from scarce to moderate depending on the ligand scaffold.[139] Nevertheless, to achieve tumour selectivity, conjugation of the cages to cancer-cell-specific ligands such as used in virus-like particles[388], was explored as the best strategy, resulting in the first example of bioconjugation of self-assembled Pd_2L_4 cages to a linear model peptide.[389]

In the present study, the investigation into peptide bioconjugation of the cages was extended to integrin-binding ligands.

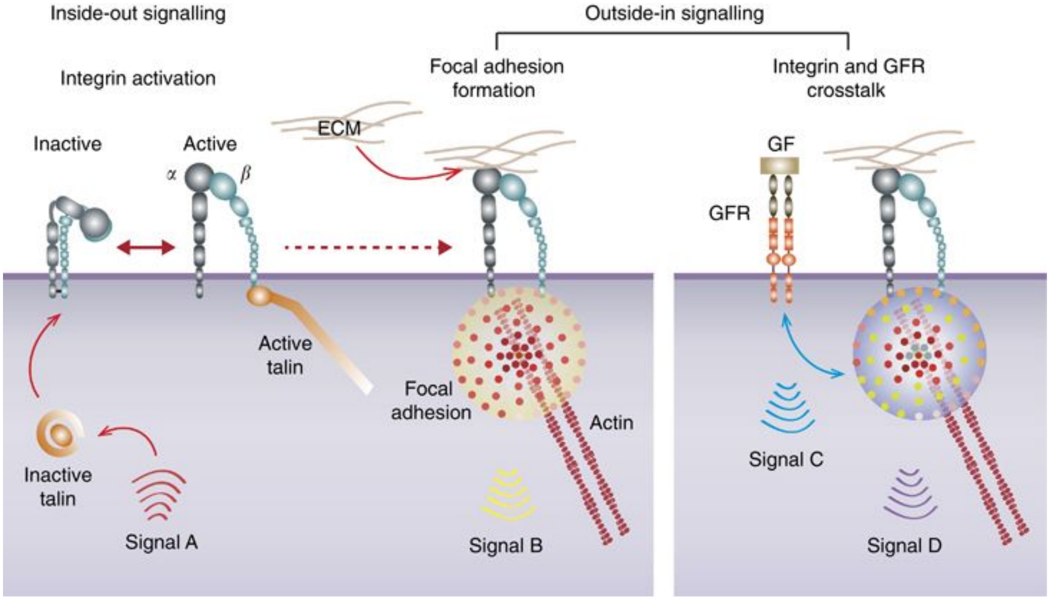

Figure 5.1: Integrin occur in two conformations, i) a closed and bent state when inactive and ii) an open active conformation with high affinity for ligand binding. Activation can be achieved via multiple signals within the cell (signal A) or outside the cell (signal B, C or D). Inside-out signalling is achieved via the binding of intracellular proteins such as talin. Outside-in signalling in turn via for example integrin – extracellular matrix (ECM) interaction, produces intracellular signals (signal B), induces focal adhesion formation and actin cytoskeletal reorganisation that affect downstream cellular processes. Finally, growth factor receptors (GFR) are capable of i) eliciting specific signals (signal C) or ii) in crosstalk with integrins feed into the same pathways to generate unique signals (signal D) in response to ECM cues (outside-in signalling). Image reproduced from Hamidi et al. 2016. [390]

Integrins are heterodimer bidirectional signalling molecules on the cell-surface, composed of α/β subunits. To date, 24 human integrin subtypes are known, which can be triggered by signals from both inside as outside the cell as illustrated in Figure 5.1. In mammals, there are eight integrin subtypes that recognize arginine-glycine-aspartic acid (RGD) motifs in their ligands, which interact with the extracellular matrix (ECM) and thereby regulate many crucial cellular functions important for tumour biology, such as proliferation, migration, and survival.[391,392] Interestingly, members of this subgroup with among them αvβ3 and α5β1, are expressed in cancer tissue and involved in promoting tumour metastasis, and therefore extensively studied as potential drug targets.[392] This has resulted in the design of numerous small peptidic or peptidomimetic molecules to selectively address various integrin sub-types in treatment of different pathologies or for imaging.[393–399] The most successful being the cyclic pentapeptide *cyclo*(RGDfV)[400] and the related Cilengitide[401], which were found to be potent ligands for the integrins αvβ3, αvβ5, and α5β1. Cilengitide (Figure 5.2) is currently the subject of phase II trials for several tumours and granted orphan drug status by the European Medicines Agency (EMA) in 2008.[391,402] The availability of a potent inhibitor greatly contributed to elucidate the exact mechanisms inducing conformation alterations that integrins undergo from resting state to activation.[391,397,402]

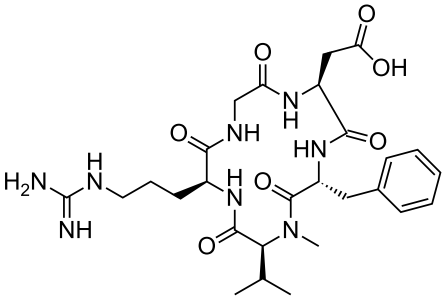

Figure 5.2: *Chemical structure of Cilengitide*

In an effort to exploit the integrin pathway for drug uptake, attempts have been made to directly tether integrin binding peptides to cytotoxic platinum complexes. For example, *Lippard et al.* explored the targeting ability of linear and cyclic RGD and Asn–Gly–Asp (NGR) integrin targeting ligands, and synthesized a Pt(IV) series comprising mono- and difunctionalized complexes. This was shown to improve the cisplatin anticancer activity, once the Pt(IV) compound is reduced to cisplatin in the intracellular environment.[403] More recently, the scope was expanded to other Pt(II) and Pt(IV) complexes, functionalised with cyclic and multimeric RGD-containing peptides.[404,405] Interestingly, the conjugation of a photoactivatable Pt(IV) prodrug to a cyclic RGD-containing peptide led to increased phototoxicity in melanoma cancer cells, which overexpress the αvβ3-integrin receptor.[405] These targeting approaches however do not address the problem of metallodrug *speciation* that occurs until the target is reached. The possibilities of cisplatin encapsulation into a targeted drug delivery vector are therefore extremely appealing.

Inspired by the possibility to improve selectivity of platinum anticancer drugs with integrin targeting-platinum conjugates, four integrin ligands conjugated to a Pd_2L_4 metallacage were developed in collaboration with the research group of Prof. Horst Kessler at the Technical University of Munich, to create subtype specific targeting of human integrin αvβ3 (compounds **1-3)**[399,400,406] and α5β1 (compound **4)**[407].[396,397,408,409] A general scheme of the concept is presented in Figure 5.3.

αvβ3 integrin present in endothelial cells and α5β1integrin mainly expressed in oral squamous cell carcinoma and ovarian cancer cells

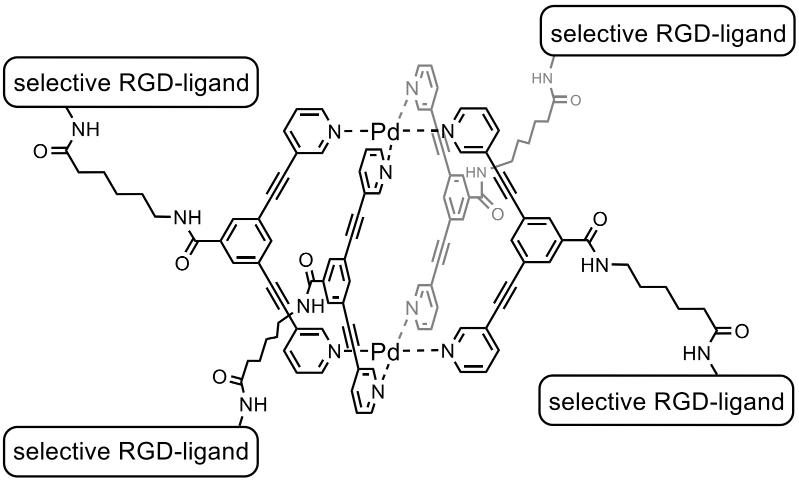

Figure 5.3*: General scheme of Pd_2L_4 metallacage conjugated to selective RGD-ligands.*

5.2 Results and Discussion

Both integrin targeting peptides as RGD-functionalised ligands were synthesised and characterised by the research group of Prof. Horst Kessler at the Technical University of Munich. Ligand ***L0*** *was synthesised adapting a previously reported procedure by Dr. B. Woods, and* ***L3*** *was synthesised by Dr. M. Wenzel.*[141]

In brief, to achieve the bioconjugation of the metallocages, the amino-functionalized ligands **1-4** were coupled to ligand L0 first, to form the cage precursors **L1-L4** (Figure 5.4). After product formation was confirmed with NMR spectroscopy, cage formation of **C0-C4** was achieved by self-assembly upon addition of 2 eq. of the Pd^{2+} precursor (Pd(MeCN)$_4$(BF$_4$)$_2$). The self-assembly was monitored by ^{1}H NMR and remained stable in solution for at least 24 h. The method of peptide conjugation to ligand is preferable over tethering directly to the cage, as reported previously.[389]

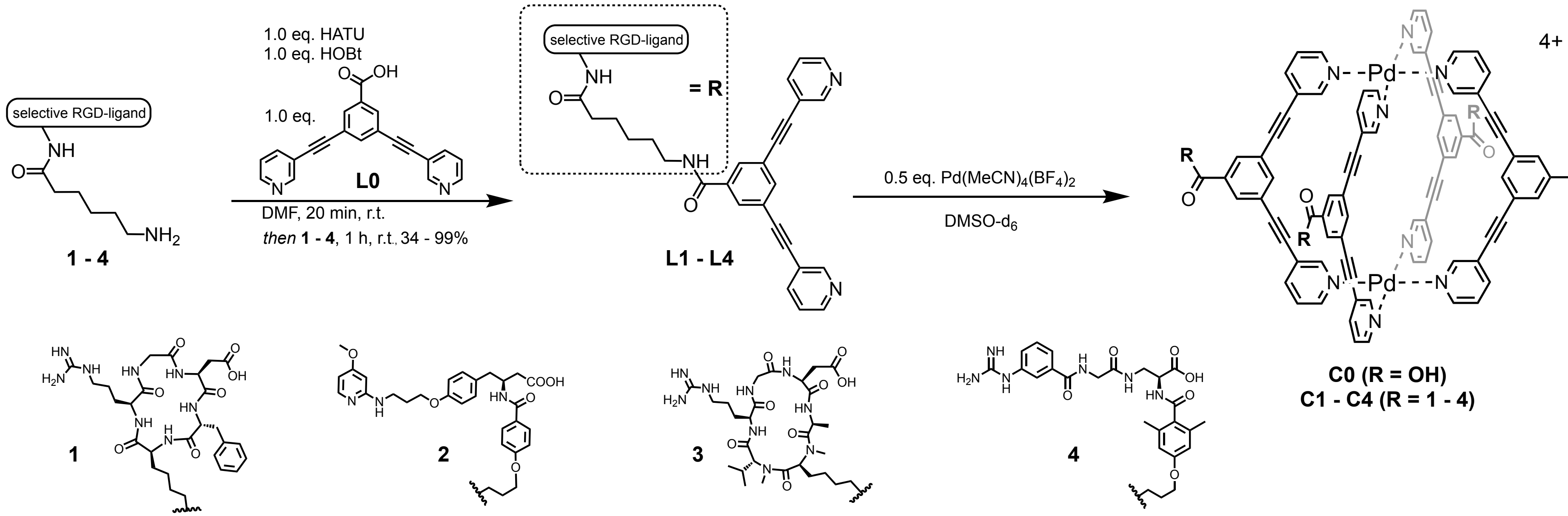

Figure 5.4: *Synthesis of the bioconjugated ligands L1-L4 and of cages C0 and C1-C4 via metal-mediated self-assembly. (HATU = hexafluorophosphate azabenzotriazole tetramethyl uronium, HOBt = hydroxybenzotriazole). Compounds* ***1-4*** *are the integrin binding ligands for αvβ3 (**1**-**3**) and α5β1 (**4**). The integrin ligands were originally described in the following literature:* ***1***[400,408], ***2***[397,406], ***3***[399], *and* ***4***[396,407]**.**

5.2.1 Metallacage integrin binding affinity and selectivity

The integrin binding affinity and selectivity of both bioconjugated cages **C1-C4** as well as their precursors **L1-L4** was assessed by our collaborator dr. F. Reichart from TUM, Germany, using an established enzyme-linked immunosorbent assay (ELISA)-like solid-phase binding assay that involves coated extracellular matrix (ECM) proteins and soluble integrins.[398,410] The integrins of interest are non-covalently immobilised to a solid phase (coating with ECM proteins), followed by incubation of compound (ligand or cage). Unbound compound is subsequently removed by washing and the bound complex exposed to a peroxidase conjugated antibody and detected using spectroscopy. The newly synthesised ligands were compared to an internal standard: Cilengitide.[401,402] Table 5.1 shows a strong binding for **C1-C3** αvβ3 and **C4** α5β1 complexes, as expected from the original binding affinity of the parent ligands **L1-L4**,[398] while the unsubstituted cage **C0** displayed no binding affinity at all. Compared to the internal standard Cilengitide, the metallacages **C1-C4** show higher selectivity for their target integrin with affinities in the low nanomolar range. In line with previous published work concerning RGD-containing ligands,[411,412] multimerisation improves the binding affinity of ligands.[413,414] The role of multimerization is especially important for integrins[415] since multimeric integrin ligands might help to enter cells via endocytosis. This effect is also observed in viruses such as foot and mouth disease[416] and virus-like-particles.[388] Within the group of αvβ3 active cages **C1-C3**, the nature of the integrin binding ligand has an influence on the varying selectivity towards the other integrins. Whereas the cyclic peptides in **C1** and **C3** display increased affinity for all tested integrins upon cage formation, the peptidomimetic **C2** displays in addition an enhanced selectivity for its target integrin αvβ3. The peptidomimetic α5β1 targeting cage **C4**, like its precursor **L4**, show very high selectivity for the integrin α5β1. The binding affinity of **L4** however is quite higher, with an activity for α5β1 far below 1 nM. This might be attributed to additional unspecific interactions between **L4** and the integrin due to the aromaticity of the former, an effect that should disappear with cage formation.

Table 5.1: *IC_{50} values of metallacages **C0-C4** and their ligand precursors **L1-L4** for binding to RGD-recognizing integrin subtypes α5β1, αvβ3, αvβ5 and αvβ6.*

	IC_{50} [nM] [a]			
Compound	**α5β1**	**αvβ3**	**αvβ5**	**αvβ6**
C0	>10000	>10000	>10000	>10000
C1	20 ± 2	2.1 ± 0.8	49 ± 6	159 ± 18
C2	1025 ± 331	0.98 ± 0.24	6580 ± 911	644 ± 66
C3	193 ± 62	0.38 ± 0.01	24 ± 6	13 ± 2
C4	1.77 ± 0.15	>10000	>10000	2370 ± 303
Cilengitide[b]	14.9 ± 3.1	0.61 ± 0.06	8.4 ± 2.1	2050 ± 640

[a] The reported IC_{50} values were calculated using a sigmoidal fit to 16 data points, obtained from two serial dilution rows, with the Origin software package. All IC_{50} values determined were referenced to the affinity of the internal standard and are presented as mean ± SD.

[b] IC_{50} values of Cilengitide as previously reported.[398]

Our group previously reported on the ability of unsubstituted Pd_2L_4 cages to be able to encapsulate up to two molecules of cisplatin as determined by X-ray diffraction and NMR spectroscopy.[135,139] After careful testing of the cisplatin encapsulation properties of the protected form of cage **C0** using the same technique, the observed results were in line with the previously reported data. The protected cage was used instead of cage **C0** due to its higher solubility in the selected NMR conditions. Additional ^1H DOSY NMR spectra of free cisplatin showed a markedly different profile for 2 eq of cisplatin (no cisplatin signal) vs 3 equivalents of cisplatin (reappearance of free cisplatin signal).

5.2.2 Antiproliferative activity studies

To further validate the targeting concept based on higher affinity of binding from the ligands in a more complex biological system, the study extended its scope to *in vitro* testing. Thus, the antiproliferative effects of the coordination cages **C1**-**C3**, alone and encapsulating cisplatin [cisplatin⊂(**C1**-**3**)] were evaluated against two different cell lines, in comparison to free cisplatin. In addition, the non *exo*-functionalised metallacage C0 and its corresponding ligand L0 were also included, alone and encapsulating cisplatin [cisplatin⊂(**C0**)]. Cell lines were selected based on their different αvβ3 integrin expression pattern. Specifically, the malignant melanoma cell line A375 has been shown to overexpress αvβ3,[417] while the human lung cancer cell line A549 is reported to have no expression.[418] Additionally, A549 is known for its resistance to cisplatin. Hence, cells were treated with increasing concentrations of both cages and ligands; concentrations higher than 60 μM were usually not reached due to the toxic effect induced by the presence of DMSO which would taint the resulting cytotoxicity, particularly in the A375 cells. Prior to each experiment, drug encapsulation in each cage system was assessed by ^{1}H NMR and confirmed encapsulation of 2 eq. of cisplatin per eq. of cage (data not shown). The cisplatin stock solutions were as well freshly prepared in aqueous solution (1 mM) to avoid ligand exchange reactions with DMSO.

The results are summarized in Table 5.2 and show that cages **C1**-**C3** have no intrinsic cytotoxicity towards the two cell lines, while cisplatin is as expected moderately toxic only in the A375 cells ($EC_{50} = 33.9 \pm 2.9$ μM). The Pd^{2+} precursor, as well as the different ligands **L0** and **L1-L4** were also studied and resulted to be non-toxic at the highest tested concentrations in both cell lines. Representative values are reported in Table 5.2 for **L0**. Interestingly, while treatment with cisplatin encapsulated in the "untargeted" cage **C0** ([cisplatin⊂(**C0**)]) does not change the drug's antiproliferative effects, cisplatin encapsulated in the bioconjugated cage **C2** showed a significantly increases in its cytotoxic potency towards the αvβ3 integrin expressing A375 cells (ca. 2-fold more potent with respect to free cisplatin, $p<0.01$). This effect is seen in the first 24 h, while a 72 h study (data not shown) revealed no difference between the free and encapsulated cisplatin, indicating the cage provides a kinetic advantage. Against the A459 cells lacking expression of αvβ3, the same [cisplatin⊂(**C2**)] formulation demonstrated a different effect: no increase in the cisplatin toxicity. Cages **C1** and **C3,** however, did both not significantly increase the cytotoxicity of cisplatin in the A375 cell line. The differences among the cisplatin-cages systems partly reflect the differences in the binding affinity towards the αvβ3 integrin receptors of the respective cages (Table 5.1). However, based on the affinity of **C3** for integrin binding, this complex should be the most efficient in delivery of the drug. Instead, **C2** is markedly more effective. This effect could also be related to the lower selectivity against α5β1 and/or αvβ5 (Table 5.1) or be the result of differences in stability and drug release properties of the cages in the biological environment.

***Table 5.2**: Antiproliferative activity (EC_{50} values) of different cages and cage:cisplatin (1:2) formulations in human A375 and A549 cancer cells compared to free cisplatin after 24 h incubation. Concentrations shown relate to cisplatin.*

	EC_{50} [μM] [a]	
Treatment	**A375 (melanoma) αvβ3 ++**	**A549 (lung) αvβ3 –**
Ligand **L0**	> 50	> 100
cage **C0**	> 50	82.6 ± 15.1[b]
[cisplatin⊂(**C0**)]	31.5 ± 3.0	> 60
cage **C1**	> 50	> 60
[cisplatin⊂(**C1**)]	32.4 ± 1.2	> 60
cage **C2**	> 50	> 60
[cisplatin⊂(**C2**)]	15.80 ± 3.35*	> 60
cage **C3**	> 50	> 60
[cisplatin⊂(**C3**)]	29.5 ± 0.6	> 60
cisplatin	33.9 ± 2.9	63.2 ± 5.2

[a] The reported EC_{50} values are presented as mean (± SEM) of at least four independent experiments. [b] Value taken from reference [141]. * ($p < 0.01$) indicate the difference is significant when compared to samples treated with cisplatin only.

5.2.3 Ex vivo studies

To function as an optimal drug delivery system, metallacages should be deprived of intrinsic toxic effects in normal "healthy" tissues, and preferably reduce the toxicity exerted by the encapsulated drug which are often the cause of side-effects. Therefore, as proof of concept, cage **C0**, alone or encapsulating cisplatin, was tested for its toxicity on healthy rat kidney and liver tissues *ex vivo* using the precision-cut tissue slices (PCTS) technique by collaborator dr. J. Han at the University of Groningen.[86,419–422] PCTS are thin (150-250 μm) slices of viable tissue. This model has the advantage of cells remaining in their natural environment, thus maintaining the original cell-cell and cell-matrix contacts, which are absent in classical 2D cell cultures *in vitro*. Approved by the FDA as a model for drug toxicity and metabolism studies, it is also useful to determine drug uptake/efflux mechanisms. [86,419–422] Recently, the PCTS method was successfully used to study the toxic effects of several experimental anticancer organometallic compounds, including aminoferrocene-containing prodrugs, ruthenium-based kinase inhibitors, as well as gold(I) carbenes and gold(III) cyclometalated cytotoxic agents. [86,419–422]

The viability of the rat liver and kidney slices was determined by incubating the PCTS with different concentrations of cage **C0** (5 μM, 15 μM and 25 μM with 0.83% DMSO v/v), alone (10 μM, 30 μM and 50 μM) or encapsulating cisplatin ([cisplatin⊂(**C0**)] = [cisplatin]:[cage] of 5/10 μM, 15/30 μM and 25/50 μM with 0.83% DMSO v/v for the final concentration of [cisplatin⊂(**C0**)]), for 24 h. For each PCTS, both ATP as protein levels were determined. ATP was measured using the ATP Bioluminescence Assay kit CLS II (Roche, Mannheim, Germany), and the content corrected for the protein amount of each slice and expressed as pmol/μg protein. The protein content of the PCTS was determined by the Bio-Rad DC Protein Assay (Bio-Rad, Munich, Germany) using bovine serum albumin (BSA, Sigma-Aldrich, Steinheim, Germany) for the calibration curve. For comparison, cisplatin was also administered in the same range of concentrations. It is important to note that the PCLS and PCKS of each liver/kidney sample were exposed to all three compounds, as well as controls, to limit bias introduced by non-biological experimental variation. Due to this experimental design, interindividual variation between compound's classes, as well as between compounds and controls, is limited. Data for liver and kidney is presented in Figure 5.5 (A and B). As expected, and in line with previous results,[421] cisplatin alone causes a marked decrease in slice viability for both organs. The ATP production of the liver slices for example was dramatically reduced at 30 μM and completely obliterated at 50 μM cisplatin. Instead, cage **C0** was substantially not toxic, even at the highest tested concentration in the liver slices. Corresponding ligand **L0** and Pd^{2+} precursor were also non-toxic above 100 μM (data not shown). Interestingly, the encapsulated cisplatin ([cisplatin⊂(**C0**)]) showed a significantly reduced toxicity in both liver and kidney slices compared to free cisplatin.

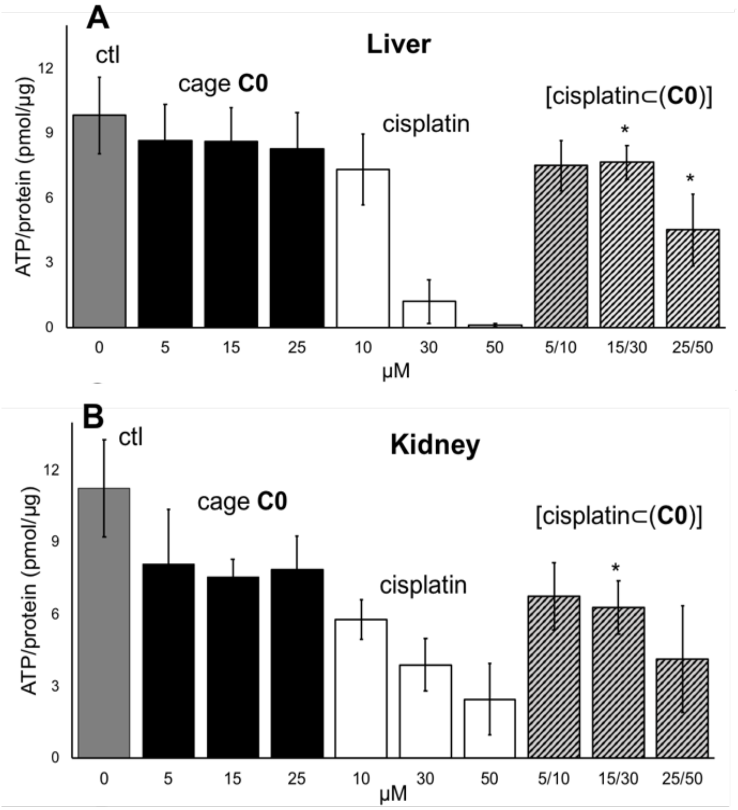

Figure 5.5*: Viability of Precision Cut Tissue Slices (PCTS) from liver (**A**) and kidney (**B**), treated for 24 h with different concentrations of cisplatin (5, 10 and 25µM), cage C0 (10, 30 and 50 µM) and encapsulated cisplatin [cisplatin⊂(**C0**)] ([cage]/[cisplatin] = 5/10, 15/30, 25/50 µM). Adapted with permission from Han et al, Bioconjugate Chem. 2018, 29, 11, 3856–3865. Copyright (2018) American Chemical Society.*

To evaluate the relation between toxicity and intracellular metal accumulation, the Pt and Pd content of tissue slices exposed to cisplatin alone or encapsulated in cage **C0** was determined by inductively coupled plasma mass spectrometry ICP-MS by our collaborator from the University of Copenhagen. PCTS were collected after incubation with the different concentrations of cisplatin, cage **C0** or of the cage/cisplatin complex [cisplatin⊂(**C0**)], washed with ice-cold Krebs-Henseleit buffer and snap-frozen and stored at -80°C until the analysis by mass spectrometry. Data for liver and kidney are presented in Figure 5.6 and show that the metal concentration in PCTS increases in a concentration dependent manner. As expected,[423] the Pt content is generally lower in liver (Figure 5.6-A) than in kidney (Figure 5.6-B), but in contrast the accumulation of Pd is somewhat higher in the liver than in the kidney PCTS. Moreover, the results suggest that Pd accumulation in the PCTS is not influenced by cisplatin encapsulation. Cisplatin encapsulated in cage **C0** is markedly less accumulated than free cisplatin in the liver slices (Figure 5.6-A). A similar trend is visible for the kidney samples although the differences are not as significant (Figure 5.6-B). With these results, another indirect evidence has been obtained to demonstrate that cisplatin encapsulation in the metallacage is mostly preserved even in biological environment.

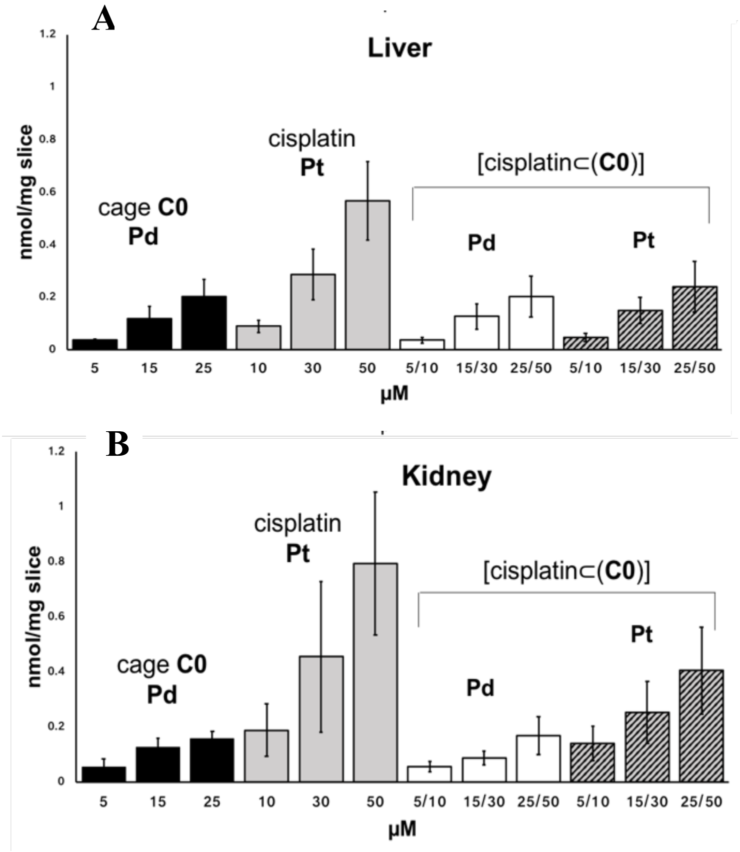

Figure 5.6*: Total metal content of Pd and Pt (nmol/mg slice) determined by ICP-MS in PCTS of liver (****A****) and kidney (****B****) treated for 24 h with different concentrations of cisplatin, cage C0 and encapsulated cisplatin ([cisplatin⊂(C0)]). deviation of at least three independent experiments. * (*$p \leq 0.01$*) indicates the difference is significant when compared to treatment with cisplatin at the same concentration. Adapted with permission from Han et al, Bioconjugate Chem. 2018, 29, 11, 3856–3865. Copyright (2018) American Chemical Society.*

Depending on the origin of tissue, the content of Pd and Pt in the [cisplatin⊂(**C0**)] treated slices can diverge from the predicted metal stoichiometry (Pd:Pt). The liver values are roughly in accordance with the prediction, but surprisingly, the Pt content in the kidney is higher than the Pd content, which should be further investigated. One explanation might be related to the possibility of Pd being partly excreted from the tissue over 24 h, while Pt is not (or less). Alternatively, a part of cisplatin may be released from the cage before uptake and enter the tissue more efficiently in the kidney than in the liver. In that case, the overall Pt content may actually be the result of accumulation of both encapsulated and free cisplatin. However, this latter explanation may be less likely to occur in liver as such an effect is not seen in this organ.

5.3 Conclusions

In conclusion, this work presents an integrin-selective supramolecular drug delivery system for cisplatin based on the Pd_2L_4 metallacage scaffold. Pd_2L_4 cages (L = ligand) have been conjugated to four integrin ligands with different binding affinity and selectivity for tumour cells. Cage formation and encapsulation of cisplatin was monitored and validated by NMR spectroscopy. Remarkably, cisplatin encapsulated in the RGD-modified metallacage exhibits increased anticancer effects *in vitro* compared to the free compound in melanoma A375 cells overexpressing αvβ3 integrins*,* whilst the same combination has a decreased toxicity against healthy tissues *ex vivo*. This decreased toxic effect is based on the reduced platinum uptake in healthy tissues, as evidenced by analysis of metal content using ICP-MS. Further studies are necessary to fully characterise the properties of these metallacages as drug delivery systems, including their stability in physiological conditions and drug release properties, toxicity of cages conjugated with integrin ligands in healthy tissue, as well as study of the effects in *in vivo* models. However, this work constitutes a first proof-of-concept of the possible use of supramolecular coordination complexes for directed drug delivery.

5.4 Materials and Methods

5.4.1 Synthesis and Characterisation

*The ligands (**L1-L4**) were synthesized by the collaborators from the TU München. The cages **C1-C4** were achieved by self-assembly. Experimental procedures for the synthesis, characterisation via NMR and mass spectrometry, IR and X-ray crystal. ^{1}H-NMR encapsulation studies performed by Dr. B. Woods.*[424]

5.4.2 Self-assembly evaluation by ^{1}H-NMR

To monitor the self-assembly of cages **C0-C4** from ligands **L0-L4** and to study the subsequent cisplatin encapsulation, ^{1}H-NMR studies were conducted directly in DMSO/H_2O with a capillary of $CDCl_3$ as presented in Figure 5.7**,** to use the fresh solution directly for further biological studies.

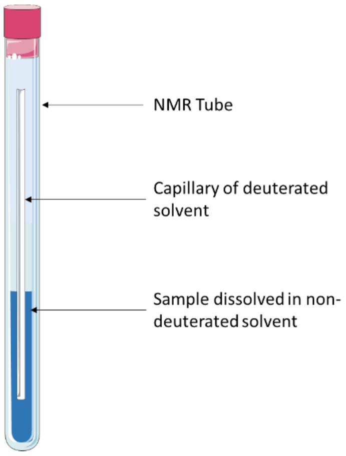

***Figure 5.7**: Setup for ^{1}H NMR studies using an NMR tube with a $CDCL_3$ capillary.*

Each cage was dissolved in 1 mL of DMSO (max 20%) in H_2O (stock solution 3 mM, 1 eq.) and added to a NMR tube containing a closed capillary of $CDCl_3$. Only in the case of cage **C0** the initial stock solution 3 mM was prepared in 100% DMSO due to poor solubility. ^{1}H NMR spectra were recorded before and after addition of 2 eq. of cisplatin to assess drug encapsulation.

5.4.3 Cell culture maintenance

Human malignant melanoma cancer cell line A375 and human lung cancer cell line A549 were obtained from ATCC and maintained in culture as described by the provider. The cells were cultured in DMEM (Dulbecco`s Modified Eagle Medium, Corning), supplemented with 10% fetal bovine serum (FBS, Eu-approved South

American Origin, Thermo Fisher Scientific) and 1% penicillin/ streptomycin (Gibco) at 37 °C and 5% CO_2.

5.4.4 Antiproliferative assays

Following confirmation of the encapsulation process, cage solutions were extracted from the NMR tube and further diluted for the cell viability studies (0.1 to 60 µM) in full DMEM medium. To avoid interference of the solvent in the antiproliferation studies, DMSO concentrations were limited to maximal 0.1%, except in the case of the least soluble cage **C0** (0.5%). In this latter case, control experiments with different concentration of DMSO were conducted to exclude possible effects on cells viability. Concentrations higher than 50 µM were not tested in A375 cells to again avoid toxic effects of DMSO. Dilutions of cisplatin (Sigma-Aldrich) ranging between 0.1 to 100 µM were used as reference compound from a 1 mM stock freshly prepared in aqueous solution prior each experiment. To evaluate the possible cell growth inhibition, cells were seeded in 96-well plates (Corning) at a concentration of 15000 cells/well and grown for 24 h in 200 µL complete medium. After 24 h incubation, old medium was removed and 200 µL of the compounds' dilutions were added to each well and the cells were incubated for additional 24 h. Afterwards, the medium containing compound was removed and 3-(4,5-dimethylthiazol-2-yl)-2,5-diphenyltetrazolium bromide (MTT, Fluorochem) in 10x PBS (Phosphate Buffered Saline, Corning) was added to the cells, at a final concentration of 0.3 mg/mL and incubated for 3-4 h to allow formation of violet formazan crystals. Then, the MTT solution was discarded and replaced with DMSO to dissolve the formed crystals. The optical density was quantified in quadruplicate at 550 nm using a VICTOR X5 multi-well plate reader (Perkin Elmer). Using the ratio of absorbance of treated to untreated cells, the percentage of surviving cells was calculated and the EC_{50} value (concentration causing 50% decrease in cell viability) determined via nonlinear fitting of cell viability vs [treatment] with GraphPad Prism software.

5.4.5 Statistics

Data is presented as mean ± SEM of at least three independent experiments. Statistical testing was performed using a Two Sample t-Test, to compare the [cisplatin$\subset$(**C0-3**)] treated samples with its control samples (treatment with cisplatin at the same concentration). A *p*-value of ≤0.01 was considered significant.

Chapter 6: Imaging metallacages in cancer cells - part I

This chapter is based on unpublished results as well as on the following paper:

Highly luminescent metallacages featuring bispyridyl ligands functionalised with BODIPY for imaging in cancer cells

Ben Woods, Daniel Döllerer, **Brech Aikman**, Margot N. Wenzel, Edward J. Sayers, Fritz E. Kühn, Arwyn T. Jones and Angela Casini

DOI: 10.1016/j.jinorgbio.2019.110781

Metallacages synthesis and characterisation performed by Dr. B. Woods and Mr. Daniel Döllerer.

6.1 Introduction

Metallacages, part of the supramolecular coordination complexes (SCCs) family, show great promise as tuneable drug delivery vehicles in the search for the next anticancer drug delivery system. [425] [426,427] Based on the concept of drug encapsulation driven by hydrophobic interactions between the cargo molecule and the host cavity or non-covalent interactions within the host cavity, metallacages of the $[Pd_2L_4]^{4+}$ type (L = 3,5-bis(3-ethynylpyridine)phenyl), inspired by the work of Therrien,[428,429] Crowley[430] and others,[426,431] were explored as novel drug delivery systems for the anticancer drug cisplatin, a well-known chemotherapeutical with severe side effects.[432] Specifically, the aim was to exploit the host-guest properties of the cages to encapsulate cisplatin, protecting it from speciation. NMR spectroscopy and X-ray diffraction studies confirmed encapsulation of two cisplatin molecules per cage unit.[432] Since the selected metallacages are non-toxic in both cells and tissues, they are very suitable as drug delivery vectors.[432] Additionally, in an effort to optimize targeting of metallacages to cancer sites, a method was developed to bioconjugate Pd_2L_4 cages to peptides based on amide bond formation between the cage-ligands and amino or carboxylic acid groups in the peptide chain.[433] In detail, peptidic ligands were selected for targeting of integrins overexpressed in cancer cells, as discussed in Chapter 5.[434] Promising results showed that cisplatin encapsulated in the bioconjugate targeted cages had a two-fold increase in cytotoxic potency in melanoma cells after only 24 h of incubation, whilst a reduced toxicity of cisplatin encapsulated in integrin-targeted metallacages was demonstrated using healthy tissues *ex vivo*.[434]

Despite showing great promise as cisplatin delivery vehicle, the mechanism of cancer cell uptake of $[Pd_2L_4]^{4+}$ cages is still not fully understood, preventing their optimisation as targeted drug vectors. Therefore, in order to study the cages` intracellular accumulation and sub-cellular localisation, introduction of luminescent moieties would allow analysis with fluorescence microscopy. This technique is preferred, due to its use of intact cells while avoiding complex cell fractionation steps which may lead to reduced analyte recovery, and lack of reproducibility.

The ligands used to build metallacages are highly luminescent due to their aromaticity but are subjected to quenching upon self-assembly due to the so-called ‘heavy metal’ effect.[432] Though the emissive properties of metallacages have been discussed,[435,436] examples of highly emissive $[Pd_2L_4]^{4+}$ cages are quite rare. Earlier attempts to *exo*-functionalize $[Pd_2L_4]^{4+}$ cages with luminescent moieties such anthracenyl groups[437] and Ru(II) polypyridyl ligands[438] met with different outcomes, as the first did not display sufficient luminescence due to the lowered probability of π-π* excitation upon conjugation of the fluorophore to the ligand scaffold,[437] and whilst the latter did achieve strong emission, excitation in the UV region was required,[438] which is not ideal for conventional microscopy analysis.

To address these issues, a new family of $[Pd_2L_4]^{4+}$ cages was developed, *exo*-functionalized with highly fluorescent boron dipyrromethene (BODIPY) scaffolds. BODIPYs are a well-known family of fluorescent dyes, applied for various purposes such as solar cells [439], photodynamic therapy[440] and imaging [441]. Utilising their characteristic fluorescence by conjugating the BODIPY moieties to metallacages would therefore enable intracellular detection with fluorescence microscopy. BODIPY ligand use has been reported in other supramolecular structures, such as the Ru(II) metalla-rectangles, but with the aim to develop cytotoxic agents instead of drug delivery systems. [442,443]

Here, three new BODIPY cages were synthesized by self-assembly, of which two feature an amide bond and the other two a 1,2,3-triazole ring to tether the cage bispyridyl scaffold to the fluorophore, characterised by various methods such as NMR spectroscopy, high-resolution mass spectrometry and fluorescence microscopy.

The stability of the cages was investigated in aqueous solution with UV-Vis spectroscopy and their interaction with physiologically relevant concentrations of glutathione (GSH), a common intracellular antioxidant with increased levels in cancer cells, was investigated by ^{1}H NMR spectroscopy. Finally, the antiproliferative effects of the cages were assessed in the human malignant melanoma A375 cell line to evaluate possible cytotoxic effects, while the uptake and sub-cellular distribution of selected metallacages were studied using both fluorescence wide-field as confocal microscopy.

6.2 Results & Discussion

6.2.1 Pd_2L_4 cages *exo*-functionalised with BODIPY

All complexes were synthesised by Dr. Ben Woods and Daniel Döllerer, and characterised by various methods, such as NMR spectroscopy and high-resolution mass spectrometry, adapting previously reported procedures.[444–446]

Briefly, the synthesis of the highly luminescent Pd_2L_4 metallacages was achieved by the conjugation of the BODIPY fluorophore to the bispyridyl ligand scaffold, formed either *via* amide bond formation or by copper catalysed azide-alkynyl cycloaddition (CuAAC) reaction depending on the functional groups of the fluorophore and ligand. Two types of green-emitting BODIPY fluorophores were produced, a carboxylic acid functionalised BODIPY (**B1**) and alkynyl functionalised BODIPY (**B2**) (Figure 6.1). The amine functionalised ligand (**L1**) was synthesised according to a previously reported procedure,[438] and adapted to form the azide functionalised ligand (**L2**). **L1** was used for coupling to **B1** to form cage precursor **L1** (Figure 6.1), as **L2** was coupled to **B2** to achieve cage precursor **L2**, respectively.

Finally, the BODIPY *exo*-functionalised Pd_2L_4 metallacages were formed *via* self-assembly by mixing 4 equiv. of ligand **L1** or **L2** with 2 equiv. of the Pd^{2+} precursor to achieve cage **C1.X** (X = BF_4^-, NO_3^-) or **C2.NO$_3$,** respectively (Figure 6.1).

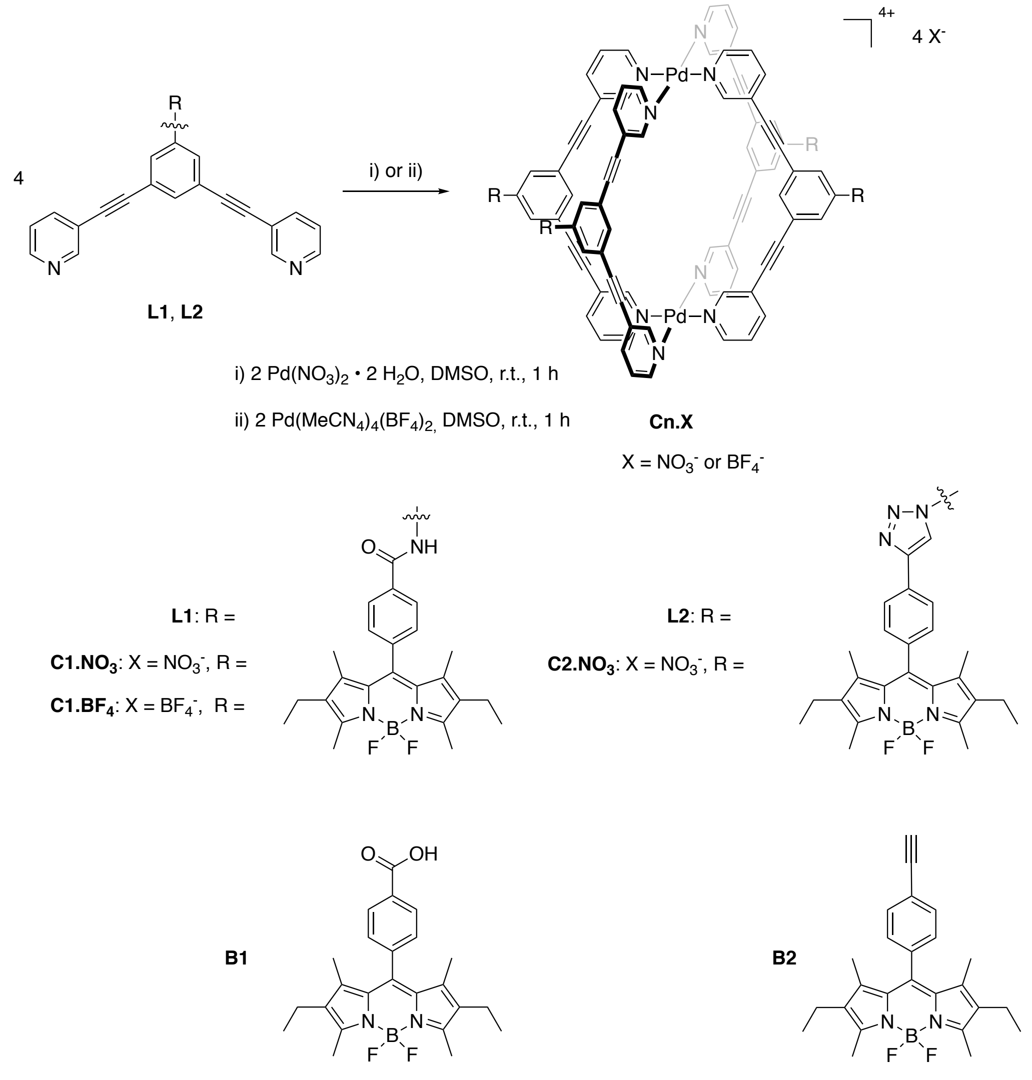

***Figure 6.1**: General synthetic schemes of $[Pd_2L_4]^{4+}$ cages and their respective ligands*

6.2.2 Photoluminescent properties and UV-Visible spectrophotometry stability studies

First, the emission properties and respective quantum yields of fluorescence (Φ_F) were investigated for the cages and their corresponding ligands using UV-Vis spectrophotometry and fluorescence spectroscopy. The results are presented in Table 6.1. The green-emitting fluorophores and ligands displayed excellent quantum yield values ranging between 72 and 76%, which interestingly, and at variance with previously reported metallacages *exo*-functionalised with different fluorophores,[437] were maintained quite well upon BODIPY-cage formation (Φ_F **C1.BF$_4$** = 64%, **C1.NO$_3$** = 50% and **C2.NO$_3$** = 70%, respectively). Introduction of an extension between the fluorogenic moiety and the ligand **L** using slightly longer 'linkers' in the scaffold design may have reduced the conjugation between the two systems preventing the quenching of the fluorescence upon self-assembly, with respect to previously reported cages.[437]

Table 6.1: *Photophysical data obtained by UV-Visible spectrophotometry and fluorescence spectroscopy for the BODIPY fluorophores (**B1**, **B2**), BODIPY functionalised bispyridyl ligands (**L1**, **L2**), and the fluorescent Pd$_2$L$_4$ metallacages (**C1.NO$_3$**, **C1.BF$_4$**, and **C2.NO$_3$**) in DMSO.*

Compound	**$\lambda_{max\ (Abs)}$ [nm]**	**ε_{max} [M^{-1} cm^{-1}]**	**$\lambda_{max\ (Em)}$ [nm]**	**ϕ_F [%]^a**
B1	525	53 300	544	72
B2	525	72 700	543	75
L1	290, 525	66 600	544	76
L2	525	50 000	543	74
C1.NO$_3$	291, 527	42 100	544	50
C1.BF$_4$	291, 525	111 000	544	64
C2.NO$_3$	291, 525	160 000	543	70

[a] Reference standard for QY assessment was Rhodamine 6G (φ = 94% in degassed EtOH at room temperature)[327,328]

Next, the stability of the metallacages **C1.BF$_4$**, **C1.NO$_3$** and **C2.NO$_3$** was studied by UV-Visible spectrophotometry prior further biological testing. Tests were performed in both water and 1x PBS buffer (pH 7.4) to mimic biologically relevant conditions. The absorption spectra of the four cages were measured between 250 and 800 nm at regular time intervals during 24 h at room temperature. An example of **C1.BF$_4$** is shown in Figure 6.2.

All cages feature two main band at ca. 300 nm and ca. 530 nm, the latter contributed to the BODIPY-fluorophore, as shown in Figures 6.2-4. **C1.BF$_4$**, **C1.NO$_3$** and **C1.NO$_3$** were completely stable in water over 24 h (Figures 6.2-4, right). Additional testing in 1x PBS solution (pH 7.4) of metallacages **C1.BF$_4$** and **C1.NO$_3$** revealed a marked reduction of the two absorption bands was observed at 4 h incubation and continued over the 24 h period, forming a precipitate ((Figures 6.2 and 6.3, left). This was partly restored to the original absorption spectrum upon shaking of the cuvette. **C1.BF$_4$** and **C1.NO$_3$** were deemed sufficiently stable for further *in vitro* experiments to study compound cell uptake.

It should be noted that a number of factors contribute to the solubility of metallacages, such as the properties of the main ligand scaffolds, the metal ion, as well as the type of counter ion balancing the cage overall positive charge. It is therefore difficult to establish what causes cage precipitation and/or instability in solution in such a complex interplay of elements. Furthermore, it should be noted that the BODIPY-ligand system also presents some issues of solubility/stability in buffered solution, most probably due to the hydrolysis of the B-F bond. Certainly, from the obtained UV-visible data, the presence of other anions in the buffer (pH 7.4) favours the observed spectra changes, and formation of a precipitate in solution.

The spectrum of metallacage **C2.NO$_3$** in PBS solution underwent even more pronounced reduction of intensity after only 2 h (Figure 6.4), and any attempt to re-dissolve the precipitate would not restore the original signal intensity. Therefore, Pd_2L_4 metallacage **C2.NO$_3$** was not used for further biological characterisation due to its poor solubility in physiological media. The enhanced instability of the **C2.NO$_3$** cage with respect to the BF_4^- derivatives may be attributed to possible increased encapsulation of the nitrate ion into the cavity,[136] as well as to its higher coordinating affinity towards the Pd(II) centres.

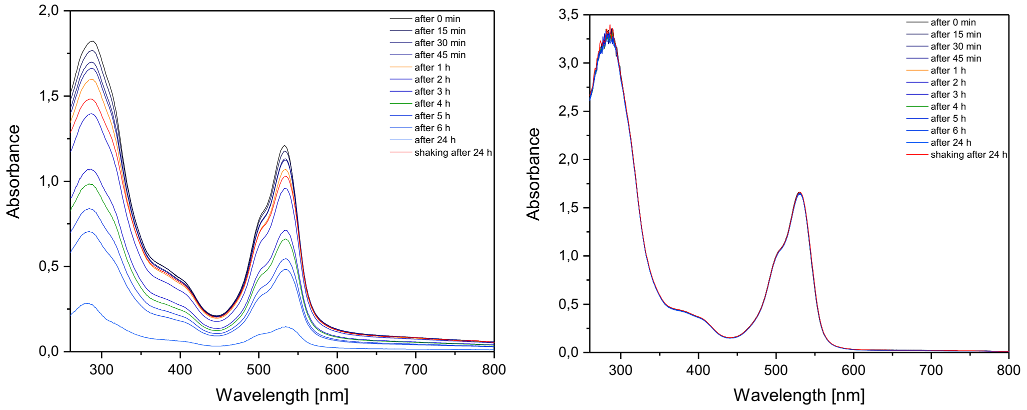

Figure 6.2*: UV-Visible spectra of* ***C1.BF$_4$*** *[25 x 10^{-6} M] in 1x PBS (left); and in water (right) recorded over 24 h (not stirred) and shaken cuvette afterwards (red line). Adapted from ref* [447].

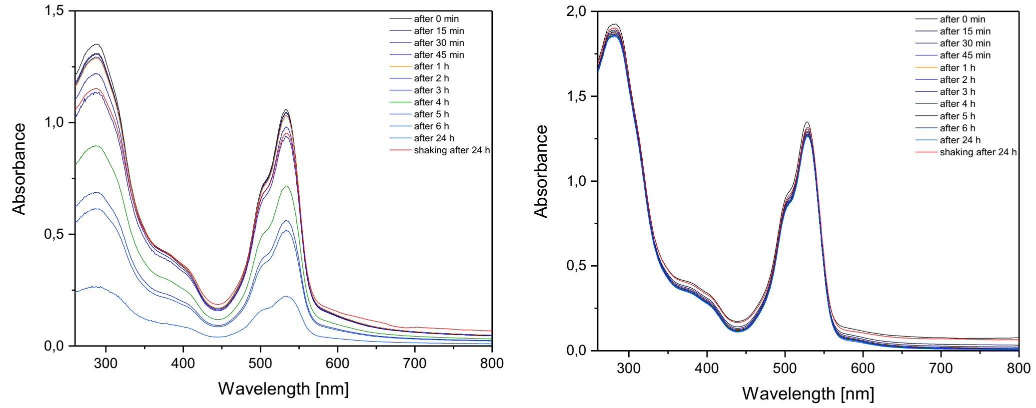

Figure 6.3*: UV-Visible spectra of* ***C1.NO$_3$*** *[55 x 10^{-6} M] in 1x PBS (left); and in water (right) recorded over 24 h (not stirred) and shaken cuvette afterwards (red line). Adapted from ref* [447].

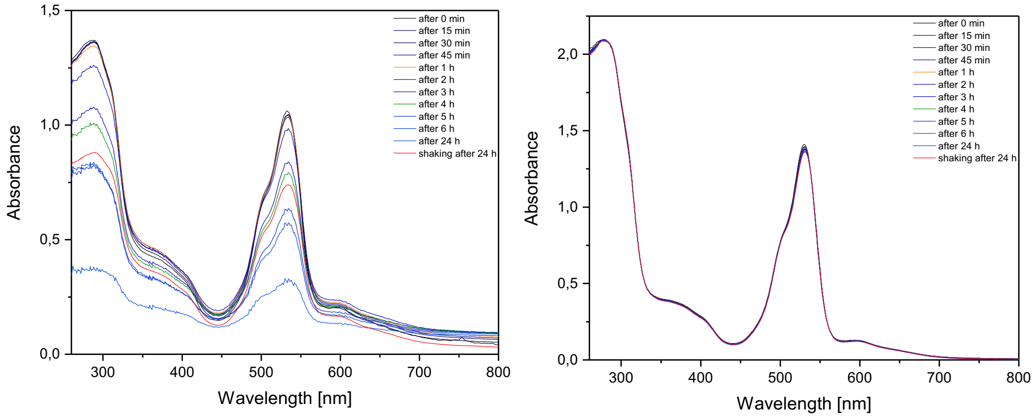

Figure 6.4*: UV-Visible spectra of* ***C2.NO$_3$*** *[86 x 10^{-6} M] in 1x PBS (left); and in water (right) recorded over 24 h (not stirred) and shaken cuvette afterwards (red line). Adapted from ref* [447].

6.2.3 Interactions with GSH

To evaluate the stability of the metallacages in physiologically relevant conditions, **C1.BF$_4$** was incubated with glutathione (GSH) and monitored by NMR spectroscopy. GSH is a nucleophilic tripeptide, abundantly present throughout the body and among other things, involved in detoxification of xenobiotic and endogenous compounds, scavenging oxidants. Plasma concentrations of 0.3 - 0.5 mM have been reported in humans, and though cell types can express quite a large range, the average intracellular concentration was 1-2 mM.[448,449] Excess GSH concentrations have been reported to induce disassembly in Pd^{2+} and Pt^{2+} metallacages.[450]

Specifically, GSH was added to a solution of cage **C1.BF$_4$** in DMSO-d_6:D$_2$O (9:1) to achieve a 2 mM GSH concentration. ^{1}H NMR spectra were recorded over time over 18 h (Figure 6.5) and compared to spectra obtained prior GSH addition of **L1** and **C1.BF$_4$** to compare. By comparing the integral values of peaks for both ligand and cage, an estimate can be made regarding the dissociation. Indeed, upon addition of GSH, a disassembly of metallacage can be observed after t = 5 min as shown by the appearance of peaks characteristic of its precursors **L1**. Interestingly, ca. 30% of the C1.BF$_4$ remains stable over time, needing an additional excess of GSH to completely disintegrate (Figure 6.5), supporting the hypothesis that the cage can partly remain intact in the cytosol.

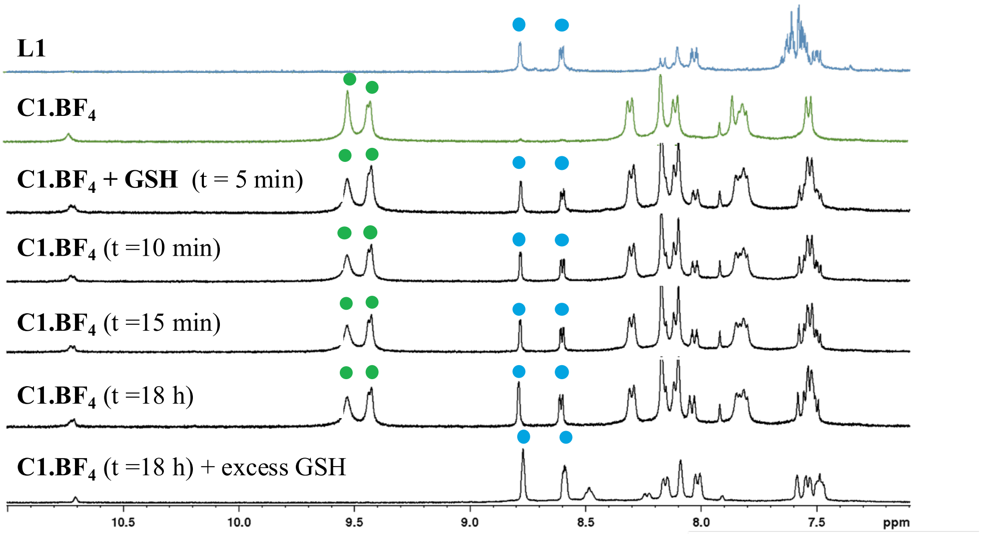

***Figure 6.5**: Stacked ^{1}H NMR spectra of ligand **L1** (top) and of the corresponding metallacage **C1.BF$_4$** (second trace from top) in 9:1 ratio of DMSO-d_6: D$_2$O, in the presence of 2 mM GSH over time. At 18 h, a further addition of excess GSH was administered to achieve complete cage dissociation (bottom spectrum). Blue dots indicate ligand signals, and green for cage. Adapted from ref*[447].

6.2.4 Encapsulation of cisplatin

Following a previously established method, encapsulation of cisplatin within the Pd_2L_4 metallacages was demonstrated with the use of ^1H NMR spectroscopy with DMF-d_7 as solvent by Dr. B. Woods.[389,451] Briefly, metallacages **C1.BF$_4$** and **C1.NO$_3$** were dissolved in DMF-d_7 and their ^1H NMR spectra were recorded recorder prior and after addition of the equivalent of two molecules of cisplatin vs one molecule of cage and compared. Chemical shifts before and after cisplatin addition were compared. Indeed, for both cages, chemical shifts changes were observed for the same three proton signals: two signals corresponding to the protons facing the internal cavity (H_a and H_e), as well as the signal of the *exo*-facing proton (H_b), in line with previous reported work.[451] Specifically, for **CG1.BF$_4$** vs (cisplatin)$_2$⊂**CG1.BF$_4$**, a downfield shift was observed for cavity facing H_a and H_e of +0.03 ppm and +0.08 ppm, respectively, with a broadening of signal suggesting interaction of cisplatin with the cage. However, for **CG1.NO$_3$** vs (cisplatin)$_2$⊂**CG1.NO$_3$**, a small upfield shift was observed for H_a and H_e of -0.02 ppm. This might be contributed to the NO_3^- counterion, which has been reported to undergo encapsulation in P_2L_4, whereas BF_4^- does not.[136,451] Presence of the negatively charged counterion as guest would impose a more downfield shift, compared to the otherwise neutral solvent molecules. Therefore, upon cisplatin addition, displacement of the NO_3^- counter ion by the cisplatin guest would show a slight upfield shift of the cavity facing protons.

6.2.5 Antiproliferative effects

To evaluate the antiproliferative effects of free cisplatin versus cisplatin encapsulated in **C1.BF$_4$**, the complexes were screened against the human malignant melanoma A375 cell line. Studies were performed with 24 h incubation, since the free metallodrug is known to be poorly active in this time frame. This also allowed for microscopy analysis at suitable metallodrug concentration levels (see Methods for details). Instead of a classical MTT assay, the antiproliferative effects were determined with a CellTiter-Blue® viability assay, to avoid bias introduced by the fluorophore, which could potentially underestimate the effect. Previous studies with non-functionalised NH_2-cage and corresponding ligand illustrated the non-toxic effect of the metallacage (EC_{50} >40 uM). Introduction of the fluorescent BODIPY-moiety was hypothesized not to induce a cytotoxic factor onto the cage construct. Indeed, both *exo*-functionalised metallacages **C1.BF$_4$** & **C1.NO$_3$** and their corresponding ligand precursor were non-toxic at the highest tested concentration ($EC_{50} > 50$ µM) as shown in Table 6.2. The same experiment was performed for encapsulated cisplatin [(cisplatin)$_2$⊂**C1.BF$_4$**], compared to free cisplatin. As these cage systems are not specifically targeted to human cancer cells, we did not expect to observe the same increase in the anticancer potency of cisplatin as observed for the previously published integrin-targeted metallacages.[424] In line with our expectations, the encapsulated cisplatin did not show any significant variation of the antiproliferative activity with respect to free cisplatin (Table 6.2). To confirm that the absence of cytotoxicity is inherent to the complexes and not the result of limited cell uptake, fluorescence microscopy was applied as described in the next section.

***Table 6.2**: Antiproliferative activity (EC_{50} values) of ligand, different cage and cage:cisplatin (1:2) formulations against human A375 cells after 24 h incubation, compared to cisplatin.*

Compound	**EC_{50} (µM)[a]**
L1	> 50
C1.NO$_3$	> 50
C1.BF$_4$	> 50
(cisplatin)$_2$⊂**C1.BF$_4$**[b]	29 ± 2
cisplatin	33.9 ± 2.9

[a] Data is presented as mean ± SEM of at least three independent experiments.

[b] The EC_{50} is calculated with respect to the concentration of free cisplatin.

6.2.6 Uptake and cellular localisation studies

In an effort to elucidate the intracellular localisation or accumulation of the BODIPY-cages **C1.BF$_4$** and **C1.NO$_3$** and their respective ligand precursor **LB1**, fluorescence microscopy was used. The cages/ligand (5 µM) were incubated with A375 cells for 2 h at 37 °C, fixed and visualised by confocal laser scanning microscopy (CLSM). An advantage of CLSM over conventional widefield microscopy besides the overall improved contrast and definition, is the option to provide a multi-dimensional view by compiling a linear array of 2D sections for a 3D model.[452] Images are presented in Figure 6.6. All complexes show no presence in the cell nuclei to any significant extend. **LB1** was observed in punctate structures and as diffuse labelling, and it seems that both cages, **C1.NO3** and **C1.BF4**, were internalised independently of their respective counter ion. There was a labelling of vesicular structures that were particularly prominent for **C1.BF4**, with **C1.NO3** enriched in a juxtanuclear region. To validate intracellular accumulation opposed to aggregation and accumulation on the cell surface, which might occur due to the lipophilic nature of the BODIPY-derivative[453], a z-section analysis of cell treated with **C1.BF4** and **LB1** was performed (Figure 6.7). The intracellular localisation was confirmed, and both cage as ligand do not reach the cell nuclei. It must be noted that from these images, it is impossible to determine if the cages remain intact or are disintegrated once internalised. Nonetheless, the specific sub-cellular distribution observed for these particular BODIPY-cages is unexpected, since other studies with BODIPY-containing metal-based scaffolds showed that they internalise into more non-descript diffuse structures,[454] rather than selectively accumulating in vesicles as particularly observed for **C1.BF4**.

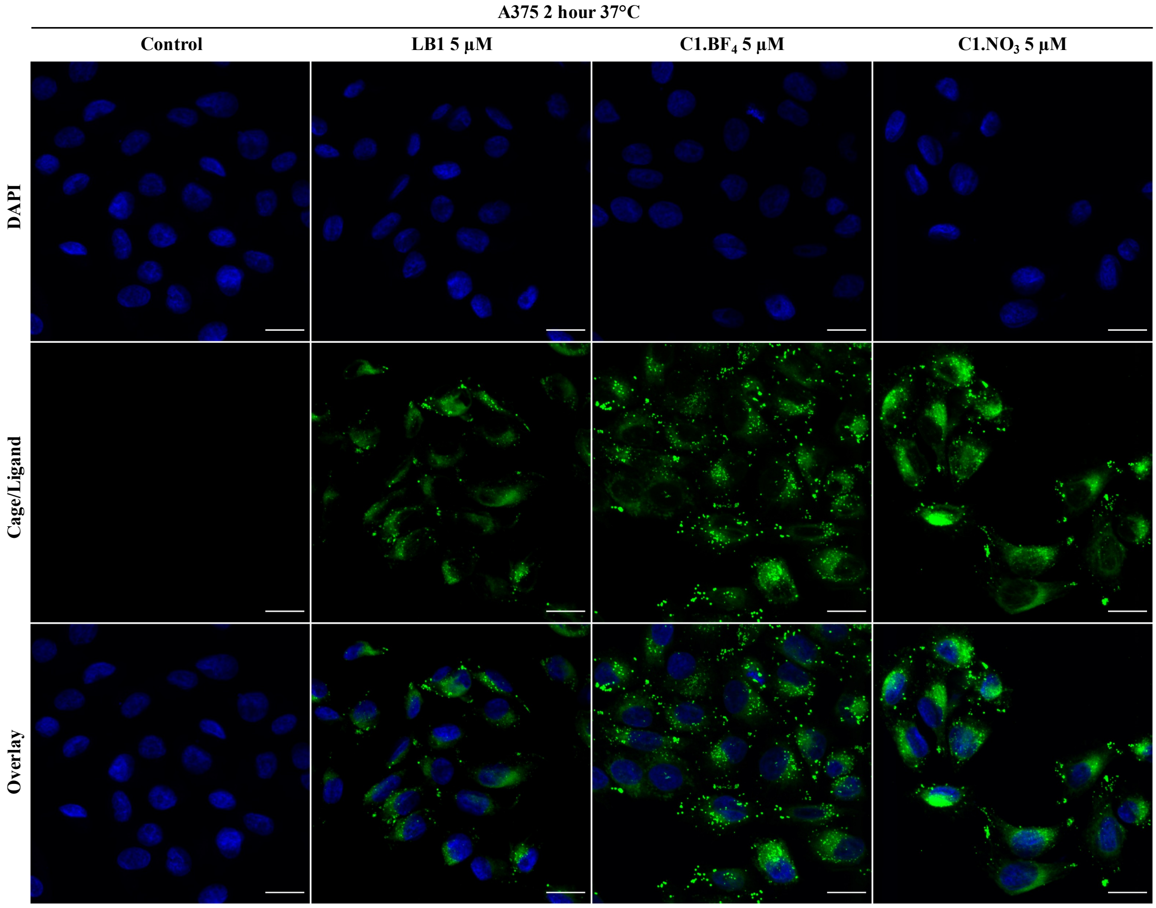

***Figure 6.6**: Confocal Laser Scanning Microscopy (CLSM) Images of fixed human A375 melanoma cells pre-treated with ligand **LB1** or cages **C1.BF$_4$** and **C1.NO$_3$** for 2 h at 37 °C. Counter staining of nucleus with DAPI. Scale bar represents 20 µm. Data represents maximum projection images.*

A) **C1.BF$_4$**

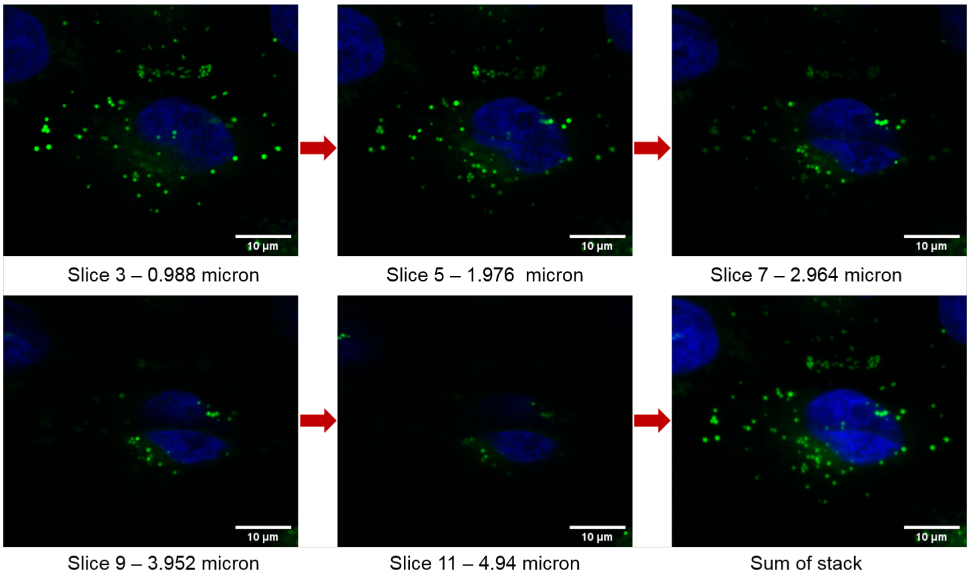

B) **LB1**

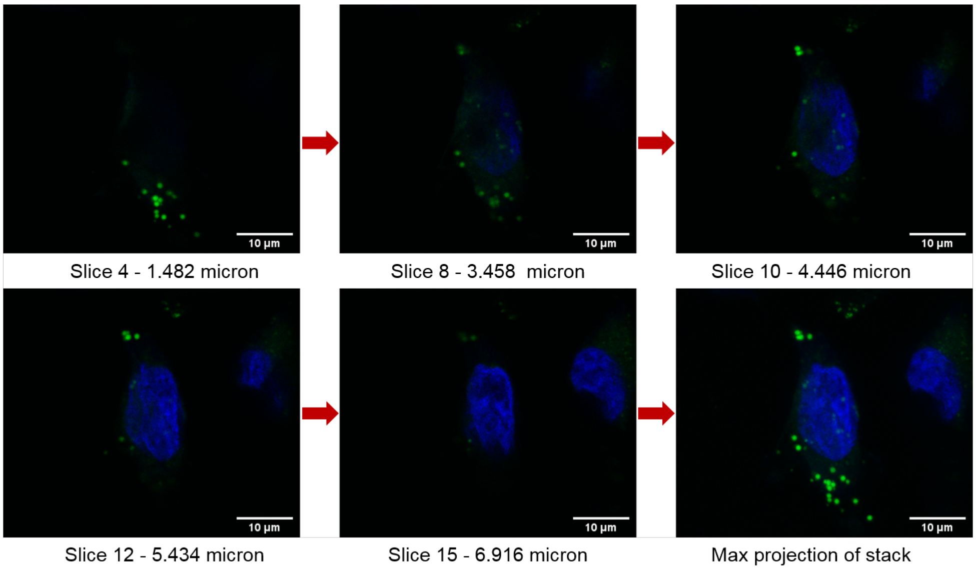

Figure 6.7*: CLSM images of a representative fixed A375 melanoma cell incubated for 2 h with* ***A)*** *5 µM* ***C1.BF$_4$*** *or* ***B)*** *5 µM* ***LB1****. Counterstaining with DAPI. Different z-slices from top to bottom are shown as well as the sum of stack/maximum projection of stack. Scale bar represents 10 µM.*

Finally, an attempt was made to investigate the mode of uptake, by exposing human melanoma A375 cells to different temperatures during a 2 h incubation with 5 µM complex (**C1.BF$_4$**, **LB1** and **B1**). By performing the same experiments at either 37 or

4 °C, a distinction can be made between active uptake requiring energy, and passive energy independent diffusion. Figure 6.8 demonstrate that no fluorescence signal can be detected in cells incubated at 4 °C, excluding a passive mode of uptake through the plasma membrane, pointing towards endocytosis instead.

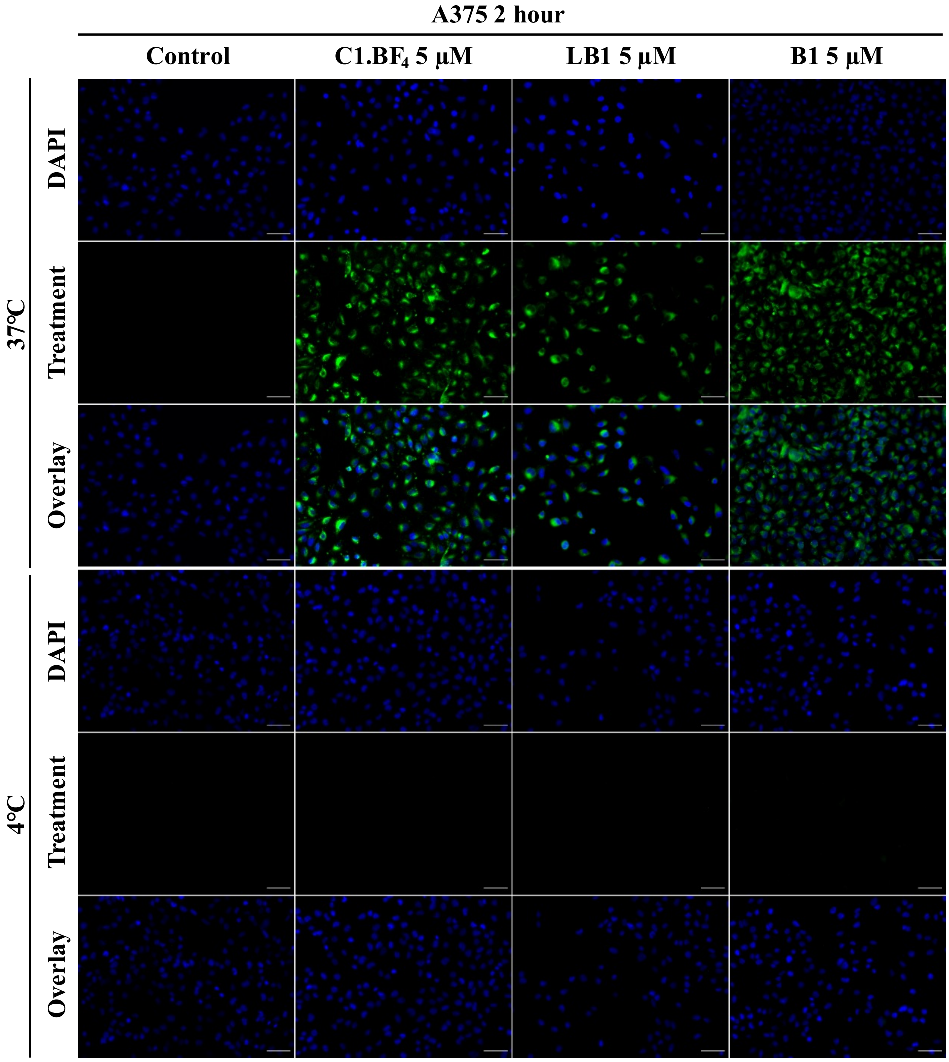

***Figure 6.8**: Fluorescence widefield microscopy (Zeiss) enhanced images of fixed cells comparing control to samples incubated with 5 µM of **C1.BF$_4$**, **LB1** or **B1** for 2 h at 37 °C (top three rows) or 4 °C (bottom three rows). Scale bar represents 50 µm.*

6.3 Conclusions

Three new Pd_2L_4 metallacages featuring 3,5-bis(3-ethynylpyridine)phenyl ligands *exo*-functionalised with BODIPY units have been reported here. The cages showed remarkable luminescent properties with quantum yields of 50-70% and excitation wavelength in the visible region (ca. 540 nm) making them suitable for *in vitro* imaging. Stability studies by UV-visible spectroscopy were performed to study the cages in aqueous solution and for their reactivity in the presence of physiologically relevant concentration of glutathione (GSH). Of note, cage **C1.NO$_3$** dissociated only partially in the presence of this cytoprotective agent. The encapsulation of the anticancer drug cisplatin as guest in the metallacages were studied with ^{1}H NMR spectroscopy, confirming that up to 2 equiv. of cisplatin can be encapsulated in a cage molecule. Evaluation of cytotoxicity of **C1.BF$_4$** and **C1.NO$_3$** in human melanoma A375 cells showed no antiproliferative effects, highlighting their suitability as non-toxic drug delivery vehicles. Additional microscopy studies to achieve a preliminary indication regarding cage uptake and identification of sub-cellular localisation in cancer cells were performed using both wide field and confocal fluorescence microscopy. Remarkably, the cages are subjected to active endocytic transport, prior to accumulation in intracellular vesicles.

Future studies should focus on the identification of the nature of the **C1.BF$_4$** labelled structures to determine if they are early endosomes, late endosomes/lysosomes or possibly other vesicular structures. It will also be important to determine how this localisation of the cage affects the cisplatin release. Further studies are necessary to exclude cisplatin release prior uptake of the host-guest system.

6.4 Materials and Methods

6.4.1 Synthesis

All complexes were synthesised by Dr. Ben Woods and Daniel Döllerer, and characterised by various methods, such as NMR spectroscopy and high-resolution mass spectrometry, adapting previously reported procedures.[444–446]

6.4.2 Quantum Yield Determination

Quantum yield of fluorescence was calculated in comparison to a reference standard (Rhodamine 6G in degassed ethanol, φ = 94% at room temperature). UV-Visible absorption spectra were recorded on a Cary 60 UV-Vis spectrometer from *Agilent Technologies*. Emission spectra were recorded on a Cary Eclipse Fluorescence Spectrophotometer from *Agilent Technologies*. The selected fluorophore was dissolved in degassed DMSO to a concentration corresponding to UV-Visible absorbance 0.8 A.U. (λ(max) = 523 - 535 nm; 25 °C). The solution was transferred to a fluorescence spectrophotometer and an emission spectrum was recorded (excitation wavelength 595 nm).

6.4.3 Stability studies by UV-Visible Spectroscopy

UV-visible absorption spectra to investigate the stability of the metallacages in solution were recorded on a Cary 60 UV-Vis spectrometer from *Agilent Technologies*. For each compound, stock solutions at a concentration of 3×10^{-3} M were prepared. An aliquot was diluted either with 1x PBS (pH 7.4) or deionised water and the UV-Vis spectra measured at different times immediately after dilution at room temperature over 24 h. The cuvette was then shaken, and another spectrum recorded, to determine if the compound was altered during the 24 h or if the reduction in absorption was only due to precipitation.

6.4.4 Cell culture maintenance

Human malignant melanoma cell line A375 was obtained from ATCC and maintained in culture according to provider instructions. Cells were cultured in a humidified atmosphere at 37 °C and 5% CO_2 using DMEM Dulbecco's Modified Eagle Medium (DMEM, 4.5 g/L glucose, Corning, Thermo Fischer Scientific) supplemented with 10% fetal bovine serum (FBS, Eu-approved South American Origin, Thermo Fisher

Scientific) and 1% penicillin/streptomycin (Gibco) and passaged when reaching confluence.

6.4.5 Antiproliferative assay

To evaluate the inhibition of cell growth, 96-well tissue culture-treated plates (Corning) were seeded in a concentration of 15000 cells/well with 200 µL full medium. Working solutions of ligand and cage samples were prepared in the required concentration by diluting fresh stock solutions (5×10^{-3} M in DMSO) of the corresponding compound in aqueous complete DMEM medium accordingly. Dilutions (1 mM stock) of reference compound cisplatin (Sigma-Aldrich) were freshly prepared in aqueous solution and mixed with the metallacages prior each experiment. Cage formation and cisplatin encapsulation were confirmed by ^{1}H NMR spectroscopy as previously reported. Following the initial 24 h incubation required for cell adhesion, cells were incubated for an additional 24 h with 200 µL of the compounds' dilution per well. Afterwards, 20 µL/well of CellTiter-Blue® reagent was added to the assay plate, shaken 10 sec and incubated for 4 hours at 37 °C and 5% CO_2 (Figure). Fluorescent intensity ($531_{Ex}/595_{Em}$ nm) from each well was quantified in quadruplicates for each experiment using a multi-well plate reader (VICTOR X5, Perking Elmer). The percentage of surviving cells was calculated, using GraphPad Prism software, from the ratio of fluorescence intensity of treated to untreated cells, corrected for the interfering fluorescence of the BODIPY. The EC_{50} value for each compound was calculated as the concentration showing 50% decrease in cell growth, when compared to controls, using a nonlinear fitting of [concentration] vs response. Data is presented as mean ± SEM of at least three independent experiments.

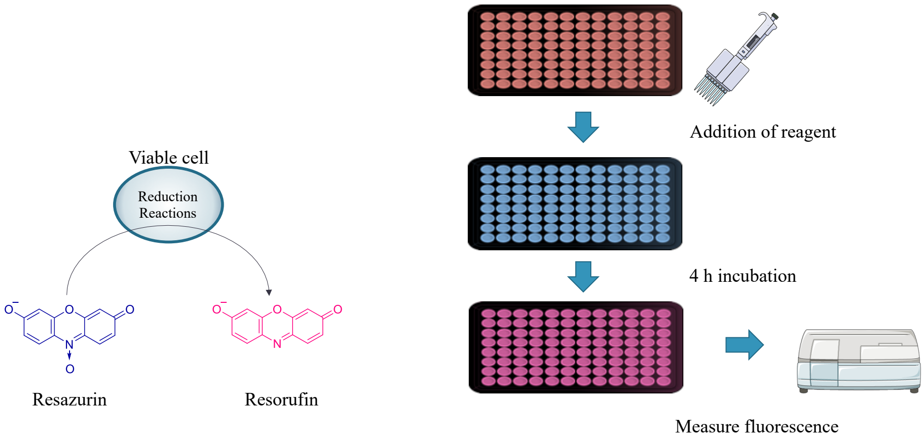

__Figure 6.9__: Scheme representing CellTiter-Blue® assay steps

6.4.6 Fluorescence microscopy assays

Round glass coverslips (Ø 13mm, VWR) sterilised by UV-light were inserted in 24-well tissue culture- treated plates (Corning). Cells were seeded at a concentration of 50.000 cells/well and incubated at 37 °C under humidified atmosphere with 5% CO_2 for 48 h. The medium was discarded and fresh medium containing 5 μM of either cage or ligand was added. Following 2 h of incubation at either 37 °C under tissue culture conditions or 4 °C in the fridge, the glass coverslips were removed from the wells, washed 4x with 1x Phosphate Buffered Saline (PBS, Corning) and fixed with 4% formaldehyde (Alfa-Aesar) for 20 min at room temperature (r.t.). The coverslips were washed 3x with 1x PBS and incubated for 1 min with 40 μL 1:1000 from a 1 mg/mL stock solution of 4',6-Diamidino-2-phenylindole dihydrochloride (DAPI, Sigma-Aldrich/ MERCK) at r.t.. After washing the coverslips thrice with 1x PBS they were mounted on glass microscope slides (VWR) using Mowiol® 4-88 (Sigma-Aldrich). Fluorescence images were obtained using either a Zeiss Axio Vert.A1 epifluorescent microscope or a Leica SP5 confocal laser-scanning microscope.

For the widefield microscope (Zeiss), four LD A-Plan objectives were available (5x/0.15 Ph1, 10x/0.25 Ph1, 20x/0.35 Ph1 and 40x/0.55 Ph1). Samples were excitated with a LED fluorescence module equipped with filter cube for UV (385 nm), Blue (475 nm), Green (555 nm) and Red (630 nm). Images captured with AxioCam MRm (Zeiss).

For confocal imaging, two laser lines were used: 405 Blue Diode (excitation wavelength 405 nm, laser intensity 30%) for DAPI and Argon 514 (excitation wavelength 514 nm, laser intensity 30%) for the complexes, captured sequentially to avoid bleedthrough. A HCX PL APO 63x 1.4 NA oil immersion objective was used for all images with Leica Type F immersion oil. Whole cell Z-acquisition was conducted 0,3 μm from bottom of imaging dish or well with steps of 0,5 μm (objective step limited to > 236 nm). Single slice images were taken ~ 1,5 μm above coverslip. Captured XYZ images from the Leica SP5 and "XY" images from the Zeiss were analysed using ImageJ.[455] All images were captured under the same settings within each experiment and treated equally following acquisition.

Chapter 7: Imaging metallacages in cancer cells - part II

Metallacages synthesis and characterisation performed by Dr. B. Woods and Daniel Döllerer.

7.1 Introduction

Supramolecular coordination complexes (SCC) have recently received increasing attention for their potential as drug delivery systems of various cytotoxic agent such as anticancer drugs like cisplatin, however there is still limited information on their mechanism of uptake and intracellular localisation. SCC such as Pd_2L_4 metallacages or metallacycles are suggested to pass across the cell membrane in an active fashion via endocytosis.[456,457] Our previously reported results (Chapter 6) illustrated the efficient, active uptake of two promising BODIPY *exo*-functionalised metallacages (**C1.BF$_4$** and **C1.NO$_3$**) into the cytosol and accumulated in spherical vesicles, whilst no visible fluorescence in the nucleus was evidenced. It was therefore hypothesised that these metallacages are subjected to active, possibly endocytic, transport, prior to accumulation in spheric intracellular vesicles.

Endocytosis is a general term describing the mechanisms that allows for cellular uptake of endogenous and exogenous materials *via* vesicle formation which due to their nature (size, shape, polarity e.a.) are unable to cross the bilipid cell membrane by passive diffusion or channel mediated passage. As such, three mayor routes of the cellular endocytosis pathway can be described, namely phagocytosis, (macro)pinocytosis and receptor-mediated endocytosis. Phagocytosis[458], engulfment of particles and nutrients > 5 μm and (macro)pinocytosis[459], internalisation in bulk of solute molecules and extracellular fluid, mediate both non-selective uptake, whereas receptor-mediated endocytosis is the result of a targeted cell entry. Macropinocytosis in particular seems interesting as an effective mechanism for intracellular drug delivery.[460] Receptor mediated cell entry (guided by integrin targeting[424] as discussed previously in Chapter 5) might not be the mechanism of membrane transport for the fluorescent labelled cage and ligand, as they are to our knowledge not similar to a known receptor substrate. Once internalised, vesicles carrying cargo will be subjected to recycling or degradation depending on their origin.[461] Some vesicles resulting from receptor-mediated uptake for example are translocated to endosomes to enable membrane receptor recycling, whereas other vesicles enter into the late endosome/lysosome pathway resulting in degradation of internalised load (Figure 7.1).

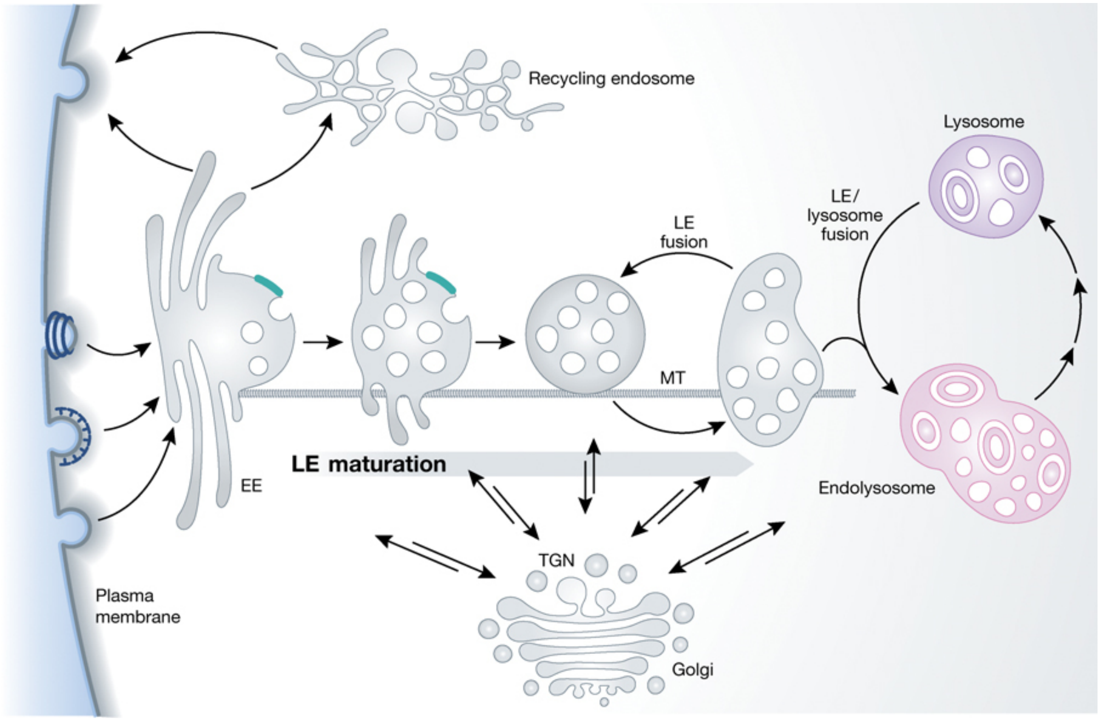

Figure 7.1*: Endosome/Lysosome maturation system. Following cargo uptake, endocytic vesicles deliver their content and membrane to the early endosomes (EE) in the peripheral cytoplasm. Next, after cargo accumulation and support recycling back toward the plasma membrane, conversion of EE to late endosomes (LE) occurs, moving along microtubule (MT) towards the perinuclear space. Fusion with lysosomes follows after LE maturation, producing an endolysosome in which active degradation of cargo occurs. Finally, the endolysosome is converted to a lysosome. Reprinted from "Endosome maturation" by Huotari, J. Helenius A. EMBO J, Volume: 30, Issue: 17, Pages: 3481-3500, First published: 31 August 2011, DOI: (10.1038/emboj.2011.286). Copyright (2011) by John Wiley and Sons. Reproduced with permission.*[461]

In an effort to further elucidate the mode of cage uptake and sub-cellular localization using fluorescent microscopy, two new BODIPY *exo*-functionalised cages are presented (Figure 7.2) with an improved stability profile, addressing the solubility limitations in biologically relevant medium.

7.2 Results and Discussion

7.2.1 Pd_2L_4 cages exo-functionalised with BODIPY

All complexes were synthesized and characterized by Dr. Ben Woods and Daniel Döllerer, using various methods including ^{1}H, ^{13}C, ^{11}B *and* ^{19}F *NMR spectroscopy and high-resolution mass spectrometry, in line with previously reported studies.*[139,424,462]

The synthesis of highly luminescent Pd_2L_4 metallacages was achieved by the conjugation of the BODIPY fluorophore to the bispyridyl ligand scaffold, formed *via* amide bond formation. The carboxylic acid functionalized ligand **L1** was synthesised according to a previously reported procedure.[438] The BODIPY fluorophore was synthesized by adapting a previously reported method to produce the amine functionalized BODIPY **G1** (Figure 7.2). **L1** was used for coupling to **G1**, forming cage precursor **LG1** (Figure 7.2). Finally, the BODIPY *exo*-functionalised Pd_2L_4 metallacages were formed *via* self-assembly by mixing 4 equiv. of ligand **LG1** with 2 equiv. of the Pd^{2+} precursor to achieve cage **CG1.X** (X = BF_4^-, NO_3^-), respectively (Figure 7.2).

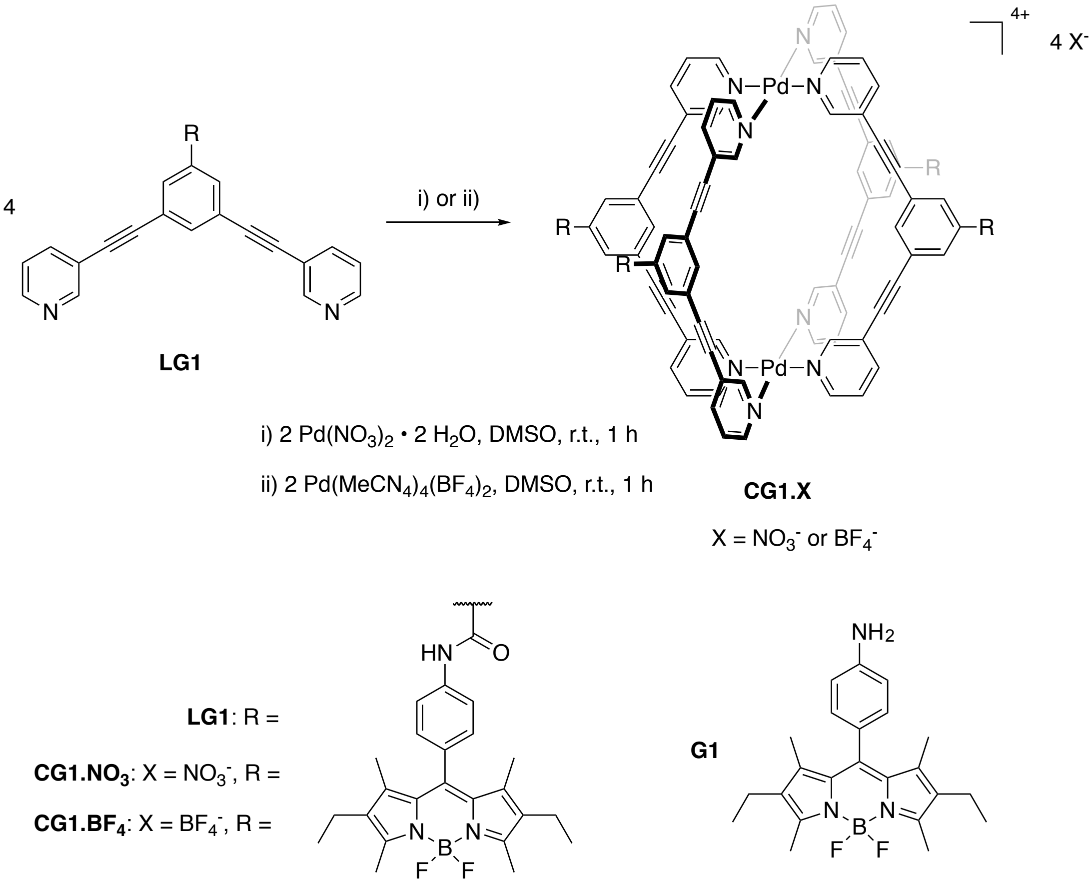

Figure 7.2: General synthetic schemes of $[Pd_2L_4]^{4+}$ *cages and respective ligands.*

7.2.2 Photoluminescent and Absorption properties

Firstly, the emission properties and quantum yields of fluorescence (ϕ_F) of the new cages (**CG1.X**), corresponding ligand (**LG1**) and BODIPY fluorophore (**G1**) were investigated using UV-Visible spectrophotometry and fluorescence spectroscopy. The results are presented in Table 7.1 (corresponding graphs in Appendix C, Figures S48-S50). Notably, the amine functionalized BODIPY fluorophore **G1** quantum yield is quite low (6%) compared to previously discussed fluorophore **B1** (Chapter 6, ϕ_F = 72%), despite only minor chances to the scaffold. However, coupled to the carboxylic acid bipyridyl ligand, the resulting **LG1** displayed an excellent quantum yield value of 82%. What's more, the highly luminescent nature was maintained upon BODIPY-cage formation. Therefore, the low quantum yield might be the result of a photoinduced electron transfer quenching upon excitation due to the presence of the amine group, which donor properties are lost upon binding.[463,464]

***Table 7.1**: Photophysical data acquired by UV-visible spectrophotometry and fluorescence spectroscopy for the BODIPY fluorophore (**G1**), BODIPY functionalised bispyridyl ligand (**LG1**), and the fluorescent Pd_2L_4 metallacages (**$CG1.BF_4$** & **$CG1.NO_3$**) in DMSO.*

Compound	$\lambda_{max\ (Abs)}$ **[nm]**	ε_{max} **[M^{-1} cm^{-1}]**	$\lambda_{max\ (Em)}$ **[nm]**	ϕ_F **[%]**[a]
G1	525	61 500	539	6
LG1	290, 525	80 000	541	82
$CG1.BF_4$ / $CG1.NO_3$	290, 525	228 600	541	80

[a] Reference standard for QY assessment was Rhodamine 6G (φ = 94% in degassed EtOH at room temperature).[327,328]

Afterwards, the stability of the metallacages in water and phosphate buffered saline (PBS, pH 7.4) was studied by UV–Visible spectrophotometry. As shown in Figure 7.3, the absorption spectra of **$CG1.NO_3$**, featuring two main bands at ca. 300 and 530 nm, was completely stable in water over 24 h (exact same behaviour for **$CG1.BF_4$**, not shown). The metallacages were also sufficiently stable in PBS solution (pH 7.4) although marked reduction of the two absorption bands was observed at 3 h incubation and continued over the 24 h period. While over 24 h a precipitate was formed in solution, shaking of the cuvette partly restored the original absorption spectrum.

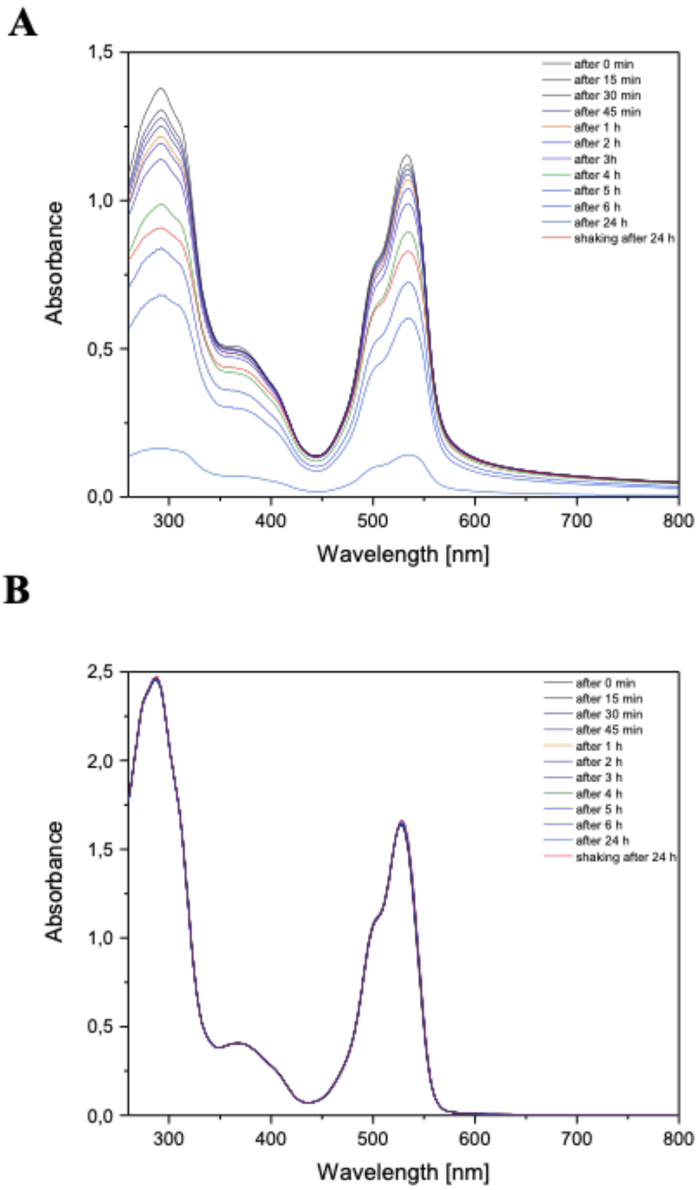

***Figure 7.3**: UV-Visible spectra of **CG1.NO$_3$** [15 x 10^{-6} M] in **A**) 1x PBS and in **B**) water recorded over 24 h and shaking of cuvette afterwards.*

7.2.3 **CG1.BF$_4$** interaction with GSH

Pd^{2+} metallacages have been reported to undergo disassembly in the presence of the intracellular reducing agent glutathione (GSH).[450] Physically relevant human plasma conditions of glutathione average 0.3 - 0.5 mM and intracellular values are found of 1-2 mM, although there is a heterogenicity of concentration depending on cell type and organelle.[448,449,465,466] Thefore, the reactivity of the BODIPY exo-functionalized metallacage exposed to 2 mM GSH was monitored by ^{1}H NMR spectroscopy. After recording a spectrum of cage **CG1.BF$_4$** in DMSO-d_6:D$_2$O (9:1), GSH was added and a series of spectra were recorder over 24 h. The image in Figure 7.4 indicated that, upon addition of GSH, the metallacage dissociates into the precursor **LG1**, illustrated by the appearance of peaks characteristic of the ligand. Exposed to GSH resulted in an estimated disassembly of 21% after 10 min of exposure, calculated comparing the integral value of peak of the metallacage to the peak of the ligand. It must be noted that monitoring this process over time (> 20 min) was severely hindered by the scarce solubility of **LG1**, as it crushed out in the experimental conditions. However, the results highlight that the metallacage can remain partly intact in the cytosol and disassembles over time in the presence of GSH.

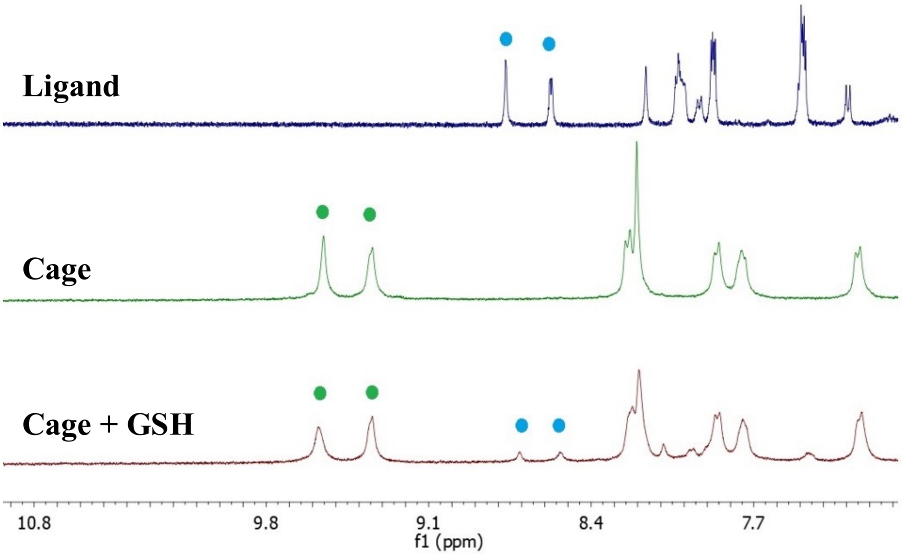

Figure 7.4: Stacked ^{1}H NMR (400 MHz, DMSO-d_6:D_2O 9:1) spectra of the ligand ***LG1*** *(top), the cage* ***CG1.BF$_4$*** *(middle) and the cage* ***CG1.BF$_4$*** *in 2 mM GSH (bottom) at t = 10 min. Blue dots indicate ligand signals, and green for cage.*

7.2.4 Encapsulation of cisplatin

To demonstrate encapsulation of cisplatin within the Pd_2L_4 metallacages, ^{1}H NMR spectroscopy with DMF-*d_7* as solvent was used. Spectra were recorder prior and after addition of the equivalent of two molecules of cisplatin vs one molecule of **CG1.BF$_4$** and compared. A zoomed overlay spectrum displaying **CG1.BF$_4$** and [(cisplatin)$_2$$\subset$**CG1.BF$_4$**] is shown in Figure 7.5. The two signals corresponding to the protons facing the internal cavity (H_a and H_e), as well as the signal of the *exo*-facing proton (H_b), were observed to undergo chemical shifts due to cisplatin encapsulation, as previously reported.[451] Specifically, a downfield shift was observed for H_a and H_e of +0.02 ppm and +0.06 ppm, with a broadening of signal. H_b had a downfield shift as well of +0.02 ppm respectively.

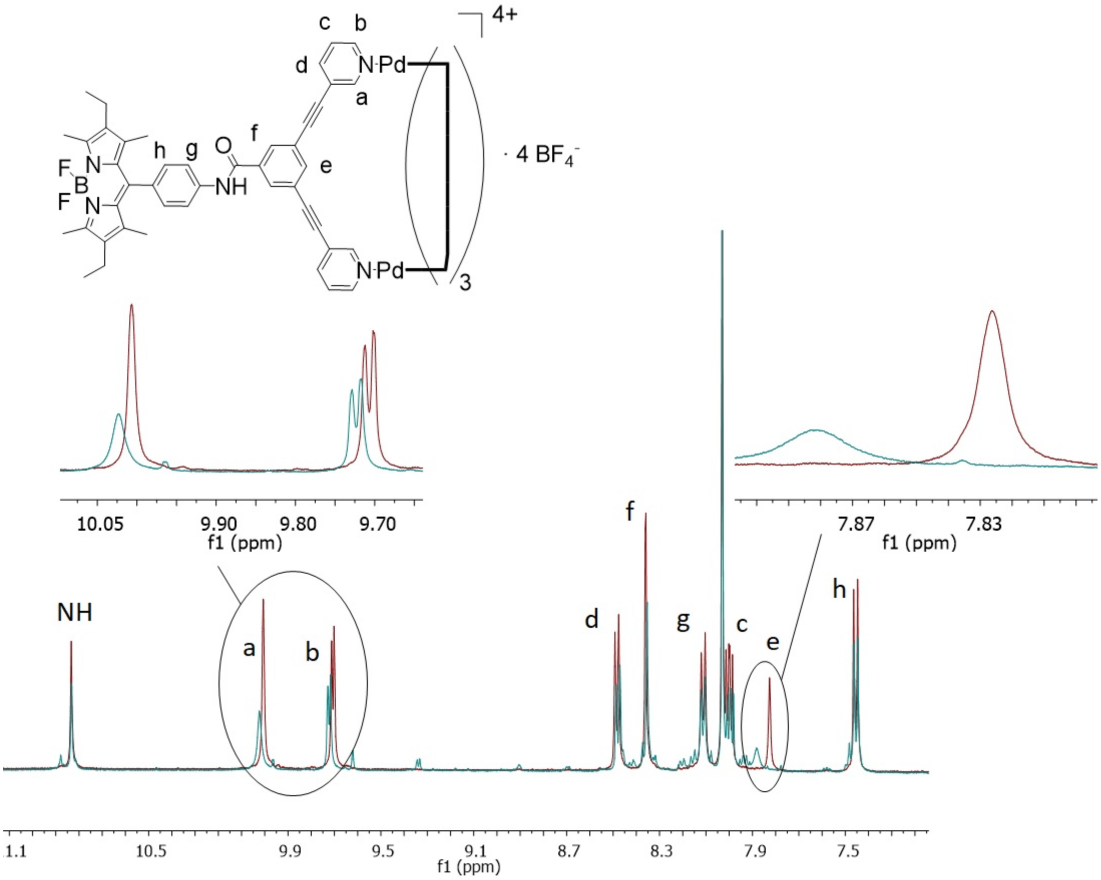

***Figure 7.5**: ^{1}H NMR (500 MHz, DMF-d_7) spectra zoomed into the aromatic region of **CG1.BF**$_4$ alone (red) and [(cisplatin)$_2$⊂**CG1.BF**$_4$] (green). Upon cisplatin encapsulation, there is a broadening and downfield shift in H_a, H_b and H_e signals.*

7.2.5 Antiproliferative activity studies

The antiproliferative effects of the coordination cages and corresponding ligand were evaluated prior imaging studies in three cancerous human cell lines, including A375 (melanoma), MCF-7 (breast) and SK-BR-3 (breast) using a CellTiter-Blue® viability assay. The breast adenocarcinoma cell lines have a different overexpression of estrogen receptor (ER) and Human Epidermal growth factor Receptor 2 (HER2), both associated with cancer: MCF-7 is ER+, whereas SK-BR-3 is ER- and HER2+.[467,468] The obtained results are presented Table 7.2. It is worth mentioning that preliminary screening had already determined that the cage scaffold, without BODIPY fluorophore attached, was non-toxic in A375 even after 72 h of incubation (EC_{50} >40 µM). The new results showed that, in all cell lines, the cages and ligand systems exert scarce antiproliferative activities after 24 h with EC_{50} (effective concentration at which 50% of the cell proliferation is inhibited) values >30 or 50 µM. No precipitation was observed for either cages or ligand after incubation in DMEM cell culture medium, but solubility of the tested **CG1** and **LG1** was limited in RPMI medium, therefore restricting the concentration range applied in MCF-7 cells. Based on the EC_{50} result, we can therefore assume that the complexes have either no cytotoxicity or are limited in their uptake/accumulation. The latter will be investigated by fluorescence microscopy in the next sections. Moreover, no effect of the different counter ions on the observed antiproliferative activity could be evidenced.

Table 7.2*: Antiproliferative activity (EC_{50} values) of different cage and ligand formulations against human MCF-7, A375 and SK-BR-3 cells after 24 h incubation.*

Compound	**EC_{50} (μM)**[a]		
	A375	**MCF-7**	**SK-BR-3**
LG1	>50	> 30	>50
$CG1.BF_4$	>50	> 30 [b]	>50
$CG1.NO_3$	>50	n.d.	n.d.

[a] Data is presented as mean ± SEM of at least three independent experiments.

[b] Solubility was limited when mixing cage with RPMI medium >30 μM

n.d. = not determined

7.2.6 Uptake and cellular localisation studies

7.2.6.1 Cell uptake of cages and ligands in A375 fixated cells

Initially, the intracellular uptake of all complexes was to be confirmed. Simultaneously, the mode of uptake was investigated by exposing human melanoma A375 cells to different temperatures during 2 h incubation with 5 µM of fluorophore **G1**, ligand **LG1** and cage **CG1.NO$_3$**. By lowering the temperature to 4°C, active mechanisms facilitating transport across the cell membrane are limited due to a lower availability of energy generated by enzymic processes.[463,464] Any observed uptake under these conditions would therefore be contributed to a passive, energy independent diffusion. Images obtained with an epifluorescent microscope (Zeiss) of both temperatures are presented in Figure 7.6-A, with a zoom of the cells exposed to the three complexes at 37°C shown in Figure 7.6-B. The fluorescent intensity of **G1** is most prominent, followed by **CG1**, with the lowest intensity observed for **LG1** at 37°C. Surprisingly, **G1** maintains marked fluorescence intensity and, therefore, uptake at 4°C, indicating passive transport as the main mechanism of cell entry (Figure 7.6-A). The fluorophore **G1** is most likely to be present as a neutral species in the medium and able to diffuse across the cell membrane. A dramatic reduction in uptake at 4°C is seen for the ligand and cage, implying transport only occurs in an active fashion. Due to the difference in observed fluorescence, we might even assume that the structural integrity of the BODIPY moiety regarding ligand and cage is retained during incubation.

In Figure 7.6-B, we can see not only a difference of fluorescent intensity when comparing complexes, but a slightly alternate cellular distribution as well. Although all images present accumulation in spherical fluorescent spots, **G1** seems much more diffuse in the cytoplasm compared to **CG1** and **LG1**.

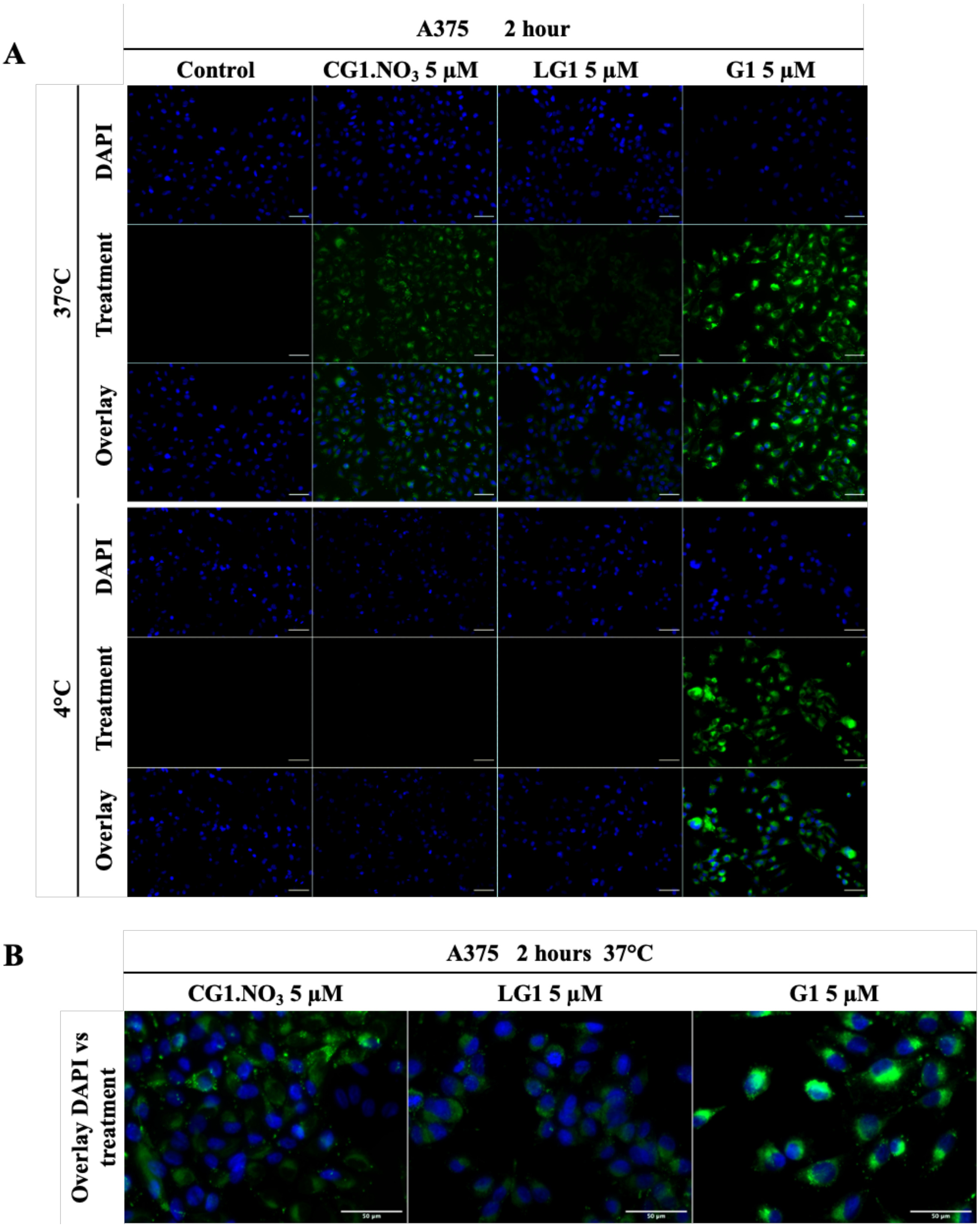

__Figure 7.6__: Fluorescence widefield microscopy (Zeiss) images of fixed human A375 melanoma cells __A__) comparing control to samples incubated with 5 µM of **$CG1.NO_3$***, __LG1__ or __G1__ for 2 h at 37 °C (top three rows) or 4 °C (bottom three rows). __B__) Zoom of the DAPI and Treatment overlay, illustration different fluorescent intensities and intracellular distribution. Scale bar represents 50 µm.*

7.2.6.2 Confocal analysis using fixated cells

To get a closer look at the intracellular localisation, A375 cells were incubated for 2 h at 37°C with 5 µM of fluorophore, ligand and cage, respectively, fixed and visualised by confocal laser scanning microscopy (CLSM). Compared to conventional widefield microscopy, contrast and definition is improved due to spatial filtering of out-of-focus light with pin-point illumination and its possible to provide a multi-dimensional view by compiling a linear array of 2D sections for a 3D model.[452] Images are presented in Figure 7.7, displayed at maximum projection for visual inspection with additional zoom of selected cells. A distinct pattern can be observed for all complexes, showing a diffuse presence in the cytosol and accumulation in spheric vesicles, but with no significant entry of the nuclei. **CG1** and **G1** exude fluorescence mostly in vesicles, whereas the intracellular distribution of **LG1** appears more profound in the cytosol. Interestingly, there seems to be a difference in intensity across the structures. Especially **G1** has a strong presence, seemingly labelling the cytoskeleton (possibly microtubules) in addition to the vesicles. Experimental conditions must be taken into account, since this labelling might be an artifact of the fixation. [452] Interaction with the mounting medium however is unlikely, since the cells are clearly differentiated from the background. The seemingly lower accumulation of **LG1** in vesicles could be a result of reduced cellular entry. It must be noted that from these images, one cannot distinguish if the complexes are intact or degraded upon internalisation. Furthermore, the intensity of the spheric structures might be enhanced by aggregation-induced emission instead of intravesical accumulation, although the well-defined spheric form indicates the latter. [469] However, some BODIPY-derivatives have a tendency to accumulate in subcellular membranes due to their high lipophilicity, possibly creating an illusion of uptake. [453,470] Thus, z-sections were exploited to rule out extracellular aggregation or accumulation only on the cell surface, as illustrated in Figure 7.8. The sections highlight vesicle labelling at the cell periphery and in close proximity of the nucleus but no intranuclear presence.

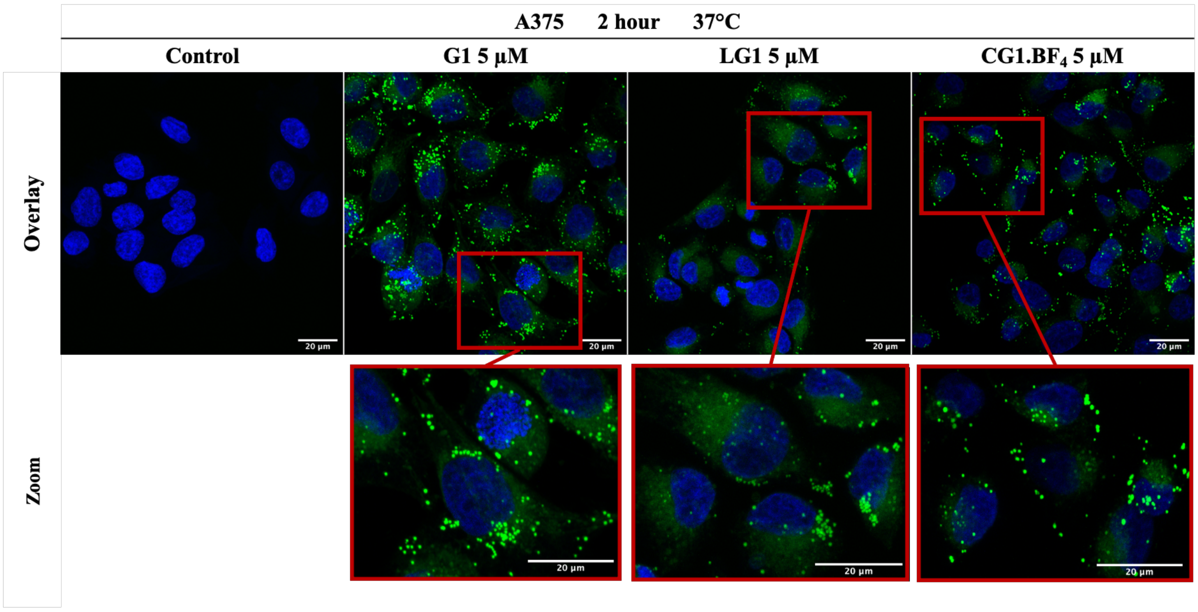

Figure 7.7: Confocal Laser Scanning Microscopy (CLSM) images and zoom of fixed human A375 melanoma cells pre-treated with 5 µM ***G1****, ligand* ***LG1*** *or cages* ***CG1.BF$_4$*** *for 2 h at 37 °C. Counterstaining of nuclei with DAPI. Scale bar represents 20 µm. Max projection of images.*

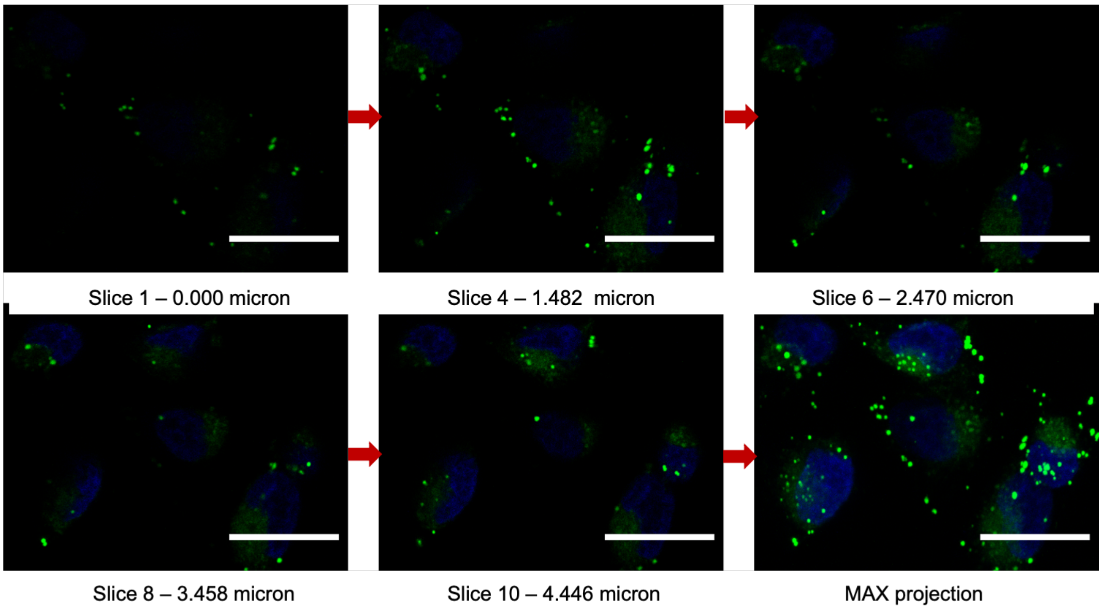

Figure 7.8: CLSM z-stack images of zoomed section of fixed human A375 melanoma cells pre-treated with 5 µM ***CG1.BF$_4$****. Final image is max projection of stack. Scale bar represents 20 µm.*

7.2.6.3 Live cell plasma membrane staining

The previous images were the result of fixated cells, which despite being excellent for initial screening purposes, might give an altered image due to interferences with fixation.[452] Therefore, the use of live cell imaging would enable analysis of intracellular compound's distribution in more detail. Here, we aimed to clearly define the intracellular position of the observed ligand and cage clusters in live cells by marking the plasma membrane with CellMask^{TM} Red. The dye consists of amphipathic molecules, where the lipophilic moiety ensure membrane loading and the hydrophilic negatively charged part securing the probe in the plasma membrane for 30-90 min in live cells. Hoechst, a water soluble blue fluorescent DNA dye, was used for counterstaining of the nucleus. A375 cells were incubated for 2 h with **LG1** or **CG1.NO$_3$**. Images are presented in Figure 7.9. Overlay between the CellMask^{TM} Red and the brightfield filter in the control cells present a correct labelling of the cell boundaries. Images seem to confirm an intracellular presence for the complex loaded vesicles, as they reside within the CellMask^{TM} Red defined cell membrane borders. Accumulation is more prone near the edges of the cells, and interestingly, the vesicles seem quite homogenous in size. Dissection of the cells using z-oriented slices emphasizes the localisation for the **CG1.NO$_3$**, as seen in the selection presented in Figure 7.10. Again, there is no presence of the complex in the nucleus. The complete z-stacks for **CG1.NO$_3$** total view and single cell can be found in Appendix C (Figures S51 and S52).

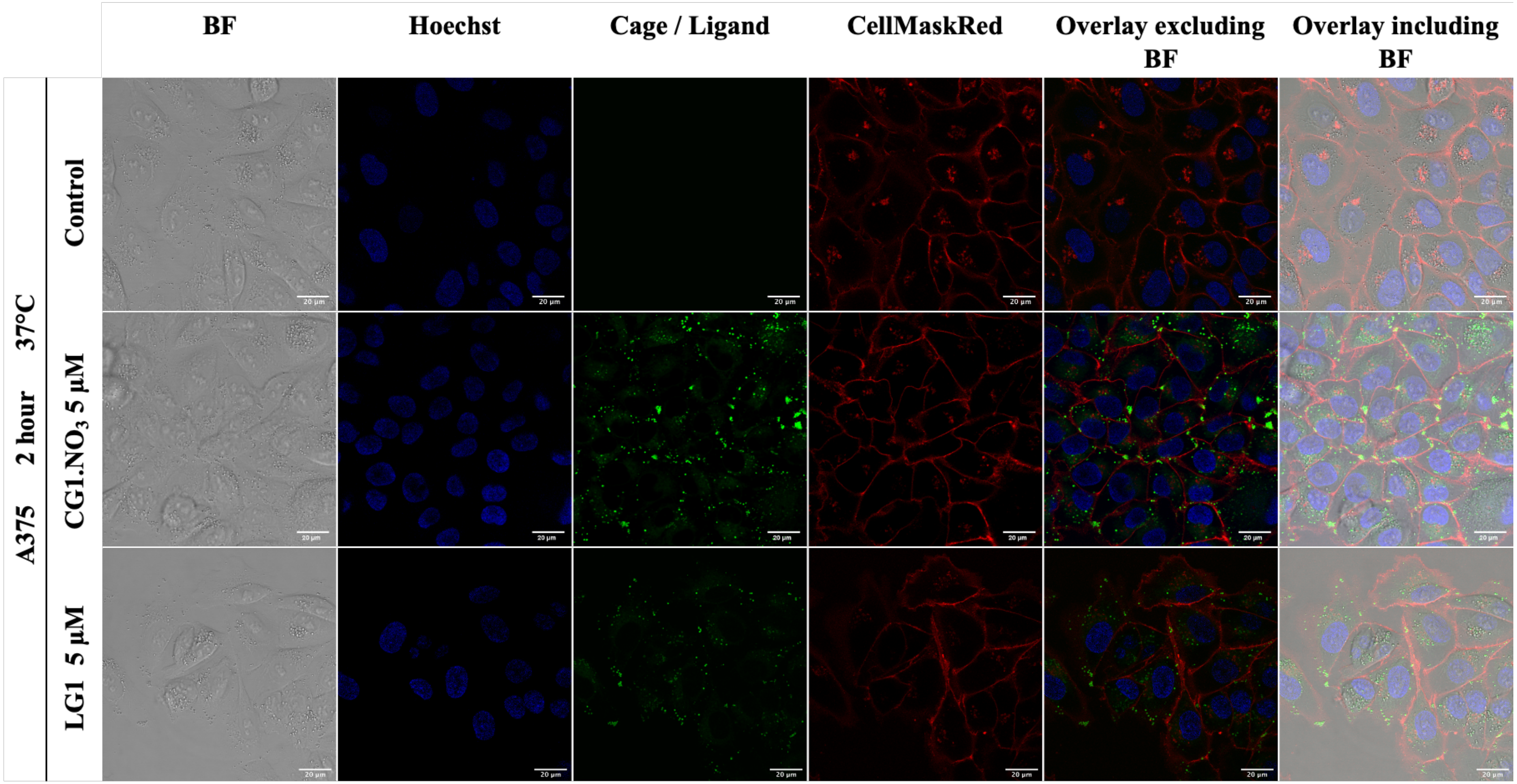

***Figure 7.9**: Live cell images obtained with CLSM of A375 cells incubated with 5 µM of **LG1** or **CG1.** $\mathbf{NO_3}$ for 2 h. BF= bright field. Images enhanced after acquisition. Scale bar 20 µm.*

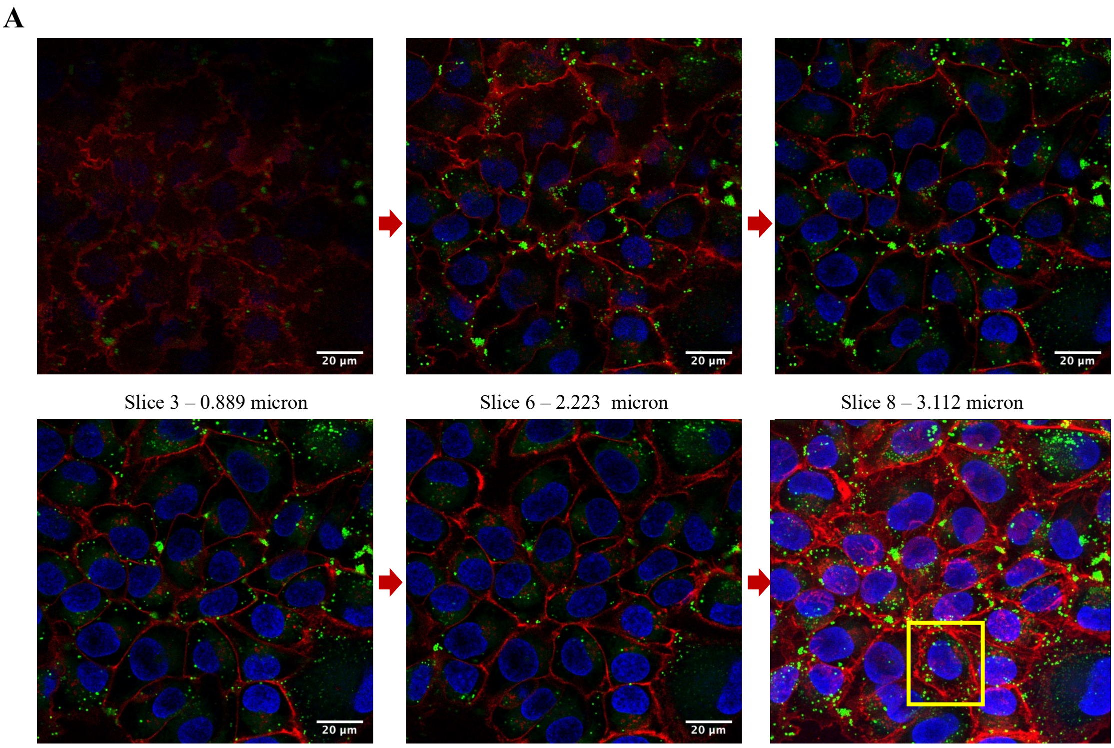

Slice 3 – 0.889 micron   Slice 6 – 2.223 micron   Slice 8 – 3.112 micron

Slice 10 – 4.001 micron   Slice 13 – 5.335 micron   MAX projection

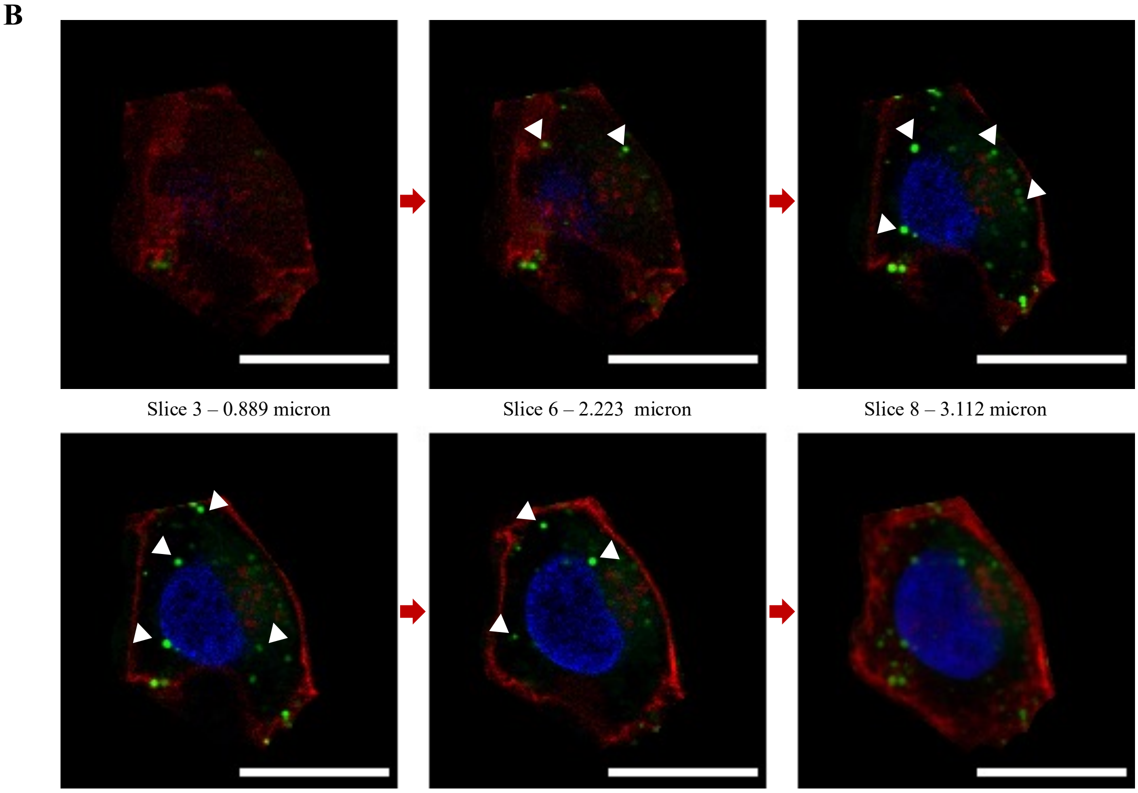

Slice 3 – 0.889 micron   Slice 6 – 2.223 micron   Slice 8 – 3.112 micron

Slice 10 – 4.001 micron   Slice 14 – 5.780 micron   Sum of stack

***Figure 7.10**: Selection of z-stack CLSM images of A375 cells treated with 5 µM **A) CG1.NO$_3$** for 2 h, and **B**) single cell selected from A) as highlighted in MAX projection slice. Arrows highlighting a few intracellular vesicles in B). Images enhanced after acquisition. Scale bar represents 20 µm.*

7.2.6.4 Live cell time-lapse monitored uptake of **CG1** in A375

After confirming accumulation of the complexes is indeed intracellular, a time-laps movie was recorded of A375 cells grown on 35 mm polystyrene imaging dishes exposed to 5 µM of **CG1** using a thermostatic chamber at 37 °C under 5% CO_2 atmosphere. To limit background interference, phenol-red free medium was used. After 4 minutes of acclimatisation, XYT-images were obtained with a 30 sec time interval. To limit possible stress induced by frequent lase exposure, imaging ceased after 1 h. Images acquired at t = 4,5 min and t = 64,5 min are displayed in Figure 7.11-A, with the corrected intensity plotted over time in Figure 7.11-B. Nuclear counterstaining was absent in this specific setup to prevent time dependent photocytotoxicity induced by Hoechst staining (imaging > 30 min) and frequent exposure to UV-light. [471,472]

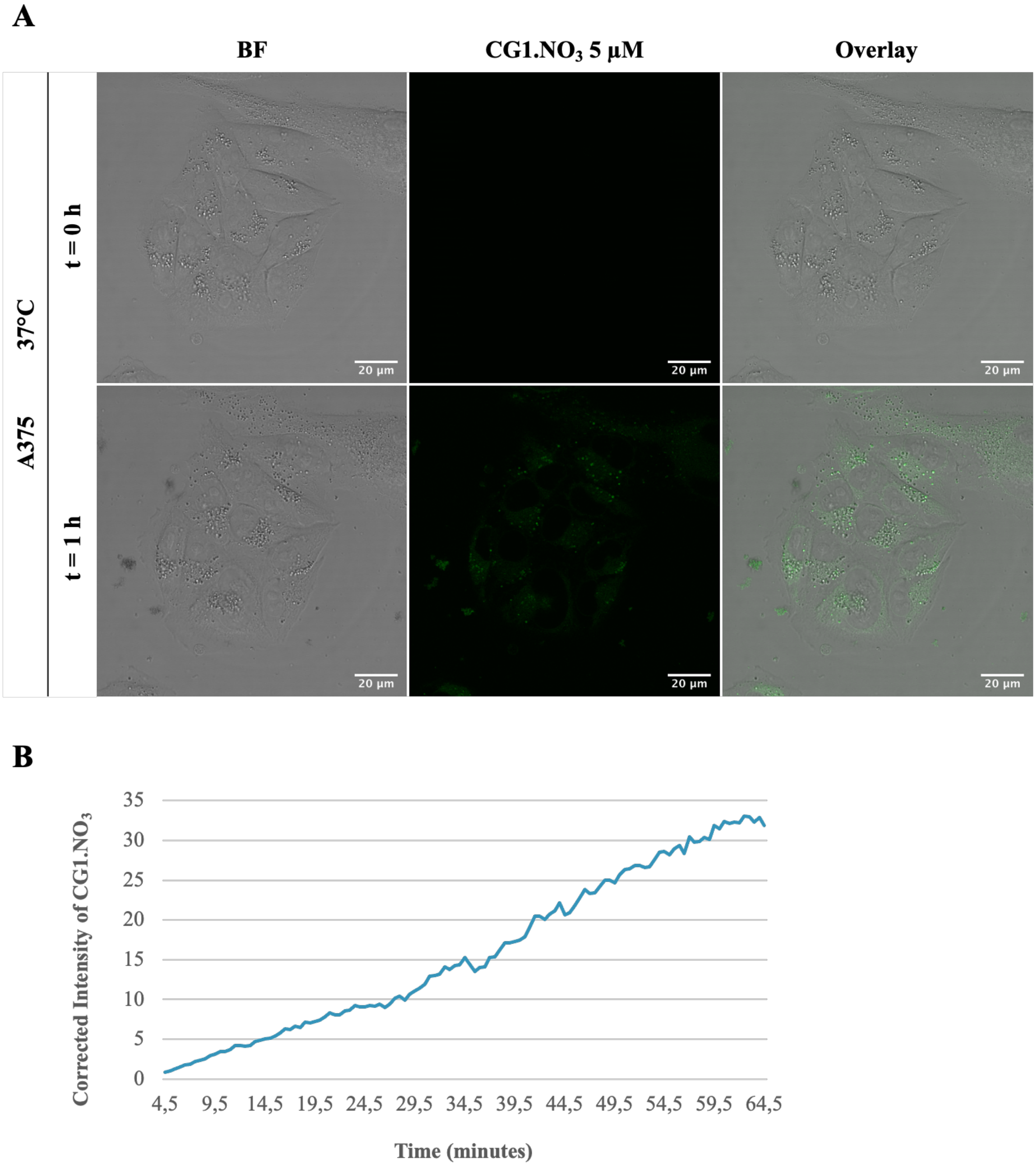

Figure 7.11*: **A)** CLSM images of human A375 melanoma cells exposed to 5 µM of* ***CG1.NO*****$_3$** *cage at t= 0 h and t = 1 h. Scale bar is 20 µm. BF= bright field.* ***B)*** *Graph detailing fluorescent intensity after* ***CG1.NO*****$_3$** *administration, calculated for mean of five representative intracellular regions of interest (ROI) and corrected for corresponding background intensity over time. Time lag due to acclimatisation of cells before acquisition.*

Introduction of **CG1** did not lead towards pronounced morphology alterations, as seen in the brightfield filter of Figure 7.11-A. Over time, there is visible intracellular presence of cage: a more diffuse manifestation in the cytosol combined with the previously observed well defined spheric accumulation in fixed cells. Both seem to intensify simultaneously and become more prominent after 30 mins. Interestingly, some of the fluorescent vesicles seem to be subjected to intracellular trafficking. Additionally, the cytoplasmic distribution mentioned as diffuse has no homogenous presentation, possibly due to transport in smaller vesicles or other subcellular organelles as well. There is also an occurrence of extracellular fluorescent cluster formation, [470,473] as the cell-medium was not refreshed following compound's administration, although some of these seem to originate from the cells and undergo intercellular exchange. The overall increase is reflected in the corresponding graph (Figure 7.11-B). Fluorescent intensity rises gradually over time in a slight S-curve fashion, seemingly approaching a plateau at the end of acquisition. This observed dip could be caused by several factors, such as saturated transport since the previous experiment strongly evidenced an active form of uptake, limiting intracellular accumulation or related to the luminescence ability of the complex, as prolonged excitation might degrade the chromophore or influence the structural integrity of the cage. However, this experiment does highlight the excellent photostability of the developed BODIPY fluorophore.

Overall, the intracellular accumulation observed in vesicles in combination with an active mode of transport for both ligand and cage strongly suggest an endosomal form of uptake.

7.2.6.5 Early endosome immunolabeling

An attempt was made with EEA1-Cy5 antibodies to see if cage and ligand are taken up via early endosomes in human A375 melanoma cells. EEA1, or early endosome antigen 1, is a hydrophilic peripheral membrane protein present in early endosomes, involved in early endosomal fusion.[474–476] Cy5 is a fluorescent dye in the far-red region. To analyse if the complexes would behave in a similar way regardless of the cell line, human MCF-7 breast cancer cells were used as well. In detail, cells were fixed prior immunolabeling, since the **LG1** and **CG1** need at least 1 to 2 h of incubation for their uptake to allow proper fluorescent distinction from background, at which time the EEA1 might be recycled from the cell when co-incubating. The results of MCF-7 are presented in Figure 7.12 and for A375 in Figure 7.13, respectively.

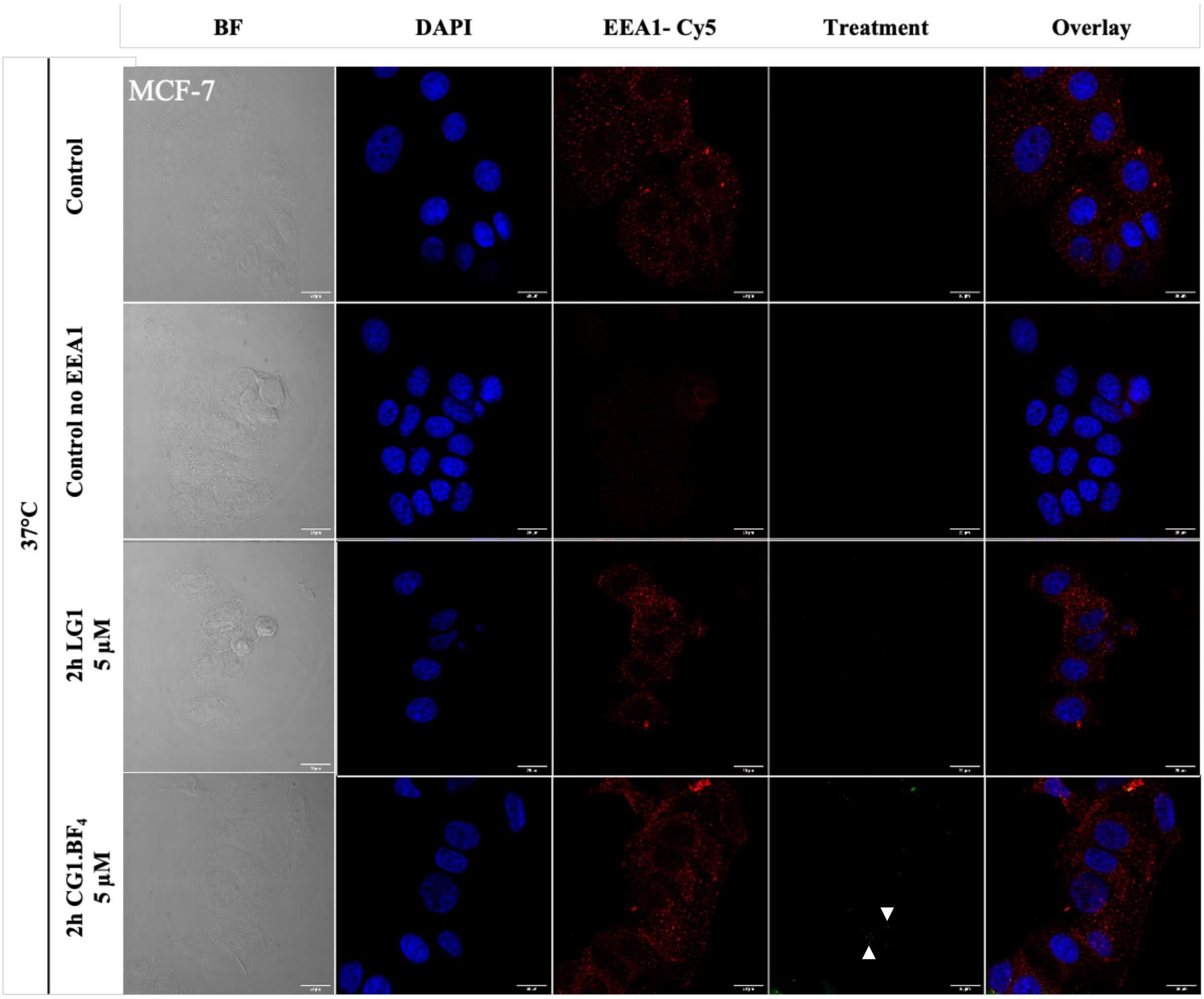

Figure 7.12: *CLSM images of fixed MCF-7 cells exposed to 5 µM of* ***LG1*** *or* ***CG1.BF$_4$*** *for 2 h. Early endosomes labelled with EEA1-Cy5. Counterstaining of nucleus with DAPI. Scale bar is 20 µm.*

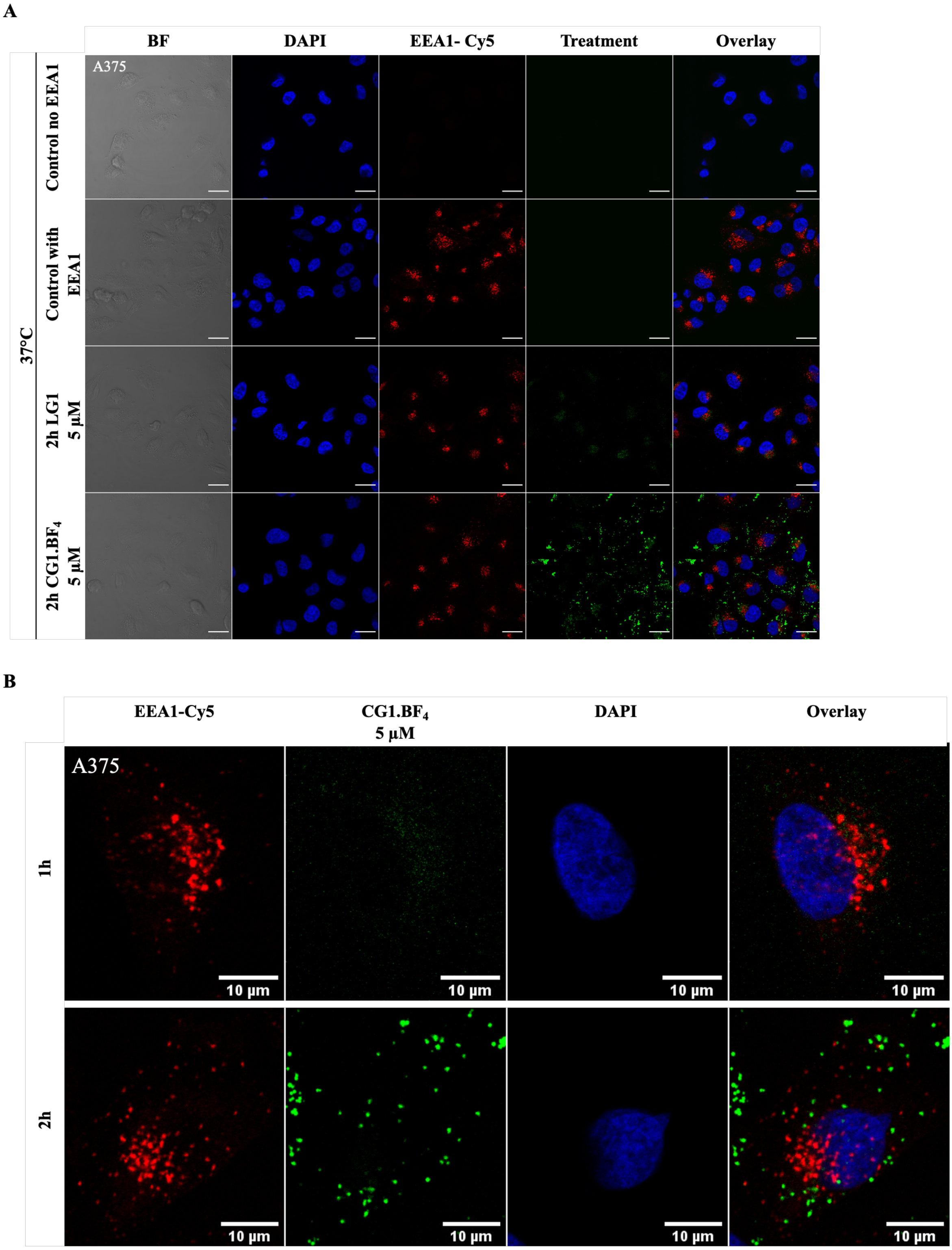

***Figure 7.13**: **A**) CLSM images of fixed A3757 cells exposed to 5µM of **LG1** or **CG1.BF$_4$**. Early endosomes labelled with EEA1-Cy5. Counterstaining of nucleus with DAPI. Scale bar is 20 µm. **B**) Zoomed image of single cells incubated for 1 h and 2 h with 5µM of **CG1.BF$_4$**. Scale bar is 10 µm.*

Surprisingly, there was almost no uptake visible of **LG1** or **CG1.BF$_4$** in MCF-7 samples as seen in Figure 7.12. Only a few fluorescent spots could be detected for **CG1.BF$_4$** (zoomed image in Appendix C, Figure S53) after 2 h of incubation. The complexes might be subjected to recycling or may not be taken up at all. Another possible explanation for the almost non-existing intracellular presence might be the stability in RPMI medium.[477] An interaction with medium components might occur that could lead to degradation of fluorophore or the complete structure before uptake. In any case, this example highlights the value of intracellular imaging in addition to antiproliferative screening, to confirm if an effect if based on actual low intrinsic toxicity or the result of in the case of MCF-7, no visible uptake.

For the A375 cells, there was a clear intracellular accumulation of **CG1.BF$_4$** after 2 h of incubation, with a less pronounced presence of **LG1**. (Figure 7.13-A). At first glance, there is virtually no overlap between the labelled early endosomes and either cage or ligand in the A375 cells. The fluorescent signal of the treatment was not strong enough after 1 h of incubation to clearly distinguish from EEA1, as illustrated in Figure 7.13-B. Apparently, a 2 h incubation is required to observe a strong fluorescence for the **CG1.BF$_4$**, suggesting accumulation in vesicles might lead to an aggregation induced fluorescent effect.[469,470] Even if the early endosomes are involved in the transport of the complex, visualisation will be limited due to the time acquired for a strong compound signal, by which time the complex might reside in a different organelle such as lysosomes. In this case, the results can neither confirm nor rule out involvement of early endosomes. A further investigation might involve higher concentrations of compounds. For now, the involvement of lysosomes will be investigated in the next section.

7.2.6.6 Colocalization with lysosomes

To evaluate lysosomal transfer of **LG1**, **CG1.NO$_3$** and **CG1.BF$_4$**, a colocalization experiment was conducted where prior complex incubation, cells were exposed to a 4 h pulse with fluid phase endocytosis probe Dex-647, a dextran labelled with fluorescent Alexa-647, to image the lysosomes. Live cell images were taken after 2, 3 and 5 h following incubation with ligand, cage and Dex-488 as a control. A representative image of the 3 h time point is shown in Figure 7.14 (Images of 2 h and 5 h not shown).

Colocalization defined by visual inspection is specified by the occurrence of yellow, when images of green and red overlap. As illustrated in Figure 7.14-A, there is yellow present mainly in the control sample at 3 h. For the first (2 h) and last timepoint (5 h), there is a heterogenous manifestation of yellow among green and red spots. A slight overlap is observed in the images of the cage and ligand at 2 h, but the colour is lacking at 3 h (Figure 7.14-A) and 5 h. A closer inspection into the small cytosolic fraction supposedly displaying colocalization of **LG1** and both **CG1** indicates this might actually be co-occurrence, thus not correlated to the lysosomes.[478] The lack of overlap is especially clear for the vesicles, where the complexes accumulate are unmistakably separated from the lysosomes as seen in Figure 7.14-B.

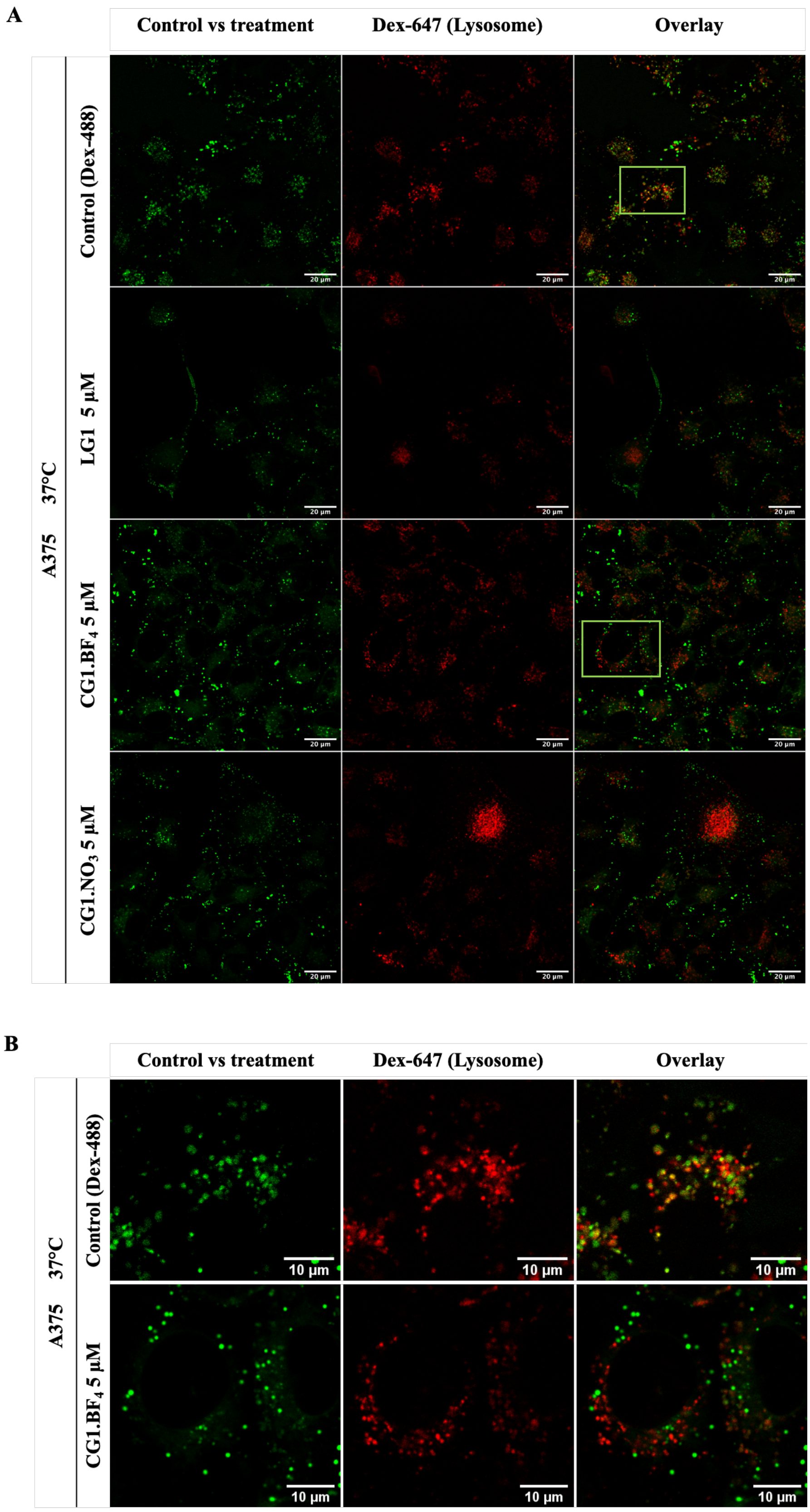

***Figure 7.14**: A) CLSM images of human A375 melanoma cells pulse chased with Dex-647 and exposed to 5 µM of **CG1.BF$_4$** cage, **CG1.NO$_3$** cage, ligand **LG1** and 200µg/mL Dex-488 imaged after 3 h. Scale bar is 20 µm. **B**) Zoom of sections indicated in A), highlighting an*

overlap of control with lysosomal dye Dex-647 (yellow spots) but a clear separation compared to cage. Scale bar is 10 µm.

Although visual examination of the colocalization experiment gives an indication of whether overlap befalls or not, result can be influenced due to differences in fluorescent intensity. This can be illustrated using the control samples where a variety of colours manifest, thus suggesting partial overlap, whilst in reality both colours occur in the same location, but one is less defined. Therefore, quantification of the overlap fraction would be necessary to determine the nature of correlation between lysosomes and complexes/control. Figure 7.15 and Figure 7.16 illustrate the possible difference profiles for control (colocalization) and **CG1.BF$_4$** (co-occurrence).

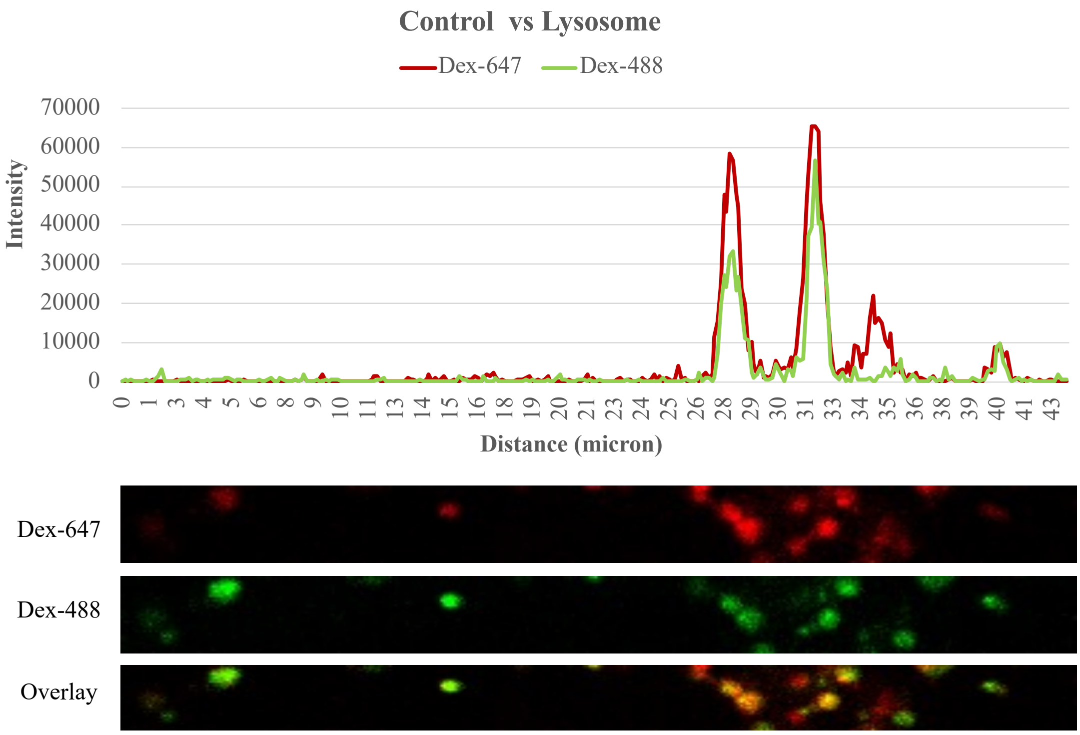

***Figure 7.15**: Illustrating influence of difference in fluorescent intensity to observing overlap at 3 h. Graph of the intensities of pixels along a line within the image. The x-axis represents distance along the line and the y-axis is the pixel intensity. Almost all of the red (Dex-647) and green (Dex-488) overlap, however this is not reflected in the overlay where yellow is seen as indication for colocalization, due to fluorescent heterogeneity in intensity.*

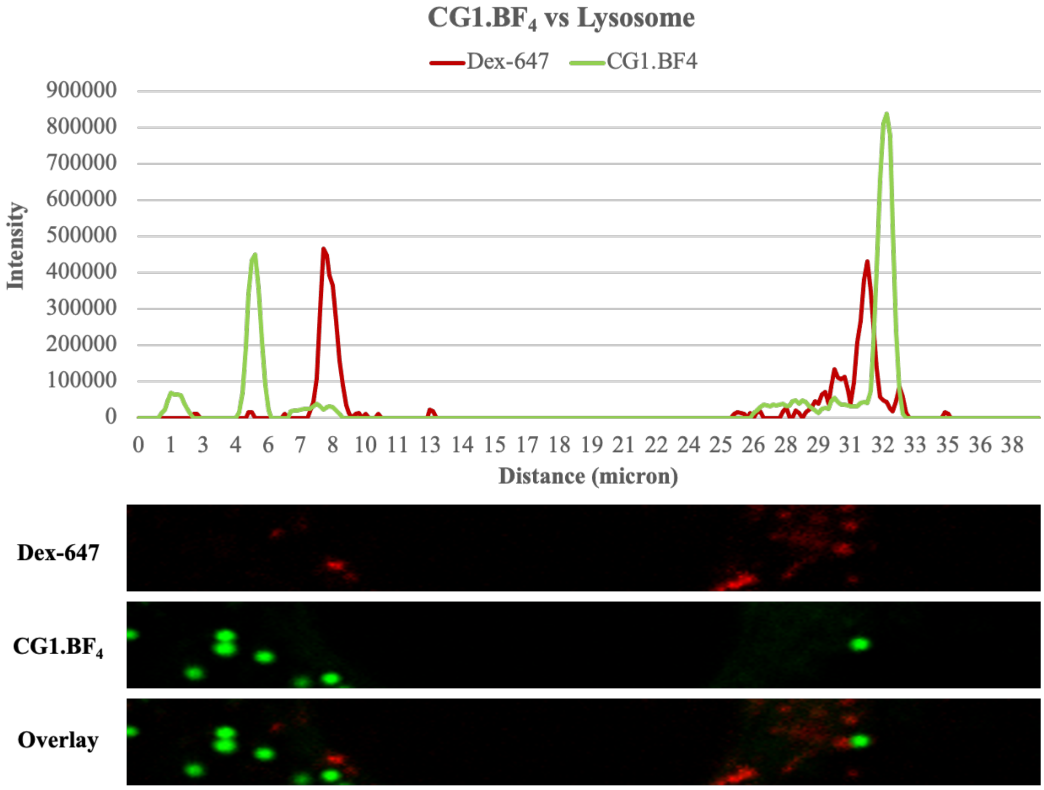

Figure 7.16: *Graph displaying the intensities of pixels along a line within the image at 3 h. The x-axis represents distance along the line and the y-axis is the pixel intensity. Almost no overlap between the lysosomal marker Dex-647(red) and* ***CG1.BF$_4$*** *(green), only co-occurrence of separate vesicles.*

In an attempt to quantify pixel overlap, the intensity over time for compounds/control vs lysosomes was analysed using the JACop ImageJ plugin to obtain both Pearsons r and Manders M1 & M2.[479] To limit contribution of noise and background, the Otsu threshold was applied as mask prior program use. Pearsons correlation coefficient (PCC) reflects correlation between fluorophores based on differences of the mean intensity, with -1 indicating a complete but negative correlation and +1 a perfect correlation. PCC values are subjected to fluorescent intensity variations or heterogenous colocalisation within a sample, two consequences of imaging live biological samples that make interpretation ambiguous as only pixels containing both colours are analysed.[480,481] Therefore, Manders coefficients (MCs) were calculated as well since they use absolute intensities for its determination of correlation.[481,482] Two values (M1 and M2) are produced, calculating for each fluorophore the fraction of total intensity that co-occurs ranging from 0 to +1. M1 in this case is the summed intensity of pixels from the compound/control that have intensity above zero in the red Dex-647 image, and M2 vice versa. The values are the average of 5 different images per timepoint with corresponding standard deviation and presented in Figure 7.17.

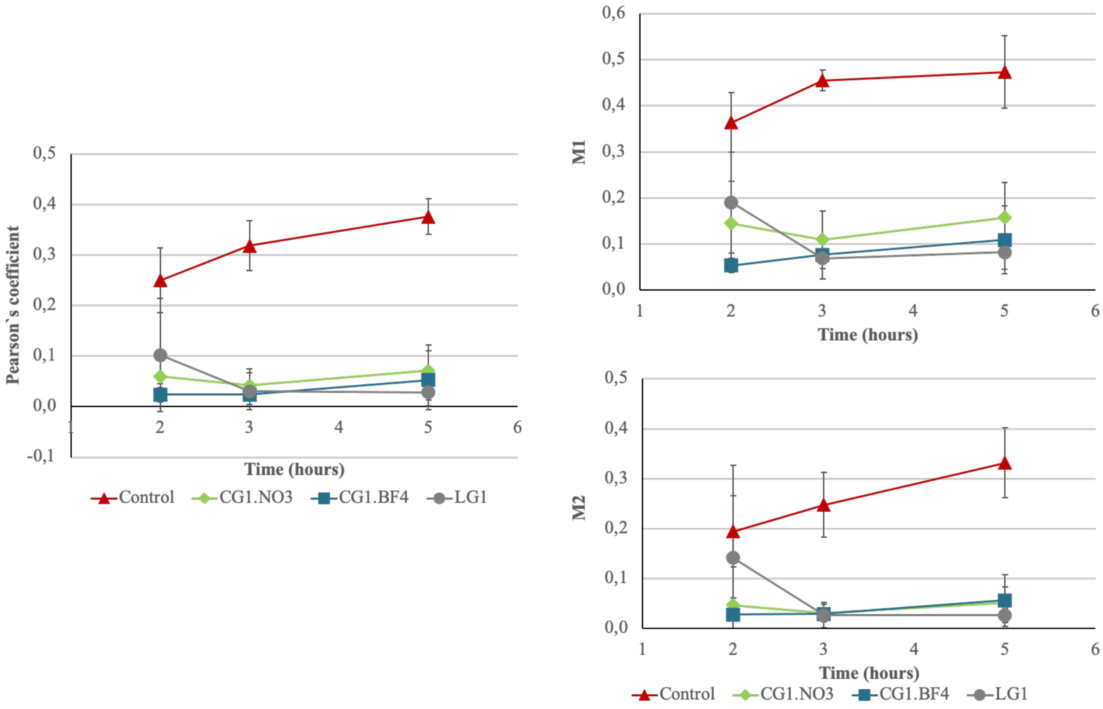

***Figure 7.17**: Pearson`s correlation coefficient and Manders M1 & M2 with corresponding standard deviation describe fluorescent intensity overlap between complexes/control and lysosomes labelled with Dex-647.*

Control displays partial positive correlation with lysosomes, increasing over time as presumably, there is more lysosomal trafficking. The opposite is evidenced for both cage and ligand with a Pearson`s correlation coefficients close to zero decreasing over time. This is in line with the visual inspections of the images. We can therefore conclude that the imaged vesicles containing the complexes are not late endosomes or lysosomes.

Surprisingly, an overlap was observed between the fluorescent complex labelled vesicles and the dark coloured spots visible only in the brightfield filter (Figure 7.18). The slight brown to black coloured vesicles are also present in the control samples and seem to be a phenotype inherent to this cancer cell line. Specifically, since A375 cells are melanoma cells expressing melanosomes, the vesicles may contain melanin pigments.[483]

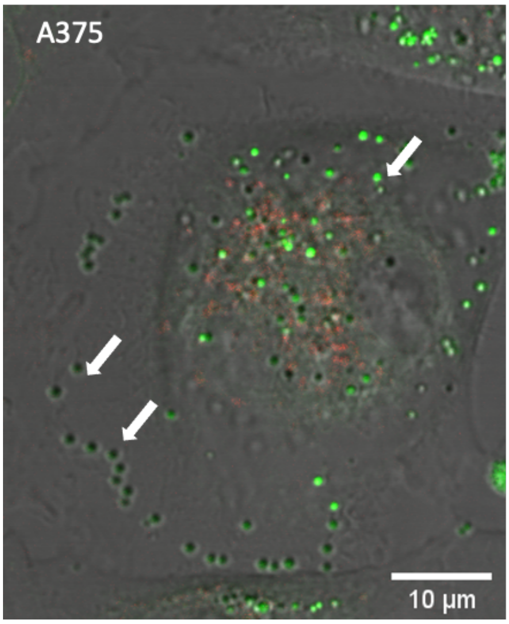

***Figure 7.18**: CLSM image of single A375 cell incubated for 2 h with **CG1.BF$_4$** after pulse with lysosomal dye Dex-647. Arrows highlight intracellular compound accumulation overlap with dark pigmented vesicles. Overlay of brightfield, **CG1.BF$_4$** (green) and Dex-647 (red). Scale bar represents 10 µm.*

7.2.6.7 Melanosome accumulation

In an effort to identify the aforementioned vesicles of compound accumulation in the A375 cells, primary endocytic pathway suspects such as late endosomes or lysosomes have been ruled out with the help of fluorescent labels. As an alternative, the cage complexes seem to gather in melanosomes. Melanosomes are unique melanocyte-specific intracellular organelles and are involved in the synthesis and storage of melanin pigments.[483] Melanin pigments are biopolymers of various indoles and catecholic species derived from the amino acid tyrosine, and two main types can be found in mammals: black insoluble eumelanin and yellow-reddish soluble pheomelanin (Figure 7.19).[484–486] A mixture of both is present in skin and hair, with different ratios resulting in colour variations, to protect cells from damage by sunlight and oxidants. Initially considered to be lysosome-related organelles, recent data uncovered they might originate from early endosomal membranes, as illustrated in Figure 7.20.[487]

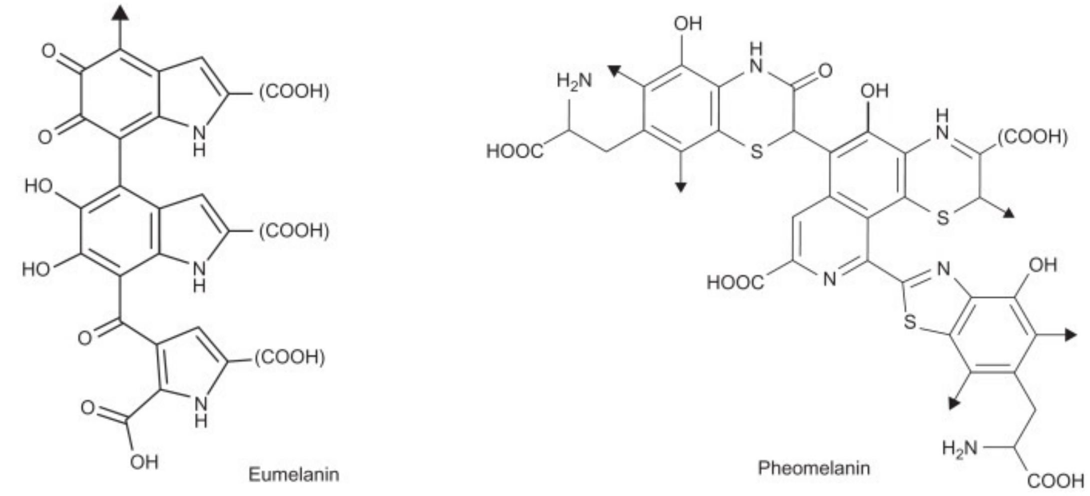

Figure 7.19: Eumelanin and pheomelanin structures. Arrows indicate continuation of polymerization.[486]

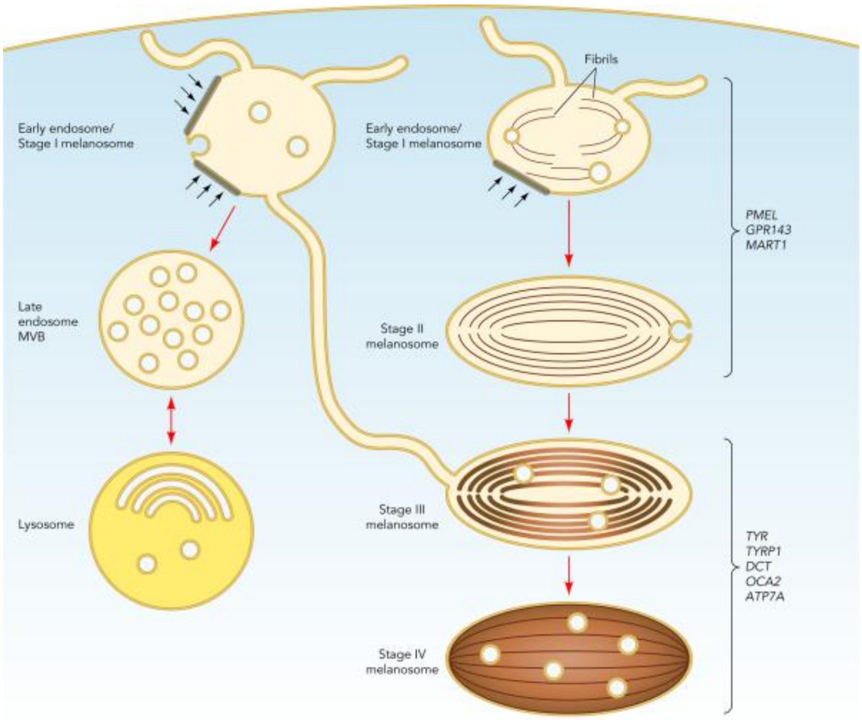

Figure 7.20: Maturation of melanosomes segregated from endocytic organelles. Following endocytosis, selected cargo is delivered to melanosome from early endosomes. Figure adapted from Sitaram et al.[488]

Maturation of melanosomes consist of four morphologically different stages, with the first stages lacking pigment as melanin synthesis start at the end of stage II, maturing to a thick and black structure in stages III and IV. The stage IV melanosomes are also subjected to translocation along cell microtubules from the centre to actin-rich cell edges with myosin or dynein motors, ready to be transferred to neighbouring cells (keratinocytes) in distress (Figure 7.21).[483,489] Movement along the cytoskeleton is bidirectional. The stages exemplify the diversity of colour found in melanosomes, ranging from slight brown to black.

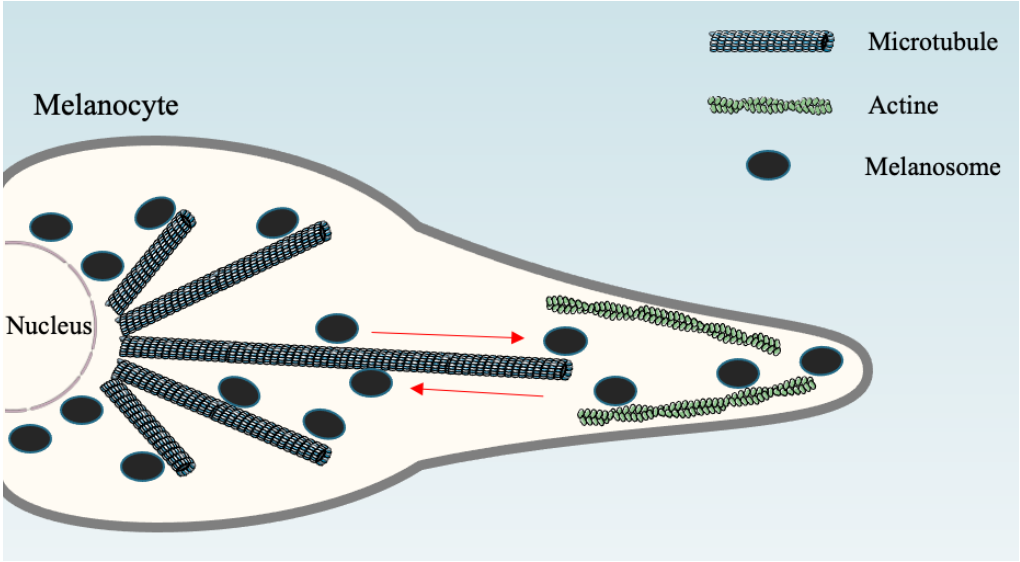

Figure 7.21: Model illustrating translocation of mature melanosomes within melanocytes along microtubules towards actin filaments in the cell periphery. Movement is bidirectional. Adapted from references [484,489]*. Figure created using images from Servier Medical Art Commons Attribution 3.0 Unported License. (http://smart.servier.com).*

The ability to create protrusions in order to deliver melanosomes from the cell periphery to neighbouring cells is a distinctive trait of melanocytes. This behaviour has been observed during the experiments, where the **LG1** labelled melanosomes were seeminlgy oriented towards a cell in distress via a cell protrusion as shown in Figure 7.22, further supporting the idea of complex accumulation in melanocytes.

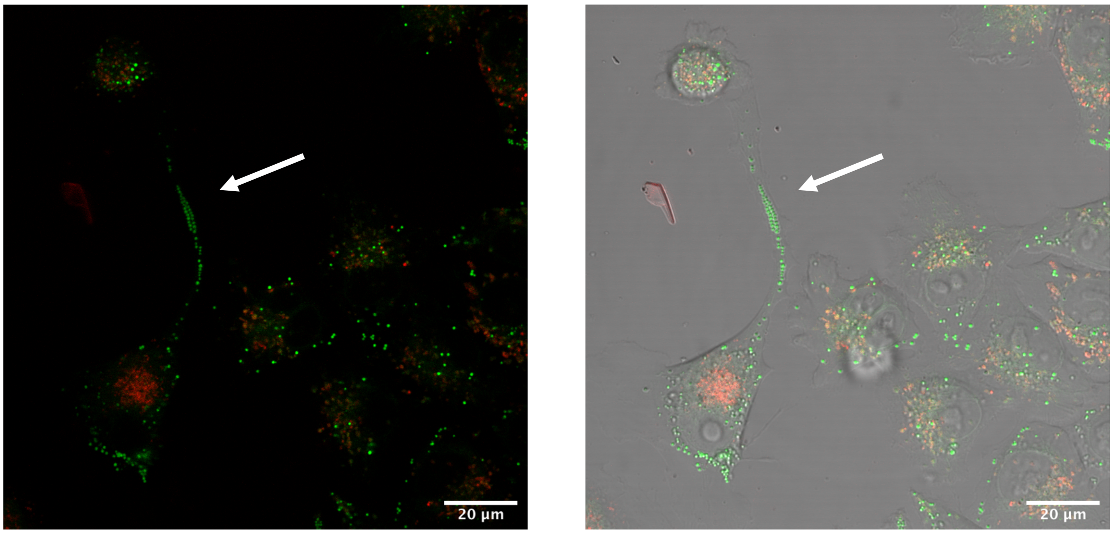

***Figure** 7.22: Dendritic protrusion with melanosome vesicles labelled with 5 µM **LG1** indicated with arrow moving along microtubule/actin cytoskeleton to a neighbouring cell in distress. Left: overlay of **LG1** (green) and Dex-647 (red). Right: brightfield, **LG1** (green) and Dex-647 (red). Image obtained 1 h after 2 h incubation with compound. Scale bar represents 20 µm.*

Both eumelanin and pheomelanin are supramolecular structures thought to form in situ by aggregation as a result of π-stacking.[485] It might be possible that the aromatic structures of the cage and ligand have affinity for binding to the pigments via π-π interactions and other supramolecular forces (e.g. H-bonding, Van der Waals etc.).[490] Quite a range of organic drugs are known to have affinity for melanin, such as chloroquinine.[491,492] Thus after endocytosis, ligand or cage are excluded from the regular endocytosis pathway at the early endocytosis step and instead subsequently captured by the melanosomes.

Uptake and accumulation of the metallacages and ligands to melanosomes would explain the distinctive fluorescent intensity of the complexes in the vesicles and the cytoplasma. During transport from early endosomes towards melanosomes, intensity is lower. Upon reaching the melanosomes, accumulation can occur and induce an even stronger AIE (aggregation-induced emission).[469]

The serendipitous discovery of potential melanosome labelling by these fluorescent cages would be of interest, as to the best of our knowledge, only one such protein has been reported so far in the last decade.[493,494] Research into melanosmes, especially focused on elucidating the fate of the mature and extracellular variety has been limited[495,496] due to the absence of a proper marker or antibody, relying on electron microscopy or brightfield light confocal microsocopy for visualisation.[483] The first only allows analysis of fixed cell or tissue samples, whereas the image quality of the latter hinders the rendering of proper 3D images. As such, these particular BODIPY *exo*-functionalised Pd_2L_4 metallacages could contribute as a novel visualisation tool, for example in the melanosome transfer to keratinocytes. Further research is required to investigate the nature and selectivity of compound accumulation in melanosomes.

7.2.6.8 Imaging encapsulated cisplatin

Finally, a preliminary screening was performed to analyse the effect of encapsulation of cisplatin on the uptake and sub-cellular distribution of cage **CG1.BF₄**. The [(cisplatin)$_2$⊂**CG1.BF$_4$**] host-guest complex was prepared as previously reported.[497] To observe compound's uptake and intracellular localization in the absence of melanosomes, the tests were performed also using two human breast cancer cell lines SK-BR-3 and MCF7. Before imaging, the antiproliferative effect of the cage-cisplatin construct was tested in the respective cell lines to monitor possible enhancement of cisplatin effects of cell viability. Though the previously discussed results indicated MCF-7 cell do not internalize the cage, the cells were still included in the panel as a negative control. Results are presented in Table 7.3.

Table 7.3: *Antiproliferative activity (EC_{50} values) of cage:cisplatin (1:2) formulation against human A375 and SK-BR-3 cells after 24 h incubation, compared to cisplatin.*

Compound	**EC_{50} (μM)**[a]		
	SK-BR3	**A375**	**MCF-7**
(cisplatin)$_2$⊂**CG1-BF$_4$**[b]	29 ± 5	16 (n=1)	36 (n=1)
cisplatin	>50	16 (n=1)	38 (n=1)

[a] Data is presented as mean ± SEM of at least three independent experiments unless otherwise indicated.

[b] The EC_{50} is calculated with respect to the concentration of free cisplatin.

Of note, the cytotoxicity of encapsulated vs free cisplatin is quite different for SK-BR-3. There is an at least two-fold increase in the antiproliferative effect of the encapsulated fraction (Table 7.3), suggesting the cage enables enhanced intracellular delivery of cisplatin. Instead, as expected, no difference in the antiproliferative activity of free cisplatin was observed in MCF-7 cells, in accordance with the poor uptake of the cages in this cell type.

No difference in EC$_{50}$ values was also observed between free cisplatin and [(cisplatin)$_2\subset$**CG1.BF**$_4$] in the case of the A375 cells. Possibly, even if the [(cisplatin)$_2\subset$**CG1.BF**$_4$] complex is likely to be internalized in melanoma cells, its fast accumulation in melanosomes prevents part of the still encapsulated drug from exerting its cytotoxic effects. Of note, these data should be further confirmed (n =1).

Afterwards, the [(cisplatin)$_2\subset$**CG1.BF**$_4$] complex was imaged in SK-BR-3 and A375 cells by CLSM. Live cells were incubated for 2 h with [(cisplatin)$_2\subset$**CG1.BF**$_4$], with cage-cisplatin ratios of 20:10 µM for SK-BR-3 and 10:5 µM for A375, respectively. The higher concentration of cage (10 µM) was required in SK-BR-3 to obtain proper images. Counterstaining of the nucleus was performed using Hoechst. Results are shown in Figure 7.23.

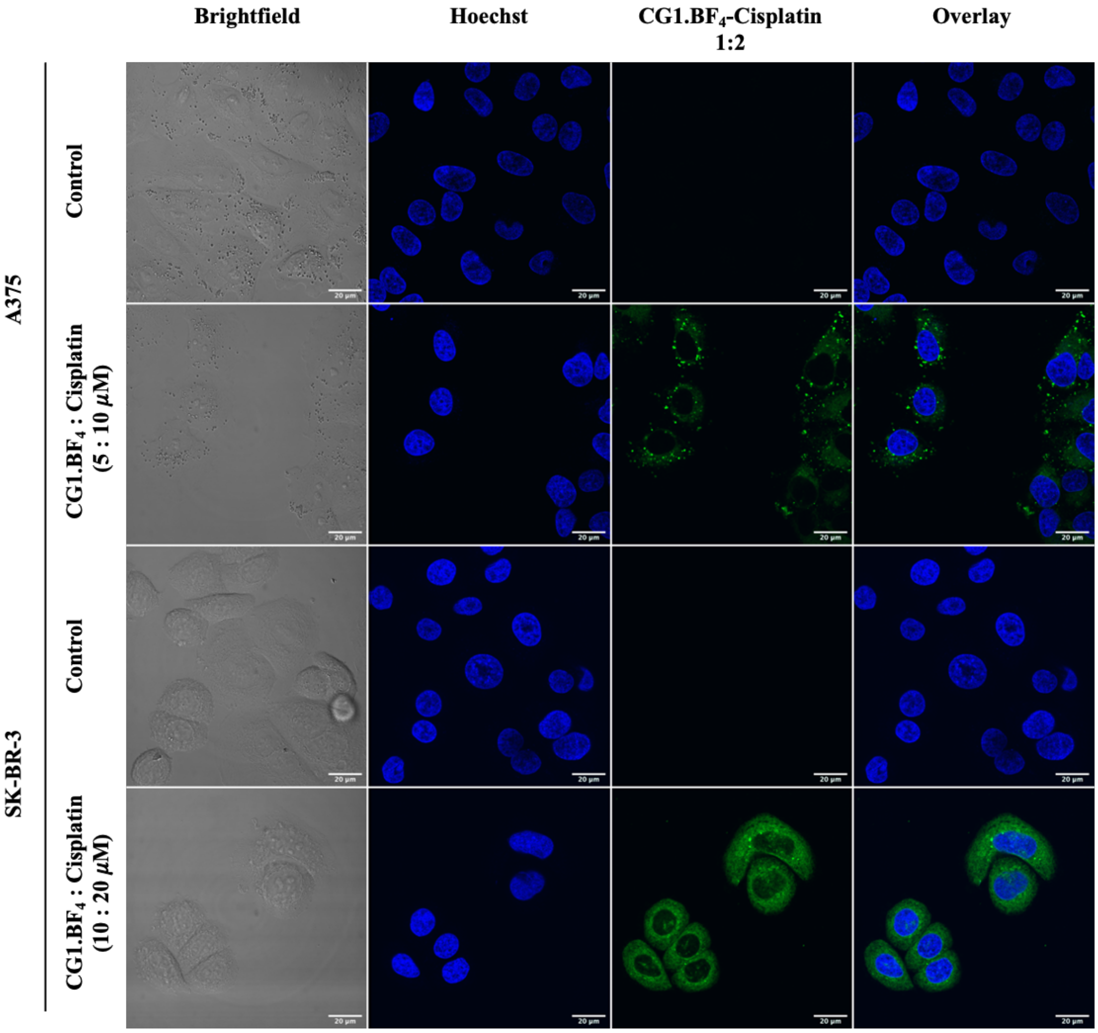

***Figure 7.23**: CLSM live cell images of A375 and SK-BR-3 cells incubated for 2 h with different concentrations of [(cisplatin)$_2\subset$**CG1.BF**$_4$] at 37°C with 5% CO$_2$. Counterstaining with Hoechst. Images enhanced after acquisition. 20 µm scale bar.*

In the case of A375 cells, the presence of encapsulated cisplatin did not seem to influence cage uptake compared to the studies performed using the empty **CG1.BF$_4$** (see previous sections). Thus, cage accumulation is observed in melanosomes and no fluorescent signal is detected in the nuclei.

However, the intracellular profile however is quite different in the case of SK-BR-3 cells. Instead of accumulating in well-defined vesicles, the fluorescent cage complexes were actually dispersed throughout the whole cytoplasm. Z-stack images (Figure 7.24) demonstrated accumulation in a few spots close to the nucleus, but no intranuclear presence. These results might enlighten us into the enhanced anticancer effects measured in this cell line in the case of encapsulated cisplatin. The diffuse cytoplasmic fluorescence seen in SK-BR-3 might make the cage cargo (cisplatin) available for binding to its intracellular targets, since there is no extra step involved to escape vesicle boundary, as in the case of A375 cells. Therefore, cisplatin carried into the SK-BR-3 cell has the opportunity to carry out its cytotoxic effect.

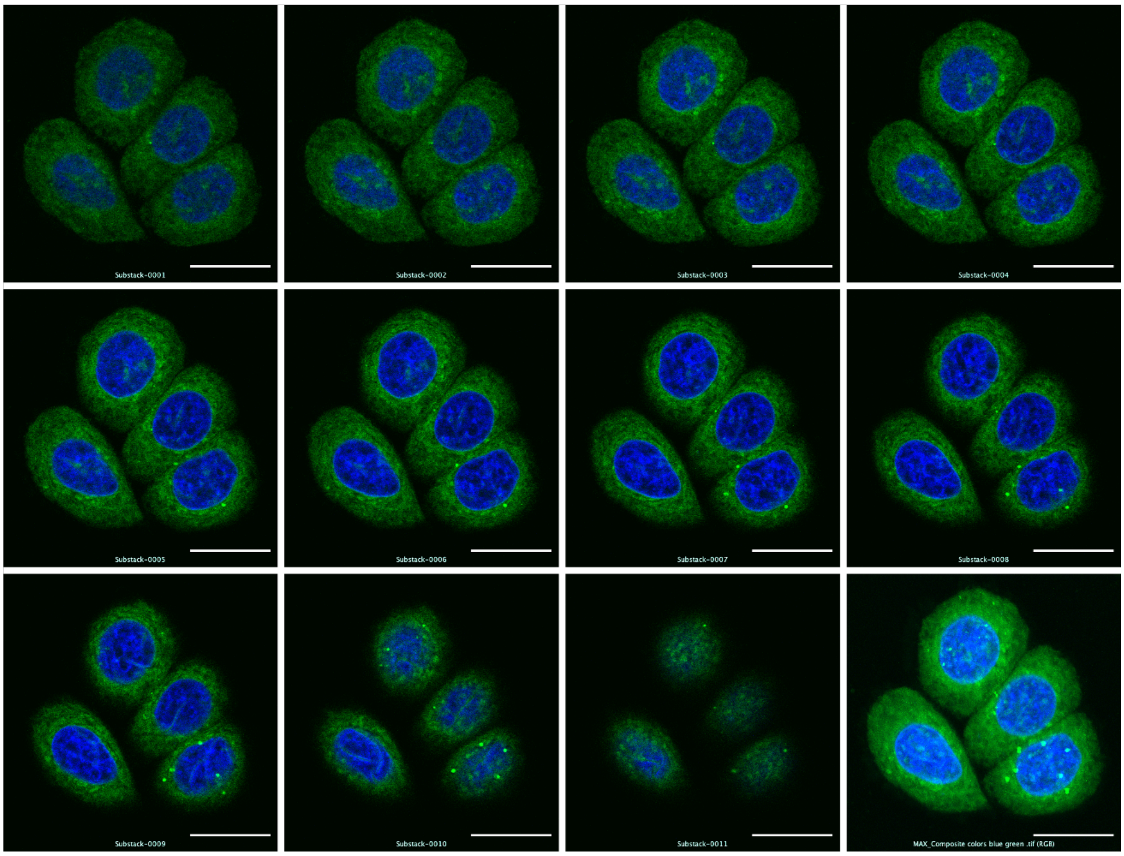

***Figure 7.24**: Z-stack of live cell CLSM images SK-BR-3 incubated with [(cisplatin)$_2$⊂**CG1.BF$_4$**] [20:10] µM and Hoechst. Top left image starts at cell bottom, z-stack moving upwards. Last slice is the max projection of the stack. Images enhanced after acquisition. Scale bar is 20 µm.*

7.3 Conclusions and Future perspectives

Here, we have reported on two new $[Pd_2L_4]^{4+}$ metallacages featuring 3,5-bis(3-ethynylpyridine)phenyl ligands *exo*-functionalised with green fluorescent BODIPY moieties. The excellent luminescent properties (QY_F = 80%) excitation wavelength of ca. 540 nm makes the metallacages quite promising for *in vitro* studies. Stability studies by UV-visible spectroscopy and ^{1}H NMR spectroscopy examined complex behaviour in aqueous solution and in the presence of physiologically relevant concentration of glutathione (GSH). Partial dissociation of the metallacage to the ligand precursor was observed for cage **CG1.BF$_4$** over time, which anyway should occur only intracellularly. Encapsulation of the equivalent of two guest molecules cisplatin per cage molecule was confirmed with ^{1}H NMR spectroscopy. Antiproliferative screening of **CG1.BF$_4$** and **CG1.NO$_3$** and corresponding ligand against a panel of human cancer cell lines (A375 melanoma, MCF-7 and SK-BR-3 breast cancers), showed no cytotoxic effect, highlighting their suitability as non-toxic drug delivery vehicles. Additionally, no effect of the different counter ions on the observed antiproliferative activity could be evidenced.

The presence of the BODIPY-moiety allowed for fluorescent microscopy studies to elucidate the intracellular fate of the ligand and cages. As such, active uptake and relatively fast intracellular accumulation were observed for the cages in human melanoma cells (A375). In the latter, the cages accumulated in spherical vesicles, whereas no uptake was visible in human breast cancer cells of the MCF-7 type. In an effort to identify the aforementioned intracellular vesicles, possibly the result of endocytosis, colocalization assays were performed. Interestingly, both early endosomes and lysosomes were ruled out, suggesting accumulation in melanosomes instead. Additional preliminary cytotoxicity studies revealed no change in anticancer activity for free cisplatin versus cisplatin encapsulated in **CG1.BF$_4$**, suggesting both host and guest molecules to be refrained from reacting with intracellular targets due to their immediate compartmentalisation in melanosomes. In an effort to investigate cage behaviour with and without cisplatin as guest in another cell type, SK-BR-3 cells were included. Remarkably, cisplatin encapsulated in **CG1.BF$_4$** did exhibit increased anticancer effects compared to the free compound in SK-BR-3 cells. Of note, a diffuse cytoplasmic fluorescence due to the cage intracellular accumulation is observed, instead of the pronounced vesicular accumulation seen in A375, suggesting the cage cargo (cisplatin) is available for binding to its intracellular targets in SK-BR-3.

Overall, these novel BODIPY functionalized metallacages show great promise as tools to study SCCs as drug delivery systems. The characteristic green fluorescence of the complexes provided new insights using confocal microscopy, confirming active uptake as well as localising compound accumulation in a cell-type specific fashion (e.g. in the intracellular melanosomes in A375 cells). The value of fluorescence microscopy as a powerful tool to understand the mechanisms of drug delivery and action has been demonstrated in addition to antiproliferative screening.

Future studies should focus on expanding our existing library with different BODIPY-moieties as well as using labelled cargo for a [cage $\subset$ (fluorophore)] system to elucidate guest release.[498] A first preliminary effort using a near infrared BODIPY[499] *exo*-functionalised $[Pd_2L_4]^{4+}$ metallacage has been attempted but needs further optimization for *in vitro* studies. Furthermore, the synthesis of heterolepetic metallacages featuring fluorescent ligands as well as targeting moieties in the same scaffold would in theory produce a promising monitored drug delivery system.[500,501]

It would be prudent to expand the *in vitro* screening to other types of cancerous cell lines to further investigate the mechanism of uptake when melanosomes are not present. The proposed affinity of the green emitting metallacages for melanosomes requires further investigation, as it might be possible to apply the complexes for studies into the still largely unknown extracellular behaviour and fate of these melanin containing vesicles. *In vitro* studies into cell proliferation after compound inhibition followed by co-incubation with for example keratinocytes, or *ex vivo* studies with tissue samples of healthy and cancerous skin[497] would be of interest.

7.4 Materials and Methods

7.4.1 Spectroscopic assessment of complexes

7.4.1.1 Quantum Yield Determination

Quantum yield of fluorescence was calculated by comparison to a reference standard (Rhodamine 6G in degassed EtOH, φ = 94% at room temperature).[327] UV-Visible absorption spectra were recorded on a Cary 60 UV-Vis spectrometer from *Agilent Technologies*. Emission spectra were recorded on a Cary Eclipse Fluorescence Spectrophotometer from *Agilent Technologies*. The selected fluorophore was dissolved in degassed DMSO to a concentration corresponding to UV-Visible absorbance 0.8 A.U. (λ(max) = 523 - 535 nm; 25 °C). The solution was transferred to a fluorescence spectrophotometer and an emission spectrum was recorded (excitation wavelength 595 nm).

7.4.1.2 Stability studies by UV-Visible Spectroscopy

UV-visible absorption spectra were recorded to investigate the stability of the metallacages in solution on a Cary 60 UV-Vis spectrometer (*Agilent Technologies*). For each compound, stock solutions at a concentration of 3×10^{-3} M were prepared. An aliquot was diluted either with 1x PBS (pH 7.4) or deionised water and the UV-Vis spectra measured at different times immediately after dilution at room temperature over 24 h. After the last timepoint, the cuvette was shaken and another spectrum recorded, to determine if the compound was altered during the 24 h or if a reduction in absorption was due to precipitation.

7.4.1.3 Metallacage stability in the presence of L-glutathione by ^{1}H NMR spectroscopy

To evaluate interaction with GSH, **CG1.BF$_4$** was dissolved in a 9:1 ratio of DMSO-*d*$_6$:D_2O (0.5 mL) and a ^{1}H NMR spectrum was recorded. L- glutathione was added to the solution to achieve a final concentration of 2 mM L-glutathione (0.3 mg) and the first ^{1}H NMR spectrum immediately recorded. Afterwards, spectra were recorded every 5 min for the first hour, followed by every hour for the following 24 hours. The ratio of the metallacage : ligand in solution was calculated by comparing the integral value of peak H_b of the metallacage to the peak of H_b of the ligand.

7.4.1.4 Cisplatin encapsulation studies using ^{1}H NMR spectroscopy

The metallacage **CG1.BF$_4$** was dissolved in 1 mL DMF-d_7 at a concentration of 4.4 µM (1.00 eq.) and a ^{1}H NMR spectrum was recorded. Afterwards, 8.8 µM Cisplatin (2.00 eq.) was added to the same NMR tube and the deuterated solution was stirred for 10 min before a second ^{1}H NMR spectrum was recorded. Finally, both NMR spectra were compared to evaluate any chemical shifts due to the encapsulation of cisplatin. The spectra were calibrated to the residual solvent signal of the carbonyl proton of DMF (8.03 ppm).

7.4.2 Cell culture maintenance

Three human cell lines were used in the experiments. Malignant melanoma (A375) and breast carcinoma (MCF-7) were obtained from ATCC and breast carcinoma with high Her2 expression (SK-BR-3) was kindly gifted by the group of Prof. Arywn Jones at Pharmacy, Cardiff. All cell lines were maintained in culture according to provider instructions and cultured in a humidified atmosphere at 37 °C and 5% CO_2. A375 and SK-BR-3 were cultured in DMEM Dulbecco's Modified Eagle Medium (DMEM, 4.5 g/L glucose, Corning, Thermo Fischer Scientific) supplemented with 10% Fetal Bovine Serum (FBS, Eu-approved South American Origin, Thermo Fisher Scientific) and 1% penicillin/streptomycin (Gibco) and passaged when reaching confluence. MCF-7 was grown in Roswell Park Memorial Institute (RPMI, L-glutamine, Corning) medium, supplemented with 10% FBS and 1% penicillin/streptomycin, and appropriately passage diluted upon reaching confluence. All cells were subjected to routine mycoplasma testing.

7.4.3 Antiproliferative assay

To evaluate the antiproliferative effect of the compounds the cell lines, 96-well tissue culture-treated black plates (Cellstar®, Greiner Bio-one) were seeded in a concentration of 15000 cells/well for A375 and 10000 cells/well for MCF-7 and SK-BR-3 with 200 µL full medium. Working solutions of ligand and cage samples were prepared in the required concentration by diluting fresh stock solutions (5×10^{-3} M in DMSO) of the corresponding compound in aqueous complete DMEM or RPMI medium accordingly. Dilutions (1 mM stock) of reference compound cisplatin (Sigma-Aldrich) were freshly prepared in aqueous solution and mixed with the metallacages prior each experiment. Cage formation and cisplatin encapsulation were confirmed by

^1H NMR spectroscopy as previously reported.[424] Following the initial 24 h incubation required for cell adhesion, cells were incubated for an additional 24 h with 200 µL of the compounds' dilution per well. Afterwards, 20 µL/well of CellTiter-Blue® reagent was added to the assay plate, shaken 10 sec and incubated for 4 hours at 37 °C and 5% CO_2. Fluorescent intensity ($531_{Ex}/595_{Em}$ nm) from each well was quantified in quadruplicates for each experiment using a multi-well plate reader (VICTOR X5, Perking Elmer). The percentage of surviving cells was calculated, using GraphPad Prism software, from the ratio of fluorescence intensity of treated to untreated cells, corrected for the interfering fluorescence of the BODIPY. The EC_{50} value for each compound was calculated as the concentration showing 50% decrease in cell growth, when compared to controls, using a nonlinear fitting of [concentration] vs response. Data is presented as mean ± SEM of at least three independent experiments.

7.4.4 Fluorescence microscopy assays

7.4.4.1 Microscopy

7.4.4.1.1 Epifluorescence microscopy

For widefield imaging, a Zeiss Axio Vert.A1 epifluorescent microscope was used. Four LD A-Plan objectives were available (5x/0.15 Ph1, 10x/0.25 Ph1, 20x/0.35 Ph1 and 40x/0.55 Ph1). Samples were excitated with a LED fluorescence module equipped with filter cube for UV (385 nm), Blue (475 nm), Green (555 nm) and Red (630 nm). Images captured with AxioCam MRm (Zeiss).

7.4.4.1.2 Confocal microscopy

For confocal imaging, a Leica SP5 confocal laser-scanning microscope equipped with a HCX PL APO 63x 1.4 NA oil immersion objective was used by courtesy of Prof. A.T. Jones and E. Sayers from Pharmacy, Cardiff University, utilizing Leica Type F immersion oil. The following laser lines were used: 405 Blue Diode (excitation wavelength 405 nm, laser intensity 30%) for DAPI and Hoechst 33342 and Argon 514 for the complexes, Argon 488 for Dextran Alexa Fluor® 488 (Dex488) and finally Argon 633 for imaging of Dextran Alexa Fluor® 647 (Dex647), CellMask™ Deep Red and Cy5™. All Argon laser intensities were set at 30%. Images were captured sequentially to avoid fluorescence channel bleed-through. Acquisition of XY format was 1024 x 1024 pixels at speed of 200 Hz for fixed cells and 400-700 Hz for live cells, with a zoom factor of 1,73. Live cell images subjected to phase correction of -33,5 and Line average = 2, frame average = 1. Whole cell Z-acquisition was conducted 0,3 µm from bottom of imaging dish or well with steps of 0,5 µm (objective step limited to > 236 nm). Single slice images were taken ~ 1,5 µm above coverslip. Acquisition was kept under 1 min to avoid bleaching of the sample unless otherwise stated.

7.4.4.2 Fixated cell experiments

Round glass coverslips (Ø 13mm, VWR) sterilised by UV-light were inserted in 24-well tissue culture- treated plates (Corning). A375 cells were seeded at a concentration of 50.000 cells/well and incubated at 37 °C under humidified atmosphere with 5% CO_2 for 48 h. The medium was discarded and fresh medium containing 5 µM of either cage or ligand was added. Following 2 h of incubation at 37 °C under tissue culture conditions or 4 °C in the fridge for the active/passive experiment, the glass coverslips were removed from the wells, washed 4x with 1x Phosphate Buffered Saline (PBS, Corning) and fixed with 4% formaldehyde (Alfa-Aesar) for 20 min at room temperature (r.t.). The coverslips were washed 3x with 1x PBS and incubated for 1 min with 40 µL 1:1000 from a 1 mg/mL stock solution of 4',6-Diamidino-2-phenylindole dihydrochloride (DAPI, Sigma-Aldrich/ MERCK) at r.t.. After washing the coverslips thrice with 1x PBS they were mounted on glass microscope slides (VWR) using Mowiol® 4-88 (Sigma-Aldrich). Fluorescence images obtained using either a Zeiss Axio Vert.A1 epifluorescent microscope or a Leica SP5 confocal laser-scanning microscope

7.4.4.2.1 Immunofluorescence early endosome labelling with EEA1

Round glass coverslips (Ø 13mm, VWR) sterilised by UV-light were inserted in 24-well tissue culture- treated plates (Corning). Cells (MCF-7 and A375) were seeded at a concentration of 50.000 cells/well and incubated at 37 °C under humidified atmosphere with 5% CO_2 for 48 h. The medium was discarded and fresh medium containing 5 µM of either cage or ligand was added. Following 1 or 2 h of incubation at 37 °C under tissue culture conditions, the glass coverslips were removed from the wells, washed 4x with 1x Phosphate Buffered Saline (PBS, Corning) and fixed with 4% formaldehyde (Alfa-Aesar) for 20 min at room temperature (r.t.). The coverslips were washed 3x with 1x PBS, blocked with 50 mM ammonium chloride for 10 min at r.t. and permeabilised for 5 min at r.t. with 200 µL of a mixture containing 0.2% Triton X-100 (Acros Organics) and 2% bovine serum albumin in 1x PBS. Following a blocking of 1 h with 150 µL of 2% Foetal Bovine Serum (FBS) / 2% BSA in 1x PBS, coverslips were incubated with 40 µL 1:200 goat anti-human EEA1 antibody (SC-6415, Santa Cruz) for 1 h at r.t. After a wash with 0.05% Triton X-100 in 1x PBS (5 min at r.t. twice) and 1x PBS, staining with primary antibody was followed by 1 h incubation with 40 µL mouse anti-goat antibody Cy5^{TM} protected by direct light. Coverslips were washed again with 0.05% Triton X-100 in 1x PBS (5 min at r.t. twice) and 1x PBS before incubation for 1 min with 40 µL 1:1000 from a 1 mg/mL stock solution of 4',6-Diamidino-2-phenylindole dihydrochloride (DAPI, Sigma-Aldrich/ MERCK) at r.t.. After washing the coverslips thrice with 1x PBS and once with H_2O, they were mounted on glass microscope slides (VWR) using Mowiol® 4-88 (Sigma-Aldrich). Fluorescence images obtained with Leica SP5.

7.4.4.3 Live cell imaging

7.4.4.3.1 Imaging dish cell culture preparation

Imaging dishes of 35 mm polystyrene (PS) (MatTek) with central cover glass area (Ø 18 mm) were seeded at a concentration of 70.000 cells/dish and incubated at 37 °C under humidified atmosphere with 5% CO_2 for 48 h. The medium was discarded and fresh medium containing 5 µM of either cage or ligand was added using A375, or 10 µM cage in the case of SK-BR-3. Following 2 h of incubation at 37 °C under tissue culture conditions unless otherwise indicated, medium containing treatment was removed, and cells were washed fourfold with phenol red free DMEM medium. All live cell images were obtained using a Leica SP5 confocal laser-scanning microscope.

7.4.4.3.2 Uptake time-lapse

After seeding A375 cells at a concentration of 70.000 cells per imaging dish for 48 h under humidified atmosphere with 5% CO_2, cells were washed fourfold with phenol red free DMEM. A closed thermostatic chamber at 37 C under 5% CO_2 atmosphere was set up for live cell imaging. The medium was discarded and fresh medium containing 5 µM of **CG1.NO$_3$** was added. Following image stabilization, a "xyt" image was taken with 30s-time interval of 512 x 512, with 700Hz speed and zoom of 2.5 on a Leica SP5. Focus drift correction was manual during acquisition to counter axial displacement.

Captured images were analysed after acquisition using ImageJ.[455] Pixels above ImageJ threshold "Otsu" were determined as fluorescent (Figure 7.25). Regions of interest were selected with an average area of 500 pixels representing intracellular and extracellular locations. The mean background fluorescent intensity was subsequentially subtracted from the mean intracellular fluorescent intensity per time point, giving the corrected intensity value (Figure 7.26).

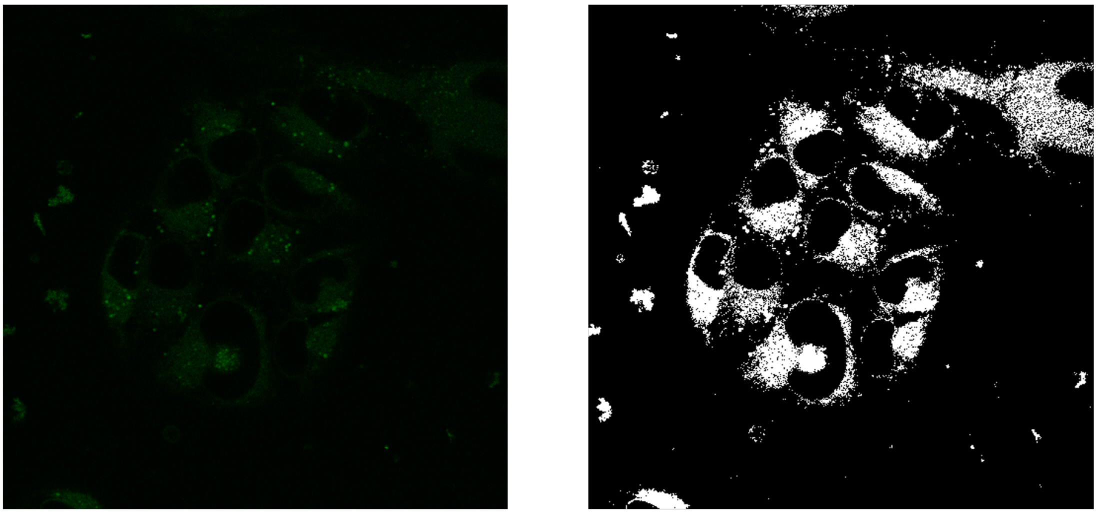

Image before processing

Otsu treshold applied

Figure 7.25*: Example illustrating use of threshold. Image on the left shows A375 cells at t = 64,5 min. Image on the right is the same shot, converted so white represent pixel intensity above threshold set by "Otsu" and black below.*

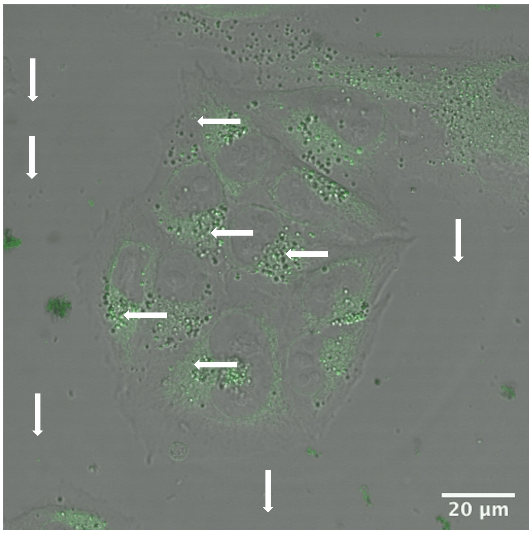

Figure 7.26*: Example illustrating use of regions of interest (ROI) indicated by arrows, with 5 background and 5 intracellular selections.*

7.4.4.3.3 Plasma membrane staining

A mixture of 1 µM Hoechst and 1 µg/mL CellMask^{TM} Deep Red Plasma membrane Stain (C10046, Invitrogen) was added to A375 cells following steps described in 7.*4.4.3.1*. After 5 min, cells were washed twice with phenol red free medium and imaged.

7.4.4.3.4 Late endosome / Lysosomal colocalisation Dextran

Imaging dishes of 35 mm polystyrene (PS) (MatTek) with central cover glass area (Ø 18 mm) were seeded at a concentration of 70.000 A375 cells/dish and incubated at 37 °C under humidified atmosphere with 5% CO_2 for 24 h. After, medium was discarded and lysosomes were labelled with a 4 h pulse of 200 µg/mL Dex-647 (10.000 mol wt. Fisher Scientific) in fresh DMEM. Probe was allowed to chase for 16 h in dextran-free medium. The medium was discarded, and cells were incubated for 2 h with fresh medium containing 5 µM of treatment (**CG1.NO$_3$**, **CG1.BF$_4$** or **LG1**) or 200 µg/mL Dex-488 (10.000 mol wt. Fisher Scientific) as control at 37°C (CO_2 5%). Cells were then washed with phenol-red free medium and imaged at 2 h and re-imaged at 3 h and 5 h. For each timepoint, five images were taken. In between imaging, cells were kept at 37 °C humidified atmosphere (CO_2 5%). Figure 7.27 illustrated the timeline of the assay.

Image analysis was performed using ImageJ.[455] For each timepoint, "Otsu" threshold was determined from brightest image and applied as mask for the other four images. Pearsons correlation coefficient (PCC) and Manders coefficients (MC) were determined and averaged with standard deviation.

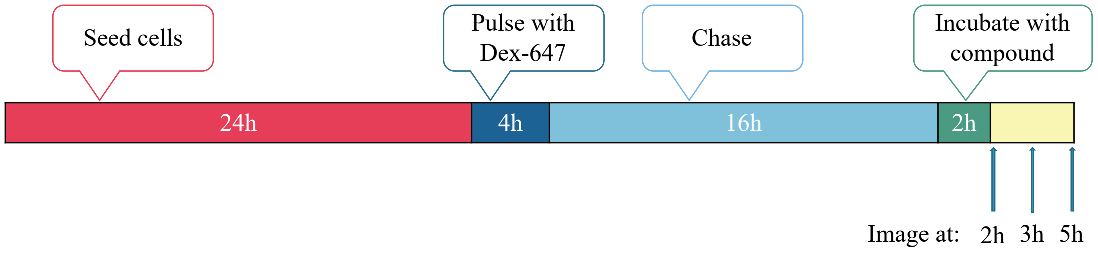

Figure 7.27:*Timeline of colocalization assay*

Chapter 8: Overall Conclusions

This researched aimed to explore the potential of gold-based compounds as anticancer agents, as well as of supramolecular metal-based entities for drug delivery. As such, **part A** of the thesis describes small molecule gold(III) complexes with different scaffolds designed as selective aquaporin (AQP) inhibitors that have been studied for their ability to target these membrane proteins, as well as for their cytotoxic effect *in vitro*. In **part B,** the potential of supramolecular coordination complexes, specifically self-assembled metallacages, as drug delivery systems for cisplatin has been studied *in vitro*. Thus, in an effort to understand the pathways of uptake and intracellular accumulation of the metallacages, of the $[Pd_2L_4]^{4+}$ type, were functionalised with either a tumour targeting biomimetic ligand or a fluorescent moiety.

Part A

The literature study of *Chapter 2* concerns the role of aquaporins in cancer disease development, and their expression correlation to cancer reveals their involvement in the carcinogenesis and pathogenesis of tumour-associated oedema, as well as in tumour cell proliferation and migration. The exact nature of this correlation is still the subject of discussion, emphasizing the need to develop selective AQPs inhibitors to study the mechanism of these potential, but still elusive, therapeutic targets. With this in mind, inspired by the selective and potent hAQP3 inhibitor **Auphen**, different families of coordination and organometallic gold(III) compounds have been designed and tested for their inhibition properties against AQP isoforms, particularly aquaglyceroporin channels, also able to transport hydrogen peroxide across cell membranes. Thus, initial structure activity relationships have been obtained and also indications of the key determinants for AQP selectivity and inhibition. In the near future, such potent and selected inhibitors could be used as chemical probes to unravel the AQPs roles in the molecular mechanisms of diseases (cancer and beyond) and to provide new tools in chemotherapy and imaging.

In *Chapter 3,* two new series of Au(III) complexes featuring bidentate N^N donor ligands were presented, the first featuring a pyridine-benzimidazole scaffold (**C1-C12**), and the second series 1,10-phenanthroline ligands (**C13-18**). Evaluation of their stability by UV-visible spectroscopy, revealed that changing the ligands' substitution patterns influences the stability of the resulting Au(III) complexes in aqueous environment. Stopped-flow spectroscopy showed most of the gold complexes are potent inhibitors of the human water and glycerol channel AQP3 in human red blood cells (hRBC), while they are inactive as inhibitors of the water channel AQP1. A few members of the phenanthroline-based series showed AQP3 inhibition properties which outperformed the benchmark compound **Auphen.** Furthermore, the antiproliferative effects of both series were studied in a small panel of human cancer cells known to express AQP3, indicating that the complexes are able to inhibit cell proliferation *in vitro* to varying degrees, not necessarily perfectly matching the observed AQP3 inhibition properties. Further studies are certainly necessary to validate the mechanisms of action of this family of compounds.

Interestingly, the computational approach elucidated that AQP3 inhibition for the Au(III) 1,10-phenanthroline complexes is the result of protein conformational changes, upon coordinative gold binding to a critical Cys residue, which in turn induces pore closure. Furthermore, the computational study highlighted the importance of non-covalent interactions between the organic phenanthroline ligand and the protein extracellular pocket which may also account for the differences in inhibitory effects.

The inhibition of glycerol permeation *via* four aquaglyceroporins in hRBCs and in an optimized *Saccharomyces cerevisiae* model by scattered light intensity and fluorescence stopped-flow spectroscopy was studied for a family of five cyclometalated Au(III) C^N compounds (**1-5**) in *Chapter 4*. The organogold complexes are known to react readily with cysteine residues in proteins. Potent and irreversible inhibition of glycerol permeation was observed especially against hAQP3 (hRBCs) and in yeast cells expressing either hAQP3 or hAQP10, whilst the effect on hAQP7 and hAQP9 were generally moderate. Additionally, in an effort to rationalize the inhibitor selectivity towards the AQPs isoform, homology model systems for all aquaglyceroporins were developed, suggesting the compound's effects to be partially dependent on the availability of Cys residues to bind Au(III) at the extracellular pore side. In some cases, gold coordination adduct formation at Cys residues can be followed by metal-templated transfer of the C^N ligand to the thiol group (C-S bond formation *via* reductive elimination) leading to irreversible binding to peptides. Further investigation into the mechanisms of hAQP10 inhibition by **2**, one of the most potent inhibitors of the series, was performed using metadynamics. In details, the advanced atomistic simulation revealed that upon covalent binding of the C^N ligand of complex **2** to Cys209, an overall protein conformational change is induced that leads to pore shrinkage, significantly reducing glycerol conductance.

Overall, the AQPs inhibition properties of both coordination and organometallic Au(III) complexes hold promise to develop them as chemical probes to study the function of such membrane channels in biological systems. However, the organogold compounds are certainly more attractive as possible drug leads, being endowed with higher stability in physiological conditions as well as being endowed with a peculiar reactivity leading to irreversible protein modification at Cys sites.

Part B

Chapter 5 presented four new $[Pd_2L_4]^{4+}$ metallacages bioconjugated to integrin ligands with different binding affinity and selectivity for tumour cells, designed as drug delivery systems for the anticancer drug cisplatin, in an effort to address its issues with efficacy and applicability. After confirming cage formation and encapsulation of cisplatin by NMR spectroscopy, as well as the cages' integrin binding selectivity, cage-encapsulated cisplatin was subjected to *in vitro* testing against a panel of cancer cells. Of note, encapsulated cisplatin showed a marked increase of cytotoxicity in melanoma A375 cells overexpressing αvβ3 integrins. Interestingly, *ex vivo* studies using precision cut tissue slices indicated a reduced toxicity towards healthy liver and kidney tissues for the cage-encapsulated cisplatin compared to its free form, potentially due to a decreased Pt uptake. Indeed, metal content analysis of these tissue samples by inductively coupled plasma mass spectrometry (ICP-MS) showed a significant lower accumulation of encapsulated drug compared to free cisplatin.

In *Chapter 6*, aiming to elucidate the uptake and sub-cellular localisation in cancer cells of metallacages, three novel fluorescent $[Pd_2L_4]^{4+}$ metallacages featuring 3,5-bis(3-ethynylpyridine)phenyl ligands *exo*-functionalised with boron dipyrromethene (BODIPY) moieties were studied. The cages showed remarkable luminescent properties with QY_F of 50-70% and excitation wavelength in the visible region (ca. 540 nm). Following stability studies in physiological relevant conditions in and without presence of reducing agent GSH, metallacages **C1.BF$_4$** and **C1.NO$_3$** were selected for further analysis. Encapsulation of up to 2 equiv. of cisplatin was confirmed with ^{1}H NMR spectroscopy. A preliminary cytotoxicity screening of metallacages against a small panel of human cancer cell lines showed a scarce toxicity *in vitro*, highlighting their suitability as non-toxic drug delivery vehicles. Additional microscopy studies to achieve a preliminary indication regarding cage uptake and identification of sub-cellular localisation in A375 cancer cells were performed, using both conventional and confocal fluorescence microscopy. Remarkably, the cages appear to be subjected to active endocytic transport, prior to accumulation in intracellular vesicles.

Inspired by the promising results of *Chapter 6*, *Chapter 7* focused on the identification of the nature of the fluorescent metallacage labelled structures with two slightly optimised novel Pd_2L_4 metallacages, again *exo*-functionalised with BODIPY units. The green fluorescent BODIPY moieties contributed to the excellent luminescent properties (QY_F = 80%) at excitation wavelength of ca. 540 nm, and the stability in physiologically relevant conditions was examined by UV-visible spectroscopy and ^{1}H NMR spectroscopy. Encapsulation of the equivalent of 2 guest molecules cisplatin per cage was confirmed with ^{1}H NMR spectroscopy. *In vitro* antiproliferative screening of **CG1.BF$_4$** and **CG1.NO$_3$** and their corresponding ligand against a panel of human cancer cell lines demonstrated no cytotoxic effects. The presence of the BODIPY-moiety allowed for fluorescent microscopy studies to elucidate the intracellular fate of the ligand and cages. An active mode of uptake in human melanoma cells (A375) was confirmed, but no uptake in in human breast cancer cells of the MCF-7 type. Colocalization assays performed to identify the vesicles of complex accumulation in A375 cells ruled out early endosomes and lysosomes and pointed to melanosomes instead. Preliminary cytotoxicity studies revealed no change in anticancer activity for free cisplatin versus cisplatin encapsulated in **CG1.BF$_4$**, suggesting both host and guest to be refrained from entering the cytoplasm. Introduction of a third cancer cell line, breast cancer cells SK-BR-3, demonstrated that cisplatin encapsulated in **CG1.BF$_4$** did exhibit increased anticancer effects compared to the free compound. Fluorescence microscopy studies in SK-BR-3 with **CG1.BF$_4$** revealed a diffuse cytoplasmic fluorescence presence instead of the pronounced vesicular accumulation seen in A375, suggesting the cage cargo (cisplatin) is available for binding to its intracellular targets in SK-BR-3.

Overall, these novel integrin ligand-conjugated metallacages and BODIPY functionalized metallacages show great promise drug delivery systems, as illustrated by the improved targeting and protection from speciation of anticancer drug cisplatin. The characteristic green fluorescence of the BODIPY-complexes provided new insights using confocal microscopy, confirming active uptake as well as localising compound accumulation in a cell-type specific fashion in the intracellular cytoplasmic vesicles called melanosomes. The value of fluorescence microscopy as a powerful tool has been demonstrated in addition to antiproliferative screening.

Ongoing studies in our laboratory are attempting the conjugation of the $[Pd_2L_4]^{4+}$ cages to red-emitting BODIPY moieties, which could be suitable for imaging in tissues. Moreover, another challenge in this area, is the obtainment of heteroleptic metallacages featuring different *exo*-functionalized ligands: i.e. with targeting groups and different imaging modalities. This new generation metallacages could act as *theragnostic* systems *in vivo*.

References

1. Waldron, K. J. *et al*. Metalloproteins and metal sensing. *Nature* **460**, 823–830 (2009).
2. Kern, K. A. & Rosenberg, R. J. Preoperative lymphoscintigraphy during lymphatic mapping for breast cancer: improved sentinel node imaging using subareolar injection of technetium 99m sulfur colloid. *Journal of the American College of Surgeons* **191**, 479–489 (2000).
3. Virgolini, I. *et al.* Procedure guidelines for PET/CT tumour imaging with 68Ga-DOTA-conjugated peptides: 68Ga-DOTA-TOC, 68Ga-DOTA-NOC, 68Ga-DOTA-TATE. *European Journal of Nuclear Medicine and Molecular Imaging* **37**, 2004–2010 (2010).
4. Mjos, K. D. & Orvig, C. Metallodrugs in medicinal inorganic chemistry. *Chemical Reviews* vol. 114 4540–4563 (2014).
5. Rosenberg, B. *et al*. Inhibition of cell division in escherichia coli by electrolysis products from a platinum electrode. *Nature* **205**, 698–699 (1965).
6. Kauffman, G. B., Pentimalli, R., Doldi, S. & Hall, M. D. Michele Peyrone (1813-1883), discoverer of Cisplatin. *Platinum Metals Review* **54**, 250–256 (2010).
7. Rosenberg, B. *et al.* Platinum Compounds: a New Class of Potent Antitumour Agents. *Nature* **222**, 385–386 (1969).
8. Wang, D. & Lippard, S. J. Cellular processing of platinum anticancer drugs. *Nature Reviews Drug Discovery* **4**, 307–320 (2005).
9. McWhinney, S. R. *et al.* Platinum neurotoxicity pharmacogenetics. *Molecular Cancer Therapeutics* **8**, 10–16 (2009).
10. Karasawa, T. & Steyger, P. S. An integrated view of cisplatin-induced nephrotoxicity and ototoxicity. *Toxicology Letters* **237**, 219–227 (2015).
11. Makovec, T. Cisplatin and beyond: Molecular mechanisms of action and drug resistance development in cancer chemotherapy. *Radiology and Oncology* vol. 53 148–158 (2019).
12. *Bioinorganic Medicinal Chemistry*. (Wiley-VCH Verlag GmbH & Co. KGaA, 2011).
13. Ndagi, U. *et al*. Metal complexes in cancer therapy - an update from drug desing perspective. *Drug Design, Development and Therapy* **11**, 599–616 (2017).
14. Harrap, K. R. Preclinical studies identifying carboplatin as a viable cisplatin alternative. *Cancer Treatment Reviews* **12**, 21–33 (1985).
15. Shimada, M. *et al.* Nedaplatin: a cisplatin derivative in cancer chemotherapy. *Cancer Management and Research* 67 (2013) doi:10.2147/CMAR.S35785.
16. Lee, K. H. *et al.* Randomized, Multicenter, Phase III Trial of Heptaplatin 1-hour Infusion and 5-Fluorouracil Combination Chemotherapy Comparing with Cisplatin and 5-Fluorouracil Combination Chemotherapy in Patients with Advanced Gastric Cancer. *Cancer Research and Treatment* **41**, 12 (2009).
17. Lobaplatin. *Drugs in R & D* **4**, 369–372 (2003).
18. Harrap, K. R. *Preclinical studies identifying carboplatin as a viable cisplatin alternative*. *Cancer Treatment Reviews* vol. 2 (1985).
19. Bajpai, J. *et al.* Carboplatin hypersensitivity in relapsed ovarian carcinoma: A therapeutic challenge. *Indian Journal of Medical and Paediatric Oncology* **35**, 17 (2014).

20. Rixe, O. *et al.* Oxaliplatin, Tetraplatin, Cisplatin, and Carboplatin: Spectrum of Activity in Drug-Resistant Cell Lines and in the Cell Lines of the National Cancer Institute's Anticancer Drug Screen Panel. *Biochemical Pharmacology* vol. 52 (1996).
21. Raymond, E. *et al.* Oxaliplatin: A review of preclinical and clinical studies. *Annals of Oncology* vol. 9 1053–1071 (1998).
22. Salem, M. E. *et al.* Evaluation of the change of outcomes over a 10-year period in patients with stage III colon cancer: pooled analysis of 6501 patients treated with fluorouracil, leucovorin, and oxaliplatin in the ACCENT database. *Annals of Oncology* **31**, 480–486 (2020).
23. de Gramont, A. *et al.* Leucovorin and Fluorouracil With or Without Oxaliplatin as First-Line Treatment in Advanced Colorectal Cancer. *Journal of Clinical Oncology* **18**, 2938–2947 (2000).
24. Cassidy, J. & Misset, J.-L. Oxaliplatin-related side effects: Characteristics and management. *Seminars in Oncology* **29**, asonc02905p0011 (2002).
25. Wheate, N. J. *et al.* The status of platinum anticancer drugs in the clinic and in clinical trials. *Dalton Transactions* **39**, 8113–8127 (2010).
26. Johnstone, T. C. *et al.* The Next Generation of Platinum Drugs: Targeted Pt(II) Agents, Nanoparticle Delivery, and Pt(IV) Prodrugs. *Chemical Reviews* **116**, 3436–3486 (2016).
27. Bhargava, A. & Vaishampayan, U. N. Satraplatin: Leading the new generation of oral platinum agents. *Expert Opinion on Investigational Drugs* vol. 18 1787–1797 (2009).
28. Forastiere, A. A. *et al.* Pharmacokinetic and Toxicity Evaluation of Five-Day Continuous Infusion versus Intermittent Bolus m-Diamminedichloroplatinum(II) in Head and Neck Cancer Patients. *CANCER RESEARCH* **48**, 3869–3874 (1988).
29. Ivanov, A. I. *et al.* Cisplatin binding sites on human albumin. *Journal of Biological Chemistry* **273**, 14721–14730 (1998).
30. Khalaila, I. *et al.* A mass spectrometric and molecular modelling study of cisplatin binding to transferrin. *ChemBioChem* **6**, 1788–1795 (2005).
31. Chen, D. *et al.* Binding and Aggregation of Human g-Globulin by cis-Diamminedichloroplatinum(II) through Disulfide bond. *Biological and Pharmaceutical Bulletin* **17**, 1561–1566 (1994).
32. Sooriyaarachchi, M. *et al.* Comparative hydrolysis and plasma protein binding of cis-platin and carboplatin in human plasma in vitro. *Metallomics* **3**, 49–55 (2011).
33. CBG MEB. SmPC 1218.9v.IL Cisplatine 0,5 mg/ml PCH, concentraat voor oplossing voor infusie. https://www.geneesmiddeleninformatiebank.nl/smpc/h101429_smpc.pdf (2019).
34. CBG MEB. Cisplatine 0,5 mg/ml PCH, concentrate for solution for infusion Cisplatine 1 mg/ml PCH, concentrate for solution for infusion. *PUBLIC ASSESSMENT REPORT of the Medicines Evaluation Board in the Netherlands* 1–11 https://www.geneesmiddeleninformatiebank.nl/Pars/h101429.pdf (2009).
35. Bruno, P. M. *et al.* A subset of platinum-containing chemotherapeutic agents kills cells by inducing ribosome biogenesis stress. *Nature Medicine* **23**, 461–471 (2017).
36. Eljack, N. D. *et al.* Mechanisms of cell uptake and toxicity of the anticancer drug cisplatin. *Metallomics* **6**, 2126–2133 (2014).

37. Holzer, A. K. & Howell, S. B. The internalization and degradation of human copper transporter 1 following cisplatin exposure. *Cancer Research* **66**, 10944–10952 (2006).
38. Yonezawa, A. *et al*. Cisplatin and oxaliplatin, but not carboplatin and nedaplatin, are substrates for human organic cation transporters (SLC22A1-3 and multidrug and toxin extrusion family). *Journal of Pharmacology and Experimental Therapeutics* **319**, 879–886 (2006).
39. Hall, M. D. *et al*. The role of cellular accumulation in determining sensitivity to platinum-based chemotherapy. *Annual Review of Pharmacology and Toxicology* vol. 48 495–535 (2008).
40. CBG MED. SmPC 0519.9v.PNren Carbosin 10 MG/ML concentraat voor oplossing voor intranveneuze infusie. https://www.geneesmiddeleninformatiebank.nl/smpc/h23244_smpc.pdf (2019).
41. CBG MED. SmPC 0319.15v.IL Oxalisin 5 MG/ML concentraat voor oplossing voor infusie. https://www.geneesmiddeleninformatiebank.nl/smpc/h34033_smpc.pdf (2019).
42. Baik, M. H. *et al*. Theoretical Study of Cisplatin Binding to Purine Bases: Why Does Cisplatin Prefer Guanine over Adenine? *Journal of the American Chemical Society* **125**, 14082–14092 (2003).
43. Jamieson, E. R. & Lippard, S. J. Structure, Recognition, and Processing of Cisplatin−DNA Adducts. *Chemical Reviews* **99**, 2467–2498 (1999).
44. Swift, L. H. & Golsteyn, R. M. Cytotoxic amounts of cisplatin induce either checkpoint adaptation or apoptosis in a concentration-dependent manner in cancer cells. *Biology of the Cell* **108**, 127–148 (2016).
45. Martinho, N. *et al.* Cisplatin-membrane interactions and their influence on platinum complexes activity and toxicity. *Frontiers in Physiology* vol. 10 (2019).
46. Hahn, M., Kleine, M. & Sheldrick, W. S. Interaction of cisplatin with methionine- and histidine-containing peptides: Competition between backbone binding, macrochelation and peptide cleavage. *Journal of Biological Inorganic Chemistry* **6**, 556–566 (2001).
47. Marullo, R. *et al.* Cisplatin induces a mitochondrial-ros response that contributes to cytotoxicity depending on mitochondrial redox status and bioenergetic functions. *PLoS ONE* **8**, (2013).
48. Gordon, J. A. & Gattone Ii, V. H. Mitochondrial alterations in cisplatin-induced acute renal failure. *Am. J. Physiol* **19**, F991–F998 (1986).
49. Kubala, M. *et al.* Na+/K+-ATPase inhibition by cisplatin and consequences for cisplatin nephrotoxicity. *Biomedical Papers* **158**, 194–200 (2014).
50. Kiyonari, S. *et al.* The 1,2-diaminocyclohexane carrier ligand in oxaliplatin induces p53-dependent transcriptional repression of factors involved in thymidylate biosynthesis. *Molecular Cancer Therapeutics* **14**, 2332–2342 (2015).
51. Rocha, C. R. R. *et al.* DNA repair pathways and cisplatin resistance: An intimate relationship. *Clinics* **73**, 1–10 (2018).
52. Heffeter, P. *et al.* Resistance against novel anticancer metal compounds: Differences and similarities. *Drug Resistance Updates* **11**, 1–16 (2008).
53. Kelland, L. The resurgence of platinum-based cancer chemotherapy. *Nature Reviews Cancer* **7**, 573–584 (2007).
54. Burger, H. *et al.* Drug transporters of platinum-based anticancer agents and their clinical significance. *Drug Resistance Updates* **14**, 22–34 (2011).

55. Wen, X. *et al.* Transgenic expression of the human MRP2 transporter reduces cisplatin accumulation and nephrotoxicity in Mrp2-Null mice. *American Journal of Pathology* **184**, 1299–1308 (2014).
56. Kasparkova, J.*et al*. Unique properties of DNA interstrand cross-links of antitumor oxaliplatin and the effect of chirality of the carrier ligand. *Chemistry - A European Journal* **14**, 1330–1341 (2008).
57. Fink, D. *et al.* The Role of DNA Mismatch Repair in Platinum Drug Resistance. *CANCER* **56**, 4881–4886 (1996).
58. Okuno, S. *et al.* Role of cystine transport in intracellular glutathione level and cisplatin resistance in human ovarian cancer cell lines. *British Journal of Cancer* **88**, 951–956 (2003).
59. Mistry, P. *et al*. The relationships between glutathione, glutathione-S-transferase and cytotoxicity of platinum drugs and melphalan in eight human ovarian carcinoma cell lines. *Br. J. Cancer* **64**, 215–220 (1991).
60. Galluzzi, L. *et al.* Molecular mechanisms of cisplatin resistance. *Oncogene* vol. 31 1869–1883 (2012).
61. Reddy, S. L., Endo, T. & Reddy, G. S. *Advanced Aspects of Spectroscopy*. (InTech, 2012). doi:10.5772/2757.
62. Berners-Price, S. J. Gold-Based Therapeutic Agents: A New Perspective. in *Bioinorganic Medicinal Chemistry* (ed. Alessio, E.) 197–222 (Wiley-VCH Verlag GmbH & Co. KGaA, 2011). doi:10.1002/9783527633104.ch7.
63. Meier-Menches, S. M. *et al*. Structure-activity relationships for ruthenium and osmium anticancer agents-towards clinical development. *Chemical Society Reviews* **47**, 909–928 (2018).
64. Santini, C. *et al.* Advances in copper complexes as anticancer agents. *Chemical Reviews* **114**, 815–862 (2014).
65. Basu, U. *et al.* Recent advances in the chemistry of iron-based chemotherapeutic agents. *Coordination Chemistry Reviews* vol. 417 (2020).
66. Casini, A. *et al*. Medicinal Chemistry of Gold Anticancer Metallodrugs. in *Metallo-Drugs: Development and Action of Anticancer Agents* (eds. Sigel, A., Sigel, H., Freisinger, E. & Sigel, R. K. O.) 199–217 (De Gruyter, 2018). doi:10.1515/9783110470734-013.
67. Rademaker-Lakhai, J. M. A Phase I and Pharmacological Study with Imidazolium-trans-DMSO-imidazole-tetrachlororuthenate, a Novel Ruthenium Anticancer Agent. *Clinical Cancer Research* **10**, 3717–3727 (2004).
68. Leijen, S. *et al.* Phase I/II study with ruthenium compound NAMI-A and gemcitabine in patients with non-small cell lung cancer after first line therapy. *Investigational New Drugs* **33**, 201–214 (2015).
69. Swietach, P. *et al*. The chemistry, physiology and pathology of pH in cancer. *Philosophical Transactions of the Royal Society B: Biological Sciences* **369**, 20130099–20130099 (2014).
70. Russo, A. *et al*. Selective modulation of glutathione levels in human normal versus tumor cells and subsequent differential response to chemotherapy drugs. *Cancer research* **46**, 2845–8 (1986).
71. Hartinger, C. G. *et al.* KP1019, A New Redox-Active Anticancer Agent - Preclinical Development and Results of a Clinical Phase I Study in Tumor Patients. *Chemistry & Biodiversity* **5**, 2140–2155 (2008).
72. Stevens, S.K. *et al.* The anticancer ruthenium complex KP1019 induces DNA damage, leading to cell cycle delay and cell death in Saccharomyces cerevisiae. *Molecular Pharmacology* **83**, 225-234 (2013).

73. Alessio, E. & Messori, L. NAMI-A and KP1019/1339, Two Iconic Ruthenium Anticancer Drug Candidates Face-to-Face: A Case Story in Medicinal Inorganic Chemistry. *Molecules* **24**, 1995 (2019).
74. Kapitza, S. *et al.* Heterocyclic complexes of ruthenium(III) induce apoptosis in colorectal carcinoma cells. *Journal of Cancer Research and Clinical Oncology* **131**, 101–110 (2005).
75. Bergamo, A. & Sava, G. Ruthenium anticancer compounds: Myths and realities of the emerging metal-based drugs. *Dalton Transactions* vol. 40 7817–7823 (2011).
76. Romero-Canelón, I. Chapter 2. Ruthenium, Osmium and Iridium in the Fight Against Cancer. in *Metal-based Anticancer Agents* (eds. Casini, A., Vessieres, A. & Meier-Menches, S. M.) (2019). doi:10.1039/9781788016452-00031.
77. Carlos Lima, J. & Rodríguez, L. Applications of gold(i) alkynyl systems: A growing field to explore. *Chemical Society Reviews* **40**, 5442–5456 (2011).
78. Casini, A. *et al.* Chemistry, antiproliferative properties, tumor selectivity, and molecular mechanisms of novel gold(III) compounds for cancer treatment: A systematic study. *Journal of Biological Inorganic Chemistry* **14**, 1139–1149 (2009).
79. Abruzzo, J. L. Auranofin: A New Drug for Rheumatoid Arthritis. *Annals of Internal Medicine* **105**, 274 (1986).
80. Varghese, E. & Büsselberg, D. Auranofin, an Anti-Rheumatic Gold Compound, Modulates Apoptosis by Elevating the Intracellular Calcium Concentration ([Ca2+]i) in MCF-7 Breast Cancer Cells. *Cancers* **6**, 2243–2258 (2014).
81. Park, N. & Chun, Y. J. Auranofin promotes mitochondrial apoptosis by inducing annexin A5 expression and translocation in human prostate cancer cells. *Journal of Toxicology and Environmental Health - Part A: Current Issues* **77**, 1467–1476 (2014).
82. Marzano, C. *et al.* Inhibition of thioredoxin reductase by auranofin induces apoptosis in cisplatin-resistant human ovarian cancer cells. *Free Radical Biology and Medicine* **42**, 872–881 (2007).
83. Nobili, S. *et al.* Gold compounds as anticancer agents: chemistry, cellular pharmacology, and preclinical studies. *Medicinal Research Reviews* **29**, n/a-n/a (2009).
84. Messori, L. *et al.* Gold(III) complexes as potential antitumor agents: Solution chemistry and cytotoxic properties of some selected gold(III) compounds. *Journal of Medicinal Chemistry* **43**, 3541–3548 (2000).
85. Berners-Price, S. J. & Filipovska, A. Gold compounds as therapeutic agents for human diseases. *Metallomics* **3**, 863–873 (2011).
86. Bertrand, B. *et al.* Caffeine-based gold(I) N-heterocyclic carbenes as possible anticancer agents: synthesis and biological properties. *Inorganic chemistry* **53**, 2296–303 (2014).
87. Tong, K.-C. *et al.* Anticancer Gold(III) Compounds With Porphyrin or N-heterocyclic Carbene Ligands. *Frontiers in Chemistry* **8**, (2020).
88. Marcon, G. *et al.* Gold(III) complexes with bipyridyl ligands: Solution chemistry, cytotoxicity, and DNA binding properties. *Journal of Medicinal Chemistry* **45**, 1672–1677 (2002).
89. Messori, L. *et al.* Gold(III) complexes as potential antitumor agents: Solution chemistry and cytotoxic properties of some selected gold(III) compounds. *Journal of Medicinal Chemistry* **43**, 3541–3548 (2000).

90. Che, C. M. *et al.* Gold(III) porphyrins as a new class of anticancer drugs: Cytotoxicity, DNA binding and induction of apoptosis in human cervix epitheleoid cancer cells. *Chemical Communications* **3**, 1718–1719 (2003).
91. Giovagnini, L. *et al.* Synthesis, characterization, and comparative in vitro cytotoxicity studies of platinum(II), palladium(II), and gold(III) methylsarcosinedithiocarbamate complexes. *Journal of Medicinal Chemistry* **48**, 1588–1595 (2005).
92. Buckley, R. G. *et al.* Antitumor Properties of Some 2-[(Dimethylamino)methyl]phenylgold(III) Complexes. (1996).
93. Calamai, P. *et al.* Cytotoxic effects of gold(III) complexes on established human tumor cell lines sensitive and resistant to cisplatin. *Anti-Cancer Drug Design* **13**, 67–80 (1998).
94. Shaw, C. F. Gold-Based Therapeutic Agents. *Chemical Reviews* **99**, 2589–2600 (1999).
95. Parish, R. v. *et al.* Chemical and Biological Studies of Dichloro(2-((dimethylamino)methyl)phenyl)gold(III). *Inorganic Chemistry* **35**, (1996).
96. Bertrand, B. *et al.* Exploring the potential of gold(iii) cyclometallated compounds as cytotoxic agents: variations on the C^N theme. *Dalton Transactions* **44**, 11911–11918 (2015).
97. Thomas, S. R. & Casini, A. Gold compounds for catalysis and metal-mediated transformations in biological systems. *Current Opinion in Chemical Biology* vol. 55 103–110 (2020).
98. Wenzel, M. N. *et al.* Cyclometalated Au III Complexes for Cysteine Arylation in Zinc Finger Protein Domains: towards Controlled Reductive Elimination. *Chemistry – A European Journal* **25**, chem.201901535 (2019).
99. Thomas, S. R. *et al.* Exploring the Chemoselectivity towards Cysteine Arylation by Cyclometallated AuIII Compounds: New Mechanistic Insights. *ChemBioChem* **21**, 3071–3076 (2020).
100. Casini, A. & Messori, L. Molecular Mechanisms and Proposed Targets for Selected Anticancer Gold Compounds. *Current Topics in Medicinal Chemistry* **11**, 2647–2660 (2011).
101. de Almeida, A. *et al.* Emerging protein targets for metal-based pharmaceutical agents: An update. *Coordination Chemistry Reviews* **257**, 2689–2704 (2013).
102. Al-Maythalony, B. A. *et al.* 1H,13C NMR and UV spectroscopy studies of gold(III)-tetracyanide complex with l-cysteine, glutathione, captopril, l-methionine and dl-seleno-methionine in aqueous solution. *Inorganica Chimica Acta* **363**, 3244–3253 (2010).
103. Bindoli, A. *et al.* Thioredoxin reductase: A target for gold compounds acting as potential anticancer drugs. *Coordination Chemistry Reviews* **253**, 1692–1707 (2009).
104. Wenzel, M. N. *et al.* Selective targeting of PARP-1 zinc finger recognition domains with Au(III) organometallics. *Chemical Communications* **54**, 611–614 (2018).
105. Abbehausen, C. Zinc finger domains as therapeutic targets for metal-based compounds-an update. *Metallomics* vol. 11 15–28 (2019).
106. Mendes, F. *et al.* Metal-based inhibition of poly(ADP-ribose) polymerase-the guardian angel of DNA. *Journal of Medicinal Chemistry* **54**, 2196–2206 (2011).
107. Martins, A. P. *et al.* Targeting Aquaporin Function: Potent Inhibition of Aquaglyceroporin-3 by a Gold-Based Compound. *PLoS ONE* **7**, e37435 (2012).

108. Martins, A. P. *et al.* Aquaporin Inhibition by Gold(III) Compounds: New Insights. *ChemMedChem* **8**, 1086–1092 (2013).
109. de Almeida, A. *et al.* The mechanism of aquaporin inhibition by gold compounds elucidated by biophysical and computational methods. *Chemical Communications* **53**, 3830–3833 (2017).
110. Schneider, H. J. Binding mechanisms in supramolecular complexes. *Angewandte Chemie - International Edition* **48**, 3924–3977 (2009).
111. Zhou, J. *et al.* Supramolecular chemotherapy based on host-guest molecular recognition: A novel strategy in the battle against cancer with a bright future. *Chemical Society Reviews* **46**, 7021–7053 (2017).
112. Casini, A. *et al.* The Promise of Self-Assembled 3D Supramolecular Coordination Complexes for Biomedical Applications. *Inorganic Chemistry* **56**, 14715–14729 (2017).
113. S. Zhang. Molecular Self-assembly. in *Encyclopedia of Materials : Science and Technology* 5822–5829 (2001). doi:10.1016/B0-08-043152-6/01012-3.
114. Alberts, B. *et al.* DNA and Chromosomes. in *Molecular Biology of the Cell* 1463 (Garland Science, 2002).
115. Bohne, C. Supramolecular dynamics. *Chemical Society Reviews* vol. 43 4037–4050 (2014).
116. Varga, M. Self-assembly of nanobiomaterials. in *Fabrication and Self-Assembly of Nanobiomaterials: Applications of Nanobiomaterials* 57–90 (Elsevier Inc., 2016). doi:10.1016/B978-0-323-41533-0.00003-9.
117. Senapati, S., Mahanta, A. K., Kumar, S. & Maiti, P. Controlled drug delivery vehicles for cancer treatment and their performance. *Signal Transduction and Targeted Therapy* **3**, 7 (2018).
118. Kalepu, S. *et al.* Liposomal drug delivery system-A Comprehensive Review. *Article in International Journal of Drug Development & Research* **5**, 62–75 (2013).
119. Wakaskar, R. R. Polymeric Micelles and their Properties. *Journal of Nanomedicine & Nanotechnology* **08**, (2017).
120. Batrakova, E. v. *et al.* Polymer Micelles as Drug Carriers. *Nanoparticulates as Drug Carriers*. Imperial College Press, London 56 (2006). doi:10.1142/9781860949074_0005.
121. Gheybi, H. & Adeli, M. Supramolecular anticancer drug delivery systems based on linear-dendritic copolymers. *Polymer Chemistry* **6**, 2580–2615 (2015).
122. Kapoor, D. N. *et al.* PLGA: A unique polymer for drug delivery. *Therapeutic Delivery* **6**, 41–58 (2015).
123. Han, F. Y. *et al.* Bioerodable PLGA-based microparticles for producing sustained-release drug formulations and strategies for improving drug loading. *Frontiers in Pharmacology* vol. 7 (2016).
124. Liechty, W. B. *et al.* Polymers for drug delivery systems. *Annual Review of Chemical and Biomolecular Engineering* **1**, 149–173 (2010).
125. Iyer, A. K. *et al.* Exploiting the enhanced permeability and retention effect for tumor targeting. *Drug Discovery Today* **11**, 812–818 (2006).
126. Lammers, T. *et al.* Drug targeting to tumors: Principles, pitfalls and (pre-) clinical progress. *Journal of Controlled Release* **161**, 175–187 (2012).
127. Boulikas, T. Molecular mechanisms of cisplatin and its liposomally encapsulated form, Lipoplatin Molecular mechanisms of cisplatin and its liposomally encapsulated form, Lipoplatin^{TM}. Lipoplatin^{TM} as a chemotherapy and antiangiogenesis drug. *Cancer Therapy* **5**, 349–376 (2007).

128. Arienti, C. *et al.* Activity of lipoplatin in tumor and in normal cells in vitro. *Anti-cancer Drugs* **19**, 983–990 (2008).
129. Stathopoulos, G. P. & Boulikas, T. Lipoplatin Formulation Review Article. *Journal of Drug Delivery* **2012**, 1–10 (2012).
130. Sood, P. *et al.* Synthesis and characterization of AP5346, a novel polymer-linked diaminocyclohexyl platinum chemotherapeutic agent. *Bioconjugate Chemistry* **17**, 1270–1279 (2006).
131. Cai, M. *et al.* Metal organic frameworks as drug targeting delivery vehicles in the treatment of cancer. *Pharmaceutics* vol. 12 (2020).
132. Cook, T. R. *et al.* Metal–Organic Frameworks and Self-Assembled Supramolecular Coordination Complexes: Comparing and Contrasting the Design, Synthesis, and Functionality of Metal–Organic Materials. *Chemical Reviews* **113**, 734–777 (2013).
133. Therrien, B. *et al.* The "complex-in-a-complex" cations [(acac)2M⊂ Ru6-(p-iPrC6H4Me)6(tpt)2(dhbq)3]6+: A trojan horse for cancer cells. *Angewandte Chemie - International Edition* **47**, 3773–3776 (2008).
134. Vajpayee, V. *et al.* Hexanuclear self-assembled arene-ruthenium nano-prismatic cages: potential anticancer agents. *Chemical Communications* **47**, (2011).
135. Lewis, J. E. M. *et al.* Stimuli-responsive Pd 2L 4 metallosupramolecular cages: Towards targeted cisplatin drug delivery. *Chemical Science* **3**, 778–784 (2012).
136. Lewis, J. E. M. & Crowley, J. D. Exo - and endo -hedral interactions of counteranions with tetracationic Pd 2 L 4 metallosupramolecular architectures. *Supramolecular Chemistry* **26**, 173–181 (2014).
137. Maeda, H. Macromolecular therapeutics in cancer treatment: The EPR effect and beyond. *Journal of Controlled Release* vol. 164 138–144 (2012).
138. Danhier, F. To exploit the tumor microenvironment: Since the EPR effect fails in the clinic, what is the future of nanomedicine? *Journal of Controlled Release* **244**, 108–121 (2016).
139. Schmidt, A. *et al.* Evaluation of New Palladium Cages as Potential Delivery Systems for the Anticancer Drug Cisplatin. *Chemistry - A European Journal* **22**, 2253–2256 (2016).
140. Schmidt, A. *et al.* Self-assembly of highly luminescent heteronuclear coordination cages. *Dalton Transactions* **45**, 12297–12300 (2016).
141. Schmidt, A. *et al.* Supramolecular exo-functionalized palladium cages: fluorescent properties and biological activity. *Dalton Transactions* **45**, 8556–8565 (2016).
142. Oliveira, E. *et al.* Green and Red Fluorescent Dyes for Translational Applications in Imaging and Sensing Analytes: A Dual-Color Flag. *ChemistryOpen* **7**, 9–52 (2018).
143. Han, J. *et al.* Bioconjugation strategies to couple supramolecular exo-functionalized palladium cages to peptides for biomedical applications. *Chemical Communications* **53**, 1405–1408 (2017).
144. Preston, G. M. *et al.* Appearance of water channels in Xenopus oocytes expressing red cell CHIP28 protein. *Science (New York, N.Y.)* **256**, 385–387 (1992).
145. Agre, P. *et al.* Aquaporin CHIP: the archetypal molecular water channel. *The American journal of physiology* **265**, F463–F476 (1993).

146. Jenq, W. *et al*. Aquaporin-1 expression in proximal tubule epithelial cells of human kidney is regulated by hyperosmolarity and contrast agents. *Biochemical and biophysical research communications* **256**, 240–248 (1999).
147. Kitchen, P. *et al.* Beyond water homeostasis: Diverse functional roles of mammalian aquaporins. *Biochimica et Biophysica Acta* **1850**, 2410–2421 (2015).
148. Papadopoulos, M. C. & Saadoun, S. Key roles of aquaporins in tumor biology. *BBA - Biomembranes* **1848**, 2576–2583 (2015).
149. Yang, B. *et al.* Carbon dioxide permeability of aquaporin-1 measured in erthrocytes and lung of aquaporin-1 null mice and in reconstituted liposomes. *J. Biol. Chem.* **275**, 2686–2692 (2000).
150. Soveral, G. *et al*. *Aquaporins in health and disease: new molecular targets for drug discovery*. (CRC Press, 2016).
151. Ishibashi, K. *et al*. The role of mammalian superaquaporins inside the cell. *Biochimica et Biophysica Acta - General Subjects* **1840**, 1507–1512 (2014).
152. Itoh, T. *et al.* Identification of a novel aquaporin, AQP12, expressed in pancreatic acinar cells. *Biochemical and Biophysical Research Communications* **330**, 832–838 (2005).
153. Madeira, A. *et al.* Human Aquaporin-11 is a water and glycerol channel and localizes in the vicinity of lipid droplets in human adipocytes. *Obesity* **22**, 2010–2017 (2014).
154. Benga, G. On the definition, nomenclature and classification of water channel proteins (aquaporins and relatives). *Molecular Aspects of Medicine* **33**, 514–517 (2012).
155. Beitz, E. *et al*. Challenges and achievements in the therapeutic modulation of aquaporin functionality. *Pharmacology and Therapeutics* **155**, 22–35 (2015).
156. Krane, C. M. & Goldstein, D. L. Comparative functional analysis of aquaporins/glyceroporins in mammals and anurans. *Mammalian Genome* **18**, 452–462 (2007).
157. Sugimoto, T. *et al.* Impaired aquaporin 3 expression in reepithelialization of cutaneous wound healing in the diabetic rat. *Biological research for nursing* **15**, 347–55 (2013).
158. Rodríguez, A. *et al.* Aquaglyceroporins serve as metabolic gateways in adiposity and insulin resistance control. *Cell Cycle* **10**, 1548–1556 (2011).
159. Ribatti, D. *et al.* Aquaporins in cancer. *Biochimica et Biophysica Acta* **1840**, 1550–1553 (2014).
160. Otterbach, F. *et al.* Aquaporin 1 (AQP1) expression is a novel characteristic feature of a particularly aggressive subgroup of basal-like breast carcinomas. *Breast Cancer Research and Treatment* **120**, 67–76 (2010).
161. Liu, Y. L. *et al.* Expression of aquaporin 3 (AQP3) in normal and neoplastic lung tissues. *Human Pathology* **38**, 171–178 (2007).
162. Song, J. *et al*. Parasite aquaporins : Current developments in drug facilitation and resistance. *Biochimica et Biophysica Acta* **1840**, 1566–1573 (2014).
163. Aikman, B. *et al.* Aquaporins in cancer development: opportunities for bioinorganic chemistry to contribute novel chemical probes and therapeutic agents. *Metallomics* **10**, 696–712 (2018).
164. Murata, K. *et al.* Structural determinants of water permeation through aquaporin-1. *Nature* **407**, 599–605 (2000).

165. Kreida, S. & Tornroth-Horsefiel, S. Structural insights into aquaporin selectivity and regulation. *Current Opinion in Structural Biology* **33**, 126–134 (2015).
166. Jung, J. S. *et al*. Molecular structure of the water channel through aquaporin CHIP: The hourglass model. *Journal of Biological Chemistry* **269**, 14648–14654 (1994).
167. Vahedi-Faridi, A. & Engel, A. Aquaporin Structure and Selectivity. in *Aquaporins in Health and Disease: New Molecular Targets for Drug Discovery* (eds. Soveral, G., Casini, A. & Nielsen, S.) 33–52 (Taylor & Francis Group, 2016).
168. Wang, Y. *et al*. What Makes an Aquaporin a Glycerol Channel ? A Comparative Study of AqpZ and GlpF. *Structure* **13**, 1107–1118 (2005).
169. Chen, H. *et al.* Charge delocalization in proton channels, I: the aquaporin channels and proton blockage. *Biophysical journal* **92**, 46–60 (2007).
170. Wree, D. *et al.* Requirement for asparagine in the aquaporin NPA sequence signature motifs for cation exclusion. *FEBS Journal* **278**, 740–748 (2011).
171. Sui, H. X. *et al.* Structural basis of water-specific transport through the AQP1 water channel. *Nature* **414**, 872–878 (2001).
172. Wang, J. *et al.* Aquaporins as diagnostic and therapeutic targets in cancer: How far we are? *Journal of Translational Medicine* **13**, 96 (2015).
173. Direito, I. *et al.* Differential expression of aquaporin-3 and aquaporin-5 in pancreatic ductal adenocarcinoma. *Journal of Surgical Oncology* **9999**, 1–17 (2017).
174. Day, R. E. *et al.* Human aquaporins: Regulators of transcellular water flow. *Biochimica et Biophysica Acta* **1840**, 1492–1506 (2014).
175. Bai, C. *et al.* Lung fluid transport in aquaporin-1 and aquaporin-4 knockout mice. *Journal of Clinical Investigation* **103**, 555–561 (1999).
176. Maugeri, R. *et al.* Aquaporins and brain tumors. *International Journal of Molecular Sciences* **17**, 1029 (2016).
177. Ma, T. *et al.* Expression and function of aquaporins in peripheral nervous system. *Acta Pharmacologica Sinica* **32**, 711–715 (2011).
178. Papadopoulos, M. C. *et al.* Aquaporins and cell migration. *Pflugers Archiv European Journal of Physiology* **456**, 693–700 (2008).
179. Xie, Y. *et al.* Aquaporin 1 and aquaporin 4 are involved in invasion of lung cancer cells. *Clinical Laboratory* **58**, 75–80 (2012).
180. Saadoun, S. *et al.* Aquaporin-4 expression is increased in oedematous human brain tumours. *Journal of Neurology, Neurosurgery and Psychiatry* **72**, 262–265 (2002).
181. Saadoun, S. *et al.* Increased aquaporin 1 water channel expression in human brain tumours. *British journal of cancer* **87**, 621–3 (2002).
182. Yin, T. *et al.* Correlation between the expression of aquaporin 1 and hypoxia-inducible factor 1 in breast cancer tissues. *Journal of Huazhong University of Science and Technology* **28**, 346–348 (2008).
183. Kang, B. W. *et al.* Expression of aquaporin-1, aquaporin-3, and aquaporin-5 correlates with nodal metastasis in colon cancer. *Oncology (Switzerland)* **88**, 369–376 (2015).
184. Shen, Q. *et al.* Differential Expression of Aquaporins in Cervical Precursor Lesions and Invasive Cervical Cancer. *Reproductive sciences (Thousand Oaks, Calif.)* **23**, 1551–1558 (2016).

185. Guan, B. *et al.* Correlation between the expression of aquaporin 1 and the micro-angiogenesis in laryngeal carcinoma. *Lin chuang er bi yan hou ke za zhi = Journal of clinical otorhinolaryngology* **21**, 269–272 (2007).
186. Machida, Y. *et al.* Relationship of aquaporin 1, 3, and 5 expression in lung cancer cells to cellular differentiation, invasive growth, and metastasis potential. *Human Pathology* **42**, 669–678 (2011).
187. Yang, J. H. *et al.* The influence of aquaporin-1 and microvessel density on ovarian carcinogenesis and ascites formation. *International Journal of Gynecological Cancer* **16**, 400–405 (2006).
188. Li, C. *et al.* Elevated *AQP1* Expression Is Associated With Unfavorable Oncologic Outcome in Patients With Hilar Cholangiocarcinoma. *Technology in Cancer Research & Treatment* **16**, 421–427 (2017).
189. Driml, J. *et al.* Usefulness of Aquaporin 1 as a Prognostic Marker in a Prospective Cohort of Malignant Mesotheliomas. *International journal of molecular sciences* **17**, 1041 (2016).
190. Wu, Z. *et al.* RNAi-mediated silencing of AQP1 expression inhibited the proliferation, invasion and tumorigenesis of osteosarcoma cells. *Cancer Biology and Therapy* **16**, 1332–1340 (2015).
191. Qin, F. *et al.* Expression of aquaporin1 , a water channel protein , in cytoplasm is negatively correlated with prognosis of breast cancer patients. *Oncotarget* **7**, 8143–8154 (2015).
192. Moon, C. *et al.* Involvement of aquaporins in colorectal carcinogenesis. *Oncogene* **22**, 6699–6703 (2003).
193. Otto, W. *et al.* Loss of aquaporin 3 protein expression constitutes an independent prognostic factor for progression-free survival: an immunohistochemical study on stage pT1 urothelial bladder cancer. *BMC Cancer* **12**, 1–8 (2012).
194. Guo, X. *et al.* Prognostic value of combined aquaporin 3 and aquaporin 5 overexpression in hepatocellular carcinoma. *BioMed Research International* **2013**, 7 (2013).
195. Liu, S. *et al.* Co-expression of AQP3 and AQP5 in esophageal squamous cell carcinoma correlates with aggressive tumor progression and poor prognosis. *Medical Oncology* **30**, 636 (2013).
196. Kafé, H. *et al.* Collecting duct carcinoma: An entity to be redefined? *Virchows Archiv* **445**, 637–640 (2004).
197. Alabalık, U. *et al.* Can aquaporins be used as diagnostic and prognostic markers for uterine smooth muscle tumours? *Biotechnology & Biotechnological Equipment* **31**, 148–155 (2017).
198. Kusayama, M. *et al.* Critical role of aquaporin 3 on growth of human esophageal and oral squamous cell carcinoma. *Cancer Science* **102**, 1128–1136 (2011).
199. Chen, J. *et al.* Aquaporin 3 promotes epithelial-mesenchymal transition in gastric cancer. *Journal of Experimental & Clinical Cancer Research* **33**, 1–10 (2014).
200. Zhou, Y. *et al.* Aquaporin 3 promotes the stem-like properties of gastric cancer cells via Wnt/GSK-3β/β-catenin pathway. *Oncotarget* **7**, 16529–16541 (2016).
201. Wang, J. *et al.* Expression of aquaporin 3 in the human prostate. *International Journal of Urology* **14**, 1088–1092 (2007).
202. Satooka, H. & Hara-chikuma, M. Aquaporin-3 Controls Breast Cancer Cell Migration by Regulating Hydrogen Peroxide Transport and Its Downstream Cell Signaling. *Molecular and Cellular biology* **36**, 1206–1218 (2016).

203. Hara-Chikuma, M. & Verkman, A. S. Prevention of skin tumorigenesis and impairment of epidermal cell proliferation by targeted aquaporin-3 gene disruption. *Molecular and cellular biology* **28**, 326–332 (2008).

204. Niu, D. *et al.* Differential expression of aquaporins and its diagnostic utility in thyroid cancer. *PLoS ONE* **7**, e40770 (2012).

205. Lee, S. J. *et al.* AQP5 Expression Predicts Survival in Patients with Early Breast Cancer. *Annals of Surgical Oncology* **21**, 375–383 (2014).

206. Zhang, T. *et al.* Overexpression of AQP5 in cervical cancer: correlation with clinicopathological features and prognosis. *Medical oncology (Northwood, London, England)* **29**, 1998–2004 (2011).

207. Song, T. *et al.* Expression of aquaporin 5 in primary carcinoma and lymph node metastatic carcinoma of non-small cell lung cancer. *Oncology Letters* **9**, 2799–2804 (2015).

208. Yang, J. H. *et al.* Expression and localization of aquaporin-5 in the epithelial ovarian tumors. *Gynecologic Oncology* **100**, 294–299 (2006).

209. Jung, H. J. *et al.* Aquaporin-5: a marker protein for proliferation and migration of human breast cancer cells. *PloS one* **6**, e28492 (2011).

210. Kang, S. K. *et al.* Role of human aquaporin 5 in colorectal carcinogenesis. *The American journal of pathology* **173**, 518–25 (2008).

211. Chae, Y. K. *et al.* Human AQP5 plays a role in the progression of Chronic Myelogenous Leukemia (CML). *PLoS ONE* **3**, e2594 (2008).

212. Li, J. *et al.* Over-expression of a poor prognostic marker in prostate cancer: AQP5 promotes cells growth and local invasion. *World Journal of Surgical Oncology* **12**, 284 (2014).

213. Watanabe, T. *et al.* Involvement of aquaporin-5 in differentiation of human gastric cancer cells. *The journal of physiological sciences: JPS* **59**, 113–22 (2009).

214. Huang, Y.-H. *et al.* Aquaporin 5 promotes the proliferation and migration of human gastric carcinoma cells. *Tumor Biology* **34**, 1743–1751 (2013).

215. Zhang, Z. *et al.* Expression of aquaporin 5 increases proliferation and metastasis potential of lung cancer. *Journal of Pathology* **221**, 210–220 (2010).

216. Yan, C. *et al.* Inhibitory effect of Epigallocatechin gallate on ovarian cancer cell proliferation associated with aquaporin 5 expression. *Archives of Gynecology and Obstetrics* **285**, 459–467 (2012).

217. Ma, J. *et al.* Expression of AQP6 and AQP8 in epithelial ovarian tumor. *Journal of Molecular Histology* **47**, 129–134 (2016).

218. Lacroix, L. *et al.* Follicular Thyroid Tumors with the PAX8-PPARγ1 Rearrangement Display Characteristic Genetic Alterations. *The American Journal of Pathology* **167**, 223–231 (2005).

219. Zhu, S. *et al.* Expression of aquaporin8 in human astrocytomas: Correlation with pathologic grade. *Biochemical and Biophysical Research Communications* **440**, 173–177 (2013).

220. Shi, Y. H. *et al.* Significance and expression of aquaporin 1, 3, 8 in cervical carcinoma in xinjiang uygur women of China. *Asian Pacific Journal of Cancer Prevention* **13**, 1971–1975 (2012).

221. Vieceli Dalla Sega, F. *et al.* Intracellular cysteine oxidation is modulated by aquaporin-8-mediated hydrogen peroxide channeling in leukaemia cells. *International Union of Biochemistry and Molecular Biology* **00**, 1–11 (2016).

222. Tan, G. *et al*. Expression of the water channel protein aquaporin-9 in human astrocytic tumours: correlation with pathological grade. *The Journal of international medical research* **36**, 777–82 (2008).
223. Lindskog, C. *et al*. A Systematic Characterization of Aquaporin-9 Expression in Human Normal and Pathological Tissues. *Journal of Histochemistry & Cytochemistry* **64**, 287–300 (2016).
224. Yang, J. H. *et al*. Expression of aquaglyceroporins in epithelial ovarian tumours and their clinical significance. *Journal of International Medical Research* **39**, 702–711 (2011).
225. Zhang, W. *et al.* Aquaporin 9 is down-regulated in hepatocellular carcinoma and its over-expression suppresses hepatoma cell invasion through inhibiting epithelial-to-mesenchymal transition. *Cancer Letters* **378**, 111–119 (2016).
226. Evans, J. *et al*. P2.03b-082 AQP11 as a Novel Factor of Lung Cancer Cell Resistance to Cisplatin. *Journal of Thoracic Oncology* **12**, S985–S986 (2017).
227. Pinder, S. E. *et al.* Pathological prognostic factors in breast cancer. III. Vascular invasion: relationship with recurrence and survival in a large study with long-term follow-up. *Analysis* **24**, 41–47 (1994).
228. Schwab, A. *et al*. Role of Ion Channels and Transporters in Cell Migration. *Physiological Reviews* **92**, 1865–1913 (2012).
229. Hu, J. & Verkman, A. S. Increased migration and metastatic potential of tumor cells expressing aquaporin water channels. *The FASEB journal: official publication of the Federation of American Societies for Experimental Biology* **20**, 1892–1894 (2006).
230. Hara-chikuma, M. *et al*. Involvement of aquaporin-3 in epidermal growth factor receptor signaling via hydrogen peroxide transport in cancer cells. *Biochemical and Biophysical Research Communications* **471**, 603–609 (2016).
231. Saadoun, S. *et al*. Impairment of angiogenesis and cell migration by targeted aquaporin-1 gene disruption. *Nature* **434**, 786–792 (2005).
232. Verkman, A. S. *et al*. Biology of AQP4 and anti-AQP4 antibody: therapeutic implications. *Brain Pathology* **23**, 684–695 (2013).
233. Burstein, D. E. *et al*. A method to distinguish benign from malignant oncocytic cell tissue. (2013).
234. Jensen, H. H. *et al*. The role of aquaporin-5 in cancer cell migration: A potential active participant. *International Journal of Biochemistry and Cell Biology* **79**, 271–276 (2016).
235. Yang, J. *et al.* Effects of AQP5 gene silencing on proliferation, migration and apoptosis of human glioma cells through regulating EGFR/ERK/ p38 MAPK signaling pathway. *Oncotarget* **8**, 38444–38455 (2017).
236. He, Z. *et al.* AQP5 promotes hepatocellular carcinoma metastasis via NF-κB-regulated epithelial-mesenchymal transition. *Biochemical and Biophysical Research Communications* **490**, 343–348 (2017).
237. Endo, M. *et al.* Water channel (aquaporin 1) expression and distribution in mammary carcinomas and glioblastomas. *Microvascular Research* **58**, 89–98 (1999).
238. El Hindy, N. *et al.* The functional Aquaporin 1 -783G/C-polymorphism is associated with survival in patients with glioblastoma multiforme. *Journal of Surgical Oncology* **108**, 492–498 (2013).
239. Mou, K. *et al.* AQP-4 in peritumoral edematous tissue is correlated with the degree of glioma and with expression of VEGF and HIF-alpha. *Journal of Neuro-Oncology* **100**, 375–383 (2010).

240. Papadopoulos, M. C. *et al.* Aquaporin-4 facilitates reabsorption of excess fluid in vasogenic brain edema. *The FASEB Journal* **18**, 1–19 (2004).
241. Verkman, A. S. *et al*. Aquaporins: important but elusive drug targets. *Nature reviews. Drug discovery* **13**, 259–77 (2014).
242. Laforenza, U. *et al*. Mammalian aquaglyceroporin function in metabolism. *Biochimica et Biophysica Acta* **1858**, 1–11 (2016).
243. Reshef, L. *et al.* Glyceroneogenesis and the triglyceride/fatty acid cycle. *Journal of Biological Chemistry* **278**, 30413–30416 (2003).
244. Brisson, D. *et al*. Glycerol: A neglected variable in metabolic processes? *BioEssays* **23**, 534–542 (2001).
245. Gropper, S. S. & Smith, J. L. Carbohydrates. in *Advanced Nutrition and Human Metabolism, Sixth Edition* 93–106 (Cengage Learning, 2013).
246. Maeda, N. Implications of aquaglyceroporins 7 and 9 in glycerol metabolism and metabolic syndrome. *Molecular Aspects of Medicine* **33**, 665–675 (2012).
247. Bernardino, R. *et al.* Hepatocyte and Sertoli Cell Aquaporins, Recent Advances and Research Trends. *International Journal of Molecular Sciences* **17**, 1096 (2016).
248. Boury-Jamot, M. *et al.* Expression and function of aquaporins in human skin: Is aquaporin-3 just a glycerol transporter? *Biochimica et Biophysica Acta* **1758**, 1034–1042 (2006).
249. Hara, M. & Verkman, A. S. Glycerol replacement corrects defective skin hydration, elasticity, and barrier function in aquaporin-3-deficient mice. *Proceedings of the National Academy of Sciences of the United States of America* **100**, 7360–5 (2003).
250. Hara-Chikuma, M. & Verkman, A. S. Aquaporin-3 facilitates epidermal cell migration and proliferation during wound healing. *Journal of Molecular Medicine* **86**, 221–231 (2008).
251. Matsuzaki, T. *et al.* Water channel protein AQP3 is present in epithelia exposed to the environment of possible water loss. *The journal of histochemistry and cytochemistry : official journal of the Histochemistry Society* **47**, 1275–1286 (1999).
252. Serna, A. *et al.* Functional inhibition of aquaporin-3 with a gold-based compound induces blockage of cell proliferation. *Journal of cellular physiology* **229**, 1787–801 (2014).
253. Li, Z. *et al.* The proliferation impairment induced by AQP3 deficiency is the result of glycerol uptake and metabolism inhibition in gastric cancer cells. *Tumor Biology* **37**, 9169–9179 (2016).
254. Cantor, J. R. & Sabatini, D. M. Cancer Cell Metabolism: One Hallmark, Many Faces. *Cancer Discovery* **2**, 881–898 (2012).
255. Boroughs, L. K. & Deberardinis, R. J. Metabolic pathways promoting cancer cell survival and growth. *Nature Cell Biology* **17**, 351–359 (2015).
256. Watt, M. J. & Steinberg, G. R. Regulation and function of triacylglycerol lipases in cellular metabolism. *Biochemical Journal* **414**, 313–325 (2008).
257. Verkman, A. S. *et al*. Aquaporins - New players in cancer biology. *Journal of Molecular Medicine* **86**, 523–529 (2008).
258. Cairns, R. *et al*. Regulation of cancer cell metabolism. *Nat Rev Cancer* **11**, 85–95 (2011).
259. Jain, M. *et al.* Metabolite Profiling Identifies a Key Role for Glycine In Rapid Cancer Cell Proliferation. *Science* **336**, 1040–1044 (2012).

260. Singleterry, J. *et al.* Components of cancer metabolism and therapeutic interventions. *Mitochondrion* **17**, 50–55 (2014).
261. Koppenol, W. H. *et al.* Otto Warburg's contributions to current concepts of cancer metabolism. *Nature reviews. Cancer* **11**, 325–37 (2011).
262. Pavlova, N. N. & Thompson, C. B. The Emerging Hallmarks of Cancer Metabolism. *Cell Metabolism* **23**, 27–47 (2016).
263. Pike Winer, L. S. & Wu, M. Rapid analysis of glycolytic and oxidative substrate flux of cancer cells in a microplate. *PLoS ONE* **9**, e109916 (2014).
264. Berg, J. *et al.* Section 18.5, Many Shuttles Allow Movement Across the Mitochondrial Membranes. in *Biochemistry* (W H Freeman, 2002).
265. Mráček, T. *et al.* The function and the role of the mitochondrial glycerol-3-phosphate dehydrogenase in mammalian tissues. *Biochimica et Biophysica Acta - Bioenergetics* **1827**, 401–410 (2013).
266. Chowdhury, S. K. R. *et al.* High activity of mitochondrial glycerophosphate dehydrogenase and glycerophosphate-dependent ROS production in prostate cancer cell lines. *Biochemical and Biophysical Research Communications* **333**, 1139–1145 (2005).
267. Warth, A. *et al.* Expression of the water channel protein aquaporin-9 in malignant brain tumors. *Applied immunohistochemistry & molecular morphology: AIMM / official publication of the Society for Applied Immunohistochemistry* **15**, 193–8 (2007).
268. Jelen, S. *et al.* AQP9 Expression in Glioblastoma Multiforme Tumors Is Limited to a Small Population of Astrocytic Cells and CD15+/CalB+ Leukocytes. *PLoS ONE* **8**, e75764 (2013).
269. Fossdal, G. *et al.* Aqp 9 and Brain Tumour Stem Cells. *The Scientific World Journal* **2012**, 1–9 (2012).
270. Chetry, M. *et al.* Prognostic values of Aquaporins (AQP) mRNA expression in ovarian cancer. *Life Sciences* **194**, 34–39 (2018).
271. Berretta, R. & Moscato, P. Cancer biomarker discovery: The entropic hallmark. *PLoS ONE* **5**, e12262 (2010).
272. Antunes, F. & Cadenas, E. Estimation of H_2O_2 gradients across biomembranes. *FEBS Letters* **475**, 121–126 (2000).
273. Bienert, G. P. *et al.* Membrane transport of hydrogen peroxide. *Biochimica et Biophysica Acta* **1758**, 994–1003 (2006).
274. Bienert, G. P. *et al.* Specific aquaporins facilitate the diffusion of hydrogen peroxide across membranes. *Journal of Biological Chemistry* **282**, 1183–1192 (2007).
275. Miller, E. W. *et al.* Aquaporin-3 mediates hydrogen peroxide uptake to regulate downstream intracellular signaling. *Proceedings of the National Academy of Sciences* **107**, 15681–15686 (2010).
276. Vieceli Dalla Sega, F. *et al.* Specific aquaporins facilitate Nox-produced hydrogen peroxide transport through plasma membrane in leukaemia cells. *Biochimica et Biophysica Acta* **1843**, 806–814 (2014).
277. Watanabe, S. *et al.* Aquaporin-9 facilitates membrane transport of hydrogen peroxide in mammalian cells. *Biochemical and Biophysical Research Communications* **471**, 191–197 (2016).
278. Ferri, D. *et al.* Ontogeny, Distribution, and Possible Functional Implications of an Unusual Aquaporin, AQP8, in Mouse Liver. *Hepatology* **38**, 947–957 (2003).

279. Marchissio, M. J. *et al*. Mitochondrial aquaporin-8 knockdown in human hepatoma HepG2 cells causes ROS-induced mitochondrial depolarization and loss of viability. *Toxicology and Applied Pharmacology* **264**, 246–254 (2012).
280. Di Meo, S. *et al*. Role of ROS and RNS Sources in Physiological and Pathological Conditions. *Oxidative Medicine and Cellular Longevity* **2016**, 44 (2016).
281. Sies, H. *et al*. Oxidative Stress. *Annual Review of Biochemistry* **86**, 715–748 (2017).
282. Panieri, E. & Santoro, M. M. ROS homeostasis and metabolism: a dangerous liason in cancer cells. *Cell death & disease* **7**, e2253 (2016).
283. Sies, H. Hydrogen peroxide as a central redox signaling molecule in physiological oxidative stress: Oxidative eustress. *Redox Biology* **11**, 613–619 (2017).
284. Wu, W. S. The signaling mechanism of ROS in tumor progression. *Cancer and Metastasis Reviews* **25**, 695–705 (2006).
285. Kardeh, S. *et al*. Paradoxical action of reactive oxygen species in creation and therapy of cancer. *European Journal of Pharmacology* **735**, 150–168 (2014).
286. Rad, E. *et al*. Oncogenic signaling through mechanistic target of rapamycin (mTOR): A driver of metabolic transformation and cancer progression. *Cancers* **10**, 1–17 (2018).
287. Wu, Z. *et al*. Resveratrol inhibition of human keratinocyte proliferation via SIRT1/ARNT/ERK dependent downregulation of aquaporin 3. *Journal of Dermatological Science* **75**, 16–23 (2014).
288. Xu, H. *et al*. Aquaporin-3 positively regulates matrix metalloproteinases via PI3K/AKT signal pathway in human gastric carcinoma SGC7901 cells. *Journal of Experimental and Clinical Cancer Research* **30**, 1–6 (2011).
289. Huang, X. *et al*. Aquaporin 3 facilitates tumor growth in pancreatic cancer by modulating mTOR signaling. *Biochemical and Biophysical Research Communications* **486**, 1097–1102 (2017).
290. Hara-Chikuma, M. *et al.* Chemokine-dependent T cell migration requires aquaporin-3–mediated hydrogen peroxide uptake. *The Journal of Experimental Medicine* **209**, 1743–1752 (2012).
291. Thiagarajah, J. R. *et al*. Aquaporin-3 mediates hydrogen peroxide-dependent responses to environmental stress in colonic epithelia. *Proceedings of the National Academy of Sciences* **114**, 568–573 (2017).
292. Hara-Chikuma, M. *et al.* Aquaporin-3-mediated hydrogen peroxide transport is required for NF-κB signaling in keratinocytes and development of psoriasis. *Nature communications* **6**, 7454 (2015).
293. Hou, S.-Y. *et al.* Aquaporin-3 Inhibition Reduces the Growth of NSCLC Cells Induced by Hypoxia. *Cellular Physiology and Biochemistry* **38**, 129–140 (2016).
294. Creagan, E. T. *et al.* Failure of high-dose vitamin C (ascorbic acid) therapy to benefit patients with advanced cancer. A controlled trial. *The New England journal of medicine* **301**, 687–90 (1979).
295. Polireddy, K. *et al.* High dose parenteral ascorbate inhibited pancreatic cancer growth and metastasis: Mechanisms and a phase I/IIa study. *Scientific Reports* **7**, 1–15 (2017).
296. Chen, Q. *et al.* Pharmacologic ascorbic acid concentrations selectively kill cancer cells: Action as a pro-drug to deliver hydrogen peroxide to tissues. *Proceedings of the National Academy of Sciences* **102**, 13604–13609 (2005).

297. Erudaitius, D. *et al*. Peroxiporin expression is an important factor for cancer cell susceptibility to therapeutic H2O2: Implications for pharmacological ascorbate therapy. *PLoS ONE* **12**, 1–14 (2017).
298. Pust, A. *et al.* Aquaporin 5 expression is frequent in prostate cancer and shows a dichotomous correlation with tumor phenotype and PSA recurrence. *Human Pathology* **48**, 102–110 (2016).
299. Rodrigues, C. *et al.* Rat aquaporin-5 is pH-gated induced by phosphorylation and is implicated in oxidative stress. *International Journal of Molecular Sciences* **17**, 2090 (2016).
300. Soveral, G. & Casini, A. Aquaporin modulators: a patent review (2010-2015). *Expert Opinion on Therapeutic Patents* **27**, 49–62 (2017).
301. Zelenina, M. *et al*. Nickel and Extracellular Acidification Inhibit the Water Permeability of Human Aquaporin-3 in Lung Epithelial Cells. *Journal of Biological Chemistry* **278**, 30037–30043 (2003).
302. Zelenina, M. *et al.* Copper inhibits the water and glycerol permeability of aquaporin-3. *Journal of Biological Chemistry* **279**, 51939–51943 (2004).
303. Janosi, L. & Ceccarelli, M. The Gating Mechanism of the Human Aquaporin 5 Revealed by Molecular Dynamics Simulations. *PLoS ONE* **8**, e59897 (2013).
304. Frick, A. *et al*. Structural basis for pH gating of plant aquaporins. *FEBS Letters* **587**, 989–993 (2013).
305. Törnroth-Horsefield, S. *et al.* Structural mechanism of plant aquaporin gating. *Nature* **439**, 688–694 (2006).
306. de Almeida, A. *et al.* Exploring the gating mechanisms of aquaporin-3: new clues for the design of inhibitors? *Mol. BioSyst.* **12**, 1564–1573 (2016).
307. Preston, G. M. *et al*. The mercury-sensitive residue at cysteine 189 in the CHIP28 water channel. *Journal of Biological Chemistry* **268**, 17–20 (1993).
308. Hirano, Y. *et al.* Molecular mechanisms of how mercury inhibits water permeation through aquaporin-1: Understanding by molecular dynamics simulation. *Biophysical Journal* **98**, 1512–1519 (2010).
309. Spinello, A. *et al.* The inhibition of glycerol permeation through aquaglyceroporin-3 induced by mercury (II): A molecular dynamics study. *Journal of Inorganic Biochemistry* **160**, 78–84 (2016).
310. Graziani, V. *et al.* A Multi-Level Theoretical Study to Disclose the Binding Mechanisms of Gold(III)–Bipyridyl Compounds as Selective Aquaglyceroporin Inhibitors. *Chemistry - A European Journal* **23**, 13802–13813 (2017).
311. Madeira, A. *et al.* A gold coordination compound as a chemical probe to unravel aquaporin-7 function. *ChemBioChem* **15**, 1487–1494 (2014).
312. World Health Organization. *World health statistics 2020: monitoring health for the SDGs, sustainable development goals*. https://apps.who.int/iris/bitstream/handle/10665/332070/9789240005105-eng.pdf (2020).
313. De Almeida, A. *et al*. Emerging protein targets for metal-based pharmaceutical agents: An update. *Coordination Chemistry Reviews* **257**, 2689–2704 (2013).
314. Agre, P. Aquaporin Water Channels (Nobel Lecture). *Angewandte Chemie International Edition* **43**, 4278–4290 (2004).
315. Verkman, A. S. More than just water channels: unexpected cellular roles of aquaporins. *Journal of Cell Science* **118**, 3225–3232 (2005).
316. Verkman, A. S. Aquaporins in Clinical Medicine. *Annual Review of Medicine* **63**, 303–316 (2012).

317. Soveral, G. & Casini, A. Aquaporin modulators: a patent review (2010-2015). *Expert Opinion on Therapeutic Patents* **27**, 49–62 (2017).
318. Murray, M., Ryan, A. J. & Little, P. J. Inhibition of rat hepatic microsomal aminopyrine N-demethylase activity by benzimidazole derivatives. Quantitative structure-activity relationships. *Journal of medicinal chemistry* **25**, 887–892 (1982).
319. Sontakke, V. A. *et al.* A simple, efficient synthesis of 2-aryl benzimidazoles using silica supported periodic acid catalyst and evaluation of anticancer activity. *ISRN organic chemistry* **2013**, (2013).
320. Serratrice, M. *et al.* Synthesis, structural characterization, solution behavior, and in vitro antiproliferative properties of a series of gold complexes with 2-(2′-pyridyl)benzimidazole as ligand: Comparisons of gold(III) versus gold(I) and mononuclear versus binuclear derivat. *Inorganic Chemistry* **51**, 3161–3171 (2012).
321. Prosser, K. E. *et al.* Anticancer copper pyridine benzimidazole complexes: ROS generation, biomolecule interactions, and cytotoxicity. *Journal of Inorganic Biochemistry* **167**, 89–99 (2017).
322. Gümüş, F. *et al.* Synthesis, characterization and in vitro cytotoxic, mutagenic and antimicrobial activity of platinum(II) complexes with substituted benzimidazole ligands. *Journal of Inorganic Biochemistry* **94**, 255–262 (2003).
323. Huang, W. K. *et al.* Synthesis and electron-transfer properties of benzimidazole-functionalized ruthenium complexes for highly efficient dye-sensitized solar cells. *Chemical Communications* **46**, 8992–8994 (2010).
324. Mardanya, S. *et al.* Anion and cation triggered modulation of optical properties of a pyridyl-imidazole receptor rigidly linked to pyrene and construction of INHIBIT, OR and XOR molecular logic gates: A combined experimental and DFT/TD-DFT investigation. *Sensors and Actuators B: Chemical* **206**, 701–713 (2015).
325. Aikman, B. *et al.* Gold(III) Pyridine-Benzimidazole Complexes as Aquaglyceroporin Inhibitors and Antiproliferative Agents. *Inorganics* **6**, 123 (2018).
326. Smyth, M. S. & Martin, J. H. J. x Ray crystallography. *Molecular Pathology* **53**, 8–14 (2000).
327. Brouwer, A. M. Standards for photoluminescence quantum yield measurements in solution (IUPAC Technical Report). *Pure and Applied Chemistry* **83**, 2213–2228 (2011).
328. Montalti, M. *et al. Handbook of Photochemistry, Third Edition*. *Handbook of Photochemistry* (CRC Press, 2006). doi:10.1201/9781420015195.
329. Masuhara, H. *et al.* Fluorescence quenching mechanism of aromatic hydrocarbons by closed-shell heavy metal ions in aqueous and organic solutions. *Journal of Physical Chemistry* **88**, 5868–5873 (1984).
330. Petryszak, R. *et al.* Expression Atlas update—an integrated database of gene and protein expression in humans, animals and plants. *Nucleic Acids Research* **44**, D746–D752 (2016).
331. Alley, M. C. *et al.* Feasibility of Drug Screening with Panels of Human Tumor Cell Lines Using a Microculture Tetrazolium Assay1. *CANCER RESEARCH* **48**, 589–601 (1988).
332. Casini, A. *et al.* Biophysical characterisation of adducts formed between anticancer metallodrugs and selected proteins: New insights from X-ray

diffraction and mass spectrometry studies. *Journal of Inorganic Biochemistry* **102**, 995–1006 (2008).

333. Anthony, E. J. *et al.* Metallodrugs are unique: opportunities and challenges of discovery and development. *Chemical Science* **11**, 12888–12917 (2020).
334. de Almeida, A. *et al.* Emerging protein targets for metal-based pharmaceutical agents: An update. *Coordination Chemistry Reviews* **257**, 2689–2704 (2013).
335. Wenzel, M. N. *et al.* Insights into the Mechanisms of Aquaporin-3 Inhibition by Gold(III) Complexes: the Importance of Non-Coordinative Adduct Formation. *Inorganic Chemistry* **58**, 2140–2148 (2019).
336. Zou, T. *et al.* Chemical biology of anticancer gold(iii) and gold(i) complexes. *Chemical Society Reviews* **44**, 8786–8801 (2015).
337. Wesselinova, D. *et al.* Cytotoxicity and effects of 1,10-phenanthroline and 5-amino-1,10-phenanthroline derivatives on some immunocompetent cells. *European Journal of Medicinal Chemistry* **44**, 5099–5102 (2009).
338. Roy, S. *et al.* Phenanthroline Derivatives with Improved Selectivity as DNA-Targeting Anticancer or Antimicrobial Drugs. *ChemMedChem* **3**, 1427–1434 (2008).
339. Madeira, A. *et al.* Detecting Aquaporin Function and Regulation. *Frontiers in Chemistry* **4**, 1–8 (2016).
340. Hara-Chikuma, M. & Verkman, A. S. Aquaporin-3 functions as a glycerol transporter in mammalian skin. *Biology of the Cell* **97**, 479–486 (2005).
341. Katano, T. *et al.* Functional characteristics of aquaporin 7 as a facilitative glycerol carrier. *Drug Metabolism and Pharmacokinetics* **29**, 244–248 (2014).
342. Ohgusu, Y. *et al.* Functional Characterization of Human Aquaporin 9 as a Facilitative Glycerol Carrier. *Drug Metabolism and Pharmacokinetics* **23**, 279–284 (2008).
343. Ishii, M. *et al.* Dual Functional Characteristic of Human Aquaporin 10 for Solute Transport. *Cellular Physiology and Biochemistry* **27**, 749–756 (2011).
344. da Silva, I. V. *et al.* Revisiting the metabolic syndrome: the emerging role of aquaglyceroporins. *Cellular and Molecular Life Sciences* **75**, 1973–1988 (2018).
345. da Silva, I. V. & Soveral, G. Aquaporins in Immune Cells and Inflammation: New Targets for Drug Development. *International Journal of Molecular Sciences* vol. 22 1845 (2021).
346. Calamita, G. *et al.* Aquaglyceroporins: Drug targets for metabolic diseases? *Frontiers in Physiology* **9**, 851 (2018).
347. Mósca, A. *et al.* Molecular Basis of Aquaporin-7 Permeability Regulation by pH. *Cells* **7**, 207 (2018).
348. Gotfryd, K. *et al.* Human adipose glycerol flux is regulated by a pH gate in AQP10. *Nature Communications* **9**, (2018).
349. Hatakeyama, S. *et al.* Cloning of a new aquaporin (AQP10) abundantly expressed in duodenum and jejunum. *Biochemical and Biophysical Research Communications* **287**, 814–819 (2001).
350. Ishibashi, K. *et al.* Cloning and identification of a new member of water channel (AQP10) as an aquaglyceroporin. *Biochimica et Biophysica Acta* **1576**, 335–340 (2002).
351. Laforenza, U. *et al.* Solute transporters and aquaporins are impaired in celiac disease. *Biology of the Cell* **102**, 457–467 (2010).
352. Laforenza, U. *et al.* Aquaporin-10 Represents an Alternative Pathway for Glycerol Efflux from Human Adipocytes. *PLoS ONE* **8**, (2013).

353. Marlar, S. *et al.* Aquaporin-3 in Cancer. *International Journal of Molecular Sciences* **18**, 2106 (2017).

354. Cinellu, M. A. *et al.* Synthesis and characterization of gold(III) adducts and cyclometallated derivatives with 2-substituted pyridines. Crystal structure of [Au{NC5H4(CMe2C6H4)-2}Cl2]. *Journal of the Chemical Society, Dalton Transactions* **1**, 2865 (1995).

355. Fuchita, Y. *et al.* Synthesis, structure and reactivity of a new six-membered cycloaurated complex of 2-benzoylpyridine [AuCl2(pcp-C 1,N)] [pcp = 2-(2-pyridylcarbonyl)phenyl]. Comparison with the cycloaurated complex derived from 2-benzylpyridine. *Journal of the Chemical Society, Dalton Transactions* **12**, 791–796 (1998).

356. Cinellu, M. A. *et al.* Synthesis and characterization of gold(III) adducts and cyclometallated derivatives with 6-benzyl- and 6-alkyl-2,2′-bipyridines. *J. Chem. Soc., Dalton Trans.* 4217–4225 (1996) doi:10.1039/DT9960004217.

357. Kung, K. K.-Y. *et al.* Cyclometalated gold(III) complexes for chemoselective cysteine modification via ligand controlled C–S bond-forming reductive elimination. *Chem. Commun.* **50**, 11899–11902 (2014).

358. Babak, M. v. *et al.* Interfering with Metabolic Profile of Triple-Negative Breast Cancers Using Rationally Designed Metformin Prodrugs. *Angewandte Chemie International Edition* anie.202102266 (2021) doi:10.1002/anie.202102266.

359. Sonntag, Y. *et al.* Identification and characterization of potent and selective aquaporin-3 and aquaporin-7 inhibitors. *Journal of Biological Chemistry* **294**, 7377–7387 (2019).

360. Soveral, G. & Casini, A. Aquaporin modulators: a patent review (2010–2015). *Expert Opinion on Therapeutic Patents* vol. 27 49–62 (2017).

361. Wacker, S. J. *et al.* The identification of novel, high affinity AQP9 inhibitors in an intracellular binding site. *Molecular Membrane Biology* **30**, 246–260 (2013).

362. Jelen, S. *et al.* Aquaporin-9 Protein Is the Primary Route of Hepatocyte Glycerol Uptake for Glycerol Gluconeogenesis in Mice*. *Journal of Biological Chemistry* **286**, 44319–44325 (2011).

363. Mósca, A. *et al.* Molecular Basis of Aquaporin-7 Permeability Regulation by pH. *Cells* **7**, 207 (2018).

364. Rodrigues, C. *et al.* Human aquaporin-5 facilitates hydrogen peroxide permeation affecting adaption to oxidative stress and cancer cell migration. *Cancers* **11**, 932 (2019).

365. Pimpão, C. *et al.* The aquaporin-3-inhibiting potential of polyoxotungstates. *International Journal of Molecular Sciences* **21**, 2467 (2020).

366. Roudier, N. *et al.* Evidence for the Presence of Aquaporin-3 in Human Red Blood Cells. *Journal of Biological Chemistry* **273**, 8407–8412 (1998).

367. Zheng, X. *et al.* Analytical methods for kinetic studies of biological interactions: A review. *Journal of Pharmaceutical and Biomedical Analysis* vol. 113 163–180 (2015).

368. Gena, P. *et al.* Stopped-flow Light Scattering Analysis of Red Blood Cell Glycerol Permeability. *BIO-PROTOCOL* **10**, (2020).

369. Block, B. P. & Bailar, J. C. The Reaction of Gold(III) with Some Bidentate Coördinating Groups. *Journal of the American Chemical Society* **73**, 4722–4725 (1951).

370. Meier, S. M. *et al.* Mass Spectrometry Uncovers Molecular Reactivities of Coordination and Organometallic Gold(III) Drug Candidates in Competitive

Experiments That Correlate with Their Biological Effects. *Inorganic Chemistry* **55**, 4248–4259 (2016).

371. Hamann, S. *et al.* Measurement of Cell Volume Changes by Fluorescence Self-Quenching. *Journal of Fluorescence* **12**, 139–145 (2002).
372. Soveral, G. *et al.* Water transport in intact yeast cells as assessed by fluorescence self-quenching. *Applied and Environmental Microbiology* **73**, 2341–2343 (2007).
373. de Maré, S. W. *et al.* Structural Basis for Glycerol Efflux and Selectivity of Human Aquaporin 7. *Structure* **28**, 215-222.e3 (2020).
374. Smart, O. S. *et al.* HOLE: A program for the analysis of the pore dimensions of ion channel structural models. *Journal of Molecular Graphics* **14**, 354–360 (1996).
375. Humphrey, W. *et al.* VMD: Visual molecular dynamics. *Journal of Molecular Graphics* **14**, 33–38 (1996).
376. Baker, N. A. *et al.* Electrostatics of nanosystems: Application to microtubules and the ribosome. *Proceedings of the National Academy of Sciences* **98**, 10037–10041 (2001).
377. Pettersen, E. F. *et al.* UCSF Chimera - A visualization system for exploratory research and analysis. *Journal of Computational Chemistry* **25**, 1605–1612 (2004).
378. Pronk, J. T. Auxotrophic yeast strains in fundamental and applied research. *Applied and Environmental Microbiology* **68**, 2095–2100 (2002).
379. Soveral, G. *et al.* Membrane tension regulates water transport in yeast. *Biochimica et Biophysica Acta - Biomembranes* **1778**, 2573–2579 (2008).
380. Cook, T. R. *et al.* Biomedical and biochemical applications of self-assembled metallacycles and metallacages. *Accounts of Chemical Research* **46**, 2464–2474 (2013).
381. Kaner, R. A. *et al.* Anticancer metallohelices: nanomolar potency and high selectivity. *Chemical Science* **7**, 951–958 (2016).
382. Preston, D. *et al.* Enhanced kinetic stability of $[Pd_2L_4]^{4+}$ cages through ligand substitution. *Dalton Transactions* **45**, 8050–8060 (2016).
383. Schmitt, F. *et al.* Efficient photodynamic therapy of cancer using chemotherapeutic porphyrin–ruthenium metalla-cubes. *Bioorganic & Medicinal Chemistry Letters* **22**, 178–180 (2012).
384. Vajpayee, V. *et al.* Hexanuclear self-assembled arene-ruthenium nano-prismatic cages: Potential anticancer agents. *Chemical Communications* **47**, 5184–5186 (2011).
385. Ahmedova, A. *et al.* Anticancer Potencies of Pt II - and Pd II -linked M_2L_4 Coordination Capsules with Improved Selectivity. *Chemistry - An Asian Journal* **11**, 474–477 (2016).
386. Schmidt, A. *et al.* Self-assembled M2L4 coordination cages: Synthesis and potential applications. *Coordination Chemistry Reviews* **275**, 19–36 (2014).
387. Kaiser, F. *et al.* Self-Assembled Palladium and Platinum Coordination Cages: Photophysical Studies and Anticancer Activity. *European Journal of Inorganic Chemistry* **2016**, 5181–5181 (2016).
388. Hovlid, M. L. *et al.* Guiding plant virus particles to integrin-displaying cells. *Nanoscale* **4**, 3698 (2012).
389. Han, J. *et al.* Bioconjugation strategies to couple supramolecular exo-functionalized palladium cages to peptides for biomedical applications. *Chemical Communications* **53**, 1405–1408 (2017).

390. Hamidi, H. *et al*. The complexity of integrins in cancer and new scopes for therapeutic targeting. *British journal of cancer* **115**, 1017–1023 (2016).
391. Ley, K. *et al*. Integrin-based therapeutics: biological basis, clinical use and new drugs. *Nature Reviews Drug Discovery* **15**, 173–183 (2016).
392. Nieberler, M. *et al.* Exploring the Role of RGD-Recognizing Integrins in Cancer. *Cancers* **9**, 116 (2017).
393. Meyer, A. *et al*. Targeting RGD Recognizing Integrins: Drug Development, Biomaterial Research, Tumor Imaging and Targeting. *Current Pharmaceutical Design* **12**, 2723–2747 (2006).
394. Heckmann, D. *et al.* Probing Integrin Selectivity: Rational Design of Highly Active and Selective Ligands for the α5β1 and αvβ3 Integrin Receptor. *Angewandte Chemie International Edition* **46**, 3571–3574 (2007).
395. Schottelius, M. *et al*. Ligands for Mapping α v β 3 -Integrin Expression in Vivo. *Accounts of Chemical Research* **42**, 969–980 (2009).
396. Rechenmacher, F. *et al.* Functionalizing αvβ3- or α5β1-Selective Integrin Antagonists for Surface Coating: A Method To Discriminate Integrin Subtypes In Vitro. *Angewandte Chemie International Edition* **52**, 1572–1575 (2013).
397. Neubauer, S. *et al.* Selective Imaging of the Angiogenic Relevant Integrins α5β1 and αvβ3. *Angewandte Chemie International Edition* **52**, 11656–11659 (2013).
398. Kapp, T. G. *et al.* A Comprehensive Evaluation of the Activity and Selectivity Profile of Ligands for RGD-binding Integrins. *Scientific Reports* **7**, 39805 (2017).
399. Weinmüller, M. *et al.* Overcoming the Lack of Oral Availability of Cyclic Hexapeptides: Design of a Selective and Orally Available Ligand for the Integrin αvβ3. *Angewandte Chemie International Edition* **56**, 16405–16409 (2017).
400. Aumailley, M. *et al.* Arg-Gly-Asp constrained within cyclic pentapoptides Strong and selective inhibitors of cell adhesion to vitronectin and laminin fragment P1. *FEBS Letters* **291**, 50–54 (1991).
401. Dechantsreiter, M. A. *et al.* N -Methylated Cyclic RGD Peptides as Highly Active and Selective α V β 3 Integrin Antagonists. *Journal of Medicinal Chemistry* **42**, 3033–3040 (1999).
402. Mas-Moruno, *et al.* Cilengitide: The First Anti-Angiogenic Small Molecule Drug Candidate. Design, Synthesis and Clinical Evaluation. *Anti-Cancer Agents in Medicinal Chemistry* **10**, 753–768 (2010).
403. Mukhopadhyay, S. *et al.* Conjugated Platinum(IV)−Peptide Complexes for Targeting Angiogenic Tumor Vasculature. *Bioconjugate Chemistry* **19**, 39–49 (2008).
404. Medrano, M. A. *et al.* Nonconventional trans -Platinum Complexes Functionalized with RDG Peptides: Chemical and Cytototoxicity Studies. *European Journal of Inorganic Chemistry* **2017**, 1835–1840 (2017).
405. Gandioso, A. *et al.* An integrin-targeted photoactivatable Pt(<scp>iv</scp>) complex as a selective anticancer pro-drug: synthesis and photoactivation studies. *Chemical Communications* **51**, 9169–9172 (2015).
406. Neubauer, S. *et al.* Pharmacophoric Modifications Lead to Superpotent αvβ3 Integrin Ligands with Suppressed α5β1 Activity. *Journal of Medicinal Chemistry* **57**, 3410–3417 (2014).
407. Heckmann, D. *et al.* Rational Design of Highly Active and Selective Ligands for the α5β1 Integrin Receptor. *ChemBioChem* **9**, 1397–1407 (2008).

408. Haubner, R. *et al.* Structural and Functional Aspects of RGD-Containing Cyclic Pentapeptides as Highly Potent and Selective Integrin α V β 3 Antagonists. *Journal of the American Chemical Society* **118**, 7461–7472 (1996).
409. Mas-Moruno, C. *et al.* αvβ3- or α5β1-Integrin-Selective Peptidomimetics for Surface Coating. *Angewandte Chemie International Edition* **55**, 7048–7067 (2016).
410. Frank, A. O. *et al.* Conformational Control of Integrin-Subtype Selectivity in isoDGR Peptide Motifs: A Biological Switch. *Angewandte Chemie International Edition* **49**, 9278–9281 (2010).
411. Thumshirn, G. *et al.* Multimeric Cyclic RGD Peptides as Potential Tools for Tumor Targeting: Solid-Phase Peptide Synthesis and Chemoselective Oxime Ligation. *Chemistry - A European Journal* **9**, 2717–2725 (2003).
412. Jin, Z. H. *et al.* In vivo noninvasive optical imaging of receptor-mediated RGD internalization using self-quenched Cy5-labeled RAFT-c(-RGDfK-)4. *Molecular Imaging* (2007) doi:10.2310/7290.2007.00002.
413. Gestwicki, J. E. *et al.* Influencing receptor-ligand binding mechanisms with multivalent ligand architecture. *Journal of the American Chemical Society* **124**, 14922–14933 (2002).
414. Kiessling, L. L. *et al.* Synthetic Multivalent Ligands as Probes of Signal Transduction. *Angewandte Chemie International Edition* **45**, 2348–2368 (2006).
415. Wester, H.-J. & Kessler, H. Molecular targeting with peptides or peptide-polymer conjugates: Just a question of size? *Journal of Nuclear Medicine* **46**, 1940–1945 (2005).
416. Zhang, Y. *et al.* Induction of Partial Protection against Foot and Mouth Disease Virus in Guinea Pigs by Neutralization with the Integrin β6-1 Subunit. *Viruses* **5**, 1114–1130 (2013).
417. Pisano, M. *et al.* In vitro activity of the αvβ3 integrin antagonist RGDechi-hCit on malignant melanoma cells. *Anticancer Research* **33**, 871–880 (2013).
418. Goodman, S. L. *et al.* Matched rabbit monoclonal antibodies against v-series integrins reveal a novel v 3-LIBS epitope, and permit routine staining of archival paraffin samples of human tumors. *Biology Open* **1**, 329–340 (2012).
419. de Graaf, I. A. M. *et al.* Preparation and incubation of precision-cut liver and intestinal slices for application in drug metabolism and toxicity studies. *Nature Protocols* **5**, 1540–1551 (2010).
420. Daum, S. *et al.* Improved Synthesis of N -Benzylaminoferrocene-Based Prodrugs and Evaluation of Their Toxicity and Antileukemic Activity. *Journal of Medicinal Chemistry* **58**, 2015–2024 (2015).
421. Spreckelmeyer, S. *et al.* On the toxicity and transport mechanisms of cisplatin in kidney tissues in comparison to a gold-based cytotoxic agent. *Metallomics* **9**, 1786–1795 (2017).
422. Estrada-Ortiz, N. *et al.* Anticancer Gold N -Heterocyclic Carbene Complexes: A Comparative in vitro and ex vivo Study. *ChemMedChem* **12**, 1429–1435 (2017).
423. Spreckelmeyer, S. *et al.* Cellular Transport Mechanisms of Cytotoxic Metallodrugs: An Overview beyond Cisplatin. *Molecules* **19**, 15584–15610 (2014).
424. Han, J. *et al.* Bioconjugation of Supramolecular Metallacages to Integrin Ligands for Targeted Delivery of Cisplatin. *Bioconjugate Chemistry* **29**, 3856–3865 (2018).

425. Schmidt, A. *et al*. E. Self-assembled M 2 L 4 coordination cages : Synthesis and potential applications. *Coordination Chemistry Reviews* **275**, 19–36 (2014).
426. Casini, A. *et al*. The Promise of Self-Assembled 3D Supramolecular Coordination Complexes for Biomedical Applications. *Inorganic Chemistry* **56**, 14715–14729 (2017).
427. Cook, T. R. *et al*. Biomedical and biochemical applications of self-assembled metallacycles and metallacages. *Accounts of Chemical Research* **46**, 2464–2474 (2013).
428. Therrien, B. Drug Delivery by Water-Soluble Organometallic Cages. *Top Curr Chem* **319**, 35–55 (2012).
429. Schmitt, F. *et al.* Organometallic cages as vehicles for intracellular release of photosensitizers. *Journal of the American Chemical Society* **134**, 754–757 (2012).
430. Lewis, J. E. M. *et al*. Stimuli-responsive Pd2L4 metallosupramolecular cages: towards targeted cisplatin drug delivery. *Chemical Science* **3**, 778–784 (2012).
431. Zheng, Y.-R. *et al*. Encapsulation of Pt(IV) Prodrugs within a Pt(II) Cage for Drug Delivery. *Chem. Sci.* **6**, 1189–1193 (2015).
432. Schmidt, A. *et al.* Evaluation of New Palladium Cages as Potential Delivery Systems for the Anticancer Drug Cisplatin. *Chemistry - A European Journal* **22**, 2253–2256 (2016).
433. Han, J. *et al.* Bioconjugation strategies to couple supramolecular Exo - functionalized palladium cages to peptides for biomedical applications. *Chemical Communications* **53**, 1405–1408 (2017).
434. Han, J. *et al.* Bioconjugation of Supramolecular Metallacages to Integrin Ligands for Targeted Delivery of Cisplatin. *Bioconjugate Chemistry* acs.bioconjchem.8b00682 (2018) doi:10.1021/acs.bioconjchem.8b00682.
435. Lewis, J. E. M. *et al*. 'Click' to functionalise: synthesis, characterisation and enhancement of the physical properties of a series of exo- and endo-functionalised Pd 2 L 4 nanocages. *Chem. Sci.* **5**, 1833–1843 (2014).
436. Johnson, A. M. *et al.* Synthesis and properties of metal-ligand complexes with endohedral amine functionality. *Inorganic Chemistry* **50**, 9430–9442 (2011).
437. Schmidt, A. *et al.* Supramolecular exo-functionalized palladium cages: fluorescent properties and biological activity. *Dalton transactions (Cambridge, England : 2003)* **45**, 8556–8565 (2016).
438. Schmidt, A. *et al.* Self-assembly of highly luminescent heteronuclear coordination cages. *Dalton transactions (Cambridge, England : 2003)* **45**, 12297–12300 (2016).
439. Rousseau, T. *et al.* BODIPY derivatives as donor materials for bulk heterojunction solar cells. *Chemical Communications* 1673–1675 (2009) doi:10.1039/b822770e.
440. Kamkaew, A. *et al.* BODIPY dyes in photodynamic therapy. *Chemical Society Reviews* **42**, 77–88 (2013).
441. Terai, T. & Nagano, T. Small-molecule fluorophores and fluorescent probes for bioimaging. *Journal of Physiology* **465**, 347–359 (2013).
442. Gupta, G. *et al.* Novel BODIPY-based Ru(II) and Ir(III) metalla-rectangles: Cellular localization of compounds and their antiproliferative activities. *Chemical Communications* **52**, 4274–4277 (2016).
443. Gupta, G. *et al.* Self-Assembled Novel BODIPY-Based Palladium Supramolecules and Their Cellular Localization. *Inorganic Chemistry* **56**, 4615–4621 (2017).

444. Tomasulo, M. *et al.* Photoswitchable fluorescent assemblies based on hydrophilic BODIPY-spiropyran conjugates. *Journal of Physical Chemistry C* **112**, 8038–8045 (2008).
445. Smith, N. W. *et al.* Triazole-containing BODIPY dyes as novel fluorescent probes for soluble oligomers of amyloid Aβ1-42 peptide. *Biochemical and Biophysical Research Communications* **391**, 1455–1458 (2010).
446. Brizet, B. *et al.* Boron functionalization of BODIPY by various alcohols and phenols. *Organic and Biomolecular Chemistry* **11**, 7729–7737 (2013).
447. Woods, B. *et al.* Highly luminescent metallacages featuring bispyridyl ligands functionalised with BODIPY for imaging in cancer cells. *Journal of Inorganic Biochemistry* **199**, (2019).
448. Wendel, A. & Cikryt, P. The Level and Half-life of Glutathione in Human Plasma. *FEBS Letters* **120**, 209–211 (1980).
449. Montero, D. *et al.* Intracellular glutathione pools are heterogeneously concentrated. *Redox Biology* **1**, 508–513 (2013).
450. Ahmedova, A. *et al.* M $_2$ L $_4$ coordination capsules with tunable anticancer activity upon guest encapsulation. *Dalton Transactions* **45**, 13214–13221 (2016).
451. Woods, B. *et al.* Exo-Functionalized Metallacages as Host-Guest Systems for the Anticancer Drug Cisplatin. *Frontiers in Chemistry* **7**, 1–6 (2019).
452. Melan, M. A. Overview of Cell Fixatives and Cell Membrane Permeants. in *From: Methods in Molecular Biology* vol. 115 45–55 (Immunocytochemical Methods and Protocols, 1999).
453. Kowada, T. *et al.* BODIPY-based probes for the fluorescence imaging of biomolecules in living cells. *Chemical Society Reviews* vol. 44 4953–4972 (2015).
454. Tasan, S. *et al.* BODIPY–phosphane as a versatile tool for easy access to new metal-based theranostics. *Journal of the Chemical Society. Dalton Transactions* **42**, 6102–6109 (2013).
455. Schindelin, J. *et al.* Fiji: an open-source platform for biological-image analysis. *Nature Methods* **9**, 676–682 (2012).
456. Barry, N. P. E. *et al.* Excellent correlation between drug release and portal size in metalla-cage drug-delivery systems. *Chemistry - A European Journal* **17**, 9669–9677 (2011).
457. Zhou, J. *et al.* Highly Emissive Self-Assembled BODIPY-Platinum Supramolecular Triangles. *Journal of the American Chemical Society* (2018) doi:10.1021/jacs.8b04929.
458. Uribe-Querol, E. & Rosales, C. Phagocytosis: Our Current Understanding of a Universal Biological Process. *Frontiers in Immunology* **11**, (2020).
459. Falcone, S. *et al.* Macropinocytosis: regulated coordination of endocytic and exocytic membrane traffic events. *Journal of Cell Science* **119**, 4758–4769 (2006).
460. Lim, J. P. & Gleeson, P. A. Macropinocytosis: an endocytic pathway for internalising large gulps. *Immunology & Cell Biology* **89**, 836–843 (2011).
461. Huotari, J. & Helenius, A. Endosome maturation. *The EMBO Journal* **30**, 3481–3500 (2011).
462. Lewis, J. E. M. *et al.* 'Click' to functionalise: synthesis, characterisation and enhancement of the physical properties of a series of exo- and endo-functionalised Pd_2L_4 nanocages. *Chem. Sci.* **5**, 1833–1843 (2014).

463. Poirier, A. *et al.* Design, data analysis, and simulation of in vitro drug transport kinetic experiments using a mechanistic in vitro model. *Drug Metabolism and Disposition* **36**, 2434–2444 (2008).
464. Wenzel, M. *et al.* New Luminescent Polynuclear Metal Complexes with Anticancer Properties: Toward Structure–Activity Relationships. *Inorganic Chemistry* **55**, 2544–2557 (2016).
465. Jones, D. P. *et al.* Glutathione measurement in human plasma Evaluation of sample collection, storage and derivatization conditions for analysis of dansyl derivatives by HPLC. *Clinica Chimica Acta* **275**, 175–184 (1998).
466. M Hassan, S. S. & Rechnitz, G. A. Determination of Glutathione and Glutathione Reductase with a Silver Sulfide Membrane Electrode. *Analytical Chemistry* **54**, 1972–1976 (1982).
467. Metsiou, D. N. *et al.* The Impact of Anti-tumor Agents on ER-Positive MCF-7 and HER2-Positive SKBR-3 Breast Cancer Cells Biomechanics. *Annals of Biomedical Engineering* **47**, 1711–1724 (2019).
468. Al-Bader, M. *et al.* Analysis of estrogen receptor isoforms and variants in breast cancer cell lines. *Experimental and Therapeutic Medicine* **2**, 537–544 (2011).
469. Mei, J. *et al.* Aggregation-Induced Emission: Together We Shine, United We Soar! *Chemical Reviews* **115**, 11718–11940 (2015).
470. Descalzo, A. B. *et al.* On the Aggregation Behaviour and Spectroscopic Properties of Alkylated and Annelated Boron-Dipyrromethene (BODIPY) Dyes in Aqueous Solution. *ChemPhotoChem* **4**, 120–131 (2020).
471. Cadet', J. *et al. Photochemistry of nucleic acids in cells. Journal of Photochemistry and Photobiology B: Biology* vol. 15 (1992).
472. Purschke, M. *et al.* Phototoxicity of Hoechst 33342 in time-lapse fluorescence microscopy. *Photochemical and Photobiological Sciences* **9**, 1634–1639 (2010).
473. McMahon, H. T. & Boucrot, E. Molecular mechanism and physiological functions of clathrin-mediated endocytosis. *Nature Reviews Molecular Cell Biology* **12**, 517–533 (2011).
474. Mu, F. T. *et al.* EEA1, an early endosome-associated protein. EEA1 is a conserved α- helical peripheral membrane protein flanked by cysteine “fingers” and contains a calmodulin-binding IQ motif. *Journal of Biological Chemistry* **270**, 13503–13511 (1995).
475. Wilson, J. M. *et al.* EEA1, a Tethering Protein of the Early Sorting Endosome, Shows a Polarized Distribution in Hippocampal Neurons, Epithelial Cells, and Fibroblasts. *Molecular Biology of the Cell* **11**, 2657–2671 (2000).
476. Kamentseva, R. *et al.* Functional cycle of EEA1-positive early endosome: Direct evidence for pre-existing compartment of degradative pathway. *PLoS ONE* **15**, (2020).
477. Arora, M. Cell Culture Media: A Review. *Materials and Methods* https://www.labome.com/method/Cell-Culture-Media-A-Review.html (2013) doi:10.13070/mm.en.3.175.
478. Aaron, J. S. *et al.* Image co-localization - co-occurrence versus correlation. *Journal of cell science* **131**, (2018).
479. Cordelì, F. P. & Bolte, S. *JACoP v2.0: improving the user experience with co-localization studies*. (2008).
480. Dunn, K. W. *et al.* A practical guide to evaluating colocalization in biological microscopy. *American Journal of Physiology-Cell Physiology* **300**, C723–C742 (2011).

481. Adler, J. & Parmryd, I. Quantifying colocalization by correlation: The Pearson correlation coefficient is superior to the Mander's overlap coefficient. *Cytometry Part A* **77A**, 733–742 (2010).
482. Bolte, S. & Cordelieres, F. P. A guided tour into subcellular colocalization analysis in light microscopy. *Journal of Microscopy* **224**, 213–232 (2006).
483. Raposo, G. & Marks, M. S. Melanosomes — dark organelles enlighten endosomal membrane transport. *Nature Reviews Molecular Cell Biology* **8**, 786–797 (2007).
484. Marks, M. S. & Seabra, M. C. The melanosome: membrane dynamics in black and white. *Nature Reviews Molecular Cell Biology* **2**, 738–748 (2001).
485. Büngeler, A. *et al.* The supramolecular buildup of eumelanin: Structures, mechanisms, controllability. *International Journal of Molecular Sciences* **18**, (2017).
486. Litwack, G. Metabolism of Amino Acids. in *Human Biochemistry* 359–394 (Elsevier, 2018). doi:10.1016/b978-0-12-383864-3.00013-2.
487. Raposo, G. *et al.* Distinct protein sorting and localization to premelanosomes, melanosomes, and lysosomes in pigmented melanocytic cells. *Journal of Cell Biology* **152**, 809–823 (2001).
488. Sitaram, A. & Marks, M. S. Mechanisms of Protein Delivery to Melanosomes in Pigment Cells. *Physiology* **27**, 85–99 (2012).
489. Ohbayashi, N. & Fukuda, M. Recent advances in understanding the molecular basis of melanogenesis in melanocytes. *F1000Research* vol. 9 (2020).
490. Ninković, D. B. *et al.* What Is Special about Aromatic-Aromatic Interactions? Significant Attraction at Large Horizontal Displacement. *ACS Central Science* **6**, 420–425 (2020).
491. Schroeder, R. L. & Gerber, J. P. Chloroquine and hydroxychloroquine binding to melanin: Some possible consequences for pathologies. *Toxicology Reports* **1**, 963–968 (2014).
492. Bridelli, M. G. *et al.* Binding of chemicals to melanins re-examined: Adsorption of some drugs to the surface of melanin particles. *Biophysical Chemistry* **119**, 137–145 (2006).
493. Ishida, M. *et al.* M-INK, a novel tool for visualizing melanosomes and melanocores. *Journal of Biochemistry* **161**, 323–326 (2017).
494. Yoshikawa-Murakami, C. *et al.* A novel method for visualizing melanosome and melanin distribution in human skin tissues. *International Journal of Molecular Sciences* **21**, 1–14 (2020).
495. Moreiras, H. *et al.* Melanin transfer in the epidermis: The pursuit of skin pigmentation control mechanisms. *International Journal of Molecular Sciences* vol. 22 4466 (2021).
496. Berens, W. *et al.* Different approaches for assaying melanosome transfer. *Pigment Cell Research* **18**, 370–381 (2005).
497. Dijkgraaf, F. E. *et al.* Labeling and tracking of immune cells in ex vivo human skin. *Nature Protocols* (2020) doi:10.1038/s41596-020-00435-8.
498. Gou, X.-X. *et al.* On/off fluorescence emission induced by encapsulation, exchange and reversible encapsulation of a BODIPY-guest in self-assembled organometallic cages. *Dalton Transactions* **48**, 7236–7241 (2019).
499. Murtagh, J. *et al.* Azide Conjugatable and pH Responsive Near-Infrared Fluorescent Imaging Probes. *Organic Letters* **11**, 5386–5389 (2009).

500. Sudan, S. *et al.* Identification of a Heteroleptic $Pd_6L_6L'_6$ Coordination Cage by Screening of a Virtual Combinatorial Library. *Journal of the American Chemical Society* **143**, 1773–1778 (2021).

501. Preston, D. *et al*. Controlled Formation of Heteroleptic $[Pd_2(L_a)_2(L_b)_2]^{4+}$ Cages. *Journal of the American Chemical Society* **138**, 10578–10585 (2016).

Appendix

Appendix A

Appendix B

Appendix C

Appendix A

A1. Photophysical properties of the pyridine-benzimidazole series: Absorption and emission

Ligand L1

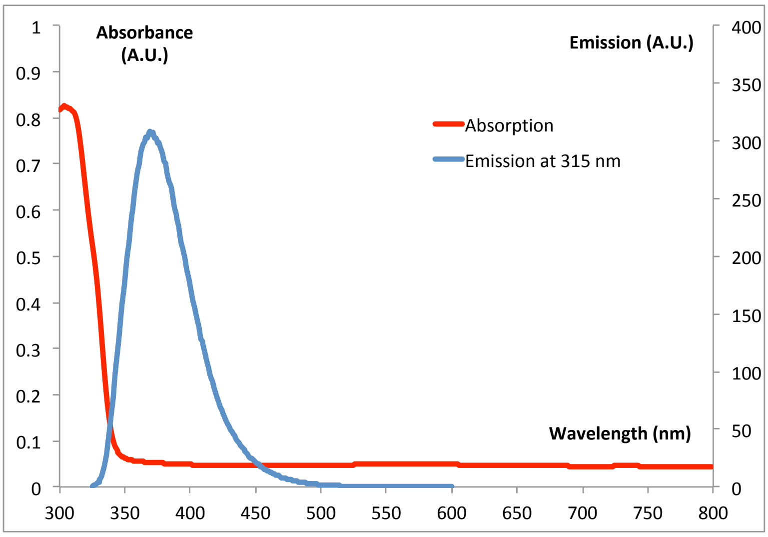

Quantum yield in DMSO at 298K: 60% (Concentration: 3.3.10^{-5}M)
UV-Vis (DMSO): λ_{max} (nm) (ε, cm^{-1}.mol^{-1}.dm^3) 311 (20260).

*Figure S1: Absorption and emission spectra of ligand **L1**.*

Complex C1

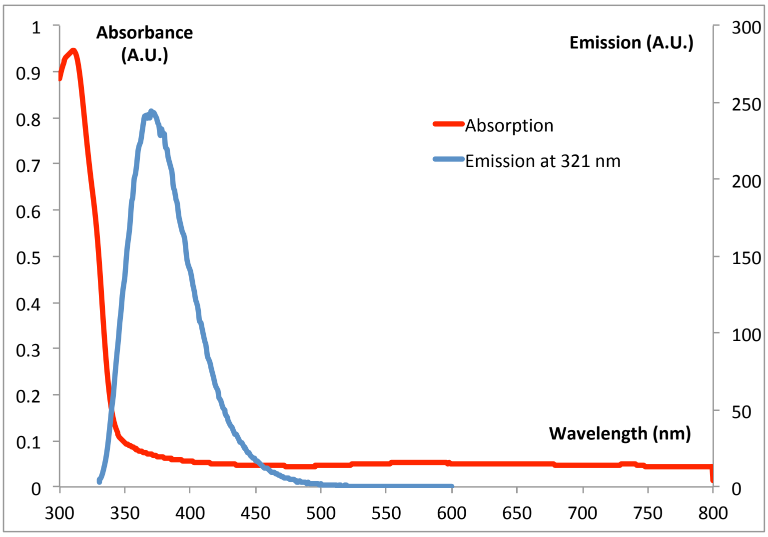

Quantum yield in DMSO at 298K: 48% (Concentration: 3.3.10^{-5}M)
UV-Vis (DMSO): λ_{max} (nm) (ε, cm^{-1}.mol^{-1}.dm^3) 314 (23949).

*Figure S2: Absorption and emission spectra of complex **C1***

Ligand L2

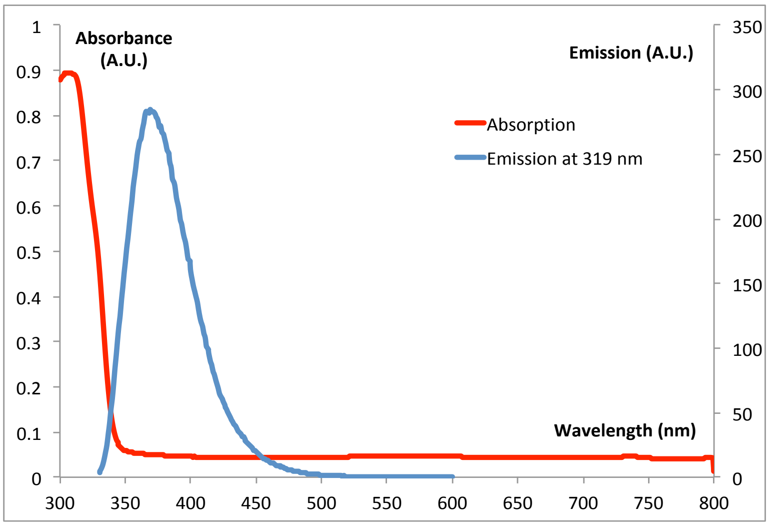

Quantum yield in DMSO at 298K: 54%

(Concentration: $3.3.10^{-5}$M)

UV-Vis (DMSO): λ_{max} (nm) (ε, $cm^{-1}.mol^{-1}.dm^3$) 312 (21645).

*Figure **S3**: Absorption and emission spectra of ligand **L2***

Complex C2

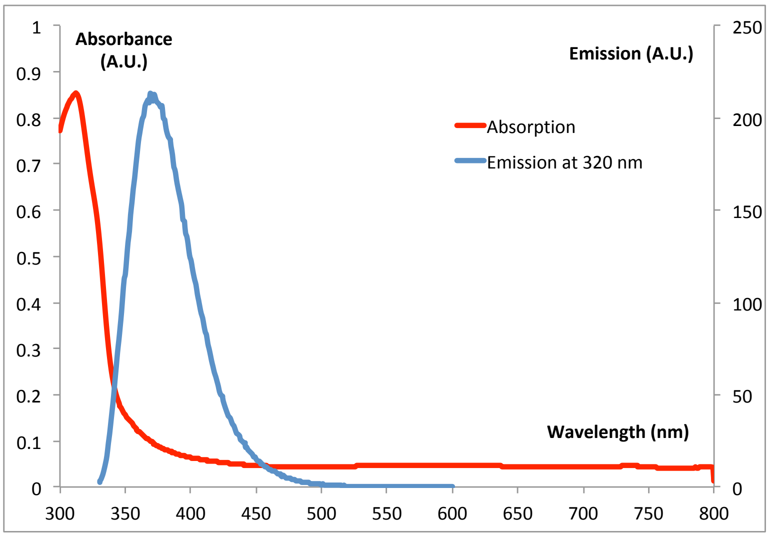

Quantum yield in DMSO at 298K: 39%

(Concentration: $3.3.10^{-5}$M)

UV-Vis (DMSO): λ_{max} (nm) (ε, $cm^{-1}.mol^{-1}.dm^3$) 316 (21654).

*Figure **S4**: Absorption and emission spectra of complex **C2***

Ligand L3

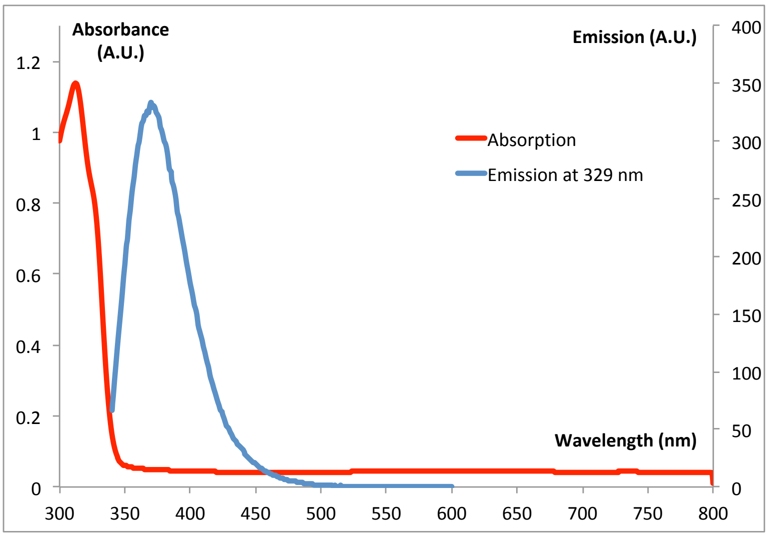

Quantum yield in DMSO at 298K: 50% (Concentration: $3.3.10^{-5}$M) UV-Vis (DMSO): λ_{max} (nm) (ε, $cm^{-1}.mol^{-1}.dm^3$) 313 (27357).

Figure S5**: Absorption and emission spectra of ligand **L3

Complex C3

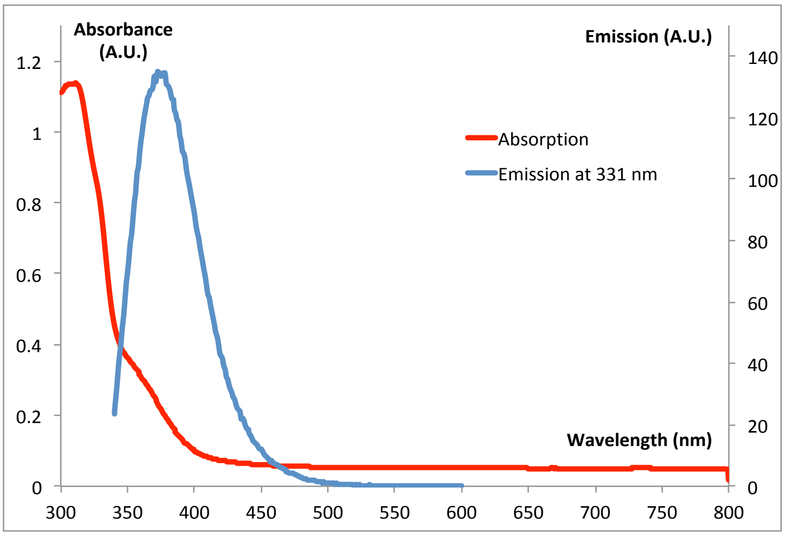

Quantum yield in DMSO at 298K: 27% (Concentration: $6.6.10^{-5}$M) UV-Vis (DMSO): λ_{max} (nm) (ε, $cm^{-1}.mol^{-1}.dm^3$) 315 (16006).

Figure S6**: Absorption and emission spectra of complex **C3

Ligand L4

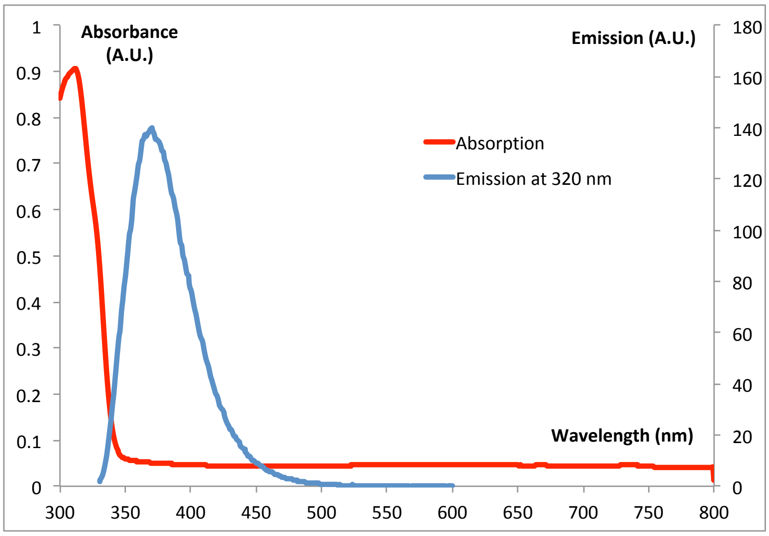

Quantum yield in DMSO at 298K: 27%

(Concentration: 3.3.10^{-5}M)

UV-Vis (DMSO): λ_{max} (nm) (ε, cm^{-1}.mol^{-1}.dm^{3}) 312 (24729).

*Figure **S7**: Absorption and emission spectra of ligand **L4***

Complex C4

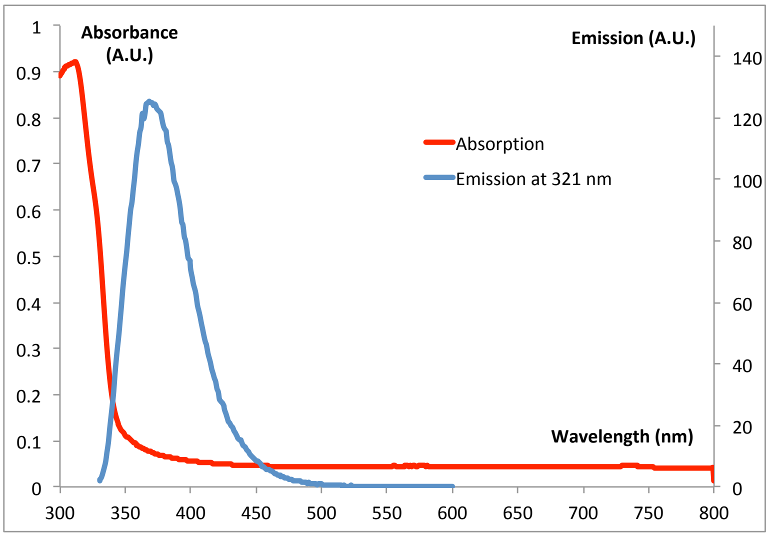

Quantum yield in DMSO at 298K: 23%

(Concentration: 3.3.10^{-5}M)

UV-Vis (DMSO): λ_{max} (nm) (ε, cm^{-1}.mol^{-1}.dm^{3}) 315 (21527).

*Figure **S8**: Absorption and emission spectra of complex **C4***

Ligand L5

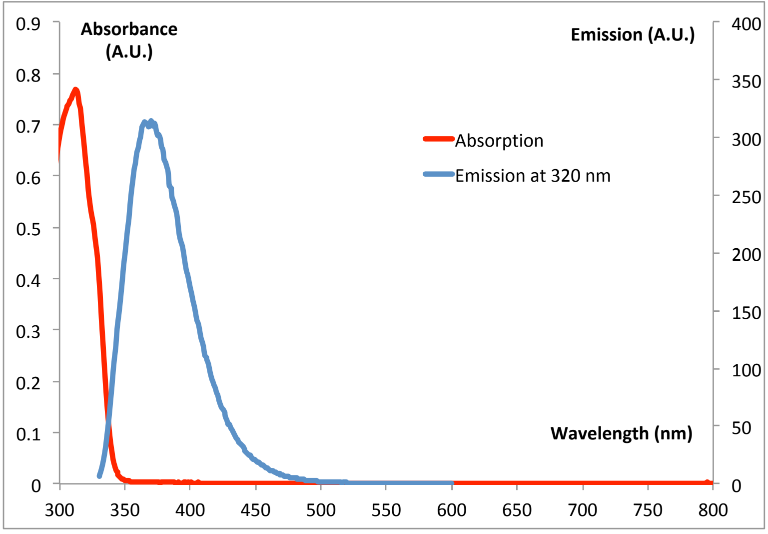

Quantum yield in DMSO at 298K: 30%

(Concentration: 4.2.10^{-5}M)
UV-Vis (DMSO): λ_{max} (nm) (ε, cm^{-1}.mol^{-1}.dm^{3}) 313 (14123).

*Figure S9: Absorption and emission spectra of ligand **L5***

Complex C5

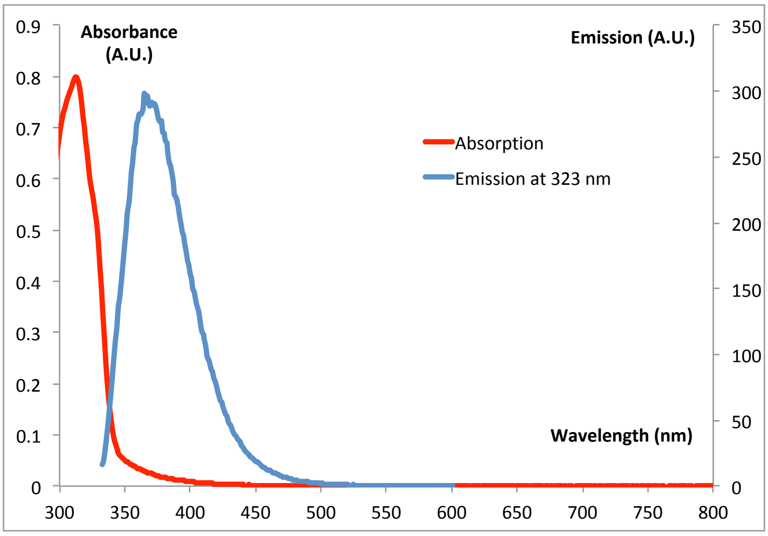

Quantum yield in DMSO at 298K: 29%

(Concentration: 3.4.10^{-5}M)
UV-Vis (DMSO): λ_{max} (nm) (ε, cm^{-1}.mol^{-1}.dm^{3}) 312 (23448).

*Figure S10: Absorption and emission spectra of complex **C5***

Ligand L6

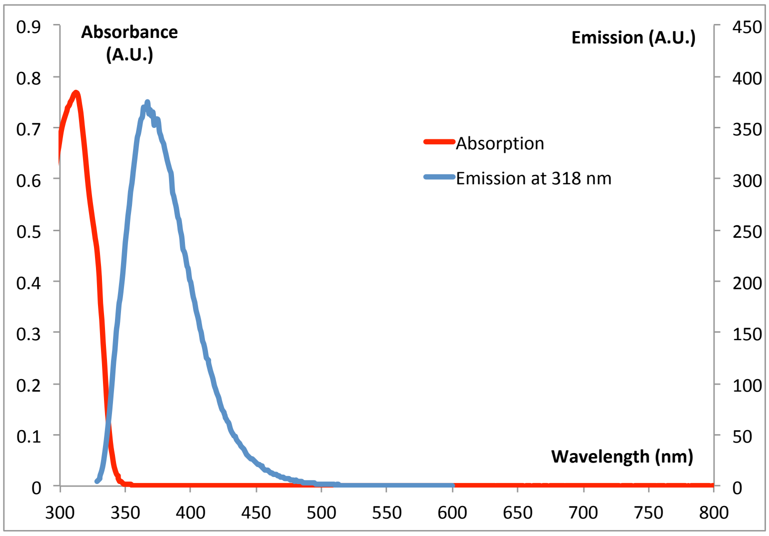

Quantum yield in DMSO at 298K: 38%

(Concentration: $3.3.10^{-5}$M)

UV-Vis (DMSO): λ_{max} (nm) (ε, $cm^{-1}.mol^{-1}.dm^3$) 313 (23130).

Figure S11: *Absorption and emission spectra of ligand **L6***

Complex C6

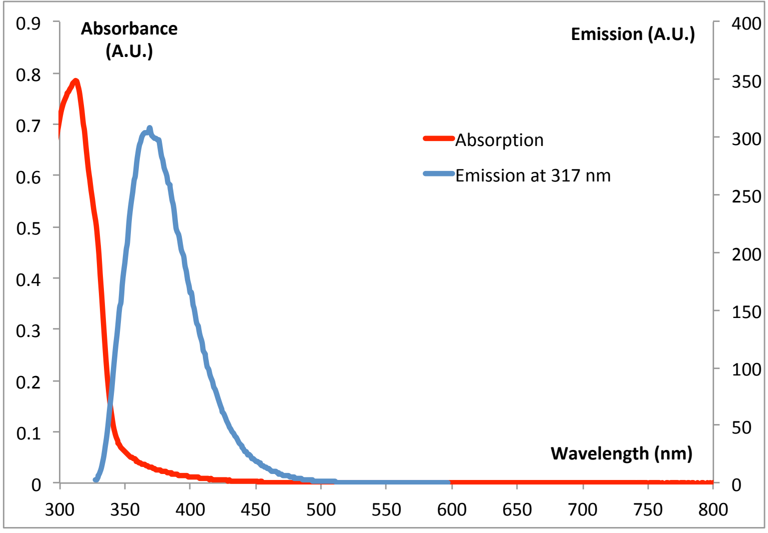

Quantum yield in DMSO at 298K: 32%

(Concentration: $2.7.10^{-5}$M)

UV-Vis (DMSO): λ_{max} (nm) (ε, $cm^{-1}.mol^{-1}.dm^3$) 312 (24699).

Figure S12: *Absorption and emission spectra of complex **C6***

Ligand L7

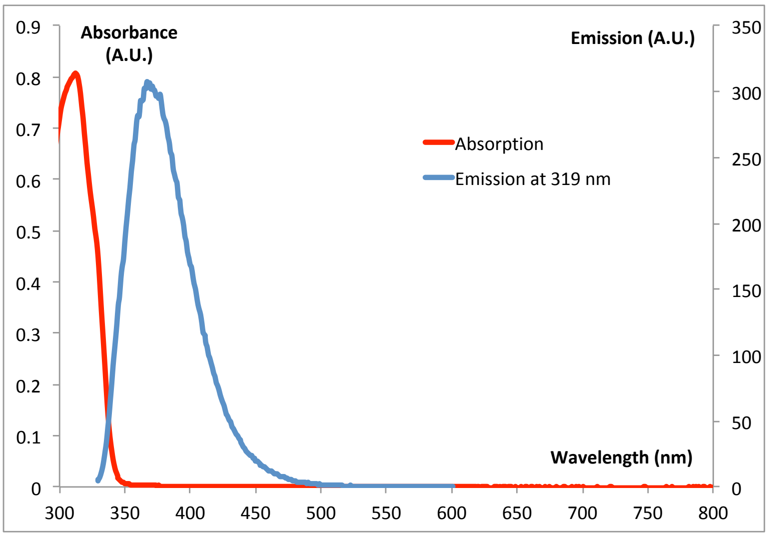

Quantum yield in DMSO at 298K: 32%

(Concentration: $3.8.10^{-5}$M)

UV-Vis (DMSO): λ_{max} (nm) (ε, $cm^{-1}.mol^{-1}.dm^3$) 312 (21244).

***Figure S13**: Absorption and emission spectra of ligand **L7**.*

Complex C7

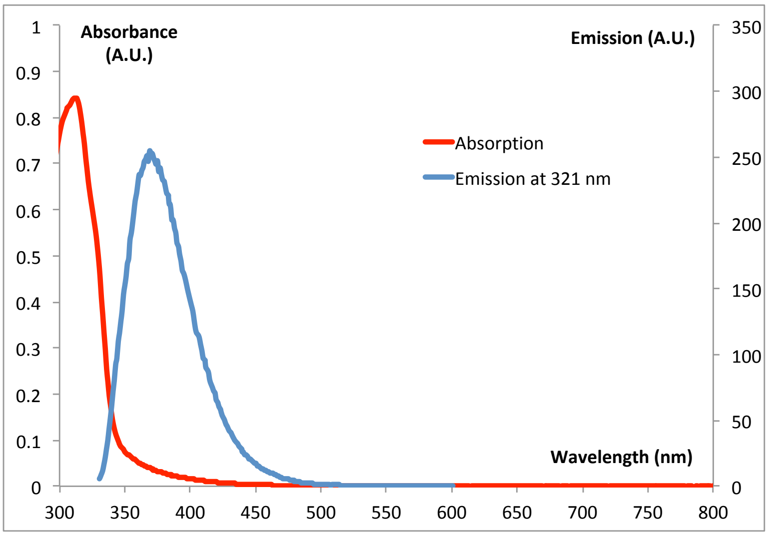

Quantum yield in DMSO at 298K: 26%

(Concentration: $2.6.10^{-5}$M)

UV-Vis (DMSO): λ_{max} (nm) (ε, $cm^{-1}.mol^{-1}.dm^3$) 312 (25542).

***Figure S14**: Absorption and emission spectra of complex **C7**.*

Ligand L8

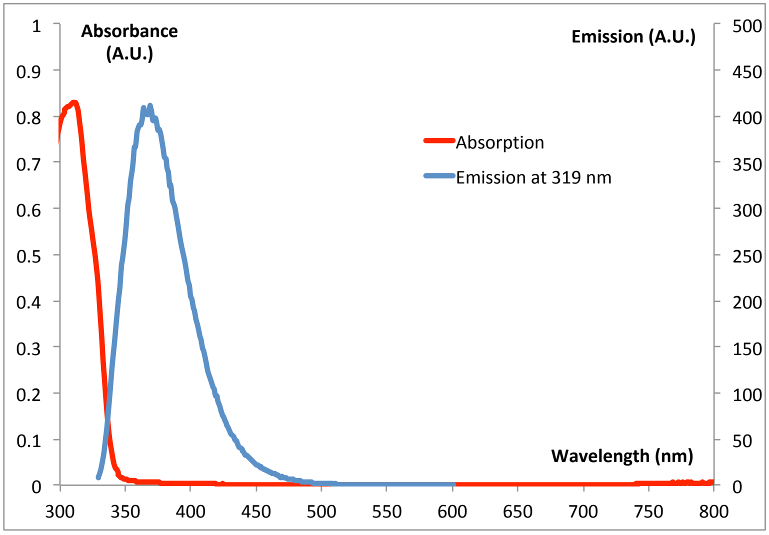

Quantum yield in DMSO at 298K: 42% (Concentration: $2.4.10^{-5}$M) UV-Vis (DMSO): λ_{max} (nm) (ε, $cm^{-1}.mol^{-1}.dm^3$) 312 (29031).

Figure S15: Absorption and emission spectra of ligand ***L8****.*

Complex C8

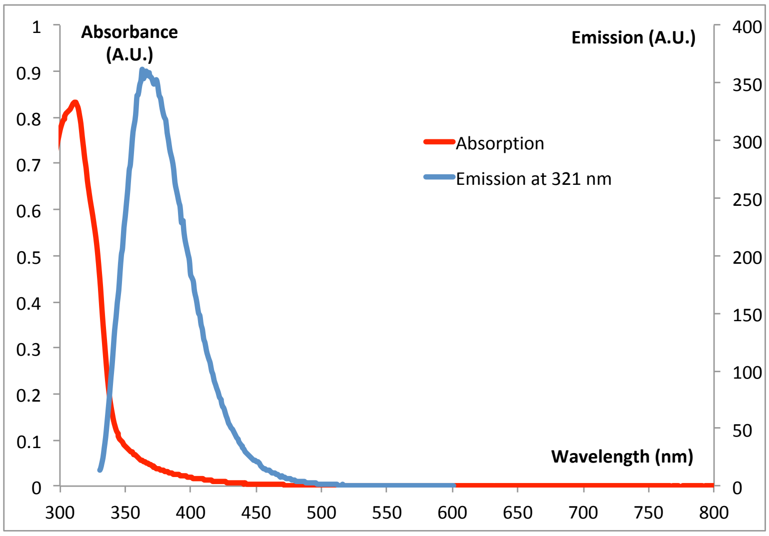

Quantum yield in DMSO at 298K: 36%

(Concentration: $2.9.10^{-5}$M) UV-Vis (DMSO): λ_{max} (nm) (ε, $cm^{-1}.mol^{-1}.dm^3$) 311 (23441).

Figure S16: Absorption and emission spectra of complex ***C8****.*

Ligand L9

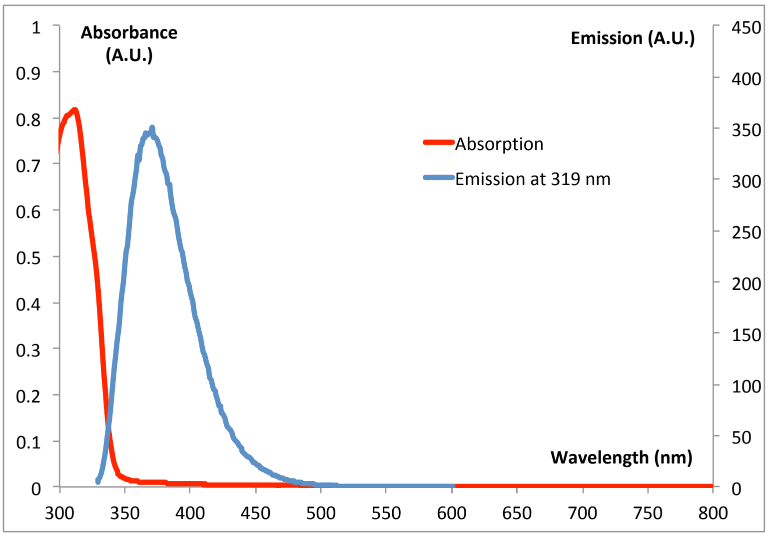

Quantum yield in DMSO at 298K: 36%

(Concentration: 3.1.10^{-5}M)

UV-Vis (DMSO): λ_{max} (nm) (ε, cm^{-1}.mol^{-1}.dm^{3}) 312 (22425).

Figure S17: Absorption and emission spectra of ligand **L9**.

Complex C9

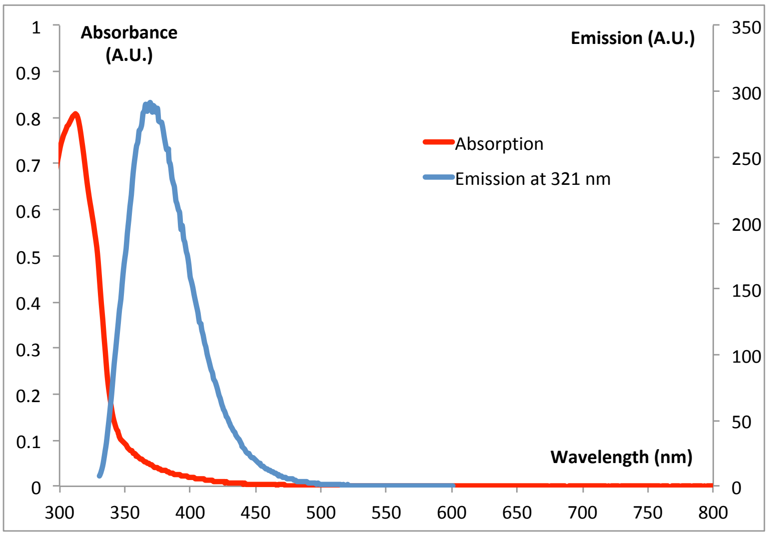

Quantum yield in DMSO at 298K: 30%

(Concentration: 3.0.10^{-5}M)

UV-Vis (DMSO): λ_{max} (nm) (ε, cm^{-1}.mol^{-1}.dm^{3}) 313 (14367).

Figure S18*: Absorption and emission spectra of complex* ***C9****.*

Ligand L10

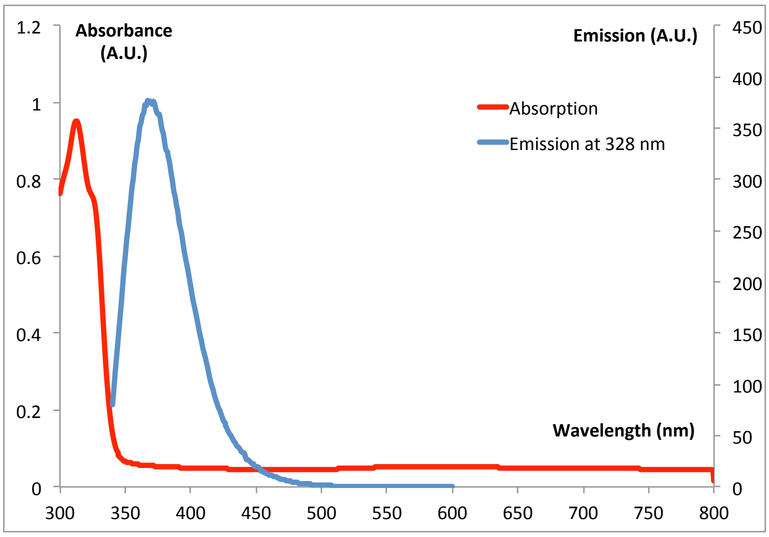

Quantum yield in DMSO at 298K: 69%

(Concentration: 3.3.10^{-5}M)

UV-Vis (DMSO): λ_{max} (nm) (ε, cm^{-1}.mol^{-1}.dm^3) 313 (24475).

Figure S19: *Absorption and emission spectra of ligand* ***L10****.*

Complex C10

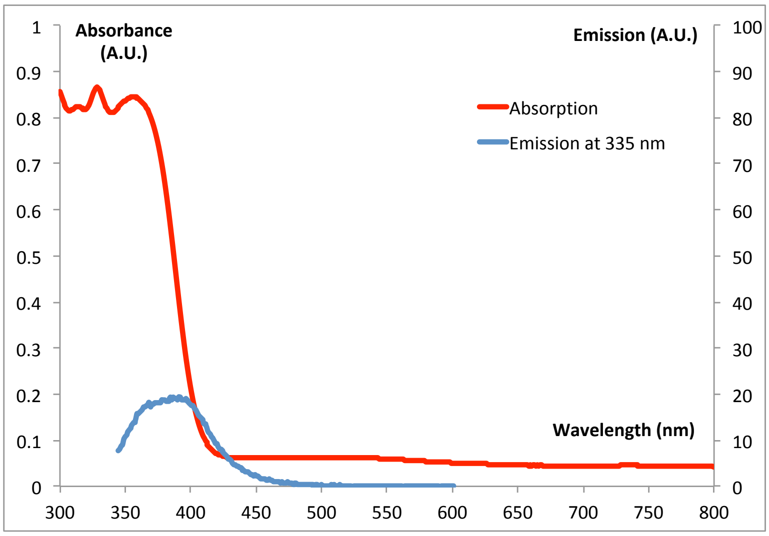

Quantum yield in DMSO at 298K: 4%

(Concentration: 5.0.10^{-5}M)

UV-Vis (DMSO): λ_{max} (nm) (ε, cm^{-1}.mol^{-1}.dm^3) 332 (12883).

Figure S20*: Absorption and emission spectra of complex* ***C10.***

Ligand L11

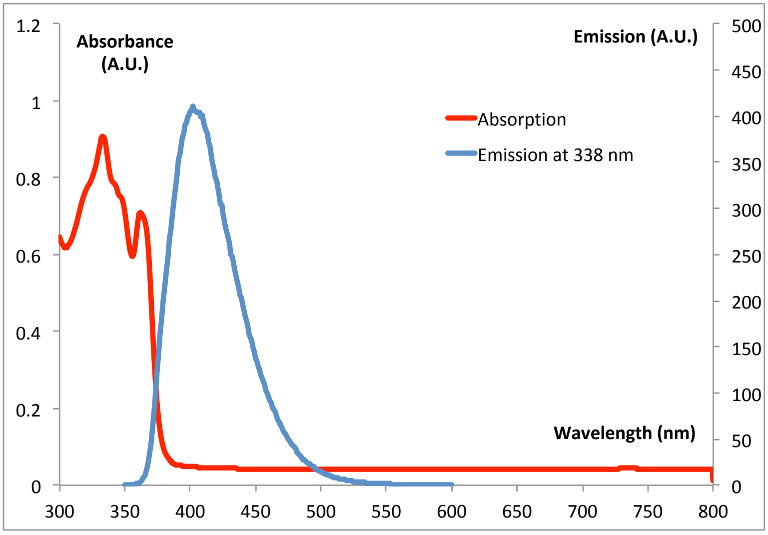

Quantum yield in DMSO at 298K: 74% (Concentration: 4.0.10^{-5}M)
UV-Vis (DMSO): λ_{max} (nm) (ε, cm^{-1}.mol^{-1}.dm^{3}) 333 (20088), 362 (15966).

Figure S21: *Absorption and emission spectra of ligand* ***L11****.*

Complex C11

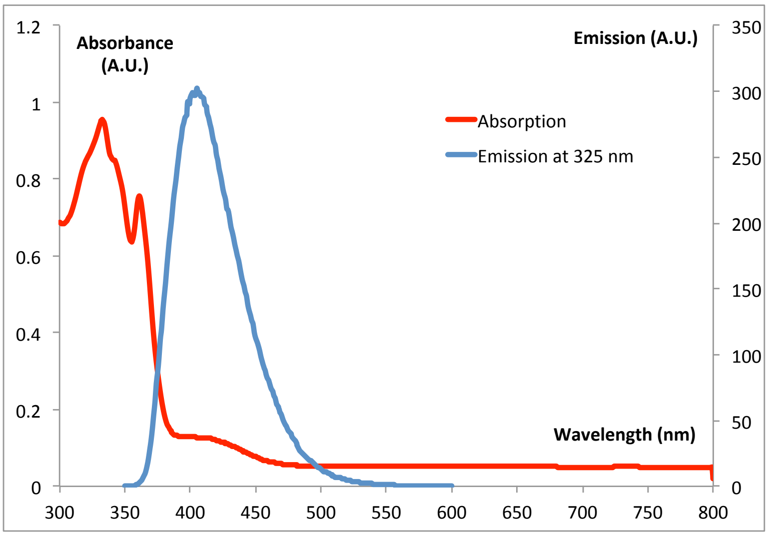

Quantum yield in DMSO at 298K: 56% (Concentration: 5.6.10^{-5}M)
UV-Vis (DMSO): λ_{max} (nm) (ε, cm^{-1}.mol^{-1}.dm^{3}) 335 (20891), 362 (16528).

Figure S22*: Absorption and emission spectra of complex* ***C11****.*

Ligand L12

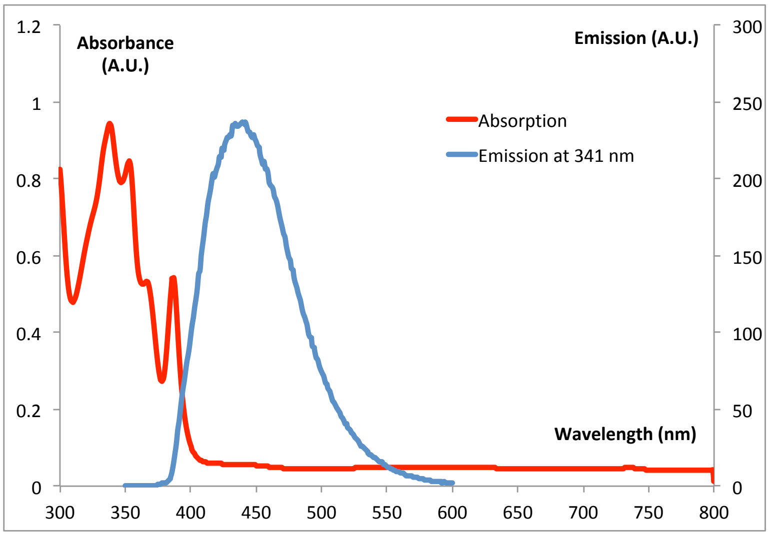

Quantum yield in DMSO at 298K: 61% (Concentration: 3.3.10^{-5}M)

UV-Vis (DMSO): λ_{max} (nm) (ε, $cm^{-1}.mol^{-1}.dm^3$) 338 (25928), 353 (24139), 366 (15420), 387 (15708).

*Figure S23: Absorption and emission spectra of ligand **L12**.*

Complex C12

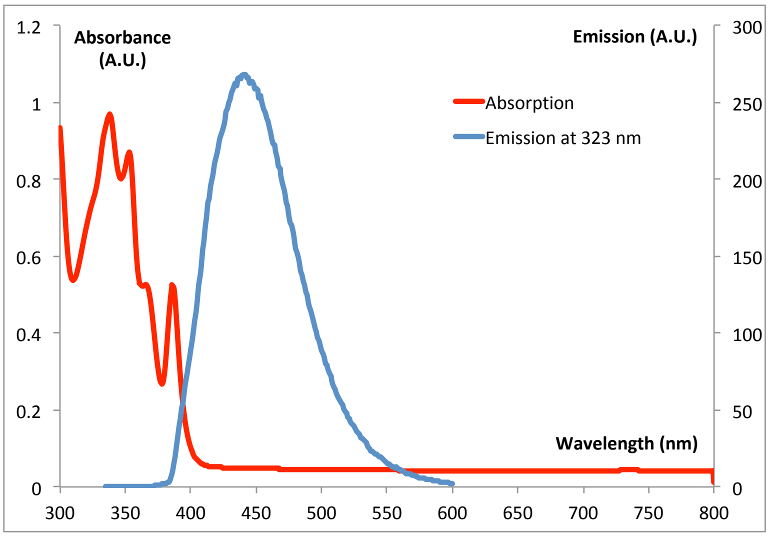

Quantum yield in DMSO at 298K: 71%

(Concentration: 2.2.10^{-5}M)

UV-Vis (DMSO): λ_{max} (nm) (ε, $cm^{-1}.mol^{-1}.dm^3$) 338 (28904), 353 (28264), 366 (19892), 388 (20031).

*Figure S24: Absorption and emission spectra of complex **C12**.*

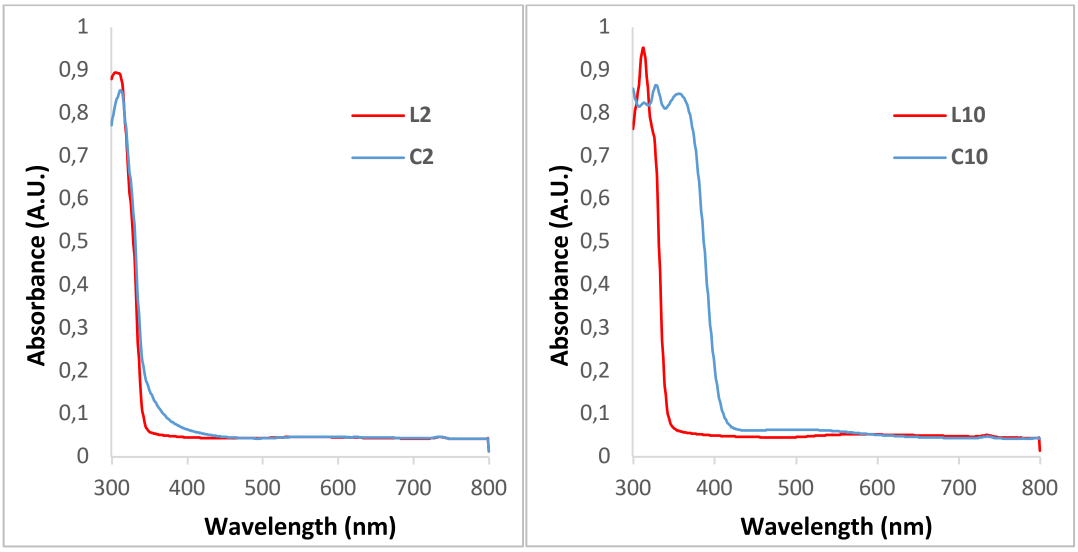

Figure S25*: Absorption spectra of complex and corresponding ligand examples of* ***C2*** *(left) and* ***C10*** *(right) in DMSO.*

A2. Stability studies of the pyridine-benzimidazole series by UV-visible spectrophotometry

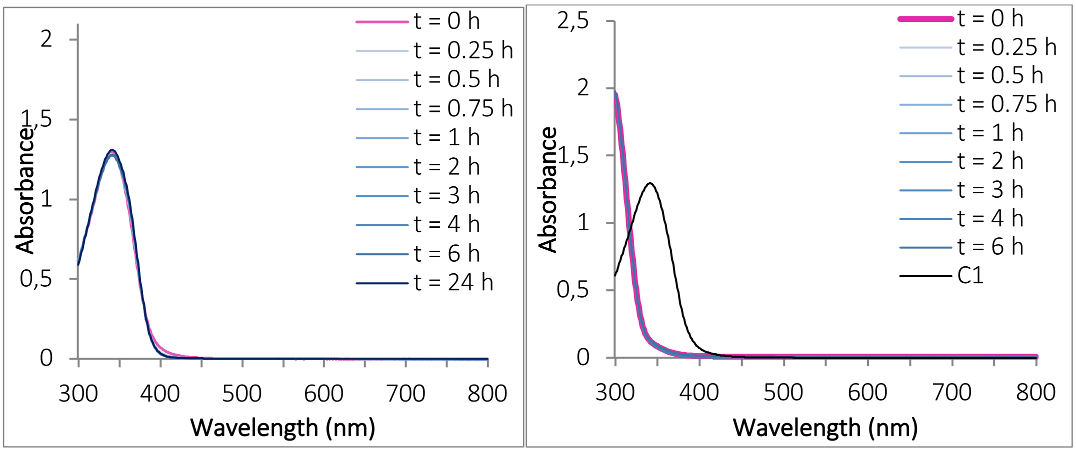

Figure S26*: UV-Visible spectra of the Au(III) complex* ***C1*** *(10^{-4} M) in in PBS (pH 7.4) recorded over time (left); and of* ***C1*** *before and after addition of GSH (2 eq.) recorded over time at room temperature (right).*

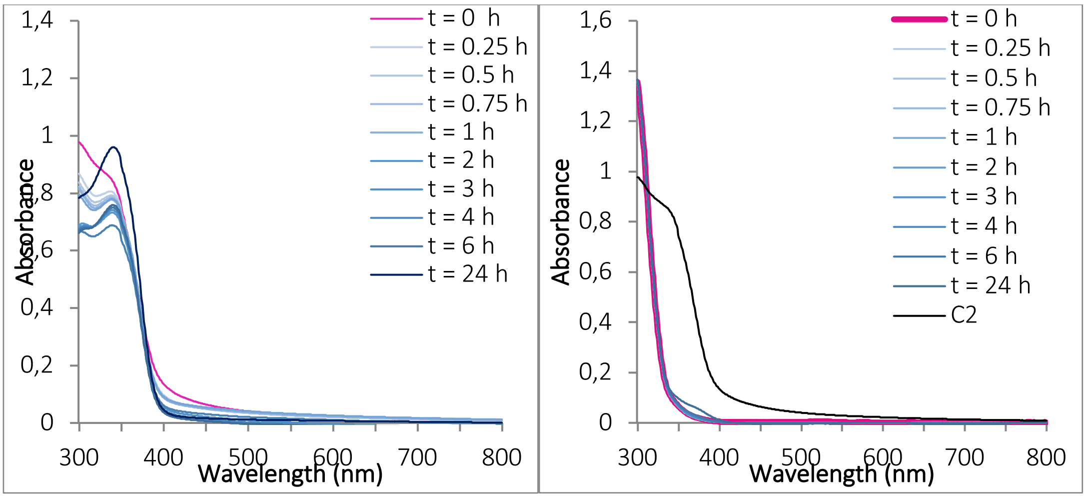

Figure S27: *UV-Visible spectra of the Au(III) complex* ***C2*** *(10^{-4} M) in in PBS (pH 7.4) recorded over time (left); and of* ***C2*** *before and after addition of GSH (2 eq.) recorded over time at room temperature (right).*

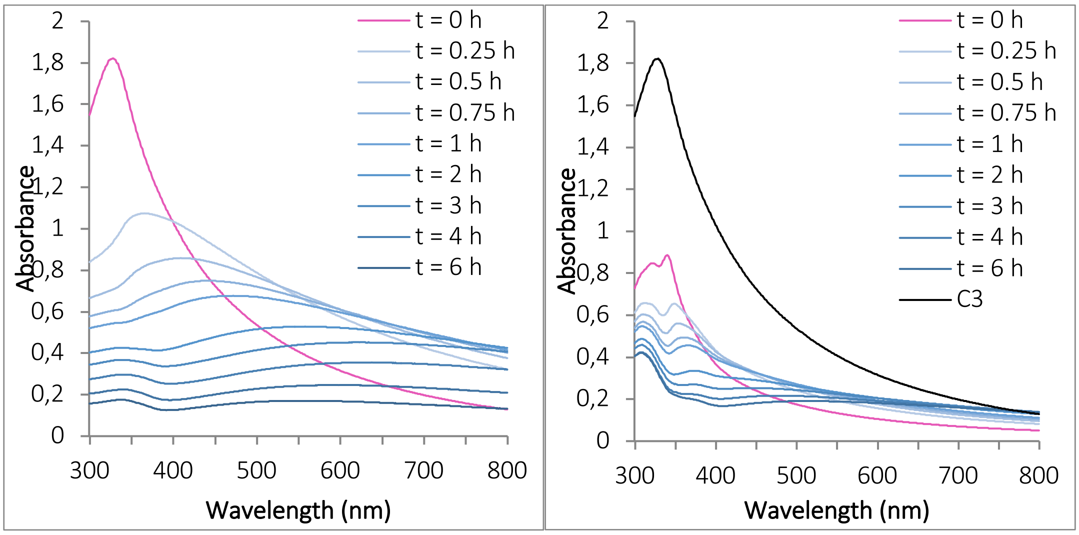

***Figure S28**: UV-Visible spectra of the Au(III) complex **C3** (10^{-4} M) in in PBS (pH 7.4) recorded over time (left); and of **C3** before and after addition of GSH (2 eq.) recorded over time at room temperature (right).*

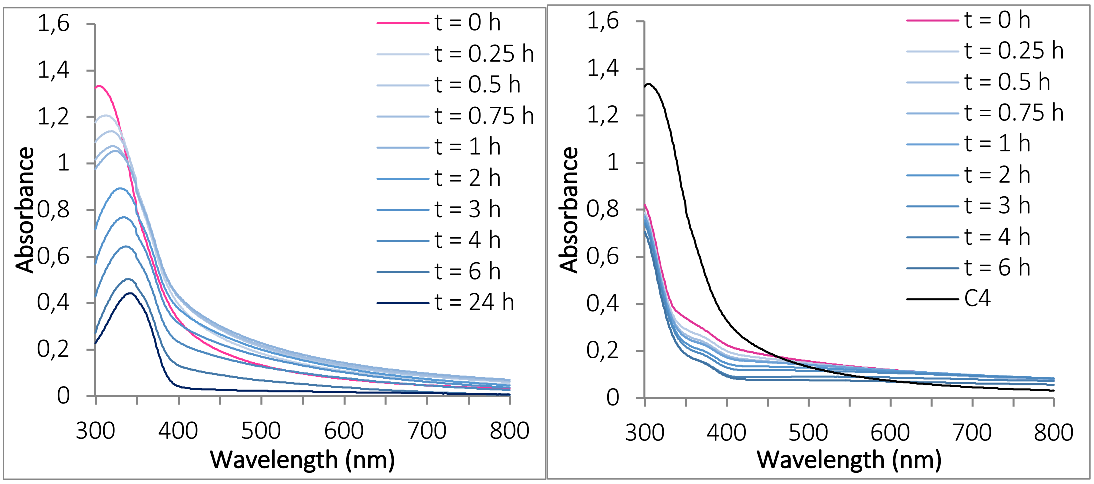

***Figure S29:** UV-Visible spectra of the Au(III) complex **C4** (10^{-4} M) in in PBS (pH 7.4) recorded over time (left); and of **C4** before and after addition of GSH (2 eq.) recorded over time at room temperature (right).*

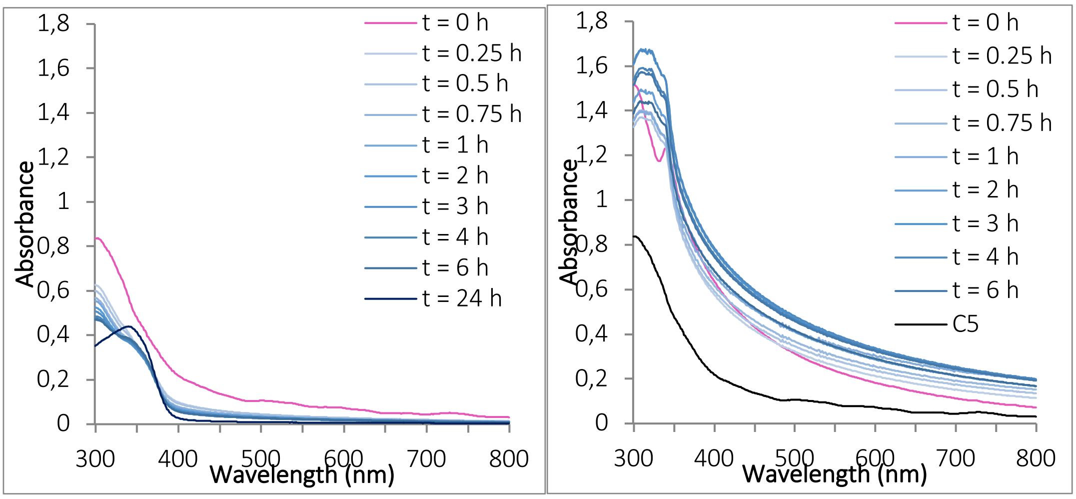

***Figure S30**: UV-Visible spectra of the Au(III) complex **C5** (10^{-4} M) in in PBS (pH 7.4) recorded over time (left); and of **C5** before and after addition of GSH (2 eq.) recorded over time at room temperature (right).*

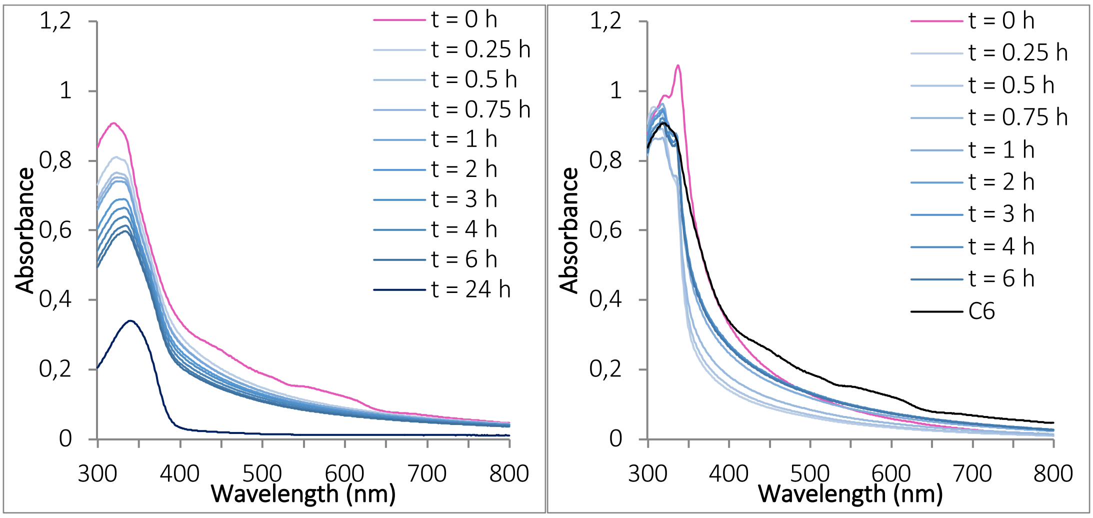

***Figure S31:** UV-Visible spectra of the Au(III) complex **C6** (10^{-4} M) in in PBS (pH 7.4) recorded over time (left); and of **C6** before and after addition of GSH (2 eq.) recorded over time at room temperature (right).*

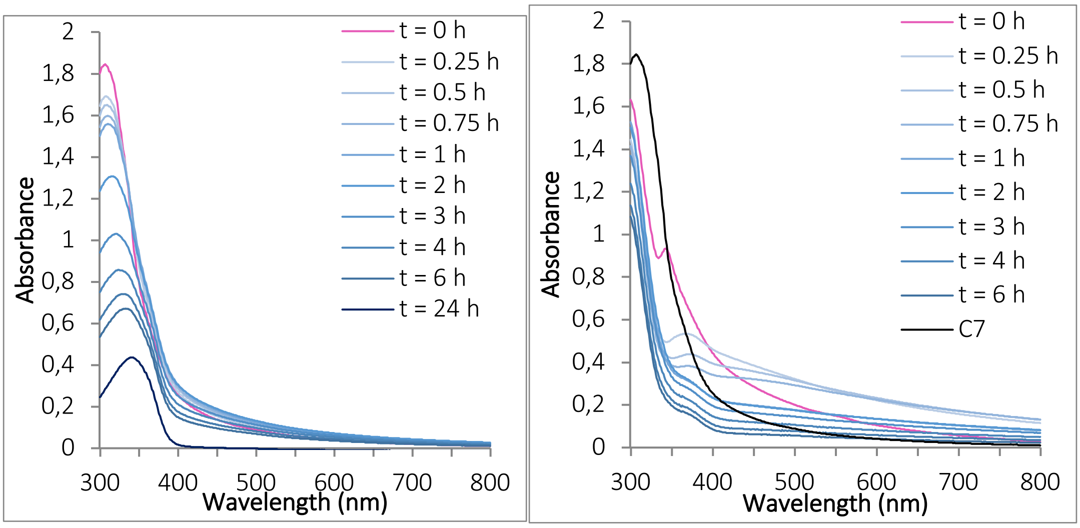

Figure S32: *UV-Visible spectra of the Au(III) complex **C7** (10^{-4} M) in in PBS (pH 7.4) recorded over time (left); and of **C7** before and after addition of GSH (2 eq.) recorded over time at room temperature (right).*

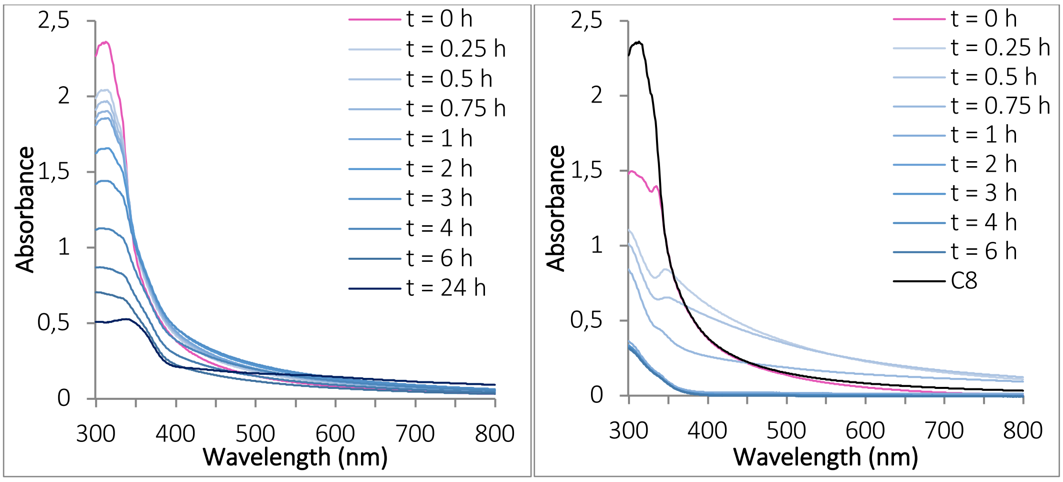

Figure S33: *UV-Visible spectra of the Au(III) complex **C8** (10^{-4} M) in in PBS (pH 7.4) recorded over time (left); and of **C8** before and after addition of GSH (2 eq.) recorded over time at room temperature (right).*

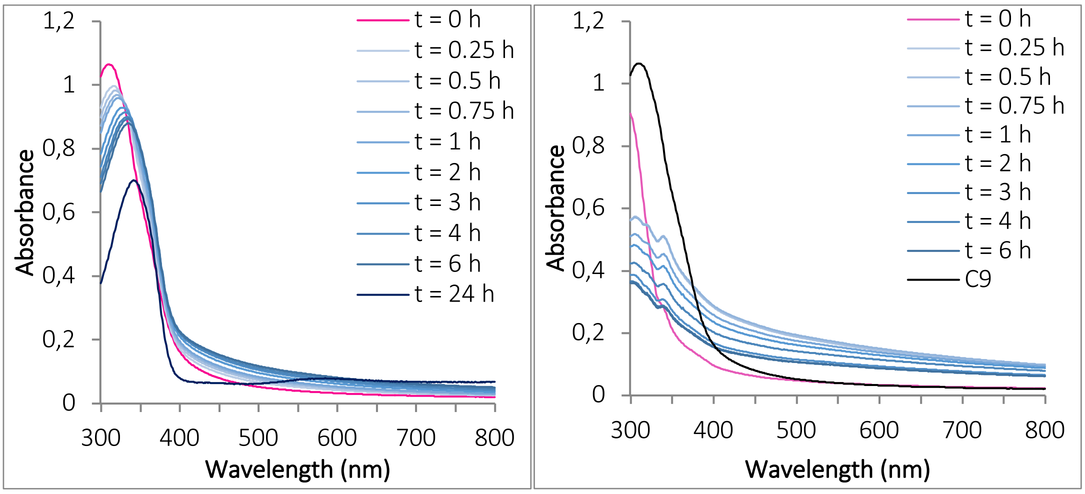

***Figure S34**: UV-Visible spectra of the Au(III) complex **C9** (10^{-4} M) in in PBS (pH 7.4) recorded over time (left); and of **C9** before and after addition of GSH (2 eq.) recorded over time at room temperature (right).*

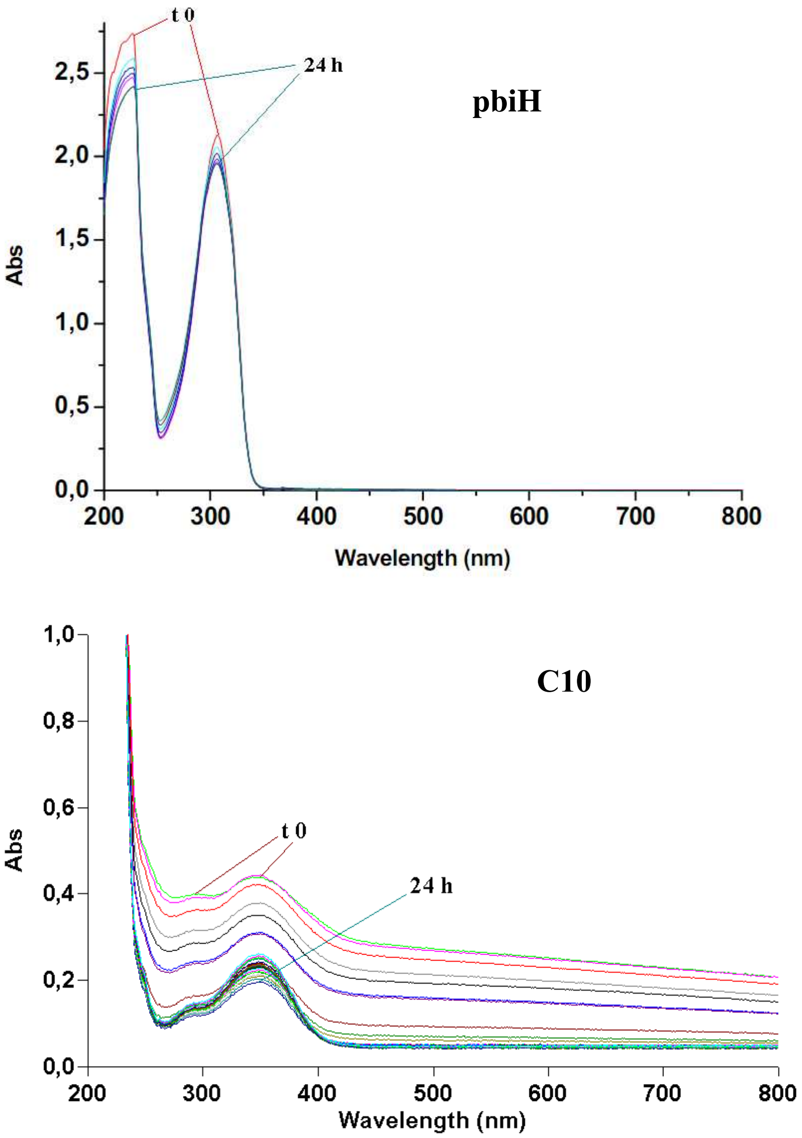

***Figure S35**: Hydrolysis profiles of ligand pbiH (top) and complexes **C10** (bottom) dissolved in PBS pH 7.4 (1% DMSO). Spectra were recorded at different times over 24 h at room temperature.*

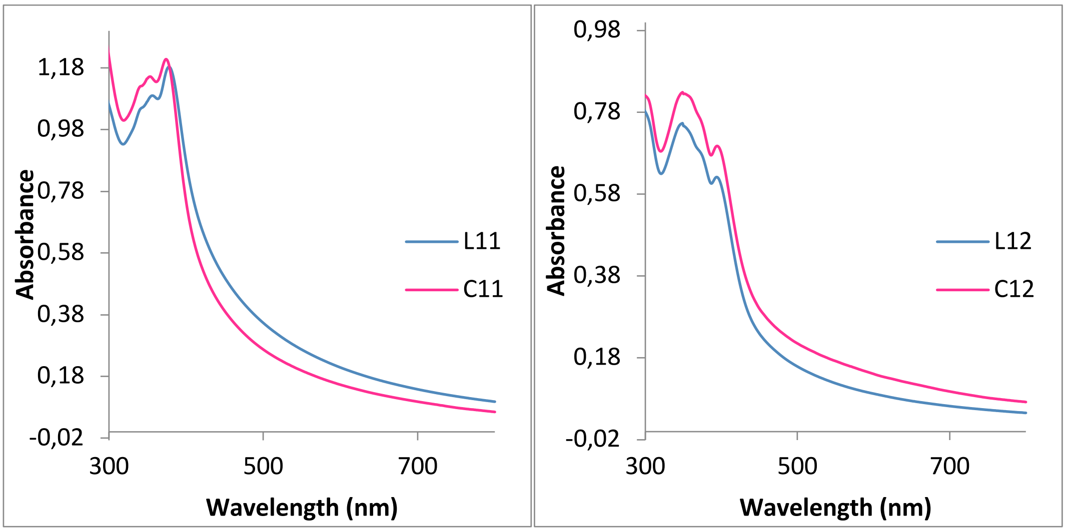

Figure S36: *Comparison between the absorption UV-Vis spectra in PBS (pH 7.4) of ligand* ***L11*** *(10^{-4} M) with related Au(III) complex* ***C11*** *(10^{-4} M) (left); and of ligand* ***L12*** *(10^{-4} M) with related Au(III) complex* ***C12*** *(10^{-4} M) (right).*

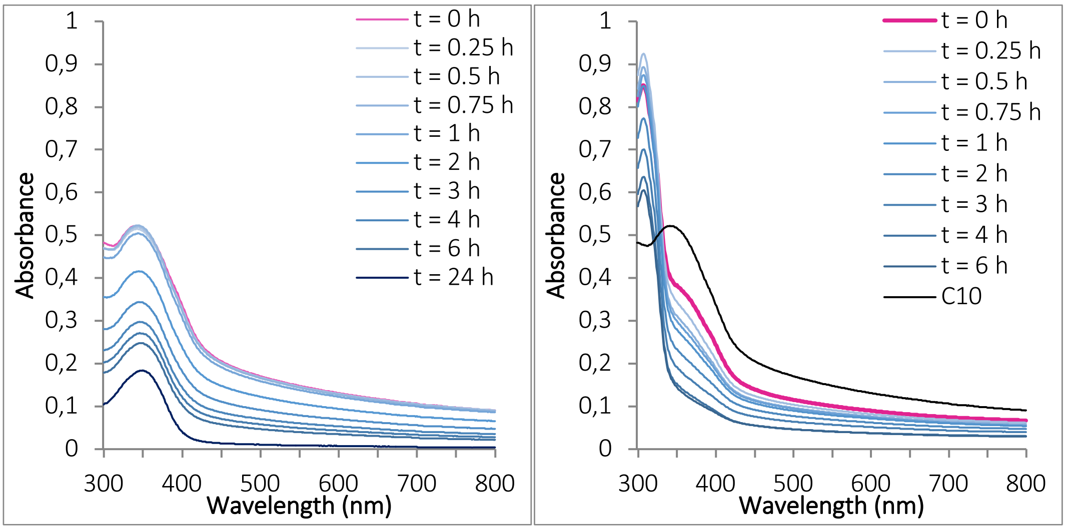

Figure S37: *UV-Visible spectra of the Au(III) complex* ***C10*** *(10^{-4} M) in PBS (pH 7.4) recorded over time (left); and of* ***C10*** *before and after addition of GSH (2 eq.) recorded over time at room temperature (right).*

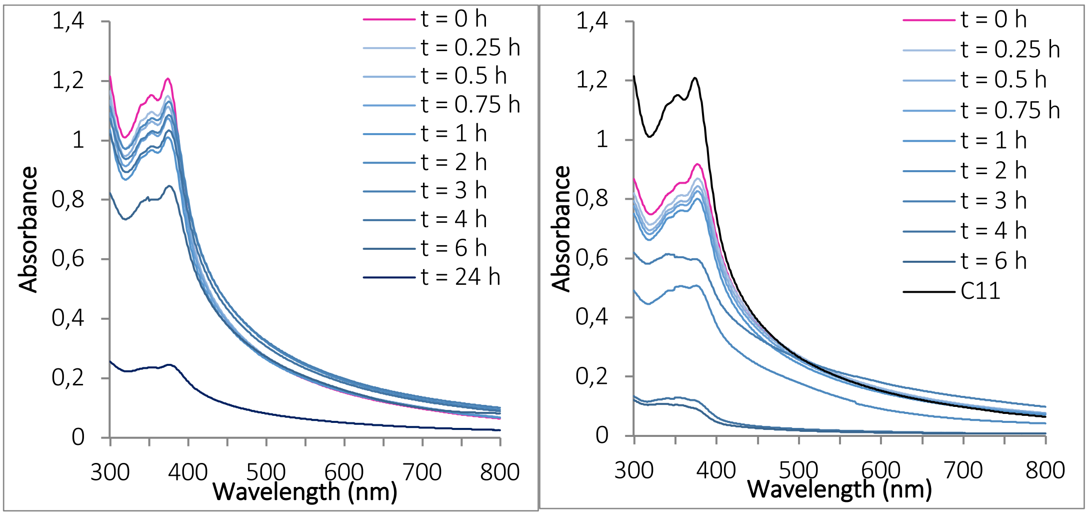

Figure S38: *UV-Visible spectra of the Au(III) complex* ***C11*** *(10^{-4} M) in PBS (pH 7.4) recorded over time (left); and of* ***C11*** *before and after addition of GSH (2 eq.) recorded over time at room temperature (right).*

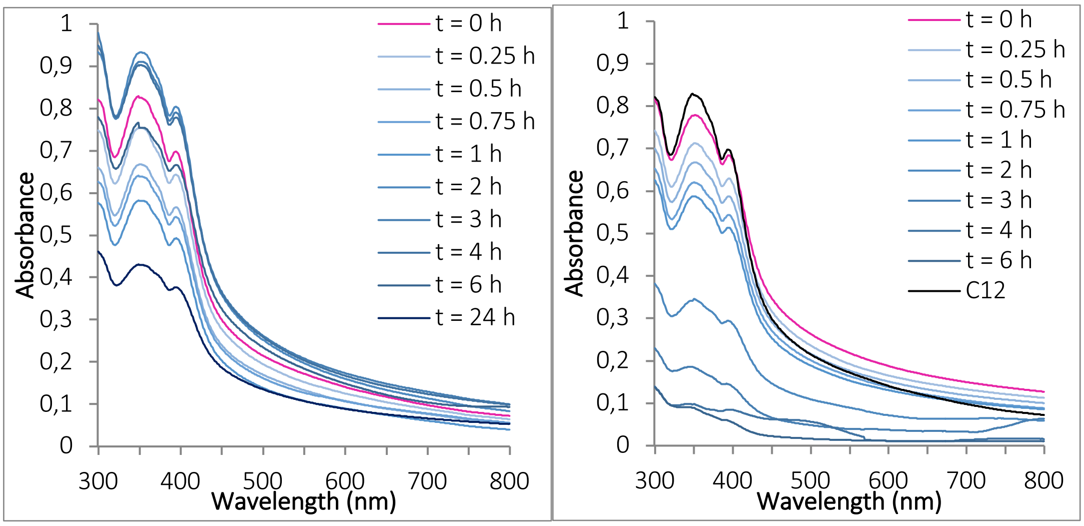

Figure S39: *UV-Visible spectra of the Au(III) complex* ***C12*** *(10^{-4} M) in PBS (pH 7.4) recorded over time (left); and of* ***C12*** *before and after addition of GSH (2 eq.) recorded over time at room temperature (right).*

A3. Stability studies of phenanthroline series by UV-visible spectrophotometry

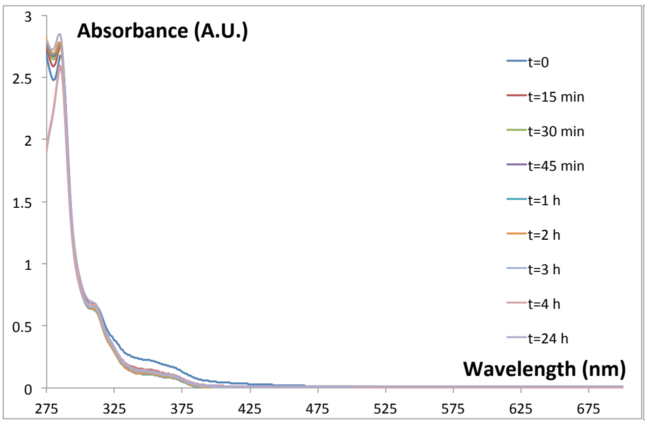

Figure S40: *UV-Visible spectra of complex **13** (10^{-4} M) in PBS (pH 7.4) over 24 h.*

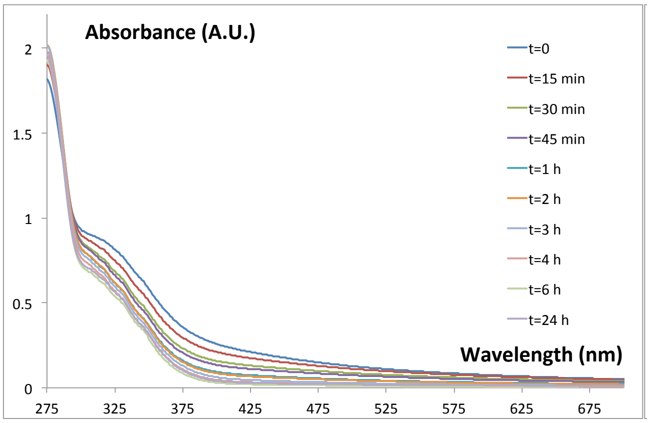

Figure S41: *UV-Visible spectra of complex **14** (10^{-4} M) in PBS (pH 7.4) over 24 h.*

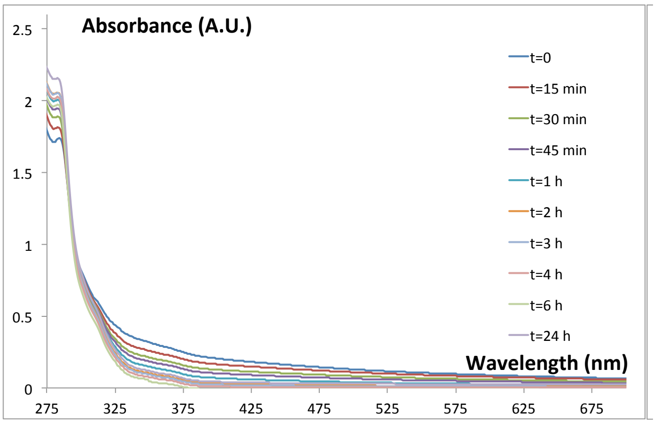

Figure S42: *UV-Visible spectra of complex **15** (10^{-4} M) in PBS (pH 7.4) over 24 h.*

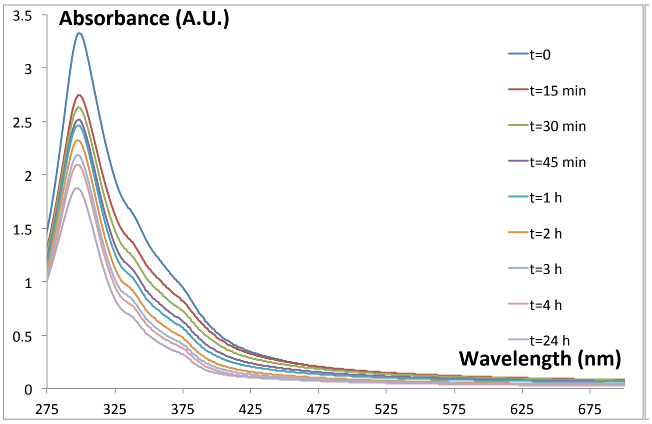

Figure S43: *UV-Visible spectra of complex* ***16*** *(10^{-4} M) in PBS (pH 7.4) over 24 h.*

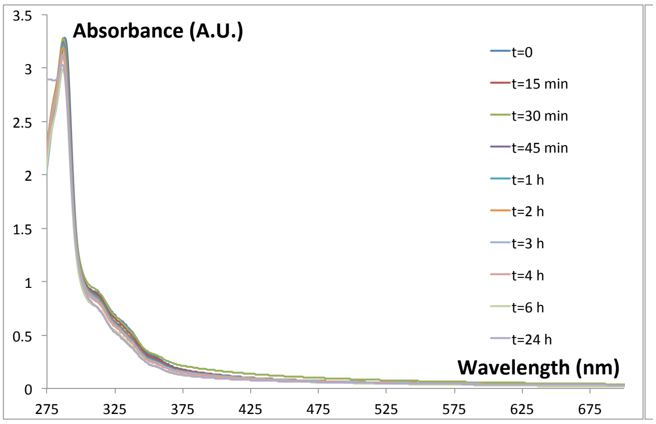

Figure S44: *UV-Visible spectra of complex* ***17*** *(10^{-4} M) in PBS (pH 7.4) over 24 h.*

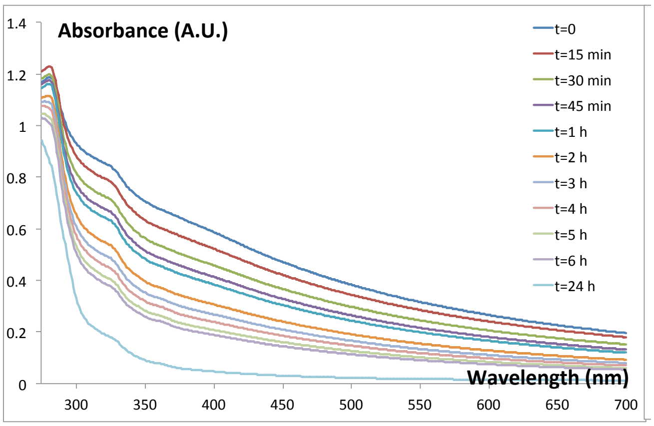

Figure S45: *UV-Visible spectra of complex* ***18*** *(10^{-4} M) in PBS (pH 7.4) over 24 h.*

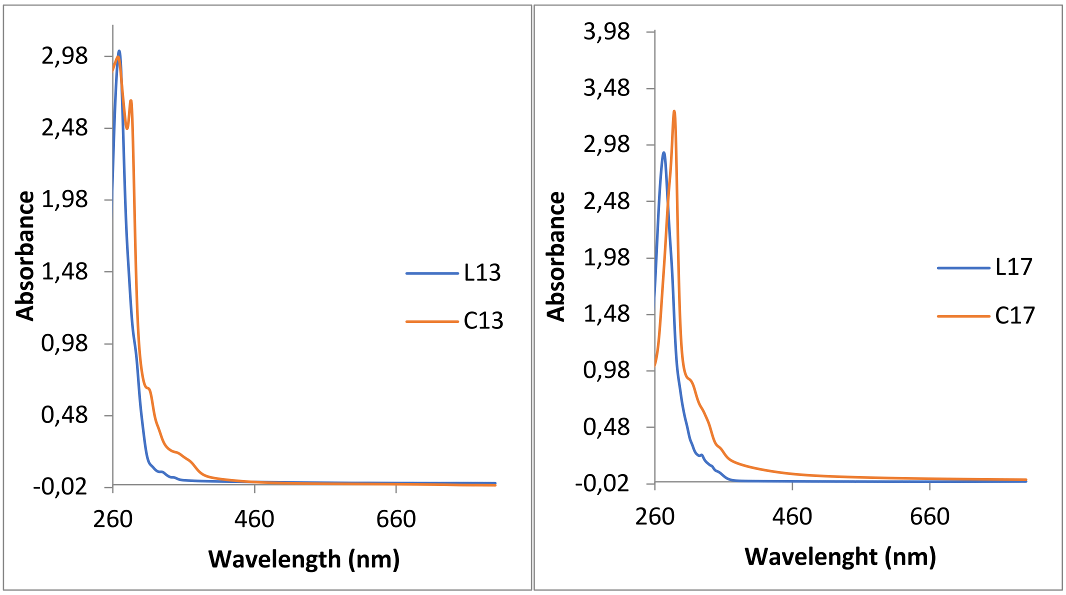

Figure S46: *Comparison between the absorption UV-Vis spectra in PBS (pH 7.4) of ligand* ***L13*** *(10^{-4} M) with related Au(III) complex* ***C13*** *(10^{-4} M) (left); and of ligand* ***L17*** *(10^{-4} M) with related Au(III) complex* ***C17*** *(10^{-4} M) (right).*

A4. Example of figures depicting the stopped-flow data analysis for a representative gold compound (C6) in human red blood cells (hRBC)

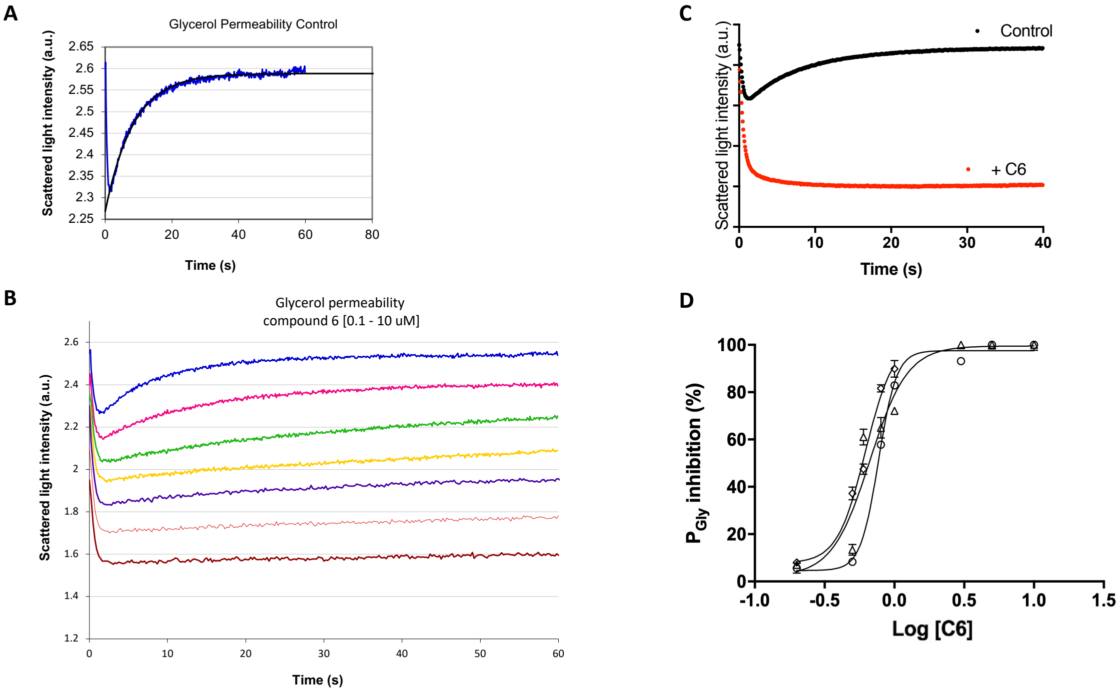

***Figure S47**: **A)** Example of stopped flow light scattering signal (blue) of the glycerol permeability control, with the exponential fit (black). **B)** Titration of hRBC with increasing concentration of compound **C6** illustrates a concentration dependent inhibition of glycerol permeability. At least 5-6 technical replicates are performed for each condition within one experiment. **C)** Glycerol permeability stopped-flow traces of control (black) compared to 5 μM **C6** (red). **D)** Three stopped-flow IC_{50} curves obtained for the inhibition of glycerol permeation via AQP3 by the Au(III) complex **C6** in hRBC after 30 min incubation. Each curve represents one biological replicate, which consist of at least 5-6 technical replicates, with corresponding mean and st.dev.. The final IC_{50} value is obtained as mean ± standard error of the mean (SEM) of at least three/four independent biological experiments.*

Appendix B

Table S1: *Osmotic permeability coefficient of both water (P_f) and glycerol (P_{gly}) for compound **1-5** and **Auphen** in hRBC (10 µM for 30 min).*

Complex	P_{gly} (% control)	P_f (% control)
Auphen	0.50 ± 0.10	105.25 ± 4.45
1	51.90 ± 7.55	101.74 ± 15.57
2	31.61 ± 3.11	99.71 ± 11.62
3	1.70 ± 1.31	101.15 ± 11.76
4	0.62 ± 0.12	86.82 ± 7.23
5	99.06 ± 10.43	94.55 ± 11.84

Data shown as means ± SD of three independent experiments

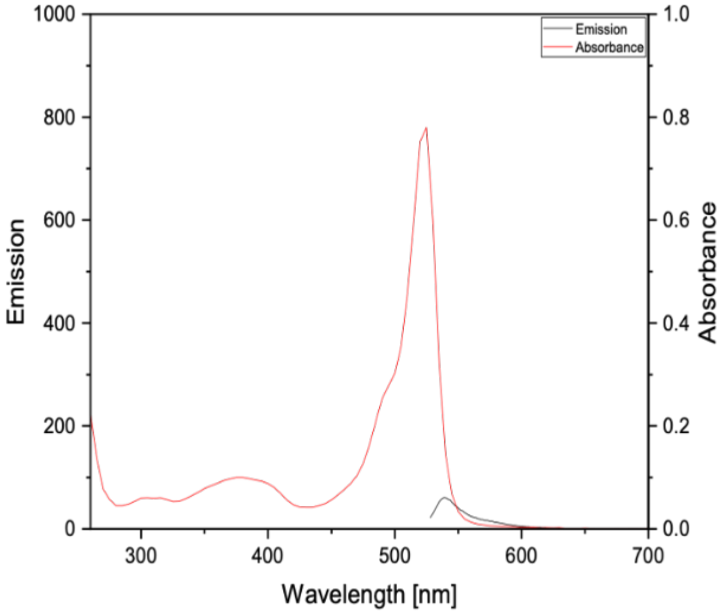

Figure S48**: Absorption and emission spectra of **G1

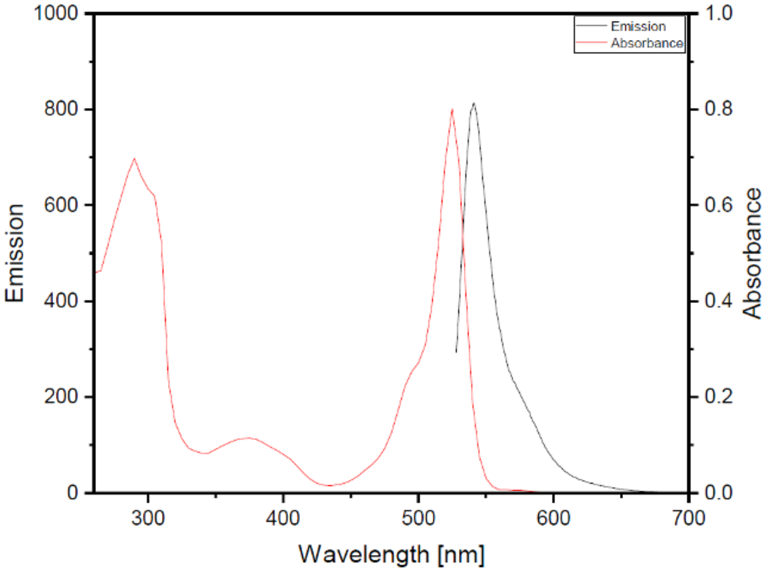

Figure S49**: Absorption and emission spectra of **LG1

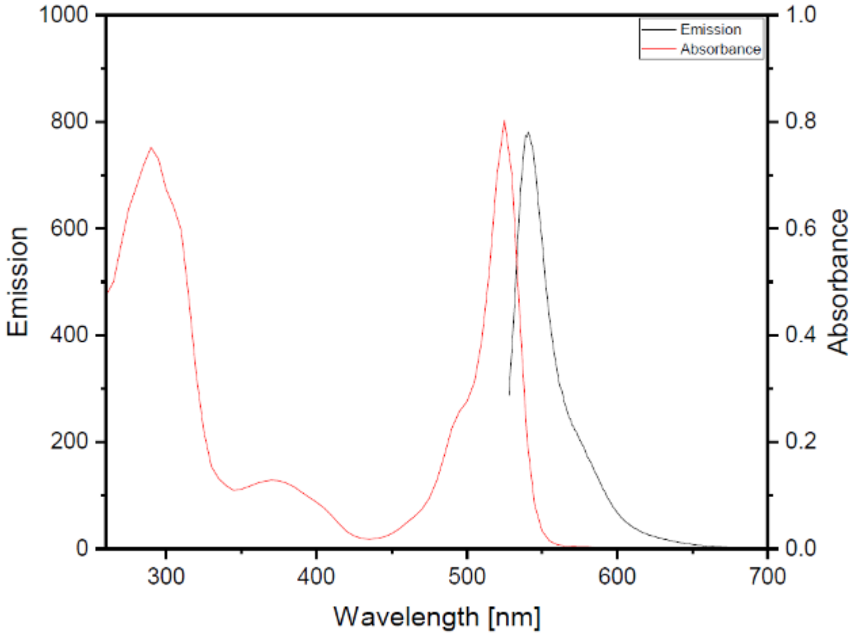

Figure S50*: Absorption and emission spectra of* ***CG1.BF$_4$***

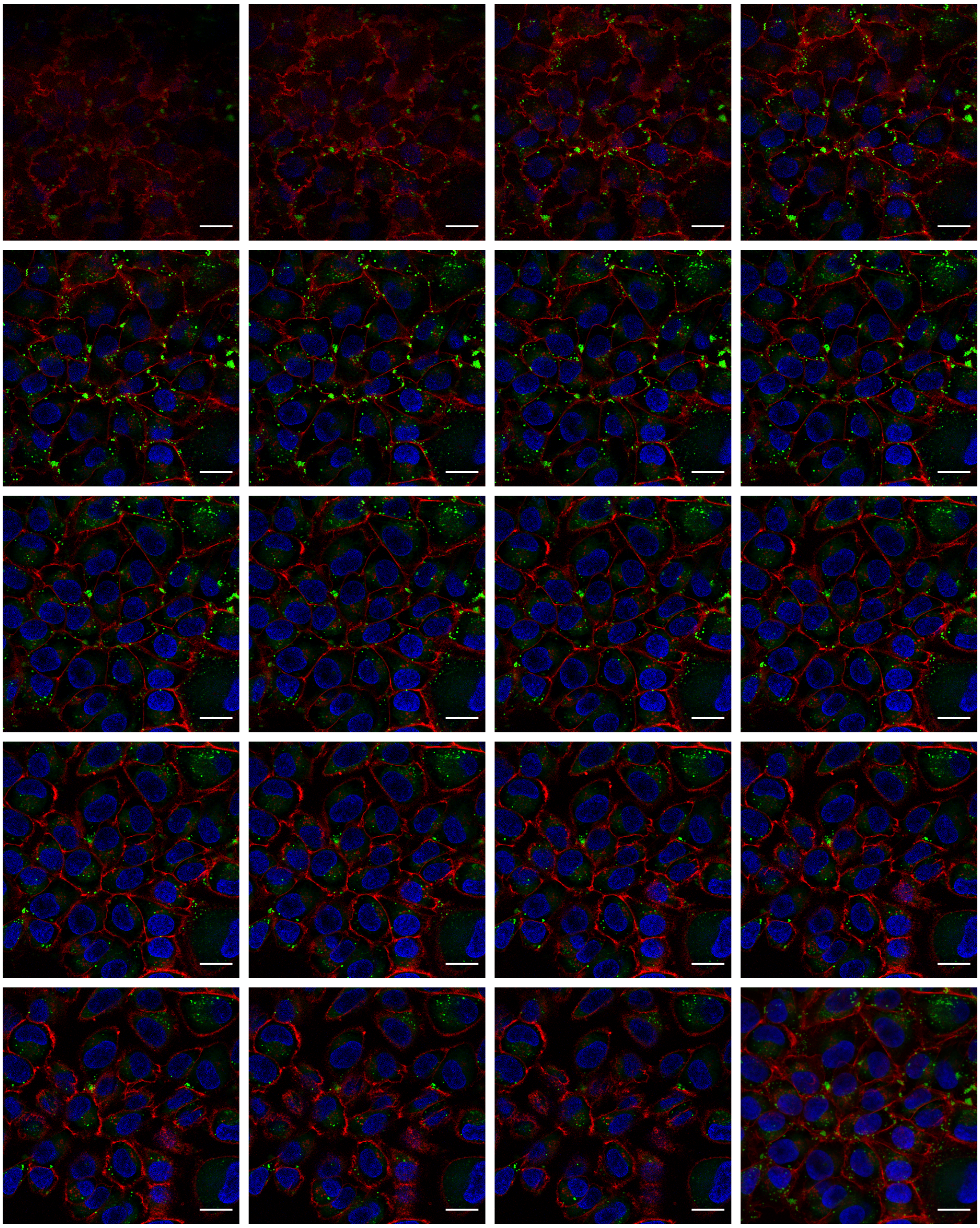

***Figure S51**: Complete z-stack CLSM images of A375 cells treated with 5 µM **CG1.NO$_3$** for 2 h. Scale bar represents 20 µm*

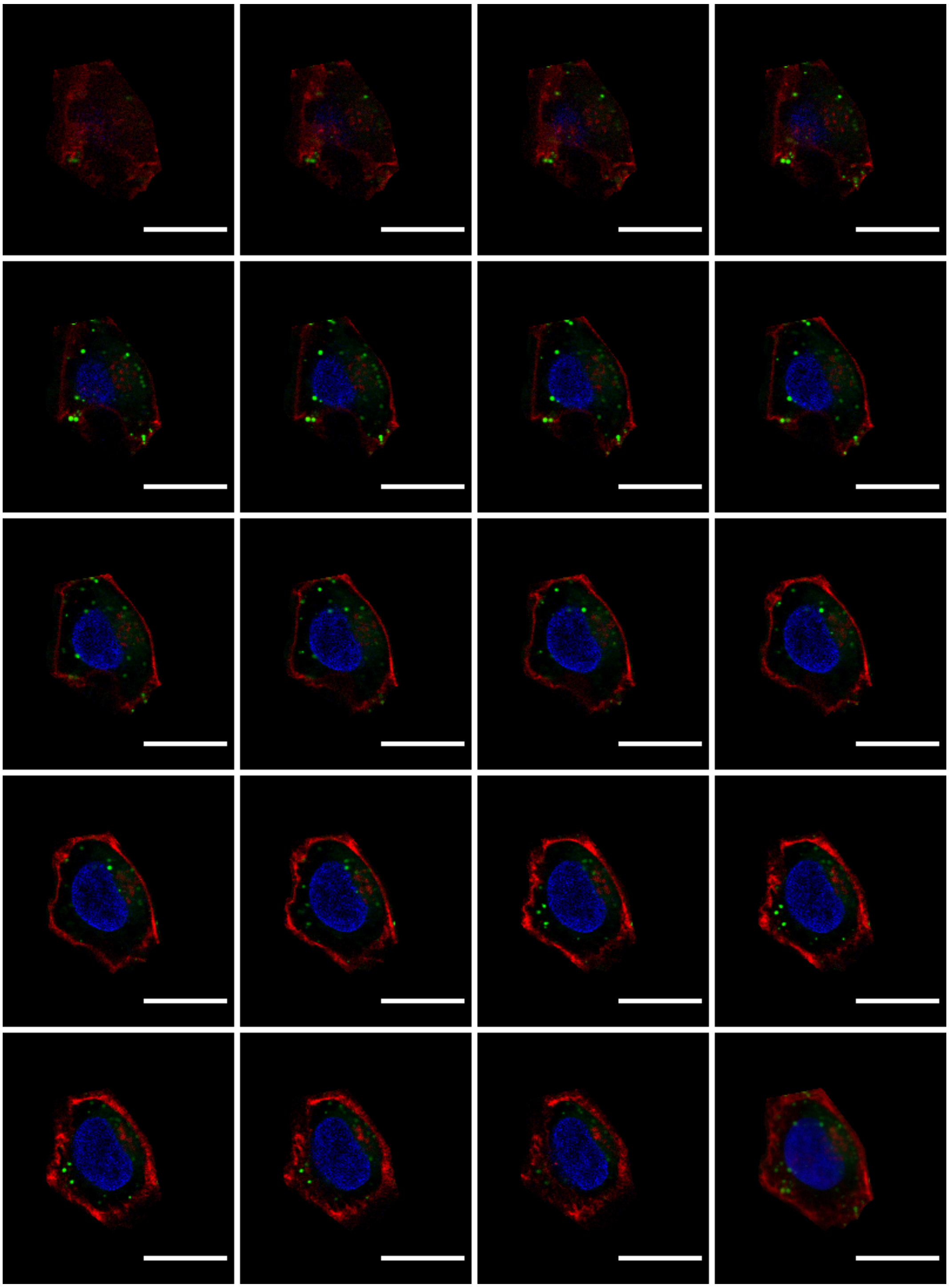

Figure S52: *Complete z-stack CLSM images of single A375 cell (selected from Figure S51) treated with 5 µM* ***CG1.NO₃*** *for 2 h. Scale bar represents 20 µm.*

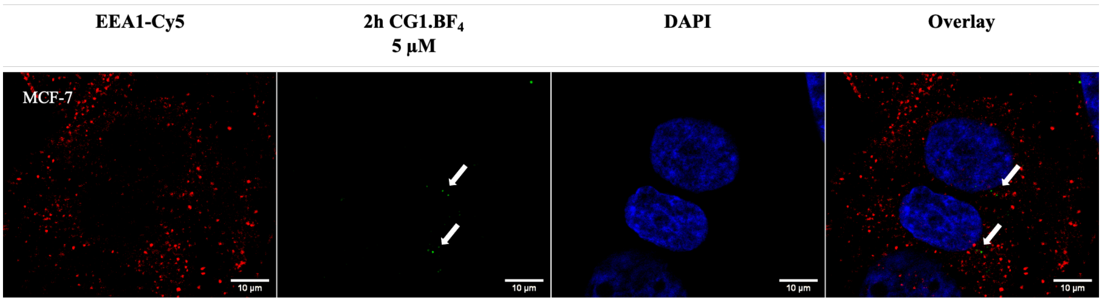

Figure S53: *Zoomed section of MCF-7 cells exposed to 2 h* ***CG1.BF$_4$*** *incubation, followed by fixation and immunolabeling of EEA1-Cy5. Arrows indicate complex presence. Scale bar represents 10 µm.*

Publications and conference attendance

Publications

Aikman B, de Almeida A, Meier-Menches SM, Casini A. Aquaporins in cancer development: opportunities for bioinorganic chemistry to contribute novel chemical probes and therapeutic agents. *Metallomics*. 2018 May 23;10(5):696-712. Doi: 10.1039/c8mt00072g.

Aikman B, Wenzel MN, Mósca AF, de Almeida A, Klooster WT, Coles SJ, Soveral G and Casini A. Gold(III) Pyridine-Benzimidazole Complexes as Aquaglyceroporin Inhibitors and Antiproliferative Agents. *Inorganics*. 2018 November 20;6(4):1-16. Doi: 10.3390/inorganics6040123

Han J, Räder AFB, Reichart F, **Aikman B**, Wenzel MN, Woods B, Weinmüller M, Ludwig BS, Stürup S, Groothuis GMM, Permentier HP, Bischoff R, Kessler H, Horvatovich P, Casini A. Bioconjugation of Supramolecular Metallacages to Integrin Ligands for Targeted Delivery of Cisplatin. *Bioconjug Chem*. 2018 November 21;29(11):3856-3865. Doi: 10.1021/acs.bioconjchem.8b00682

Wenzel MN, Mósca AF, Graziani V, **Aikman B**, Thomas SR, de Almeida A, Platts JA, Re N, Coletti C, Marrone A, Soveral G, Casini A. Insights into the Mechanisms of Aquaporin-3 Inhibition by Gold(III) Complexes: the Importance of Non-Coordinative Adduct Formation. *Inorg Chem*. 2019 February; 4;58(3):2140-2148. Doi: 10.1021/acs.inorgchem.8b03233.

Woods B, Döllerer D, **Aikman B**, Wenzel MN, Sayers EJ, Kühn FE, Jones AT, Casini A. Highly luminescent metallacages featuring bispyridyl ligands functionalised with BODIPY for imaging in cancer cells. *J Inorg Biochem*. 2019 October; 199:110781. Doi: 10.1016/j.jinorgbio.2019.110781.

Meier-Menches SM, **Aikman B**, Döllerer D, Klooster WT, Coles SJ, Santi N, Luk L, Casini A, Bonsignore R. Comparative biological evaluation and G-quadruplex interaction studies of two new families of organometallic gold(I) complexes featuring N-heterocyclic carbene and alkynyl ligands. *J Inorg Biochem*. 2020 January; 202:110844. Doi: 10.1016/j.jinorgbio.2019.110844.

Oberkofler J, **Aikman B**, Bonsignore R, Pöthig A, Platts J, Casini A, Kühn FE. Exploring the Reactivity and Biological Effects of Heteroleptic N-Heterocyclic Carbene Gold(I)-Alkynyl Complexes. *European Journal of Inorganic Chemistry*. 2020 March 27;2020(11-12):1040–1051. Doi: 10.1002/ejic.201901043.

Pimpão C, Wragg D, Bonsignore R, **Aikman B**, Pedersen PA, Leoni S, Soveral G and Casini A. Mechanisms of irreversible aquaporin-10 inhibition by organogold compounds studied by combined biophysical methods and atomistic simulations. *Metallomics*. 2021 September; 13(9): 1-11. Doi: 10.1093/mtomcs/mfab053.

Conference attendance

TUM-IAS workshop “Inorganic Chemistry meets Medicine. Die Technische Universität München (TUM), Munich, Germany. (24/10/17 – 26/10/17).

Poster contribution: New Au(III)complexes as selective aquaporin inhibitors and their potential use as chemical probes or as anticancer agents.

ISABIC-15 International Symposium on Applied Bioinorganic Chemistry. Nara Kasugano International Forum, “IRAKA”, Nara, Japan. (02/06/19 – 05/06/19).

Poster contribution: Highly Fluorescent Metallacages functionalized with BODIPYs as drug delivery systems for cisplatin.

Received the Chemical Society Reviews Poster Award.